# Light-Emitting Diodes

SECOND EDITION

E. Fred Schubert

CAMBRIDGE

Nichia Exhibit 1014
Page 1

CAMBRIDGE www.cambridge.org/9780521865388

This page intentionally left blank

# LIGHT-EMITTING DIODES

SECOND EDITION

Revised and fully updated, the Second Edition of this textbook offers a comprehensive explanation of the technology and physics of light-emitting diodes (LEDs) such as infrared, visible-spectrum, ultraviolet, and white LEDs made from III–V semiconductors. The elementary properties of LEDs such as electrical and optical characteristics are reviewed, followed by the analysis of advanced device structures.

With nine additional chapters, the treatment of LEDs has been vastly expanded, including new material on device packaging, reflectors, UV LEDs, III–V nitride materials, solid-state sources for illumination applications, and junction temperature. Radiative and non-radiative recombination dynamics, methods for improving light extraction, high-efficiency and high-power device designs, white-light emitters with wavelength-converting phosphor materials, optical reflectors, and spontaneous recombination in resonant-cavity structures, are discussed in detail. Fields related to solid-state lighting such as human vision, photometry, colorimetry, and color rendering are covered beyond the introductory level provided in the first edition. The applications of infrared and visible-spectrum LEDs in silica fiber, plastic fiber, and free-space communication are also discussed. Semiconductor material data, device design data, and analytic formulae governing LED operation are provided.

With exercises, solutions and illustrative examples, this textbook will be of interest to scientists and engineers working on LEDs, and to graduate students in electrical engineering, applied physics, and materials science.

Additional resources for this title are available online at www.cambridge.org/9780521865388.

E. Fred Schubert received his Ph.D. degree with Honors in Electrical Engineering from University of Stuttgart in 1986 and is currently a Wellfleet Senior Constellation Professor of the Future Chips Constellation at Rensselaer Polytechnic Institute. He has made several pioneering contributions to the field of LEDs, including the first demonstration of the resonant-cavity light-emitting diode (RCLED). He has authored or co-authored more than 200 publications including *Doping in III–V Semiconductors* (Cambridge University Press, 1993, 0-521-01784-X) for which he was awarded the VDE Literature Prize. He is inventor or co-inventor of 28 US Patents and a Fellow of the IEEE, APS, OSA, and SPIE. He received the Senior Research Award of the Humboldt Foundation, the Discover Award for Technological Innovation, the RD 100 Award, and Boston University's Provost Innovation Fund Award.

*Note*: This book contains many figures in which color adds important information. For this reason, all figures are available in color on the Internet at the following websites: <http://www.cambridge.org/9780521865388> and <http://www.LightEmittingDiodes.org>.

# LIGHT-EMITTING DIODES

SECOND EDITION

E. FRED SCHUBERT

*Rensselaer Polytechnic Institute,*
*Troy, New York*

CAMBRIDGE
UNIVERSITY PRESS

Nichia Exhibit 1014
Page 5

CAMBRIDGE UNIVERSITY PRESS
Cambridge, New York, Melbourne, Madrid, Cape Town, Singapore, São Paulo

Cambridge University Press
The Edinburgh Building, Cambridge CB2 8RU, UK
Published in the United States of America by Cambridge University Press, New York

www.cambridge.org
Information on this title: www.cambridge.org/9780521865388

© First edition E. Fred Schubert 2003
Second edition E. Fred Schubert 2006

This publication is in copyright. Subject to statutory exception and to the provision of relevant collective licensing agreements, no reproduction of any part may take place without the written permission of Cambridge University Press.

First published in print format 2006

ISBN-13 978-0-511-34476-3 eBook (EBL)
ISBN-10 0-511-34476-7 eBook (EBL)

ISBN-13 978-0-521-86538-8 hardback
ISBN-10 0-521-86538-7 hardback

Cambridge University Press has no responsibility for the persistence or accuracy of urls for external or third-party internet websites referred to in this publication, and does not guarantee that any content on such websites is, or will remain, accurate or appropriate.

# 11

## Packaging

### *11.1 Low-power and high-power packages*

Virtually all LEDs are mounted in a package that provides two electrical leads, a transparent optical window for the light to escape, and, in power packages, a thermal path for heat dissipation. The chip-encapsulating material advantageously possesses high optical transparency, a high refractive index, chemical inertness, high-temperature stability, and hermeticity. The refractive index contrast between the semiconductor and air is reduced by including an encapsulant thereby increasing the light extraction efficiency. Virtually all encapsulants are polymers with a typical refractive index of 1.5 to 1.8. A reduced index contrast at the semiconductor surface increases the angle of total internal reflection thereby enlarging the light escape cone and the extraction efficiency.

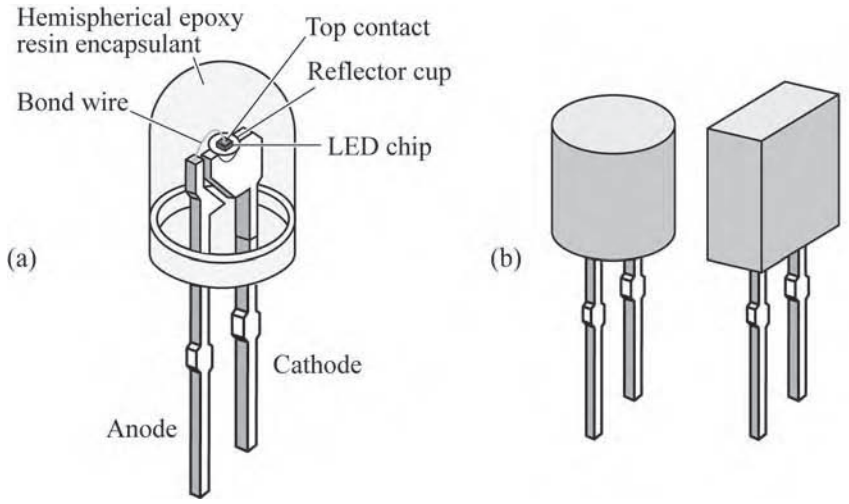


Fig. 11.1. Typical packages; (a) LED with hemispherical encapsulant; (b) LEDs with cylindrical and rectangular encapsulant.

A ***low-power package*** is shown in Fig. 11.1 (a). The active device is die-bonded or soldered to the bottom of a cup-like depression ("reflector cup") in one of the lead wires (usually the cathode lead). A bond wire connects the LED top contact to the other lead wire (usually the

anode lead). The LED package shown in the figure is frequently referred to as a “5 mm” or “T1-3/4” package.

In low-power LEDs, the encapsulant has the shape of a hemisphere, as shown in Fig. 11.1 (a), so that the angle of incidence at the encapsulant–air interface is always normal. As a result, total internal reflection does not occur at the encapsulant–air interface. There are types of LEDs that do *not* have a hemispherical shape for the encapsulant. Some LEDs have a rectangular or cylindrical shape with a planar front surface. Examples of such shapes are shown in Fig. 11.1 (b). Planar-surface LEDs are frequently used under circumstances where the intended viewing angle is close to normal incidence or where the LED is intended to blend in with a planar surface. Encapsulants provide protection against unwanted mechanical shock, humidity, and chemicals. The encapsulant also stabilizes the anode and cathode lead, the LED chip and bonding wire.

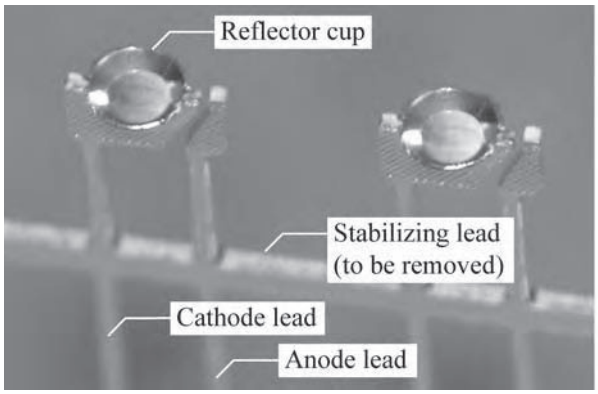


Fig. 11.2. Leadframe of a conventional 5 mm package for mounting and connecting LED chips. The stabilizing lead is cut off once mechanical stability between the anode and cathode lead has been established by the epoxy encapsulant.

A photograph of a series of LED ***leadframes*** is shown in Fig. 11.2. The individual leadframes are connected via a temporary stabilizing lead that is removed after die bonding, wire bonding, and the establishment of mechanical stability between anode and cathode lead by the epoxy encapsulant. The LED chip is die-bonded to the flat bottom of the highly reflective ***reflector cup*** with a silver-loaded electrically conductive epoxy being a common die-bonding material. Note that for power chips, metal-based solders are preferable as die-bonding materials due to their inherently lower thermal resistance compared with conductive epoxies.

A ***power package*** is shown in Fig. 11.3. Power packages have a *direct, thermally conductive path* from the LED chip, through the package, to a heat sink, e.g. a printed circuit board. The power package shown in the figure has several advanced features. Firstly, the package contains an Al or Cu heatsink slug with low thermal resistivity to which the LED submount is soldered by a metal-based solder. Secondly, the chip is encapsulated with silicone. Because standard silicone



Nichia Exhibit 1014
Page 8

retains mechanical softness in its cured state, the silicone encapsulant is covered with a plastic cover that also serves as lens. Thirdly, the chip is directly mounted on a Si submount that includes electrostatic discharge protection (ESD).

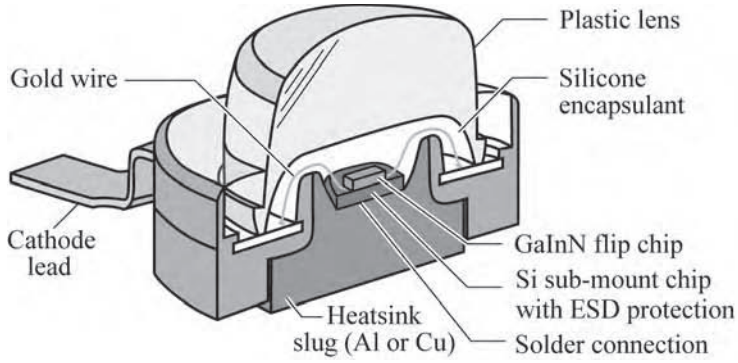


Fig. 11.3. Cross section through high-power package. The heatsink slug can be soldered to a printed circuit board for efficient heat removal. This package, called the *Barracuda package,* was introduced by Lumileds Corp. (adapted from Krames, 2003).

Photographs of the high-power package are shown in Fig. 11.4 including a high-magnification micrograph, Fig. 11.4 (b), revealing interdigitated contacts of a GaN-based LED. Fig. 11.4 (c) shows the package soldered to a printed-circuit board that possesses high thermal conductivity for efficient cooling (LED Museum, 2003). Several light-emitting diodes located on a single chip may be interconnected in series to increase operating voltage and decrease operating current of a device (Krames *et al*., 2002, 2003).

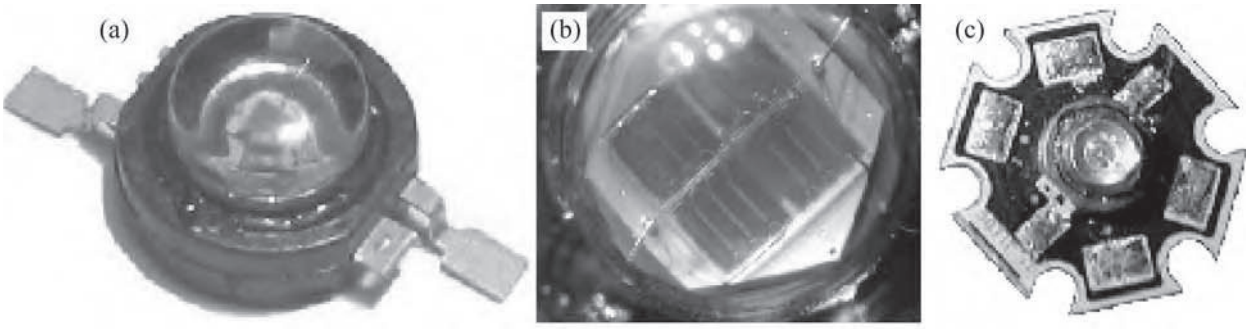


Fig. 11.4. (a) High-power package; (b) LED die in package; (c) package on printed circuit board with high thermal conductivity ((a) after Krames, 2003; (b), (c) after after LED Museum, 2003).

### *11.2 Protection against electrostatic discharge (ESD)*

Electrostatic discharge (ESD) can be a major failure mechanism for electronic and optoelectronic components (Voldman, 2004). Consider that a charge $+Q$ is brought into contact with one of the diode electrodes. Consider further that the charge $+Q$ is discharged uniformly over a time $\Delta t$, so

that a current of $I = +Q / \Delta t$ flows through the device.

Let us first assume that the charge is brought into contact with the cathode of the LED and that the anode is grounded. The current will discharge with the diode in the reverse polarity. Taking the equivalent circuit of the reverse-biased diode as a capacitor $C$ and a parallel resistor $R_p$, the voltage across the p-n junction in the steady state will rise to $IR_p$. Thus the energy dissipated in the device during the reverse discharge is then given by $I^2 R_p \Delta t$.

Let us next assume that the charge is brought into contact with the anode of an LED and that the cathode is grounded. The current will discharge with the diode in the forward polarity. Taking the equivalent circuit of the forward-biased diode as a voltage source with voltage $V_{th}$ with a series resistor $R_s$, the steady-state voltage across the p-n junction is $V_{th} + IR_s$, which, in the limit of a high current, can be approximated by $IR_s$. Thus the energy dissipated in the device during the forward discharge is approximately $I^2 R_s \Delta t$.

Because $I^2 R_p \Delta t >> I^2 R_s \Delta t$, it is evident that the energy dissipated per reverse discharge event is much higher than the energy dissipated per forward discharge event, suggesting that *reverse* discharges are more damaging than *forward* discharges. This contention has indeed been confirmed by experiments (Wen *et al*., 2004).

Wide-bandgap diodes (such as GaN-based diodes) are particularly prone to ESD failures, due to inherently high values of $R_p$ (low reverse saturation currents and high breakdown voltages). This has spurred the development of ESD protection circuits for III–V nitride diodes (Steigerwald *et al*., 2002; Sheu, 2003).

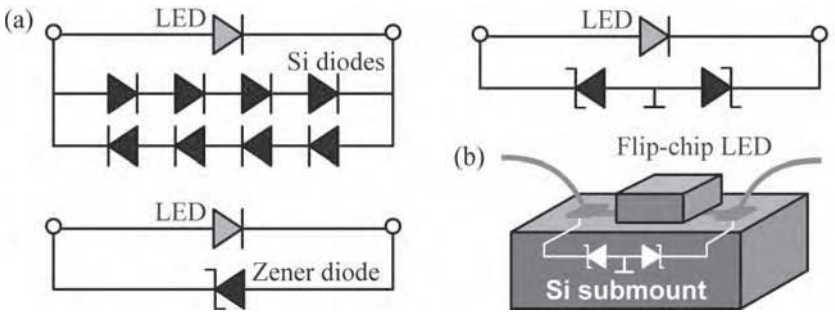


Fig. 11.5. (a) Electrostatic discharge (ESD) protection circuits using multiple Si p-n junctions, one Zener diode, and two Zener diodes. (b) ESD protection integrated into a Si submount (two-Zender diode circuit after Lumileds, 2004).

Electrostatic discharge-protection circuits can consist of a series of Si diodes, one Si Zener diode, or two Si Zener diodes, as shown in Fig. 11.5, with two Zener diodes being a common configuration (Steigerwald *et al*., 2002; Lumileds, 2004). The current caused by an electrostatic discharge will bypass the LED and flow through the ESD protection circuit, particularly for reverse discharges. ESD protection circuits have been integrated with Si submounts (Steigerwald


Nichia Exhibit 1014
Page 10

*et al*., 2002; Lumileds, 2004). Using one or two Zener diodes or placing several Si diodes in series increases the threshold voltage of the ESD circuit to values beyond the turn-on voltage of the LED. Thus, under normal operating conditions, the current through the ESD circuit is negligibly small.

Sheu (2003) proposed a Schottky diode integrated with the LED on the same chip. The structure, shown in Fig. 11.6 (a), consists of a large-area p-n junction diode and, separated by a deep trench, a small-area Schottky diode. The Schottky diode, fabricated on the n-type buffer layer of a GaInN LED, is forward biased when the LED is biased in the reverse polarity. For reverse electrostatic discharges, the current flows mostly through the Schottky diode, thereby bypassing the p-n junction and preventing damage to the p-n junction. For forward electrostatic discharges, the current flows through the p-n junction. In an alternative structure, shown in Fig. 11.6 (b), the Schottky diode is replaced by a p-n junction diode (Cho, 2005).

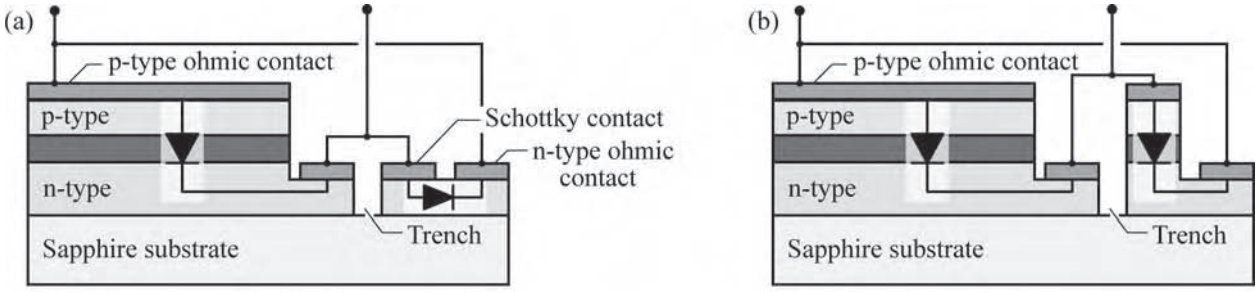


Fig. 11.6. On-chip ESD protection using (a) a small-area Schottky diode on the n-type buffer layer of a GaInN device and (b) a small-area p-n junction diode (Schottky diode circuit after Sheu, 2003).

## *11.3 Thermal resistance of packages*

The thermal resistance of LED packages together with the maximum temperature of operation determines the maximum thermal power that can be dissipated in the package. The maximum temperature of operation may be determined by reliability considerations, by the degradation of the encapsulant, and by internal-quantum-efficiency considerations. Several types of LED packages and their thermal resistance are shown in Fig. 11.7 (Arik *et al*., 2002). Early LED packages, introduced in the late 1960s and still used for low-power packages at the present time, have a high thermal resistance of about 250 K/W. Packages using ***heatsink slugs*** made of Al or Cu that transfer heat from the chip directly to a printed circuit board (PCB), which in turn spreads the heat, have thermal resistances of 6–12 K/W. It is expected that thermal resistances of

< 5 K/W will be achieved for advanced passively cooled power packages.

Note that the packages shown in Fig. 11.7 do not use ***active cooling***, i.e. fan cooling. Heatsinks with cooling fins and fan are commonly used to cool electronic microchips including Si CMOS microprocessors. They have thermal resistances < 0.5 K/W. The use of active cooling devices would reduce the power efficiency of LED-based lighting systems.

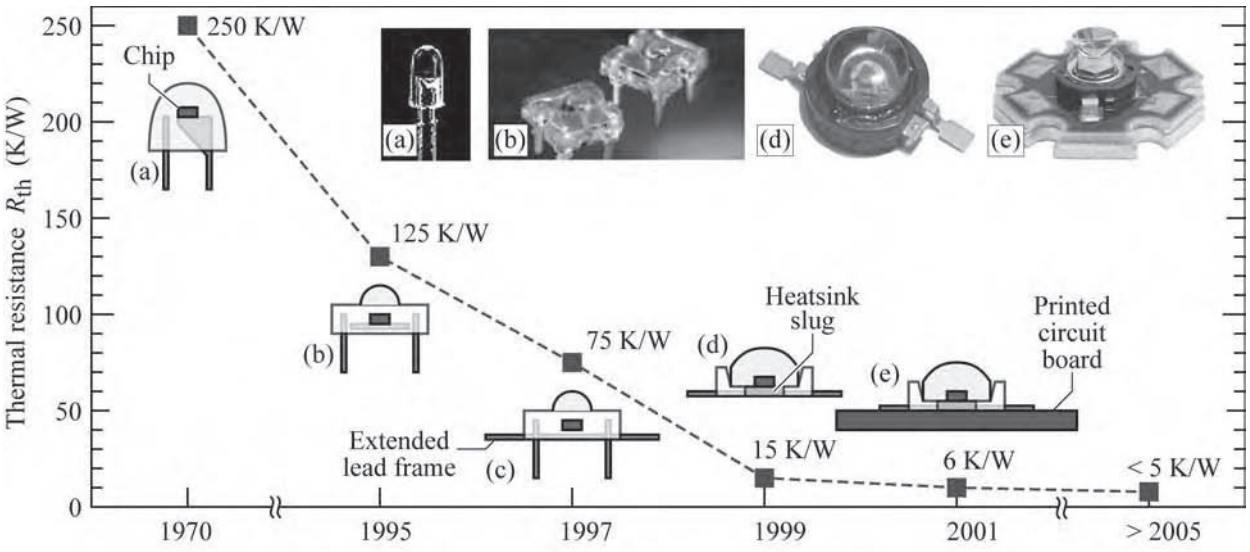


Fig. 11.7. Thermal resistance of LED packages: (a) 5mm (b) low-profile (c) low-profile with extended lead frame (d) heatsink slug (e) heatsink slug mounted on printed circuit board (PCB). Trade names for these packages are "Piranha" (b and c, Hewlett Packard Corp.), "Barracuda" (d and e, Lumileds Corp.), and "Dragon" (d and e, Osram Opto Semiconductors Corp.) (adapted from Arik *et al*., 2002).

### *11.4 Chemistry of encapsulants*

Encapsulants have several requirements including high transparency, high refractive index, chemical stability, high-temperature stability, and hermeticity. All encapsulants are based on polymers, several of which are shown in Fig. 11.8. A simple polymer molecule consisting of a hydrocarbon chain is shown in Fig. 11.8 (a). Branching and cross linking the polymer molecule results in rubber compounds as shown in Fig. 11.8 (b). Such rubber compounds lack transparency and cannot be used as LED encapsulants. However, it is well known that oxides are frequently transparent. In fact, all encapsulants used for LEDs contain oxygen.

A common encapsulant is ***epoxy resin*** (also called epoxy), which remains transparent and does not show degradation over many years for long-wavelength visible-spectrum and IR LEDs. However, it has been reported that epoxy resins lose transparency in LEDs emitting at shorter



Nichia Exhibit 1014
Page 12

wavelengths, i.e. in the blue, violet, and UV (Barton *et al*., 1998). Epoxy resins are chemically stable up to temperatures of about 120 °C. Prolonged exposure to temperatures greater than 120 °C leads to yellowing (loss of transparency).

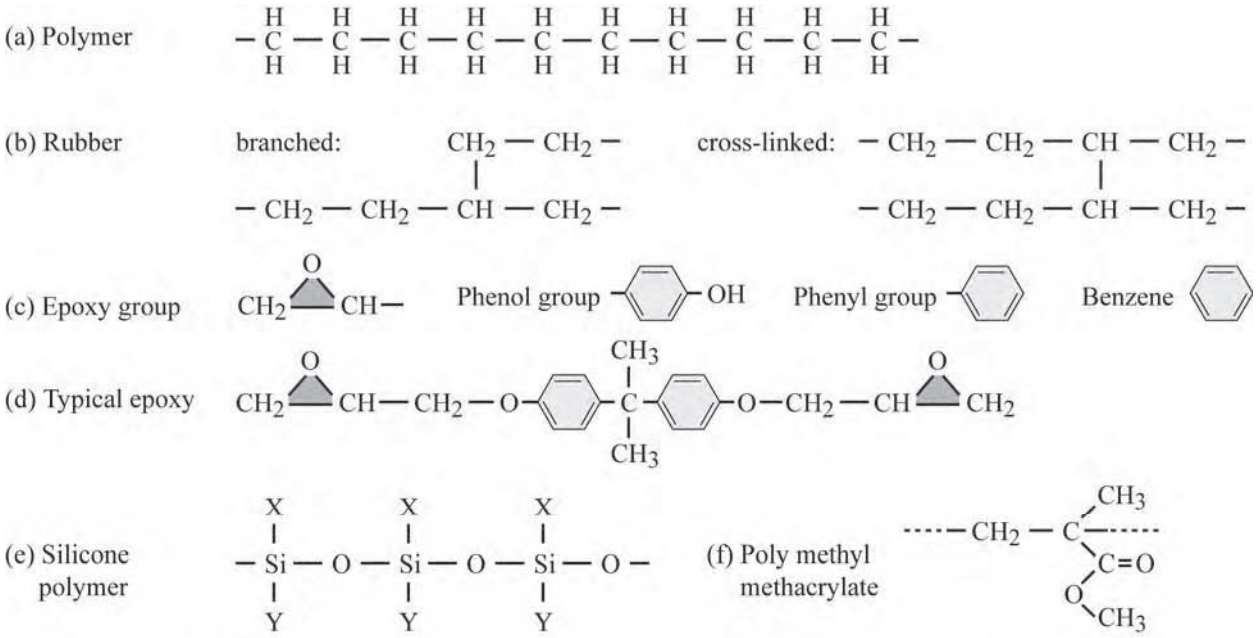


Fig. 11.8. Chemical structures of polymers. Epoxy resins, silicone polymers, and poly methyl methacrylate (PMMA) are used as LED encapsulants. In the silicone structure, X and Y represent atoms or molecules such as H, $CH_3$ (methyl), $C_6H_5$ (phenyl).

The ***epoxy group*** shown in Fig. 11.8 (c) contains an O atom attached to two C atoms already bonded to each other. Such a three-membered ring consisting of one oxygen and two carbon atoms is part of the epoxy resin structure shown in Fig. 11.8 (d). Solid epoxy resins are formed by stoichiometrically mixing two liquid compounds, an epoxide with another compound, a resin, having two hydroxyl groups. ***Resins*** are oil-like substances that frequently have phenol groups. The phenol group, $–C_6H_4–OH$, is derived from the phenyl group, $–C_6H_5$ by removing one H atom and replacing it with the hydroxyl group, –OH. The phenyl group is derived from benzene, the well-known six-atom carbon ring, $C_6H_6$, by removing one H atom. Under a thermal-setting process, the epoxide groups co-polymerize with hydroxyl groups of the resin.

Typical epoxy resins for encapsulation are thermally curable two-part liquid systems consisting of bisphenol-A based or cycloaliphatic epoxide and anhydride (Kumar *et al*., 2001). The formation of the epoxy resin requires a short high-temperature cure (120 °C). The two-part system has to be in stoichiometric proportions. Resin-rich compositions lead to lower glass transition temperatures while hardener-rich compositions may lead to discoloration of the

encapsulant. The refractive index of epoxy resin is near 1.6. Besides being transparent, epoxy resin is noted for its good mechanical properties and good thermal stability. However, prolonged exposure of the epoxy to temperatures exceeding 120 °C will lead to discoloration and loss of transparency. In addition to thermo-setting epoxy resins, UV-curable and microwave-curable epoxy resins have been reported (Kumar *et al*. 2001; Gorczyk, 2001; Flick, 1993).

To overcome the limited thermal stability of epoxies, ***silicone encapsulants*** have been used since the early 2000s. Silicone is thermally stable up to temperatures of about 190 °C, significantly higher than epoxies (Crivello, 2004). Furthermore silicone is flexible (and remains flexible for decades) thereby reducing the mechanical stress on the semiconductor chip. ***Silicone*** is a polymer whose basic structure is shown in Fig. 11.8 (e). Silicone contains Si and O thereby resembling $SiO_2$ more so than epoxy resins. This resemblance suggests that silicone encapsulants are chemically and thermally stable and do not lose transparency as easily as epoxy resins. It may be desirable to develop encapsulants that are $SiO_2$-like because $SiO_2$ has excellent thermal and chemical stability and very high transparency (Crivello, 2004). On the other hand, silica lacks the flexibility that silicones offer.

***Poly methyl methacrylate*** or briefly ***PMMA*** is a less common encapsulant used for LEDs. The chemical structure of methyl methacrylate, the elementary cell of PMMA, is shown in Fig. 11.8 (f). PMMA is also known under the name of acrylic glass and under the product name Plexiglas. The relatively low refractive index of PMMA ($\overline{n}$ = 1.49 in the wavelength range 500–650 nm) results in a limited extraction efficiency when used with high-index semiconductors.

### *11.5 Advanced encapsulant structures*

***Graded-index encapsulants*** consisting of several layers with different refractive indices were demonstrated by Lee *et al*. (2004). The layer of highest refractive index is in contact with the semiconductor chip. The outer layers of the encapsulant have lower refractive indices. Extraction efficiencies exceeding those with a constant refractive index can be attained by using such refractive-index graded encapsulants.

Encapsulants containing ***mineral diffusers*** cause light to reflect, refract, and scatter, thereby randomizing the propagation direction and isotropizing the far-field distribution. For multi-color devices (e.g. multi-chip white LEDs), mineral diffusers uniformize the color distribution. Mineral diffusers are optically transparent substances, such as $TiO_2$, $CaF_2$, $SiO_2$, $CaCO_3$, and $BaSO_4$, with a refractive index different from that of the encapsulant (Reeh *et al*., 2003).

Encapsulants containing ***nanoparticles*** with a high refractive index (e.g. titania, magnesia,



Nichia Exhibit 1014
Page 14

yttria, zirconia, alumina, GaN, AlN, ZnO, ZnSe) have been proposed by Lester *et al*. (1998). Nanoparticles embedded into a host (usually a polymer) do not scatter light if they are uniformly distributed and if their size is much smaller than the wavelength. The refractive index of the of the nanoparticle-loaded encapsulant is given by

$$\bar{n} = \frac{\bar{n}_{\text{host}} V_{\text{host}} + \bar{n}_{\text{nano}} V_{\text{nano}}}{V_{\text{host}} + V_{\text{nano}}} \tag{11.1}$$

where $V_{\text{host}}$ and $V_{\text{nano}}$ refer to the volume of the host and nanoparticles, respectively. For high loading factors, the refractive index of the encapsulant can significantly exceed that of the host, thereby enlarging the semiconductor escape cone and increasing the extraction efficiency.

## *References*


Arik M., Petroski J., and Weaver S. "Thermal challenges in the future generation solid state lighting applications: light emitting diodes" *Eighth Intersociety Conference on Thermal and Thermomechanical Phenomena in Electronic Systems* (Cat. No.02CH37258) May 30–June 1 2002, p. 113 (IEEE, Piscataway NJ, 2002)

Barton D. L., Osinski M., Perlin P., Helms C. J., and Berg N. H. "Life tests and failure mechanisms of GaN/AlGaN/InGaN light-emitting diodes" *Proc. SPIE* **3279**, 17 (1998)

Cho J., Samsung Advanced Institute of Technology, Suwon, Korea, personal communication (2005)

Crivello J. V., Rensselaer Polytechnic Institute, personal communication (2004)

Flick E. W. *Epoxy Resins, Curing Agents, Compounds, and Modifiers: An Industrial Guide* (Noyes Data Corporation/Noyes Publications, Park Ridge NJ, 1993)

Gorczyk J., Bogdal D., Pielichowski J., and Penczek P. "Synthesis of high molecular weight epoxy resins under microwave irradiation" *Fifth International Electronic Conference on Synthetic Organic Chemistry* (ECSOC-5), http://www.mdpi.org/ecsoc-5.htm, 1–30 (September 2001)

Krames M. R., Steigerwald D. A., Kish Jr. F. A., Rajkomar P., Wierer Jr. J. J., and Tan T. S. "III-nitride light-emitting device with increased light generating capability" US Patent 6,486,499 B1 (2002)

Krames M. R. "Overview of current status and recent progress of LED technology" *US Department of Energy Workshop* "*Solid State Lighting – Illuminating the Challenges*" Crystal City, VA, Nov. 13–14, 2003

Kumar R. N., Keem L. Y., Mang N. C., and Abubakar A. "Ultraviolet radiation curable epoxy resin encapsulant for light-emiting diodes" *4th International Conference on Mid-Infrared Optoelectronics Materials and Devices* (MIOMD) (2001)

LED Museum, http://ledmuseum.home.att.net/agilent.htm (2003)

Lee B. K., Goh K. S., Chin Y. L., and Tan C. W. "Light emitting diode with gradient index layering" US Patent 6,717,362 B1 (2004)

Lester S. D., Miller J. N., and Roitman D. B. "High refractive index package material and light emitting device encapsulated with such material" US Patent 5,777,433 (1998)

Lumileds Corporation *Luxeon reliability* Application Brief **AB25**, 11 (2004)

Reeh U., Höhn K., Stath N., Waitl G., Schlotter P., Schneider J., and Schmidt R. "Light-radiating semiconductor component with luminescence conversion element" US Patent 6,576,930 B2 (2003)

Sheu J.-K. "Group III–V element-based LED having ESD protection capacity" US Patent 6,593,597 B2 (2003)

Steigerwald D. A., Bhat J. C., Collins D., Fletcher R. M., Holcomb M. O., Ludowise M. J., Martin P. S., and Rudaz S. L. "Illumination with solid state lighting technology" *IEEE J. Sel. Top. Quantum Electron.* **8**, 310 (2002)

Voldman S. H. *ESD: Physics and Devices* (John Wiley and Sons, New York, 2004)
Wen T. C., Chang S. J., Lee C. T., Lai W. C., and Sheu J. K. "Nitride-based LEDs with modulation-doped AlGaN-GaN superlattice structures" *IEEE Trans. Electron Dev.* **51**, 1743 (2004)



Nichia Exhibit 1014
Page 16

and the GaAsP epitaxial layer. A large mismatch exists between GaAs and GaP (about 3.6%) so that many misfit dislocations occur when the critical thickness of GaAsP on GaAs is exceeded. As a result, the luminescence efficiency decreases substantially in GaAsP with increasing phosphorus content. GaAsP LEDs are therefore useful for low-brightness applications only.

It was realized early in the GaAsP work that the lattice mismatch between the GaAs substrate and the GaAsP epilayer reduces the radiative efficiency. It was also found that the radiative efficiency of the active p-n junction layer strongly depends on the growth conditions and, in particular, on the thickness of the GaAsP buffer layer (Nuese *et al*., 1969). A thick buffer layer reduces the dislocation density by annihilation of misfit dislocations. However, the dislocation density does not approach the low dislocation density of GaAs substrates, so that even with thick GaAsP buffer layers the dislocation density is substantial.

The band structure of GaAs, GaAsP, and GaP is shown schematically in Fig. 12.1. The figure shows that GaAsP is a direct-gap semiconductor for low phosphorus mole fractions. Beyond the direct–indirect crossover occurring at phosphorus mole fractions of about 45–50%, the semiconductor becomes indirect and the radiative efficiency drops rapidly (Holonyak *et al*., 1963, 1966). GaP is an indirect-gap semiconductor and therefore is unsuitable as an efficient LED material.

GaAsP and GaP LEDs are frequently doped with isoelectronic impurities such as nitrogen (Grimmeiss and Scholz, 1964; Logan *et al*., 1967a, 1967b, 1971; Craford *et al*., 1972; Groves and Epstein 1977; Groves *et al*. 1978a, 1978b). The isoelectronic impurities form an optically active level within the forbidden gap of the semiconductor so that carriers recombine radiatively via the nitrogen levels, as indicated in Fig. 12.1.

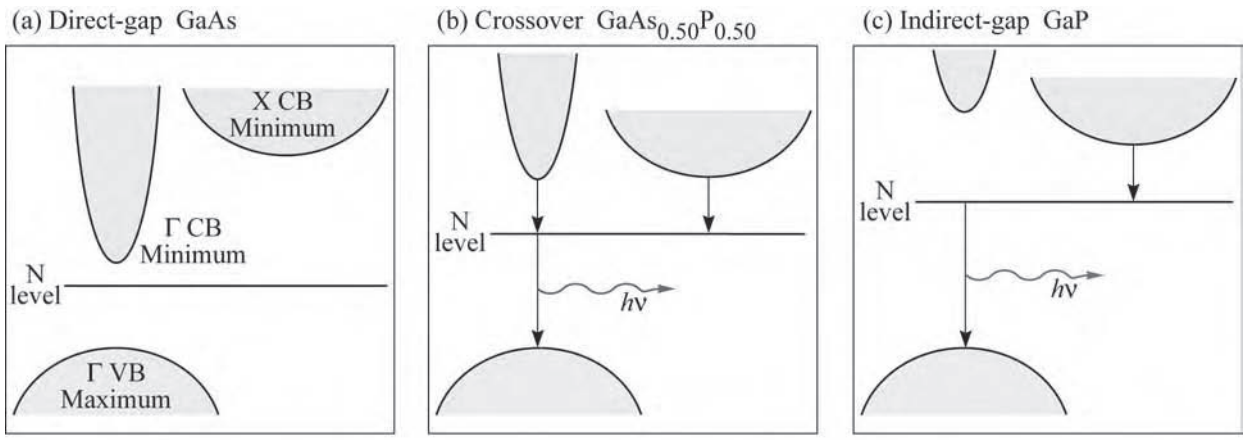


Fig. 12.1. Schematic band structure of GaAs, GaAsP, and GaP. Also shown is the nitrogen level. At a P mole fraction of 45–50%, the direct–indirect crossover occurs.



Nichia Exhibit 1014
Page 17

Isoelectronically doped LEDs are also interesting from a fundamental point of view. They are one of the first practical applications of Heisenberg's uncertainty principle. Isoelectronic impurities have an electronic wave function that is strongly localized in position space (small $\Delta x$). Therefore, the wave function is delocalized in momentum space (large $\Delta p$). Since the level is delocalized in momentum space, two vertical transitions can occur via the isoelectronic trap, with one of them being radiative. Physically speaking, the change in momentum, occurring when an electron makes a transition from the indirect X valley of the conduction band to the central Γ valley of the valence band, is absorbed by the isoelectronic impurity atom.

The emission wavelength of undoped and nitrogen-doped GaAsP is shown in Fig. 12.2 (Craford *et al*., 1972). The emission energy of GaAsP and GaP doped with the isoelectronic impurity nitrogen is below the bandgap of the semiconductor. Figure 12.2 illustrates that the emission energy is about 50–150 meV below the bandgap of the semiconductor. As a result, reabsorption effects are much less likely in nitrogen-doped structures compared with LEDs based on band-edge emission. This is a substantial advantage of LEDs doped with isoelectronic impurities.

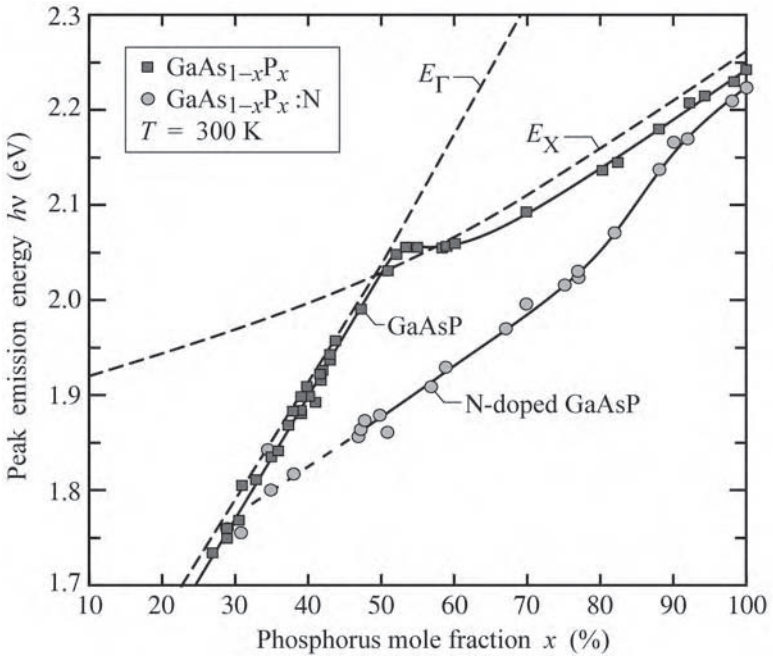


Fig. 12.2. Room-temperature peak emission energy versus alloy composition for undoped and nitrogen-doped GaAsP LEDs injected with a current density of 5 A/cm$^2$. Also shown is the energy gap of the direct-to-indirect ($E_\Gamma$-to-$E_X$) transition. The direct–indirect crossover occurs at $x \approx 50\%$ (after Craford *et al*., 1972).

Groves *et al*. (1978a, 1978b) showed that this advantage is particularly pronounced if only the active region is doped with nitrogen. In this case, the region of the p-n junction plane and the regions located within the carrier diffusion lengths from the junction plane are doped with nitrogen. Other regions, such as the confinement and window layers, are not doped with the

isoelectronic impurity, so that reabsorption of light by the isoelectronic impurities is limited to the narrow active region. Quantum efficiencies of several percent can be attained with GaP:N LEDs in which the nitrogen doping is limited to the active region.

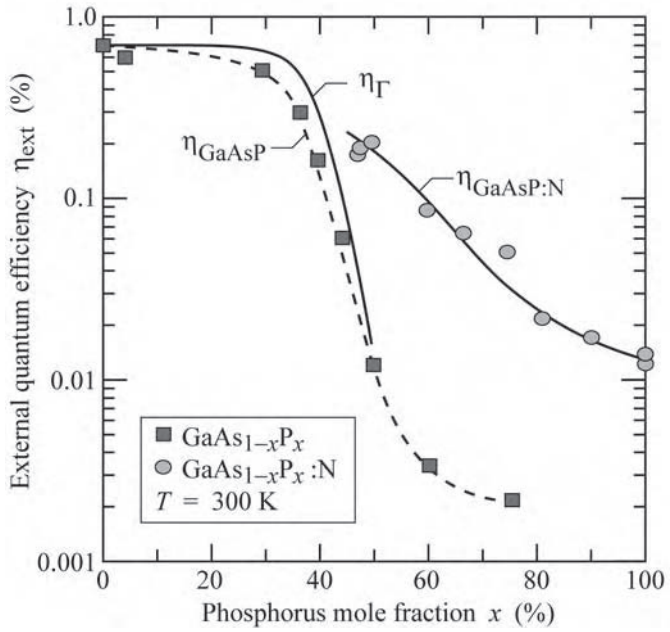


Fig. 12.3. Experimental external quantum efficiency of undoped and N-doped GaAsP versus the P mole fraction. Also shown is the calculated direct-gap (Γ) transition efficiency, $\eta_\Gamma$, and the calculated nitrogen (N) related transition efficiency, $\eta_N$ (solid lines). Note that the nitrogen-related efficiency is higher than the direct-gap efficiency in the indirect bandgap ($x >$ 50%) regime (after Campbell *et al.*, 1974).

The external quantum efficiency of undoped and nitrogen-doped GaAsP is shown in Fig. 12.3 (Campbell, 1974). Only the vicinity of the active region is doped with nitrogen. The efficiency of the nitrogen-doped LEDs is strongly enhanced over the entire composition range compared with the GaAsP LEDs without nitrogen doping.

Note that the GaAsP LED efficiency decreases by more than two orders of magnitude in the composition range $x$ = 40–60%. This decrease is due to the direct–indirect crossover occurring in GaAsP and due to the increasing dislocation density occurring at higher phosphorus mole fractions. At a phosphorus mole fraction of 75%, the GaAsP external quantum efficiency is only 0.002%.

The external quantum efficiency of undoped and nitrogen-doped GaAsP versus emission wavelength is shown in Fig. 12.4. Again, only the vicinity of the active region is doped with nitrogen. The efficiency of nitrogen-doped GaAsP is higher than that of undoped GaAsP, in particular in the orange, yellow, and green wavelength range where the improvement is a factor of 2–5. In the red wavelength range, the undoped and nitrogen-doped GaAsP LEDs have similar efficiencies.



Nichia Exhibit 1014
Page 19

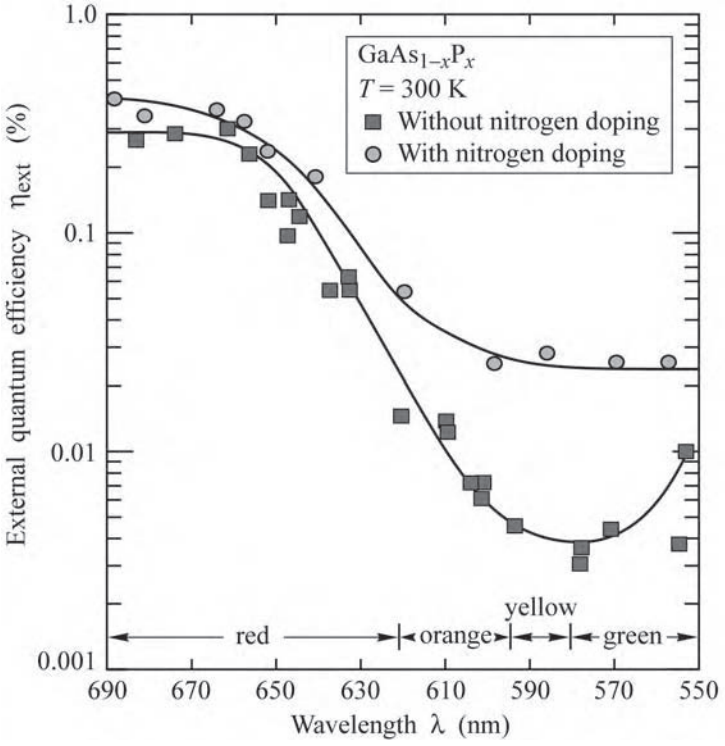


Fig. 12.4. External quantum efficiency versus emission wavelength in undoped and nitrogen-doped $GaAs_{1-x}P_x$ (after Groves *et al.*, 1978a, 1978b).

The ratio of external quantum efficiencies of undoped and nitrogen-doped GaAsP LEDs is shown in Fig. 12.5. It is inferred from the figure that nitrogen-doped devices have a higher efficiency over the entire composition range.

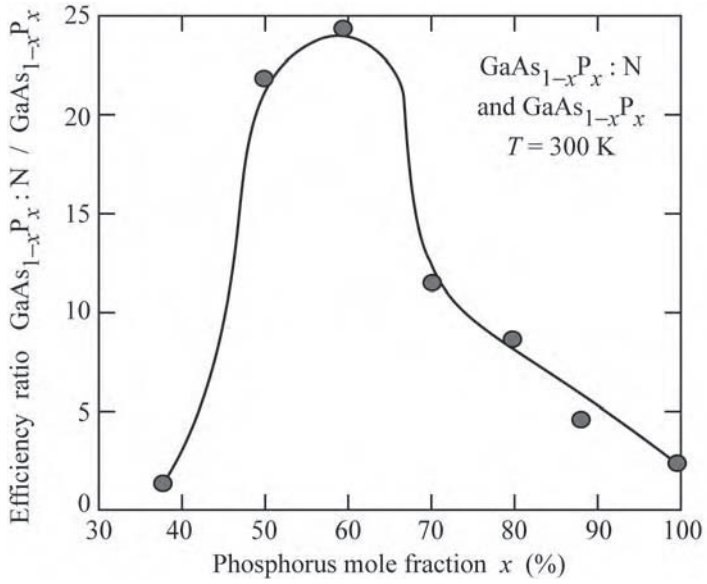


Fig. 12.5. Efficiency ratio between nitrogen-doped and undoped $GaAs_{1-x}P_x$ at 300 K (after Groves *et al.*, 1978a, 1978b).

The brightness of LEDs based on isoelectronic impurity transitions is limited by the ***finite solubility*** of nitrogen. For example, nitrogen is soluble in GaP up to nitrogen concentrations of

about $10^{20}$ $cm^{-3}$. Since an optical transition via a nitrogen level has a certain lifetime, the maximum nitrogen concentration limits the LED operation to a maximum current beyond which the LED efficiency decreases.

Commercial low-brightness green LEDs are based on nitrogen-doped GaP. The main application of GaP:N LEDs is indicator lamps. However, nitrogen-doped GaP LEDs are not suitable for high-brightness applications, i.e. for applications under bright ambient light conditions such as sunlight. High-brightness green LEDs are based on GaInN.

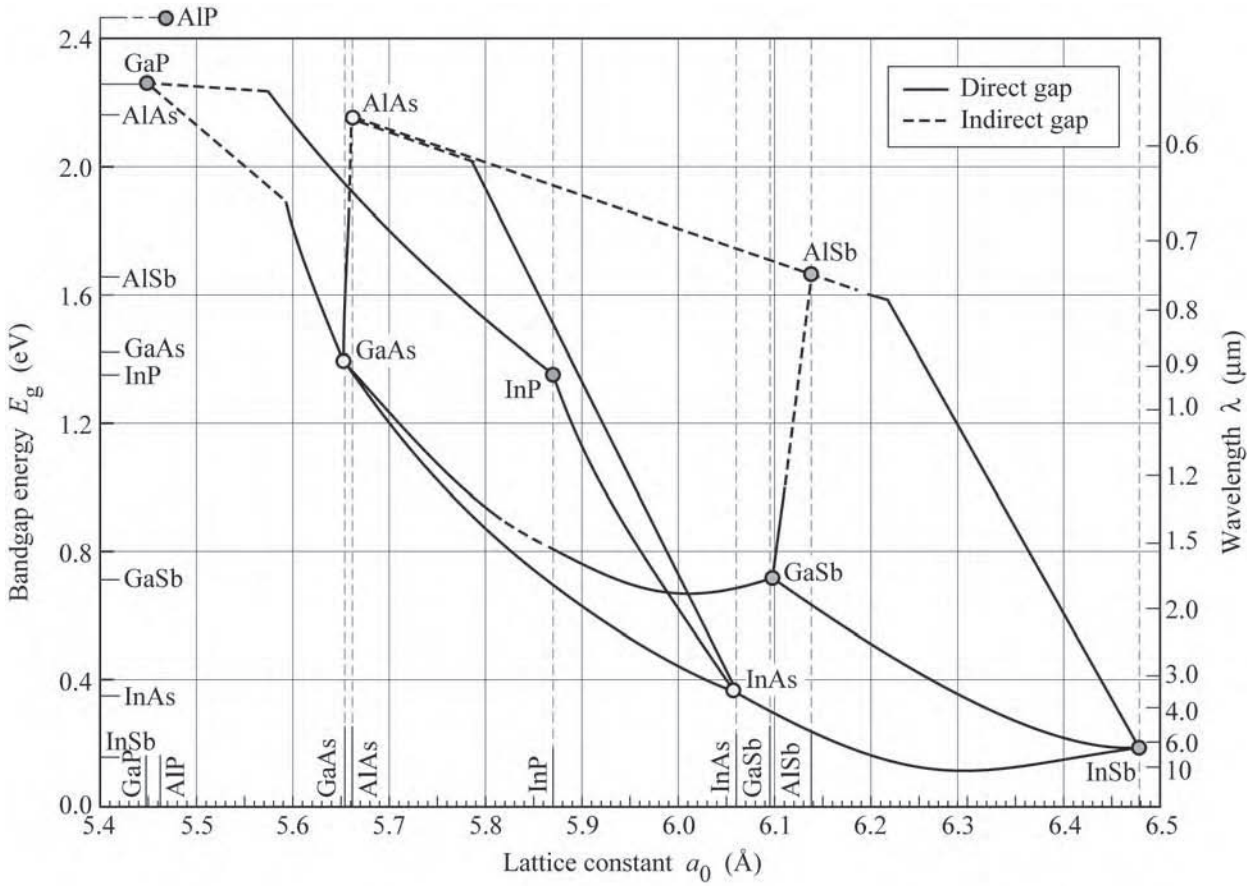


Fig. 12.6. Bandgap energy and lattice constant of various III–V semiconductors at room temperature (after Tien, 1988).

### *12.2 The AlGaAs/GaAs material system*

The $Al_xGa_{1-x}As$/GaAs material system was developed in the 1970s and early 1980s and it was the first material system suitable for high-brightness LED applications (for a review, see Steranka, 1997). Owing to the very similar atomic radii of Al (1.82 Å) and Ga (1.81 Å), the material system $Al_xGa_{1-x}As$ (or briefly AlGaAs) is lattice matched to GaAs for all Al mole



Nichia Exhibit 1014
Page 21

fractions. The lack of dependence of the lattice constant on the Al mole fraction can be inferred from Fig. 12.6, which shows the energy gap and lattice constant of several III–V semiconductors and of its ternary and quaternary alloys as a function of the lattice constant (adopted from Tien, 1988).

GaAs and $Al_xGa_{1-x}As$ for Al mole fractions $x < 0.45$ are direct-gap semiconductors. The energy gap of $Al_xGa_{1-x}As$ versus the Al mole fraction is shown in Fig. 12.7 (Casey and Panish, 1978). For Al mole fractions $x < 45\%$, the Γ conduction-band valley is the *lowest* minimum and the semiconductor has a *direct* gap. For $x > 45\%$, the X valleys are the *lowest* conduction-band minimum and the semiconductor becomes *indirect*.

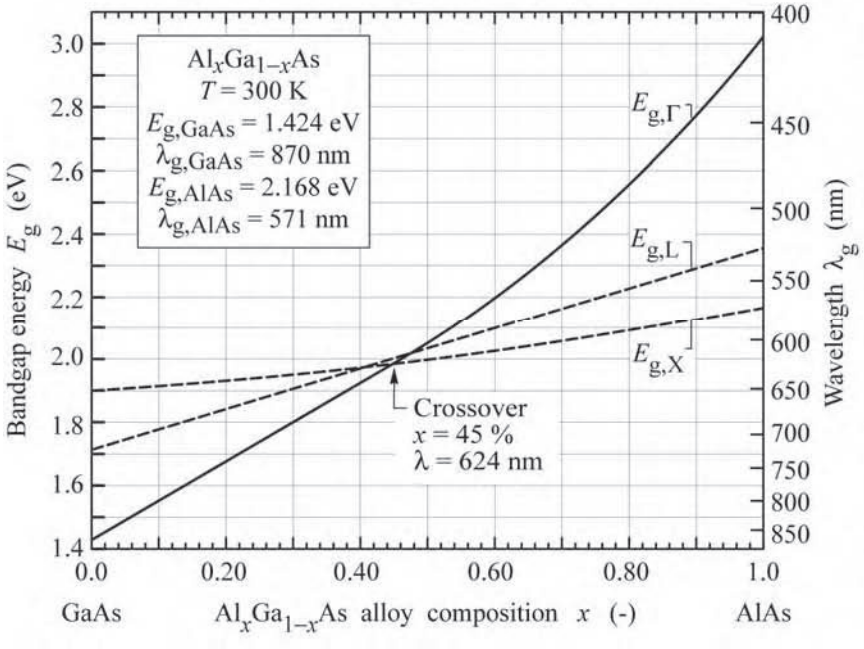


| |
|---|
| $E_{g,\Gamma}$ /eV = 1.424 + 1.247 $x$ $(0 \le x \le 0.45)$ |
| $E_{g,\Gamma}$ /eV = 1.424 + 1.247$x$ + 1.147$(x - 0.45)$ $(0.45 \le x \le 1.0)$ |
| $E_{g,L}$ /eV = 1.708 + 0.642 $x$ $(0 \le x \le 1.0)$ |
| $E_{g,X}$ /eV = 1.900 + 0.125 $x$ + 0.143 $x^2$ $(0 \le x \le 1.0)$ |

Fig. 12.7. Bandgap energy and emission wavelength of AlGaAs at room temperature. $E_\Gamma$ denotes the direct gap at the Γ point and $E_L$ and $E_X$ denote the indirect gap at the L and X point of the Brillouin zone, respectively (adapted from Casey and Panish, 1978).

The AlGaAs material system is suited for high-brightness visible-spectrum LEDs emitting in the red wavelength range. The direct–indirect crossover occurs at a wavelength of 621 nm. At that wavelength, the radiative efficiency of the AlGaAs system becomes quite low due to the direct–indirect transition. To maintain high efficiency, the emission energy must be several $kT$ lower than the bandgap energy at the direct–indirect crossover point.

There are several possible strategies for AlGaAs-based red LEDs, including $Al_xGa_{1-x}As$ bulk active regions, $Al_xGa_{1-x}As$/GaAs quantum well active regions, and $Al_xGa_{1-x}As/Al_yGa_{1-y}As$ $(x > y)$ double heterostructure active regions. The first possibility, $Al_xGa_{1-x}As$ bulk active regions, lacks the advantages of a heterostructure and this approach is therefore not used in high-brightness LEDs. The two other possibilities are more attractive due to the employment of

heterostructures. The quantum well and double heterostructure active region is used in high-efficiency red LEDs and the two structures are shown schematically in Fig. 12.8. In the $Al_xGa_{1-x}As$/GaAs quantum well case shown in Fig. 12.8 (a), size quantization is used to increase the emission energy. In the case of the $Al_xGa_{1-x}As/Al_yGa_{1-y}As$ double heterostructures shown in Fig. 12.8 (b), AlGaAs is used for both the barrier region and the well region. A drawback of the $Al_xGa_{1-x}As$/GaAs quantum well active regions is the requirement of very thin GaAs quantum wells clad by $Al_xGa_{1-x}As$ barriers. Vertical transport in multi-quantum well (MQW) structures can lead to non-uniform carrier distribution in the MQW active region unless the barriers are very thin. Consequently, the $Al_xGa_{1-x}As/Al_yGa_{1-y}As$ double heterostructure approach is usually preferred.

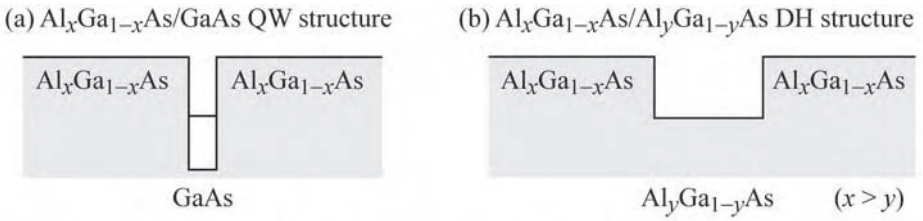


Fig. 12.8. Band diagrams of AlGaAs/GaAs structures suited for emission in the red part of the visible spectrum. (a) AlGaAs/GaAs quantum well (QW) structure with a thin GaAs well. (b) AlGaAs/AlGaAs double heterostructure (DH) with an AlGaAs active region.

AlGaAs/GaAs LEDs have been fabricated as homostructures, single heterostructures, and double heterostructures (Nishizawa *et al*., 1983). The most efficient AlGaAs red LEDs are double-heterostructure transparent-substrate (DH-TS) devices (Ishiguro *et al*., 1983; Steranka *et al*. 1988; Ishimatsu and Okuno, 1989). ***AlGaAs DH-TS LEDs*** are grown on temporary GaAs substrates and consist of a thick (e.g. 125 μm) $Al_xGa_{1-x}As$ lower confinement layer with an Al mole fraction $x > 60\%$, an $Al_xGa_{1-x}As$ active layer ($x = 35\%$, for red devices), and a thick (e.g. 125 μm) $Al_xGa_{1-x}As$ upper confinement layer, also with an Al mole fraction $x > 60\%$. For devices emitting in the IR, the Al mole fractions of the active and confinement layers can be lower. After epitaxial growth, the absorbing GaAs substrate is removed by polishing and selective wet chemical etching. AlGaAs DH-TS LEDs are more than a factor of 2 brighter than double-heterostructure absorbing-substrate (DH-AS) devices (Steranka *et al*., 1988).

In the 1980s the growth method of choice for AlGaAs DH-TS LEDs was liquid-phase epitaxy (LPE). This growth method is capable of growing, at a high growth rate, very thick high-quality AlGaAs layers with high Al content. LPE can be scaled up for high-volume production


Nichia Exhibit 1014
Page 23

(Ishiguro *et al*., 1983; Steranka *et al*., 1988; Ishimatsu and Okuno, 1989). AlGaAs/GaAs DH-AS LEDs have also been grown by OMVPE (Bradley *et al*., 1986). However, the OMVPE growth rate is lower than the LPE growth rate. OMVPE growth of thick layers, as required for DH-TS devices, is therefore difficult. Historically AlGaAs DH-TS LEDs were the first high-brightness LEDs suitable for demanding applications such as automotive brake lights and traffic lights, which must be clearly visible under bright ambient conditions.

The reliability of AlGaAs devices is known to be lower than that of AlGaInP devices that do not contain any AlGaAs. High-Al-content AlGaAs layers are subject to oxidation and corrosion, thereby lowering the device lifetime. Dallesasse *et al*. (1990) reported the deterioration of AlGaAs/GaAs heterostructures by hydrolysis. Cracks, fissures, and pinholes were found after long-term exposure to room environmental conditions, especially for thick AlGaAs layers ($> 0.1$ μm) with a high Al content such as 85%. The authors found very thin AlGaAs layers (e.g. 20 nm) to be stable, even for Al contents of 100%. Hermetic packaging is required to avoid oxidation and hydrolysis of AlGaAs layers. Steranka *et al*. (1988) stated that some AlGaAs devices on the market have exhibited severe degradation. However, accelerated aging data taken at 55 °C with an injection current of 30 mA showed no degradation at all after 1000 h of stress. Such a performance requires excellent understanding and control of the device fabrication and packaging process.

## *12.3 The AlGaInP/GaAs material system*

The AlGaInP material system was developed in the late 1980s and early 1990s and today is the primary material system for high-brightness LEDs emitting in the long-wavelength part of the visible spectrum, i.e. in the red, orange, amber, and yellow wavelength range. The AlGaInP material system and AlGaInP LEDs have been reviewed by Stringfellow and Craford (1997), Chen *et al*. (1997), and Kish and Fletcher (1997). Further reviews and recent developments were published by Mueller (1999, 2000) and Krames *et al*. (2002).

Figure 12.9 shows the energy gap and the corresponding wavelength versus the lattice constant of AlGaInP (Chen *et al*., 1997). AlGaInP can be lattice matched to GaAs. Replacing all As atoms in the GaAs lattice by *smaller* P atoms and some of the Ga atoms in the GaAs lattice by *larger* In atoms, forms GaInP, which at the particular composition $Ga_{0.5}In_{0.5}P$, is lattice matched to GaAs. Since Al and Ga have very similar atomic radii, the material $(Al_xGa_{1-x})_{0.5}In_{0.5}P$ is also lattice matched to GaAs.

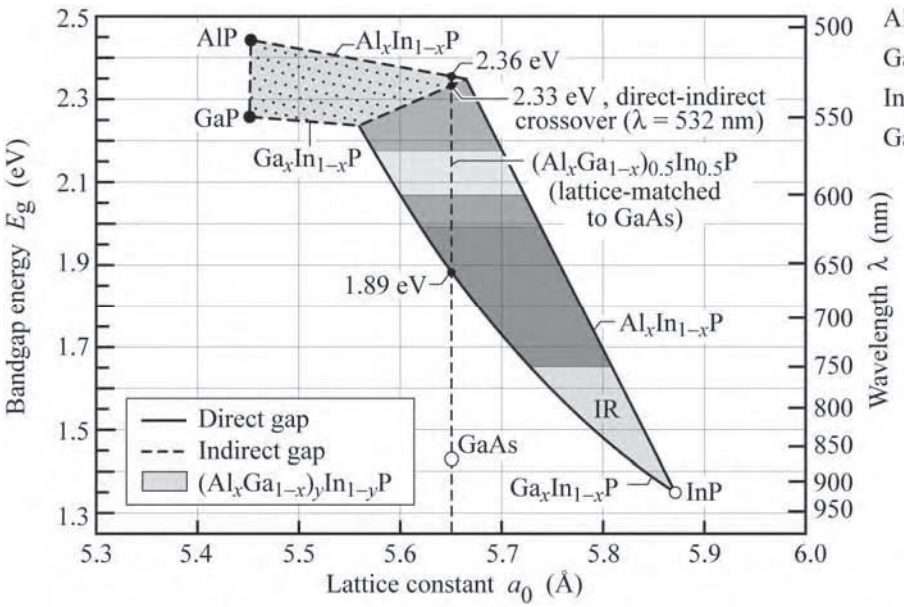


AlP: $E_g = 2.45$ eV, $a_0 = 5.4510$ Å
GaP: $E_g = 2.26$ eV, $a_0 = 5.4512$ Å
InP: $E_g = 1.35$ eV, $a_0 = 5.8686$ Å
GaAs: $E_g = 1.424$ eV, $a_0 = 5.6533$ Å

Fig. 12.9. Bandgap energy and corresponding wavelength versus lattice constant of $(Al_xGa_{1-x})_yIn_{1-y}P$ at 300 K. The vertical dashed line shows $(Al_xGa_{1-x})_{0.5}In_{0.5}P$ lattice matched to GaAs (adapted from Chen *et al*., 1997).

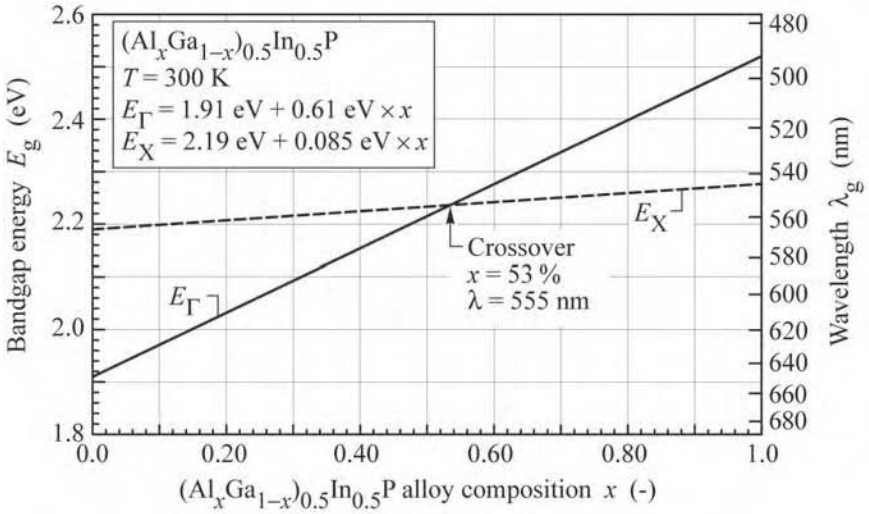


Fig. 12.10. Bandgap energy and emission wavelength of unordered AlGaInP lattice matched to GaAs at room temperature. $E_\Gamma$ denotes the direct gap at the Γ point and $E_X$ denotes the indirect gap at the X point of the Brillouin zone (after Prins *et al*., 1995 and Kish and Fletcher, 1997).

According to Chen *et al*. (1997), $(Al_xGa_{1-x})_{0.5}In_{0.5}P$ has a direct bandgap for $x < 0.5$ and an indirect bandgap for $x > 0.5$. At the crossover point ($x = 0.5$), the bandgap energy is 2.33 eV, corresponding to a wavelength of 532 nm. Kish and Fletcher (1997) compiled data from Prins *et al*. (1995) and concluded that $(Al_xGa_{1-x})_{0.5}In_{0.5}P$ is a direct-gap semiconductor for Al mole fractions $x < 0.53$. The energy gap versus Al mole fraction is shown in Fig. 12.10 (Prins *et al*., 1995; Kish and Fletcher, 1997). At Al mole fractions $x < 53\%$, the Γ conduction-band valley is the lowest minimum and the semiconductor has a direct gap. For $x > 53\%$, the X valleys are the lowest conduction-band minimum and the semiconductor becomes indirect. The emission wavelength at the direct–indirect crossover point is approximately 555 nm. The exact



Nichia Exhibit 1014
Page 25

wavelength of the crossover point may depend on the degree of atomic ordering present in a particular material (Kish and Fletcher, 1997).

A contour plot of the lattice constant and the energy gap of the AlGaInP materials system is shown in Fig. 12.11 (Chen *et al*., 1997). The bandgap energy values and the composition of the direct–indirect crossover shown in Fig. 12.11 are slightly different from the data shown in Fig. 12.10, which can be attributed to atomic ordering in AlGaInP. Atomic ordering lowers the bandgap energy by values up to 190 meV (Kish and Fletcher, 1997).

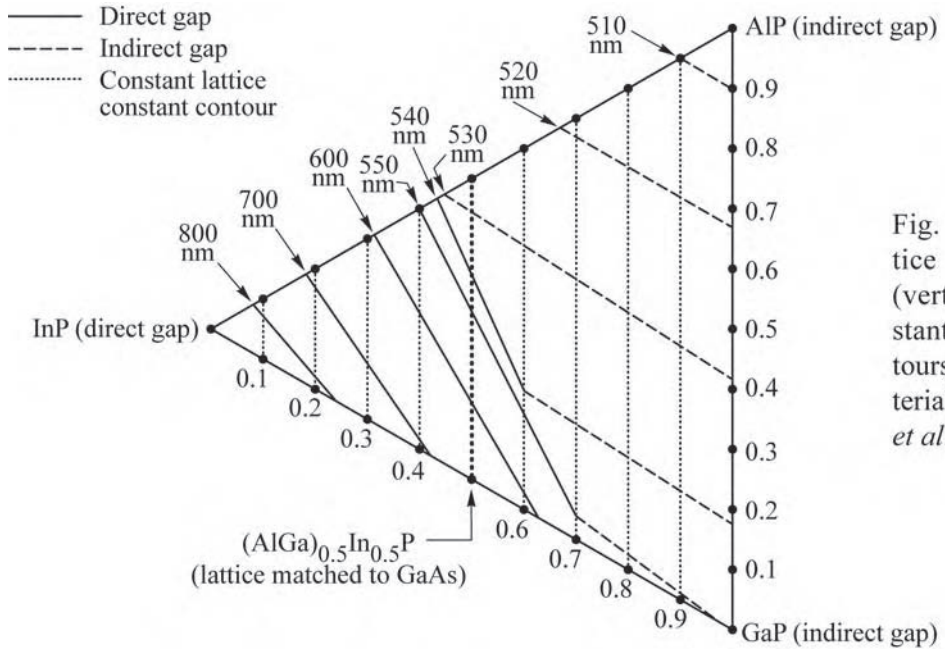


Fig. 12.11. Constant lattice constant contours (vertical lines) and constant emission line contours of the AlGaInP materials system (after Chen *et al*., 1997).

The AlGaInP material system is suited for high-brightness visible-spectrum LEDs emitting in the red, orange, amber, and yellow wavelength range. At the direct–indirect crossover the radiative efficiency of the AlGaInP system is quite low due to the direct–indirect transition. To maintain high efficiency, the emission energy should be several $kT$ lower than the bandgap energy at the direct–indirect crossover point.

### *12.4 The GaInN material system*

The GaInN material system was developed in the early 1990s. GaInN LEDs emitting in the blue and green wavelength range became commercially available in the late 1990s. To date GaInN is the primary material system for high-brightness blue and green LEDs. The GaInN material system and GaInN LEDs have been reviewed by Nakamura and Fasol (1997) and by Strite and Morkoc (1992).

One of the greatest surprises of the GaInN materials system is its high radiative efficiency despite the presence of a very high concentration of threading dislocations in GaInN/GaN epitaxial films. These threading dislocations are due to the lattice mismatch between the commonly used sapphire and SiC substrates and the GaN and GaInN epitaxial films. Typical densities of the threading dislocations are in the $10^7$–$10^9$ $cm^{-2}$ range.

In the III–V arsenide and III–V phosphide material systems, misfit dislocations have disastrous consequences for the radiative efficiency. The lack of such strongly detrimental consequences in the GaInN material system is not fully understood. However, it is believed that the small diffusion length of holes and an apparently low electrical activity of dislocations in GaN and GaInN allows for high radiative efficiencies.

It has also been postulated that fluctuations of the In content in GaInN cause carriers to be localized in potential minima, thus preventing carriers from reaching dislocations. The carriers localized in potential minima will eventually recombine radiatively. Although the physical mechanisms of the high radiative efficiency of GaInN are not yet understood in detail, it is clear that the optical properties of III–V nitrides are much less affected by dislocations than those of III–V arsenides and III–V phosphides.

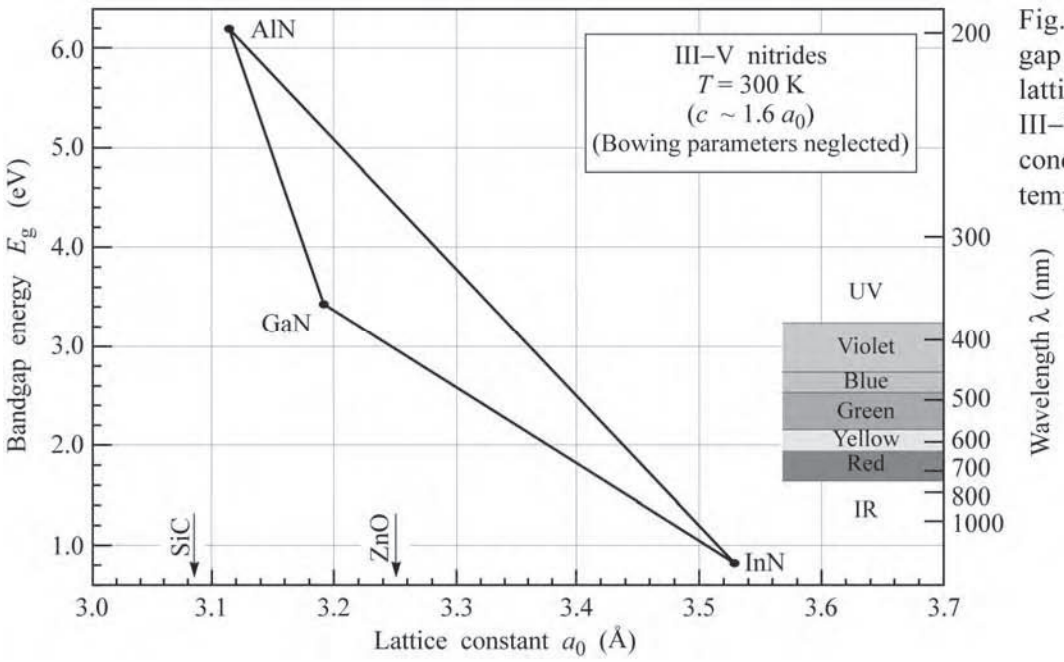


Fig. 12.12. Bandgap energy versus lattice constant of III–V nitride semiconductors at room temperature.

The bandgap energy versus the lattice constant in the nitride material family is shown in Fig. 12.12. Inspection of the figure indicates that GaInN is, in theory, suitable for covering the entire visible spectrum. However, the growth of high-quality GaInN becomes increasingly more



Nichia Exhibit 1014
Page 27

difficult as the In composition is increased, in part due to re-evaporation of In from the growth surface. As a result, the GaInN material system is exclusively used for ultraviolet (UV), blue, and green LEDs at the present time and rarely for longer wavelengths.

Prior to the year 2002, the generally accepted value for the InN bandgap energy was 1.9 eV. However, Wu *et al*. (2002a, 2002b) showed by luminescence measurements that the bandgap of InN is lower, namely between 0.7 and 0.8 eV. Luminescence measurements also indicated that the InN bandgap exhibits an unusual blue shift with increasing temperature.

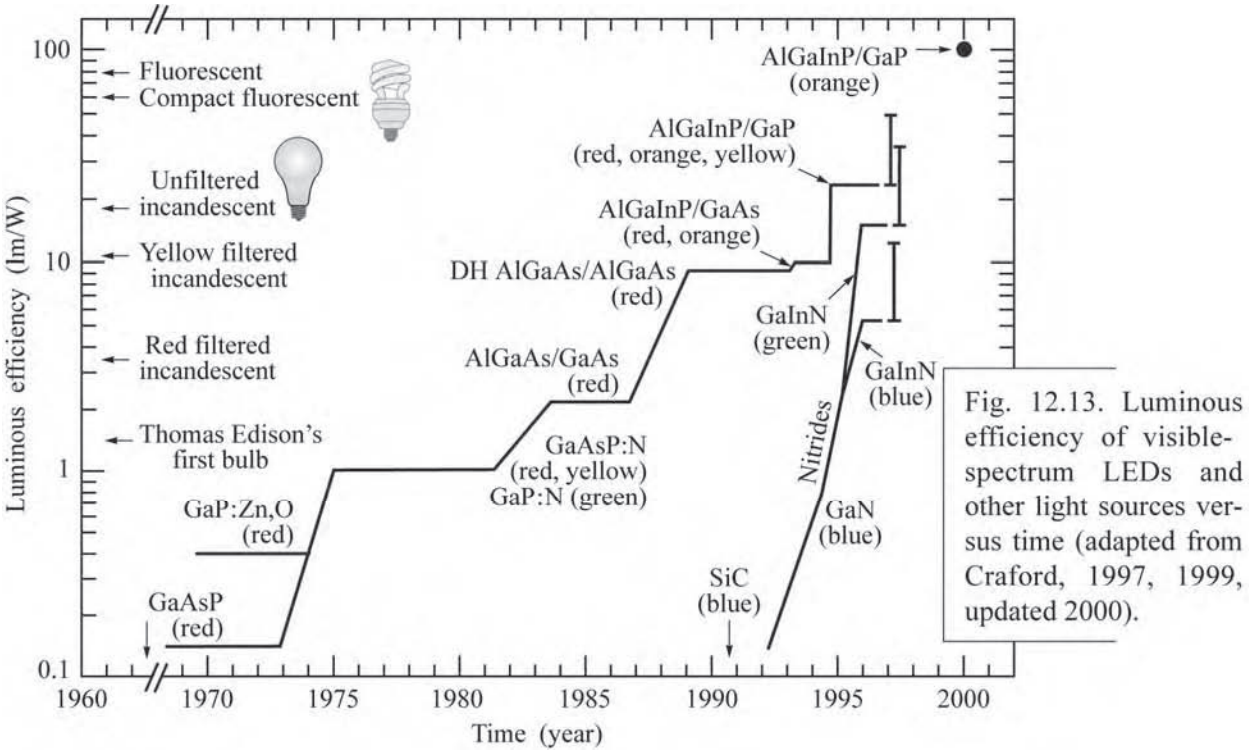


Fig. 12.13. Luminous efficiency of visible-spectrum LEDs and other light sources versus time (adapted from Craford, 1997, 1999, updated 2000).

### *12.5 General characteristics of high-brightness LEDs*

The improvement in luminous efficiency of visible-spectrum LEDs has been truly breathtaking. The advancement of LED efficiency can be compared to the advancement made in Si integrated circuits where the performance increase versus time has been characterized by "Moore's law". This "law" states that the performance of Si integrated circuits doubles approximately every 18 months.

The historical development of the luminous efficiency of visible-spectrum LEDs is shown in Fig. 12.13 (Craford, 1997, 1999). The chart illustrates the modest beginnings of visible-spectrum LED technology which started in the 1960s. If the progress from 1960 to 2000 is assumed to be

continuous, then the LED luminous efficiency has doubled every 4 years. The following types of LEDs are shown in the figure.

- GaAsP LEDs grown on GaAs substrates. The GaAsP/GaAs material system is lattice mismatched so that an abundance of misfit dislocations occurs in GaAsP epitaxial films. As a result, these LEDs have a low luminous efficiency (of the order of only 0.1 lm/W). Red GaAsP LEDs are still being manufactured due to the simple epitaxial growth and low fabrication cost.
- GaP LEDs doped with radiative recombination centers. Pure GaP is an indirect semiconductor and therefore has a low radiative efficiency. However, when doped with isoelectronic impurities such as N or co-doped with Zn and O, radiative transitions in the red and green spectral range occur via these centers.
- GaAsP/GaAs LEDs doped with N emitting in the red. Again a mismatched materials system with low efficiency due to the abundance of misfit dislocations.
- AlGaAs/GaAs LEDs emitting in the red. These LEDs employ GaAs quantum well active regions.
- AlGaAs/AlGaAs double heterostructure LEDs emitting in the red using AlGaAs active regions and AlGaAs barriers.
- AlGaInP/GaAs LEDs with absorbing GaAs substrates
- AlGaInP/GaP LEDs and with wafer-bonded transparent GaP substrates.
- Also included in the chart is a result by Krames *et al*. (1999) who reported LEDs with efficiencies exceeding 100 lm/W using AlGaInP/GaP LEDs with truncated inverted-pyramid-shaped dies.
- GaInN LEDs emitting in the blue and green wavelength range.

Figure 12.13 also shows the luminous efficiency of conventional light sources including Edison's first light bulb (1.4 lm/W) and red and yellow filtered incandescent lamps. Inspection of the figure reveals that LEDs outperform filtered red and yellow incandescent lights by a large margin.

The luminous efficiency of high-brightness LEDs and of some low-cost LEDs is shown versus wavelength in Fig. 12.14 (United Epitaxy Corp., 1999). The figure indicates that yellow (590 nm) and orange (605 nm) AlGaInP and green (525 nm) GaInN LEDs are excellent choices for high luminous efficiency devices.



Nichia Exhibit 1014
Page 29

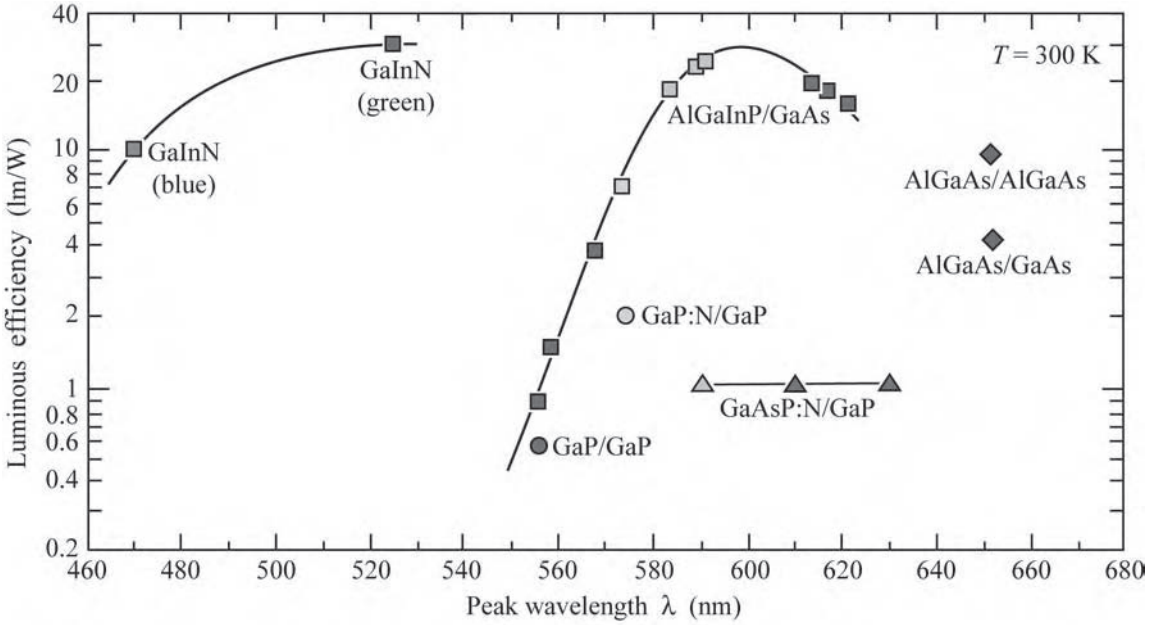


Fig. 12.14. Overview of luminous efficiency of visible LEDs made from the phosphide, arsenide, and nitride material system (adapted from United Epitaxy Corporation, 1999; updated 2000).

The fact that amber (dark yellow or orange–yellow) and orange AlGaInP LEDs provide an excellent luminous efficiency is also due to the high eye sensitivity in this wavelength range. Note that the maximum eye sensitivity occurs in the green at 555 nm, so that a green LED emitting at that wavelength appears brighter than an LED with the same optical power emitting at any other wavelength.

Owing to the high luminous efficiency and the lower manufacturing cost compared with green GaInN LEDs, amber AlGaInP LEDs are used in applications where high brightness and low power consumption are desirable, e.g. in highway signage applications. In the 1980s, such highway signs were made with power-hungry incandescent lamps powered by an electrical generator which, in turn, was powered by a gasoline engine. Today such signs use energy-saving amber LEDs powered by solar cells (during daytime) and batteries (at night).

Figures 12.13 and 12.14 also show low-power and low-cost LEDs such as GaAsP and GaP:N LEDs with much lower luminous efficiency. These LEDs are not suitable for high-brightness applications due to their inherently lower quantum efficiency. The GaAsP LEDs are mismatched to the GaAs substrate and therefore have a low internal efficiency. The GaP:N LEDs also have a low efficiency due to the nitrogen-impurity-assisted nature of the radiative transition.

Not only the *luminous efficiency* but also the *total power* emitted by an LED is of importance for many applications, in particular for applications where a high luminous flux is required. This

is the case, for example, in signage, traffic light, and illumination applications. Whereas conventional light sources such as incandescent light bulbs can be easily scaled up to provide high light power, individual LEDs are low-power devices. The historical development of the luminous flux per LED package, measured in lumens, is shown in Fig. 12.15 (Krames *et al*., 2000). The figure shows that the luminous flux per LED package has increased by about four orders of magnitude over a period of 30 years.

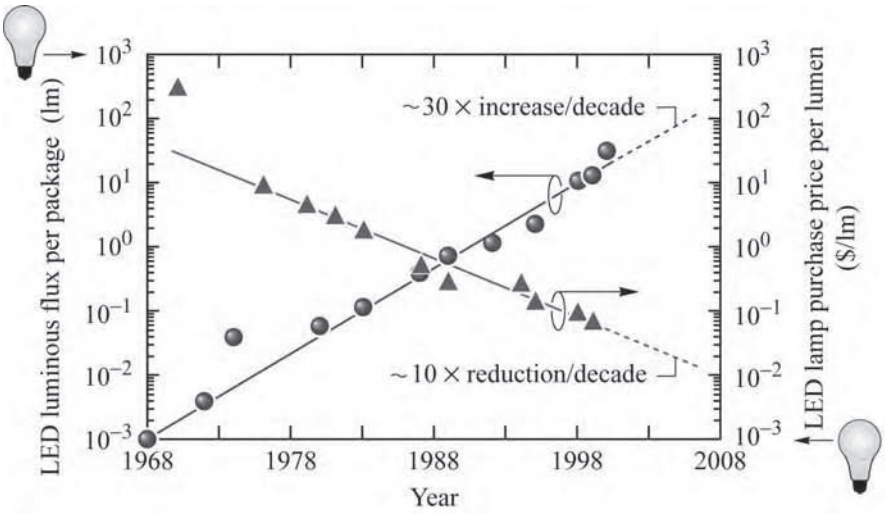


Fig. 12.15. LED luminous flux per package and LED lamp purchase price per lumen versus year. Also shown are the values for a 60 W incandescent tungsten-filament light bulb with a luminous efficiency of ~17 lm/W and a luminous flux of 1000 lm with an approximate price of 1.00 US$ (after Krames *et al*., 2000).

For comparison, Fig. 12.15 shows the luminous flux and an approximate purchase price of a 60 W incandescent light bulb with a luminous flux of 1000 lm. The figure illustrates that continued progress in the performance and manufacturing cost of LEDs is required to enable LEDs to enter into the general illumination market. Note that the cost shown in the figure is just the purchase price of the lamp and does not include the cost for the electrical power consumed over the lifetime of the lamp. The cost of the electrical power required to run an incandescent light bulb is much higher than the purchase price of the lamp so that efficient light sources can have a cost advantage over incandescent lights even if the initial purchase price is much higher.

### *12.6 Optical characteristics of high-brightness LEDs*

Optical emission spectra of red AlGaInP and green and blue GaInN LEDs are shown in Fig. 12.16 (Toyoda Gosei, 2000). Comparison of the emission spectra reveals that the green LED has a wider emission spectrum than either the blue or the red LED. This can be attributed to the well-known difficulties of growing GaInN with a high In content. It has been found that ***In-rich clusters*** or ***quantum dots*** form during the growth of GaInN, especially in GaInN with a high In



Nichia Exhibit 1014
Page 31

content. It is known that the formation of such In clusters depends strongly on the growth conditions.

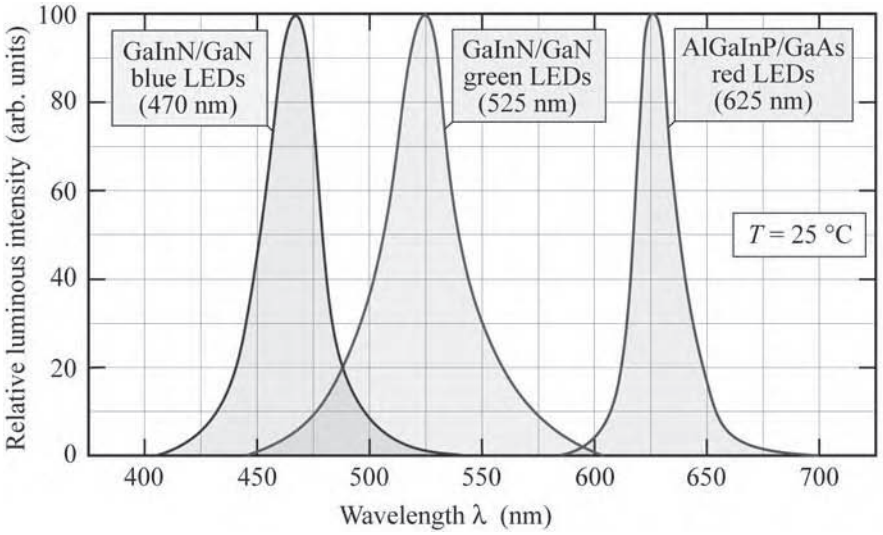


Fig. 12.16. Typical emission spectrum of GaInN/GaN blue, GaInN/GaN green, and AlGaInP/GaAs red LEDs at room temperature (after Toyoda Gosei Corp., 2000).

All LEDs shown in Fig. 12.16 have an active region composed of a ***semiconductor alloy***. Alloy broadening, i.e. the broadening of the emission band due to random fluctuations of the chemical composition of the active material, will lead to spectral broadening that goes beyond the 1.8 $kT$ linewidth expected for thermally broadened emission bands.

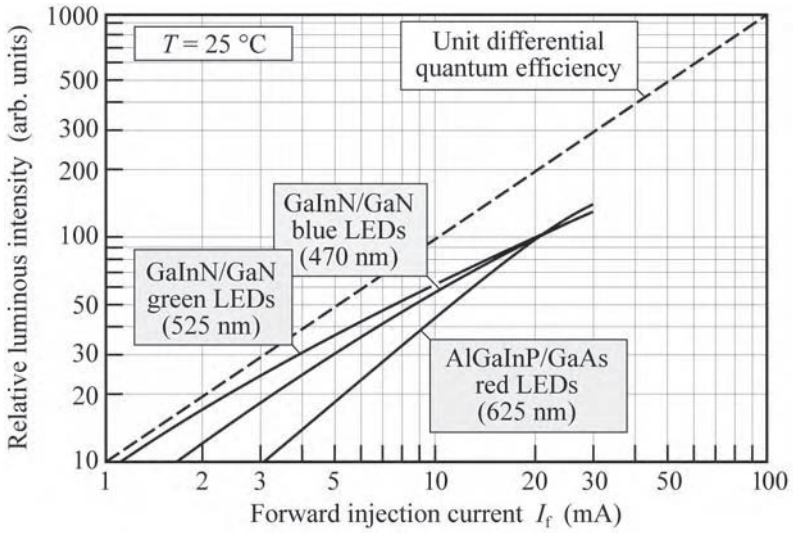


Fig. 12.17. Typical light output power vs. injection current of GaInN/GaN blue, GaInN/GaN green, and AlGaInP/GaAs red LEDs at room temperature (adopted from Toyoda Gosei Corp., 2000).

The light power versus injection current is shown in Fig. 12.17. A linear dependence with unit slope, i.e. unit differential quantum efficiency, is expected for light-versus-current curves in ideal LEDs. The unit-slope line is represented by the dashed line in Fig. 12.17. The mature

AlGaInP LED closely follows the unit-slope line. However, the green LED has a large deviation from the unit differential quantum efficiency slope due to the lower maturity of the GaInN material system, especially with high concentrations of In.

The temperature dependence of the optical emission intensity is shown in Fig. 12.18. The figure reveals that III–V nitride diodes have a much weaker temperature dependence than the AlGaInP LED. Two factors contribute to the weaker temperature dependence. Firstly, the active-to-confinement barriers are higher in the wide-gap III–V nitride material system than in other III–V material systems. Consequently, carriers in the GaInN active region are very well confined. Thus carrier leakage out of the well and carrier overflow are of little relevance in GaInN LEDs. Secondly, AlGaInP has a direct–indirect transition of the bandgap at about 555 nm. At elevated temperatures, the indirect valleys become increasingly populated so that the radiative efficiency decreases.

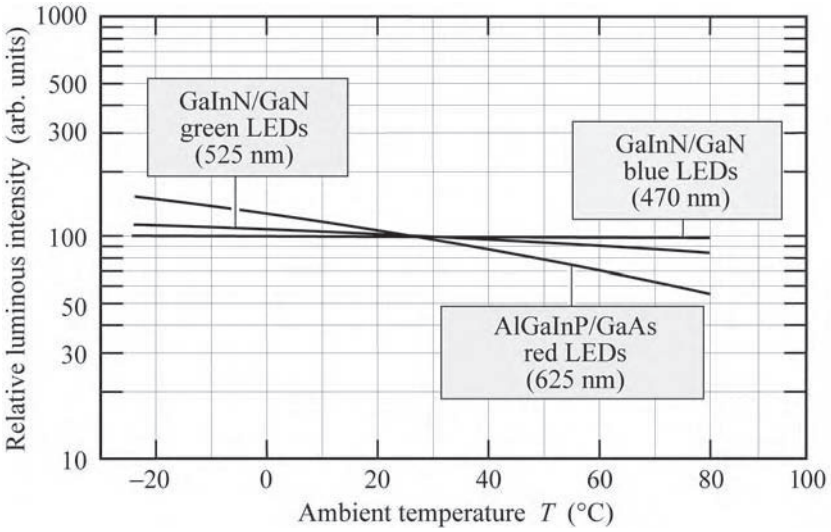


Fig. 12.18. Typical output intensity of GaInN/GaN blue, GaInN/GaN green, and AlGaInP/GaAs red LEDs versus ambient temperature (after Toyoda Gosei Corp., 2000).

### *12.7 Electrical characteristics of high-brightness LEDs*

The forward current–voltage (*I–V*) characteristics of a blue GaInN, a green GaInN, and a red AlGaInP LED are shown in Fig. 12.19. The forward turn-on voltage scales with the emission energy, indicating a well-behaved characteristic. Closer inspection of the forward voltage (at 1 mA) of the green LED ($V_{f,green} = 2.65$ V) indicates that it is very similar to the blue LED ($V_{f,blue} = 2.75$ V) even though the emission energies of the blue and green LED are quite different ($\lambda_{blue} = 470$ nm, $h\nu_{blue} = 2.64$ eV; $\lambda_{green} = 525$ nm, $h\nu_{green} = 2.36$ eV). The small difference in forward voltage indicates that carriers probably lose energy by phonon emission when injected



Nichia Exhibit 1014
Page 33

from the GaN barrier into the GaInN active region. They lose more energy when being injected from the GaN barrier into the In-richer active region of the green LED. The energy, dissipated by emission of phonons, is supplied by the external voltage applied to the LED.

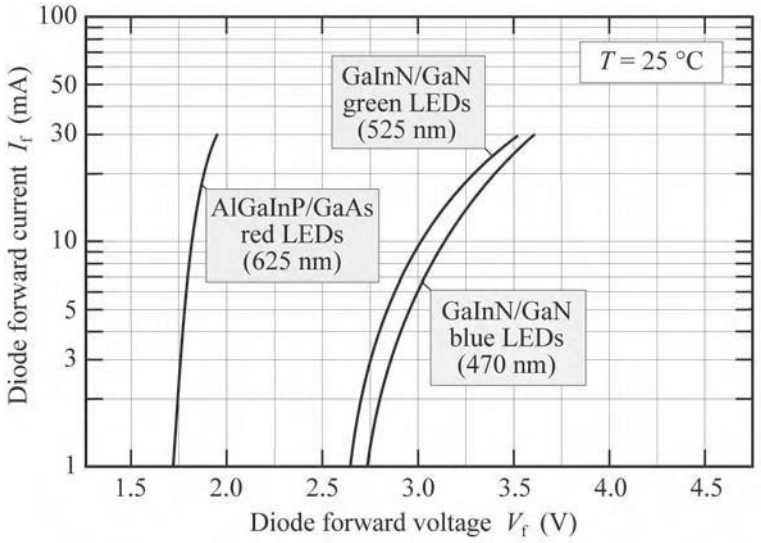


Fig. 12.19. Typical forward current–voltage ($I$–$V$) characteristic of GaInN/GaN blue, GaInN/GaN green, and AlGaInP/GaAs red LEDs at room temperature (after Toyoda Gosei Corporation, 2000).

The diode series resistance can be inferred from the slope of the $I$–$V$ characteristics. The blue and green diodes have a higher series resistance than the red AlGaInP diode. The larger resistance in GaInN LEDs can be attributed to several factors including the "lateral" resistance in the n-type buffer layer for devices grown on sapphire substrates, strong polarization effects occurring in the nitride material family, lower p-type conductivity in the cladding layer, and higher p-type contact resistance. The lower p-type conductivity is due to the high acceptor activation energy (approximately 200 meV) in GaN and GaInN so that only a small fraction of acceptors is activated.

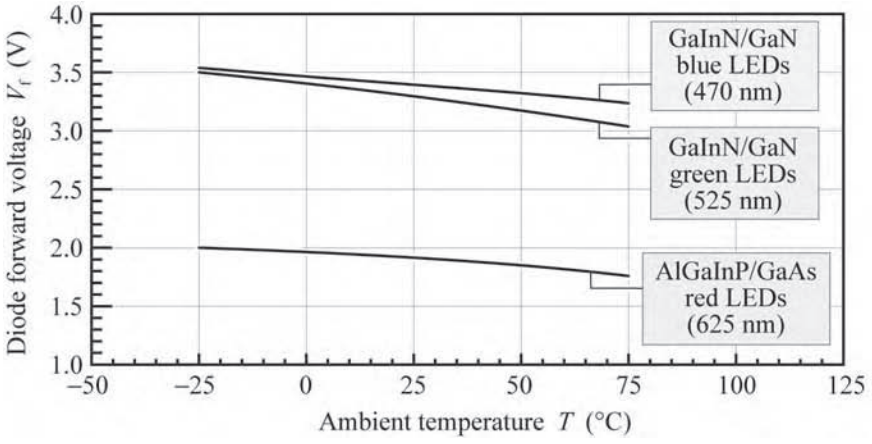


Fig. 12.20. Typical diode forward voltage at a current of 30 mA of GaInN/GaN blue, GaInN/GaN green, and AlGaInP/GaAs red LEDs versus temperature (after Toyoda Gosei Corp., 2000).

The temperature dependence of the forward voltage at a diode current of 30 mA is shown in Fig. 12.20. For all diodes shown, the forward voltage decreases as the temperature is increased. The decrease in forward voltage is due to the decrease of the bandgap energy. In the blue and green GaInN diodes, the lower forward voltage is also due to the decrease in series resistance occurring at high temperatures. This resistance decrease is due to the higher acceptor activation occurring at elevated temperatures and the resulting higher conductivity of the p-type GaN and GaInN layers.

### *References*


Bradley R. R., Ash R. M., Forbes N. W., Griffiths R. J. M., Jebb D. P., and Shepard H. E. "Metalorganic chemical vapor deposition of junction isolated GaAlAs/GaAs LED structures" *J. Cryst. Growth* **77**, 629 (1986)

Campbell J. C., Holonyak Jr. N., Craford M. G., and Keune D. L. "Band structure enhancement and optimization of radiative recombination in GaAsP (and InGaP:N)" *J. Appl. Phys*. **45**, 4543 (1974)

Casey Jr. H. C. and Panish M. B. *Heterostructure Lasers, Part A* and *Heterostructure Lasers, Part B* (Academic Press, San Diego, 1978)

Chen C. H., Stockman S. A., Peanasky M. J., and Kuo C. P. "OMVPE growth of AlGaInP for high-efficiency visible light-emitting diodes" in *High Brightness Light Emitting Diodes* edited by G. B. Stringfellow and M. G. Craford, *Semiconductors and Semimetals* **48**, (Academic Press, San Diego, 1997)

Craford M. G., Shaw R. W., Herzog A. H., and Groves W. O. "Radiative recombination mechanisms in GaAsP diodes with and without nitrogen doping" *J. Appl. Phys*. **43**, 4075 (1972)

Craford M. G. "Overview of device issues in high-brightness light-emitting diodes" in *High Brightness Light Emitting Diodes* edited by G. B. Stringfellow and M. G. Craford, *Semiconductors and Semimetals* **48** (Academic Press, San Diego, 1997)

Craford M. G. "The bright future of light-emitting diodes" Plenary talk on light emitting diodes at the MRS Fall Meeting, Boston Massachusetts December (1999)

Dallesasse J. M., El-Zein N., Holonyak Jr. N., Hsieh K. C., Burnham R. D., and Dupuis R. D. "Environmental degradation of AlGaAs–GaAs quantum-well heterostructures" *J. Appl. Phys*. **68**, 2235 (1990)

Grimmeiss H. G. and Scholz H. "Efficiency of recombination radiation in GaP" *Phys. Lett.* **8**, 233 (1964)

Groves W. O. and Epstein A. S. "Epitaxial deposition of III–V compounds containing isoelectronic impurities" US Patent 4,001,056 (1977)

Groves W. O., Herzog A. H., and Craford M. G. "Process for the preparation of electroluminescent III–V materials containing isoelectronic impurities" US Patent Re. 29,648 (1978a)

Groves W. O., Herzog A. H., and Craford M. G. "GaAsP electroluminescent device doped with isoelectronic impurities" US Patent Re. 29,845 (1978b)

Holonyak Jr. N. and Bevacqua S. F. "Coherent (visible) light emission from Ga(AsP) junctions" *Appl. Phys. Lett*. **1**, 82 (1962)

Holonyak Jr. N., Bevacqua S. F., Bielan C. V., and Lubowski S. J. "The "direct–indirect" transition in Ga(AsP) p-n junctions," *Appl. Phys. Lett*. **3**, 47 (1963)

Holonyak Jr. N., Nuese C. J., Sirkis M. D., and Stillman G. E., "Effect of donor impurities on the direct–indirect transition in Ga(AsP)" *Appl. Phys. Lett*. **8**, 83 (1966)

Ishiguro H., Sawa K., Nagao S., Yamanaka H., and Koike S. "High efficient GaAlAs light emitting diodes of 660 nm with double heterostructure on a GaAlAs substrate" *Appl. Phys. Lett*. **43**, 1034 (1983)

Ishimatsu S. and Okuno Y. "High efficiency GaAlAs LED" *Optoelectron. Dev. Technol.* **4**, 21 (1989)

Kish F. A. and Fletcher R. M. "AlGaInP light-emitting diodes" in *High Brightness Light Emitting Diodes* edited by G. B. Stringfellow and M. G. Craford, *Semiconductors and Semimetals* **48** (Academic




Nichia Exhibit 1014
Page 35

Press, San Diego, 1997)
Krames M. R. *et al*. "High-power truncated-inverted-pyramid ($Al_xGa_{1-x})_{0.5}In_{0.5}P$/GaP light emitting diodes exhibiting > 50% external quantum efficiency" *Appl. Phys. Lett*. **75**, 2365 (1999)
Krames M. R. *et al*. "High-brightness AlGaInN light emitting diodes" *Proc. SPIE* **3938**, 2 (2000)
Krames M. R., Amano H., Brown J. J., and Heremans P. L. "High-efficiency light-emitting diodes" Special Issue of *IEEE J. Sel. Top. Quantum Electron.* **8**, 185 (2002)
Logan R. A., White H. G., and Trumbore F. A. "P-n junctions in compensated solution grown GaP" *J. Appl. Phys*. **38**, 2500 (1967a)
Logan R. A., White H. G., and Trumbore F. A. "P-n junctions in GaP with external electrolumi-nescence efficiencies ~ 2% at 25 °C" *Appl. Phys. Lett*. **10**, 206 (1967b)
Logan R. A., White H. G., and Wiegmann W. "Efficient green electroluminescent junctions in GaP" *Solid State Electron.* **14**, 55 (1971)
Mueller G. (editor) *Electroluminescence I*, *Semiconductors and Semimetals* **64** (Academic Press, San Diego, 1999)
Mueller G. (editor) *Electroluminescence II, Semiconductors and Semimetals* **65** (Academic Press, San Diego, 2000)
Nakamura S. and Fasol G. *The Blue Laser Diode* (Springer, Berlin, 1997)
Nishizawa J., Koike M., and Jin C. C. "Efficiency of GaAlAs heterostructure red light emitting diodes" *J. Appl. Phys*. **54**, 2807 (1983)
Nuese C. J., Stillman G. E., Sirkis M. D., and Holonyak Jr. N., "Gallium arsenide-phosphide: crystal, diffusion, and laser properties" *Solid State Electron*. **9**, 735 (1966)
Nuese C. J., Tietjen J. J., Gannon J. J., and Gossenberger H. F. "Optimization of electroluminescent efficiencies for vapor-grown GaAsP diodes" *J. Electrochem. Soc.: Solid State Sci.* **116**, 248 (1969)
Pilkuhn M. and Rupprecht H. "Electroluminescence and lasing action in GaAsP" *J. Appl. Phys*. **36**, 684 (1965)
Prins A. D., Sly J. L., Meney A. T., Dunstan D. J., O'Reilly E. P., Adams A. R., and Valster A. J. *Phys. Chem. Solids* **56**, 349 (1995)
Steranka F. M., DeFevre D. C., Camras M. D., Tu C.-W., McElfresh D. K., Rudaz S. L., Cook L. W., and Snyder W. L. "Red AlGaAs light emitting diodes" *Hewlett-Packard Journal* p. 84 August (1988)
Steranka F. M. "AlGaAs red light-emitting diodes" in *High Brightness Light Emitting Diodes* edited by G. B. Stringfellow and M. G. Craford, *Semiconductors and Semimetals* **48** (Academic Press, San Diego, 1997)
Stringfellow G. B. and Craford M. G. (Editors) *High Brightness Light Emitting Diodes*, *Semiconductors and Semimetals* **48** (Academic Press, San Diego, 1997)
Strite S. and Morkoc H., "GaN, AlN, and InN: A review" *J. Vac. Sci. Technol.* **B 10**, 1237 (1992)
Tien P. K. Original version of the graph is courtesy of P. K. Tien of AT&T Bell Laboratories (1988)
Toyoda Gosei Corporation, Japan, LED product catalog (2000)
United Epitaxy Corporation, Taiwan, General LED and wafer product catalog (1999)
Wolfe C. M., Nuese C. J. and Holonyak Jr. N. "Growth and dislocation structure of single-crystal Ga(AsP)" *J. Appl. Phys*. **36**, 3790 (1965)
Wu J., Walukiewicz W., Yu K. M., Ager III J. W., Haller E. E., Lu H., Schaff W. J., Saito Y., and Nanishi Y. "Unusual properties of the fundamental bandgap of InN" *Appl. Phys. Lett*. **80**, 3967 (2002a)
Wu J., Walukiewicz W., Yu K. M., Ager III J. W., Haller E. E., Lu H., and Schaff W. J. "Small bandgap bowing in $In_{1-x}Ga_xN$ alloys" *Appl. Phys. Lett*. **80**, 4741 (2002b)

# 13

## The AlGaInN material system and ultraviolet emitters

### *13.1 The UV spectral range*

The ultraviolet–visible boundary is at about 390 nm, where the 1978 CIE eye sensitivity curve has a value of 0.1% of its maximum value. This chapter concentrates on materials issues of III–V nitrides, on devices emitting in the ultraviolet (UV, $\lambda < 390$ nm), and on devices emitting in the violet near the UV–visible boundary (390–410 nm). Although the latter devices emit in the visible spectrum, they are frequently classified as UV devices. For UV devices, we will differentiate between devices having a GaInN active region ($\lambda > 360$ nm) and devices having an AlGaN active region ($\lambda < 360$ nm).

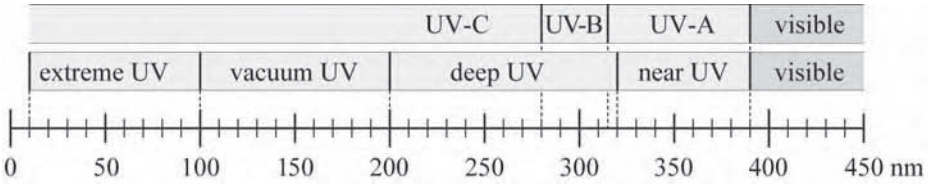


Fig. 13.1. Nomenclature of UV radiation versus wavelength (after International Congress on Light, 1932).

There are two classifications of the UV spectrum, both of which are shown in Fig. 13.1. The UV-A (315–390 nm), UV-B (280–315 nm), and UV-C (< 280 nm) classification is based on a convention established during the Second International Congress on Light in 1932 (International, 1932). UV-A radiation from the sun penetrates the earth's atmosphere (including clouds) and, due to the high energy of UV photons, creates damage to the skin, particularly to the deeper layers of the skin. UV-A radiation also causes cataracts (the clouding of the eye's lens), which can lead to total blindness. Both UV-B (partially absorbed by the earth's ozone layer) and UV-C radiation (mostly absorbed by ozone layer) create serious damage to skin and eyes. Because no natural light with $\lambda \leq 280$ nm exists at the earth's surface (i.e. in the UV-C range), this wavelength range is also referred to as the *solar-blind* range.



Nichia Exhibit 1014
Page 37

An alternative classification of UV radiation has evolved over time. This alternative classification has the following categories: Extreme UV (10–100 nm); vacuum UV (100–200 nm); deep UV (200–320 nm); and near UV (320–390 nm).

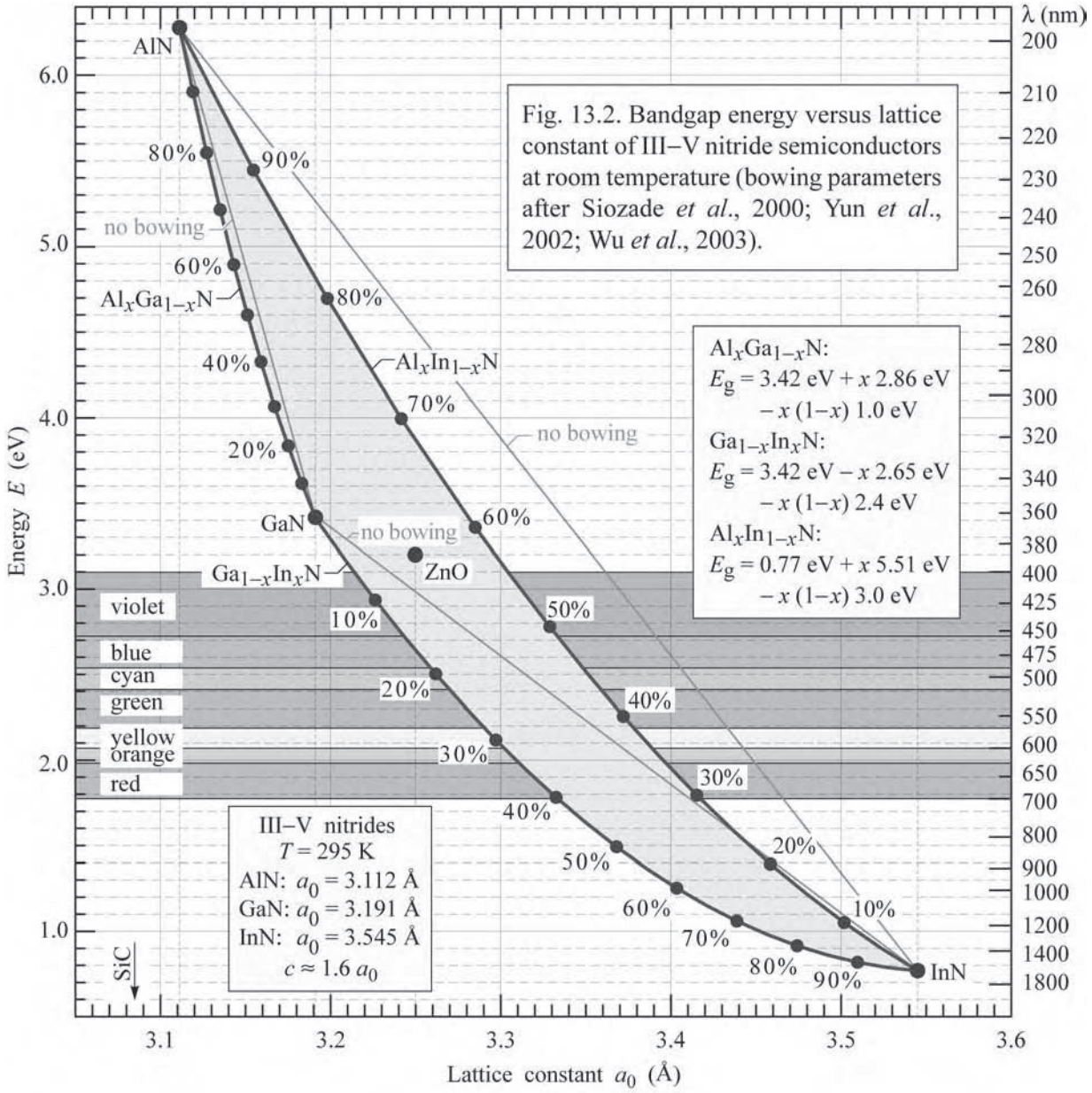


### *13.2 The AlGaInN bandgap*

The bandgap energy versus lattice constant of the AlGaInN material system is shown in Fig. 13.2. The AlGaInN material system spans a very wide range of wavelengths covering the deep UV, near UV, visible, and even the near infrared spectral range. Of the three binary

semiconductors InN, GaN, and AlN, epitaxially grown GaN has been shown to be synthesizable with the highest quality. It has generally been difficult to synthesize Al-rich AlGaN alloys and In-rich GaInN alloys with high internal quantum efficiencies.

There has been some controversy with respect to the bandgap energy of InN, which originally had been found to be about 1.9 eV. More recently, the bandgap energy was found to be much lower, namely 0.77 eV.

The energy-gap bowing can be expressed in terms of a constant, a linear term ($\propto x$) and a non-linear term [$\propto x\,(1-x)$] according to

$$E_g^{AB} = E_g^{A} + (E_g^{B} - E_g^{A})\,x + x\,(1-x)\,E_b \tag{13.1}$$

with $E_b$ called the ***bowing energy*** or ***bowing parameter***. The bowing parameters used in Fig. 13.2 for AlGaN, GaInN, and AlInN are based on data published by Siozade *et al*. (2000), Yun *et al*. (2002), and Wu *et al*. (2002; 2003). Recently additional data on the bowing energies have become available (Walukiewicz *et al*., 2004).

### *13.3 Polarization effects in III–V nitrides*

The most common epitaxial growth direction of III–V nitrides is the *c*-plane of the hexagonal wurtzite structure. III–V nitrides grown on the *c*-plane have polarization charges located at each of the two surfaces of a layer. As a result of these charges, internal electric fields occur in III–V nitrides that have a significant effect on the optical and electrical properties of this class of semiconductors.

There are ***spontaneous polarization*** charges as well as strain-induced or ***piezoelectric polarization charges*** (Bernardini *et al*., 1997; Ambacher *et al*., 1999; 2000; 2002). The direction of the internal electric field depends on the strain and the growth orientation (Ga face or N face) and is shown for different cases in Fig. 13.3.

The strain in the epitaxial layer can be compressive or tensile. In the compressive-strain case, the epitaxial layer of interest is laterally compressed ("laterally" meaning "in the plane of the wafer"). For example, GaInN is compressively strained when grown on a thick relaxed GaN buffer layer. In the tensile-strain case, the epitaxial layer of interest is expanded along the lateral direction. For example, AlGaN is under tensile strain when grown on a thick relaxed GaN buffer layer.

The calculated magnitude of the electric field for common III–V nitride alloys grown on



Nichia Exhibit 1014
Page 39

relaxed GaN is shown in Fig. 13.4 (Gessmann *et al*., 2002).

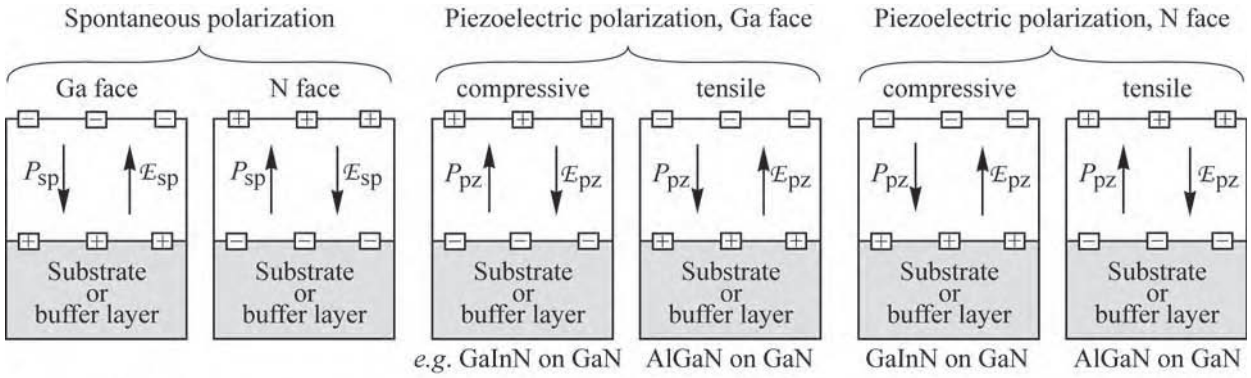


Fig. 13.3. Surface charges and direction of electric field and polarization field for spontaneous and piezoelectric polarization in III–V nitrides for Ga and N face orientation.

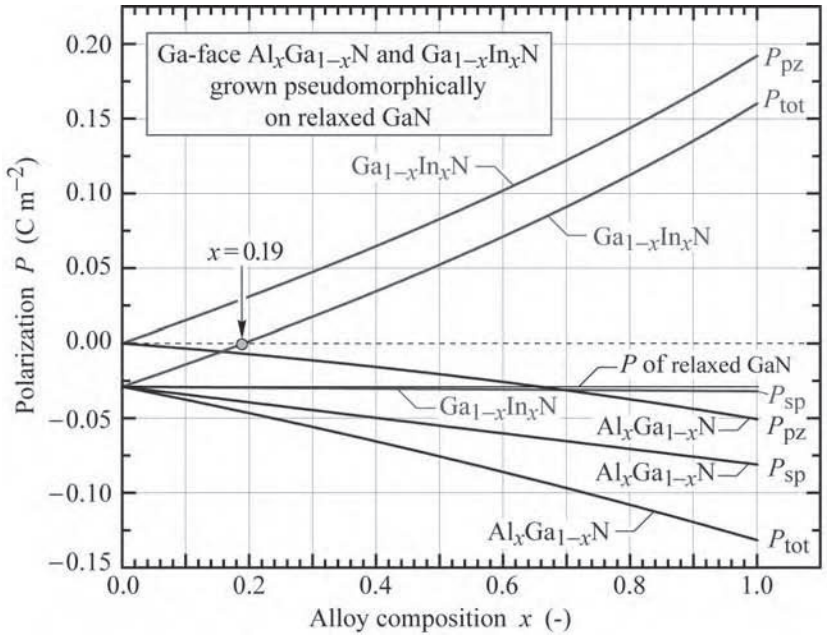


Fig. 13.4. Magnitude and direction of spontaneous and piezoelectric polarization in GaInN and AlGaN grown pseudomorphically on relaxed GaN. Relaxed GaN has a spontaeous polarization, but no piezoelectric polarization (after Gessmann *et al*., 2002).

A consequence of the polarization fields for quantum well structures is shown in Fig. 13.5. The quantum well layers have an internal electric field that spatially separates electrons and holes thereby preventing efficient radiative recombination. This is particularly true for thick quantum wells, e.g. > 100 Å. To avoid this deleterious effect, it is imperative that the quantum well layers are kept very thin. Quantum well thicknesses of 20–30 Å are typically used to minimize such electron–hole separation effects.

The large electric fields caused by the polarization effects can be screened by a high free-

carrier concentration, which can be attained through either (*i*) high doping of the active region or (*ii*) a high injection current. Screening of the internal electric field also results in a blue-shift of the emission, frequently found in GaInN LEDs as the injection current is increased.

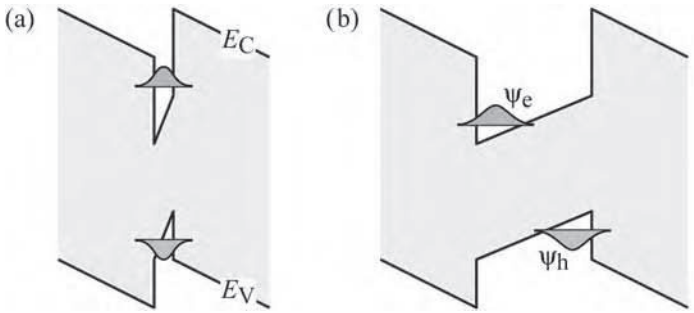


Fig. 13.5. Schematic band diagram of (a) thin and (b) thick AlGaN/GaN active regions with polarization fields for Ga-face growth (substrate on right-hand side).

Polarization effects can be used advantageously to reduce ohmic contact resistances in GaN devices. Polarization-enhanced contacts to p-type GaN employ a thin, compressively strained GaInN cap layer that is deposited on the p-type GaN. The electric field in the GaInN cap layer is polarized in such a way that the tunneling probability of holes is enhanced (Li *et al*., 2000; Gessmann *et al*., 2002). Contact resistances as low as $1.1 \times 10^{-6}$ and $2 \times 10^{-7}$ $\Omega\,cm^2$ have been reported for non-annealed and annealed polarization-enhanced ohmic contacts to p-type GaN, respectively (Kumakura *et al*., 2001; 2003). Both the concept of polarization-enhanced contacts and the very low specific contact resistances are remarkable because they represent a several orders-of-magnitude improvement over conventional contact technologies. The forward voltage of GaN-based LEDs with polarization-enhanced contacts is generally lower than the forward voltage of LEDs with conventional GaN contacts (Su, 2005).

### *13.4 Doping activation in III–V nitrides*

Another problem in III–V nitrides is the low doping activation, which is caused by two effects: (*i*) Chemical deactivation of acceptors by hydrogen atoms bonding to the acceptors. The missing electron that acceptors strive to capture is provided by a hydrogen atom. Hydrogen is available in abundance during epitaxial growth and possible sources for hydrogen passivation include the methyl ($-CH_3$) and ethyl groups ($-C_2H_5$) of the organo-metallics, ammonia ($NH_3$), and hydrogen from the $H_2$ carrier gas. (*ii*) Acceptors in III–V nitrides have a high thermal activation energy which is $>> kT$ at 300 K. As a result, only a small percentage of acceptors are ionized at room temperature.



Nichia Exhibit 1014
Page 41

**Exercise**: ***Activation of Mg acceptors in GaN***. Mg acceptors in GaN have an activation energy of $E_a = 200$ meV. (a) Calculate the fraction of acceptors that are ionized at 300 K for an acceptor concentration of $N_{Mg} = 10^{18}$ cm$^{-3}$ using the formula $p = (g^{-1} N_{Mg} N_v)^{1/2} \exp(-E_a / 2kT)$ where $g$ is the acceptor ground state degeneracy ($g = 4$) and $N_v$ is the effective density of states at the valence band edge of GaN. (b) What would be the activation of acceptors if a hydrogen atom were bonded to each acceptor?

Solution: (a) Using the formula given above, one obtains that only about 6% of the acceptors are ionized. (b) If acceptors are passivated, p-type conductivity cannot be established.

Amano *et al*. (1989) discovered that acceptor dopants can be activated by low-energy electron-beam irradiation (LEEBI). Nakamura *et al*. (1991; 1992) showed that acceptors can be activated by LEEBI as well as by thermal annealing, with thermal annealing being the preferred method. Typical annealing conditions for MOCVD-grown p-type GaN are 675–725 °C for 5 minutes in an $N_2$ atmosphere; p-type $Al_{0.30}Ga_{0.70}N$ is annealed at higher temperatures, typically at 850 °C for 1–2 minutes. It is believed that during thermal annealing the relatively weak acceptor–hydrogen bond is broken and that the hydrogen atoms are driven out of the epitaxial film. Hydrogen atoms are small and generally diffuse easily through the interstitial sites of a crystalline material. The heating caused by LEEBI is believed to have a similar effect.

The doping of AlGaN/GaN and AlGaN/AlGaN superlattices (rather than GaN or AlGaN bulk material) was postulated to strongly increase the electrical activation of deep acceptors such as Mg (Schubert *et al*., 1996). Experimental increases in conductivity by a factor of 10 and more have indeed been reported by several research groups (Goepfert *et al*., 1999, 2000; Kozodoy *et al*. 1999a, b; Kipshidze *et al*., 2002, 2003). Figure 13.6 summarizes the problems and solutions to the doping activation in GaN and AlGaN.

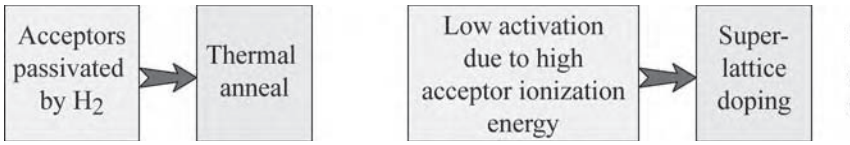


Fig. 13.6. Specific problems of p-type doping in GaN and their solution.

## *13.5 Dislocations in III–V nitrides*

The most common substrate for GaN epitaxial growth, sapphire, is a very stable substrate in terms of its thermal, chemical, and mechanical properties. However, sapphire has the complex ***corundum structure*** whereas III–V nitrides crystallize in the ***wurtzite structure***. Furthermore, the lattice constants of sapphire and GaN are different. As a result, GaN epitaxial films have misfit dislocations (threading and edge dislocations) that are typically on the order of $10^8$–

$10^9$ cm$^{-2}$.

The initial stages of GaN growth on sapphire are shown schematically in Fig. 13.7 (Nakamura and Fasol, 1997). The initial layer (called the faulted zone), grown at low temperatures (~ 500 °C) and subsequently annealed, is highly dislocated. However, dislocations undergo self-annihilation during anneal, so that subsequent layers (called the semi-sound zone and the sound zone) have much lower dislocation densities. A thorough review of the initial stages of GaN epitaxial growth on sapphire and an analysis of these initial stages using atomic-force microscopy and optical reflectometry was published by Koleske *et al*. (2004).

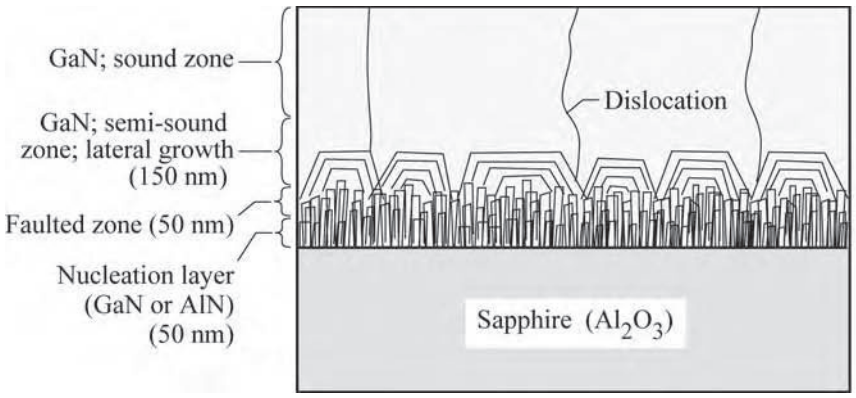


Fig. 13.7. Dislocation structure of a GaN epitaxial layer grown on sapphire by means of the GaN or AlN nucleation layer developed by Amano *et al*. (1986). The nucleation layer is normally grown at 500 °C, much lower than the following GaN epitaxial layers (after Nakamura and Fasol, 1997).

Generally, dislocation lines are electrically charged so that the region surrounding a dislocation line is either coulombically attractive or repulsive to a free carrier. The nature of the coulombic interaction (attractive or repulsive) depends on the polarity of the dislocation line and the polarity of the carrier. As an example, Fig. 13.8 shows a negatively charged dislocation line which is attractive to holes and repulsive to electrons.

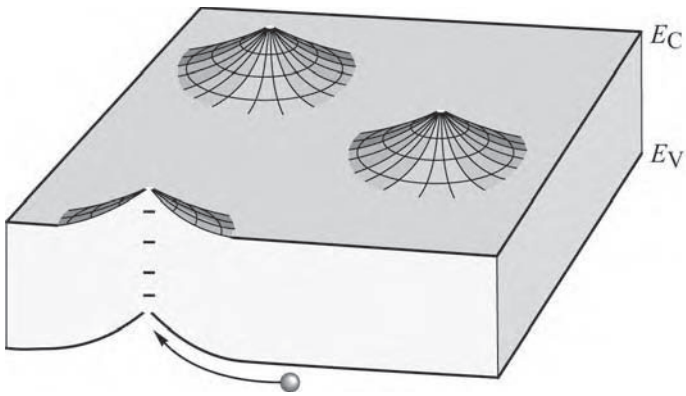


Fig. 13.8. Band diagram of semiconductor having negatively charged dislocations. Holes are attracted to dislocation lines where they must ultimately recombine with electrons.

Figure 13.9 shows the temporal development of the carrier dynamics of a positively charged



Nichia Exhibit 1014
Page 43

dislocation line. Initially, electrons are attracted but holes are repelled due to the potential created by the dislocation. However, the continued collection of electrons will screen the dislocation potential thereby reducing the repulsive barrier for holes. As a result, electrons and holes will recombine non-radiatively via electron states of the dislocation line. In Fig. 13.9, the electronic states of the dislocation are located within the bandgap.

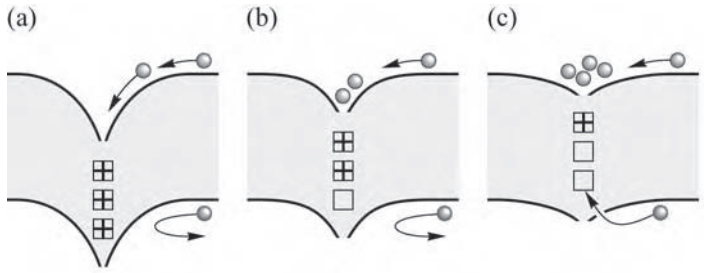


Fig. 13.9. Recombination in a positively charged dislocation. (a)–(c) Sequence shows electrons accumulating in the potential minimum thereby screening the dislocation potential and allowing holes to recombine.

A puzzling question is as to why the radiative recombination efficiency in III–V nitrides is so high despite the high density of dislocations? Several possible explanations are discussed below. However, none of these explanations has gained general acceptance.

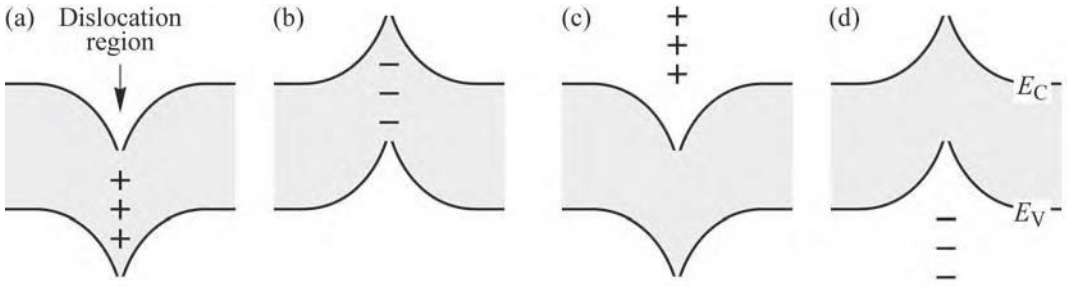


Fig. 13.10. Band diagram of dislocation: (a) donor states in gap, (b) acceptor states in gap, (c) donor states in conduction band, and (d) acceptor states in valence band. Whereas (a) and (b) lead to non-radiative recombination, (c) and (d) no not.

One possible explanation for high radiative rates in III–V nitrides is that the electronic states of the dislocation lie *outside* the forbidden gap, i.e. within the allowed bands of the semiconductor, as shown in Fig. 13.10 (c) and (d). This explanation is not in conflict with dark regions surrounding dislocations, observed in cathodoluminescence experiments (Rosner *et al*., 1997; Albrecht *et al*., 2002). Such dark regions unequivocally show the *absence* of *radiative* recombination but do not necessarily prove the *presence* of *non-radiative* recombination. The dark regions observed in cathodoluminescence could be explained by the incomplete screening of the dislocation potential, which would result in the repulsion of either electrons or holes, and

thus result in the absence of radiative recombination.

Other possible explanations for high radiative rates in III–V nitrides are the compositional alloy fluctuations, alloy clustering effects, and phase separation effects that necessarily result in a variation of the bandgap energy and lead to local potential minima, which carriers are attracted to and could be confined to (Nakamura and Fasol, 1997; Chichibu *et al*., 1996; Narukawa *et al*., 1997a, b). This explanation would be particularly suitable for ternary and quaternary alloy semiconductors such as GaInN and AlGaInN. The potential minima attract and confine carriers and prevent them from diffusing towards the dislocation lines. A band diagram showing energy-gap fluctuations and ***carrier localization*** is schematically illustrated in Fig. 13.11.

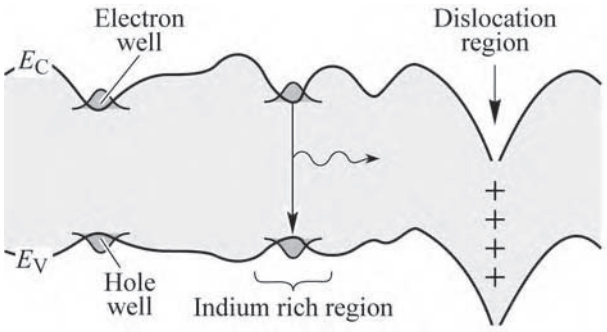


Fig. 13.11. Band diagram of GaInN having clusters of In rich regions which spatially localize carriers and prevent them from diffusing to dislocations.

Because the direct detection of indium-composition fluctuations in GaInN by transmission-electron microscopy was shown to be difficult and even ambiguous due to high-energy electron-beam induced damage, the magnitude of the indium fluctuations in GaInN is still under discussion (Smeeton *et al*., 2003).

Recently, Hangleiter *et al*. (2005) pointed out that a reduction of GaInN/GaN quantum-well thickness occurs in the vicinity of V-shaped defects of III–V nitride epitaxial layers. The authors proposed that the higher bandgap energy associated with the thinner GaInN quantum wells shields the dislocation line-defect from mobile carriers located in the thicker (planar) GaInN quantum wells. As a result, a high radiative efficiency would be maintained in quantum-well structures despite the presence of dislocation line-defects. However, this model cannot explain the high radiative efficiency of GaN thin films.

Although a generally accepted explanation has not yet been established, it remains a fact that the radiative efficiency in III–V nitrides, in particular GaInN/GaN blue emitters, exhibits low sensitivity to the presence of dislocations. That is, high radiative efficiencies are obtained in GaInN/GaN blue emitters despite high dislocation densities. This is illustrated in Fig. 13.12 which compares the normalized efficiency of different III–V semiconductors as a function of the


Nichia Exhibit 1014
Page 45

dislocation density in GaAs, AlGaAs, GaP, and GaAsP. Lester *et al*. (1995) estimated a 4% radiative efficiency for GaN with a dislocation density of $10^{10}$ cm$^{-2}$. The shaded region is the estimation of the author of this book based on blue GaInN/GaN emitters. The data shown in the figure elucidate that III–V nitrides have a much higher tolerance towards dislocations as compared to III–V arsenides and phosphides.

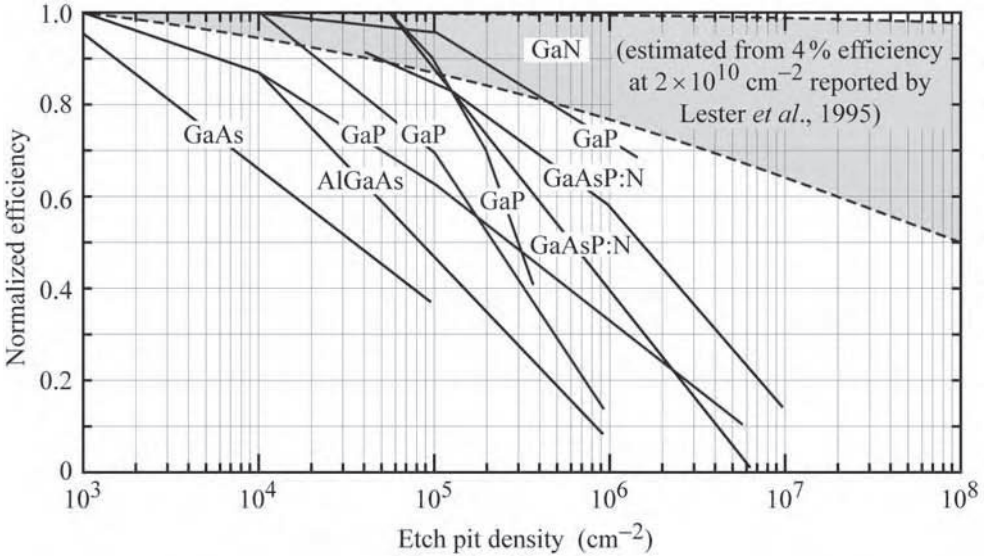


Fig. 13.12. Dependence of radiative efficiency on etch pit density (III–V arsenide and phosphide data adopted from Lester *et al*., 1995; III–V nitride data estimated by the author of this book based on data published by Lester *et al*., 1995).

### *13.6 UV devices emitting at wavelengths longer than 360 nm*

UV devices emitting at wavelengths longer than 360 nm generally have GaN or GaInN active regions. GaInN LEDs with peak wavelengths ranging from 400 nm to 410 nm were reported as early as 1993 (Nakamura *et al*., 1993a, b, 1994). The design of an early GaInN UV LED emitting at 370 nm is shown in Fig. 13.13. The device has a GaInN/AlGaN double heterostructure active region and AlGaN electron- and hole-blocking layers (Mukai *et al*., 1998). The active region and the carrier-blocking layers are clad by p-type and n-type GaN.

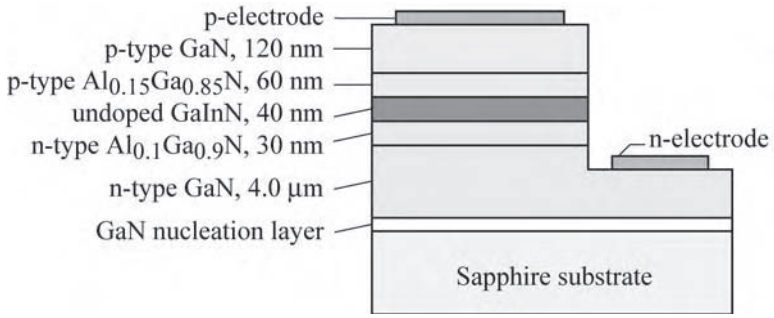


Fig. 13.13. Layer structure of GaInN UV LED grown on sapphire substrate emitting at 370 nm (after Mukai *et al*., 1998).

Figure 13.14 shows the emission spectrum of a 375 nm UV LED under pulsed and continuous wave (cw) injection conditions. Inspection of the figure reveals a small red-shift of the peak wavelength when going from pulsed to cw current injection. This shift is likely caused by junction heating, which generally leads to a lower bandgap energy and a red-shift of the emission wavelength.

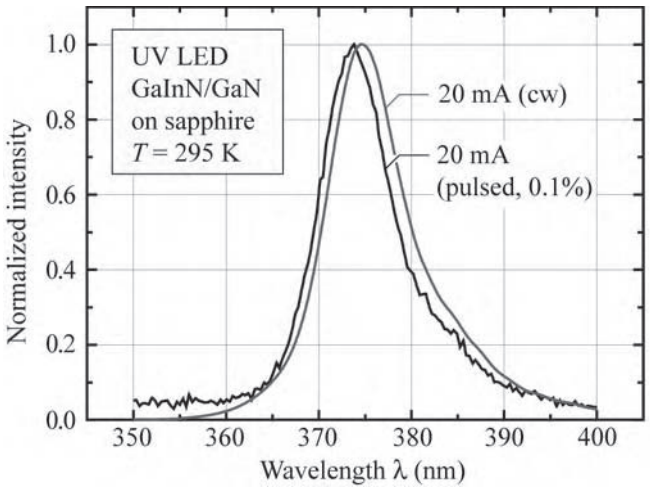


Fig. 13.14. Room temperature emission spectrum of commercial 375 nm UV LED (Nichia Corp.) under cw and pulsed conditions.

Figure 13.15 shows the emission intensity of a 375 nm UV LED as a function of the active layer thickness. The figure reveals that optimum output power is attained at 30–50 nm active layer thickness. It can be assumed that the active region is heavily doped in order to screen the polarization fields. Quantum well active regions with quantum well thicknesses < 5 nm reduce the effect of spatial electron–hole separation and for this reason, quantum well active regions have superseded the double heterostructure designs.

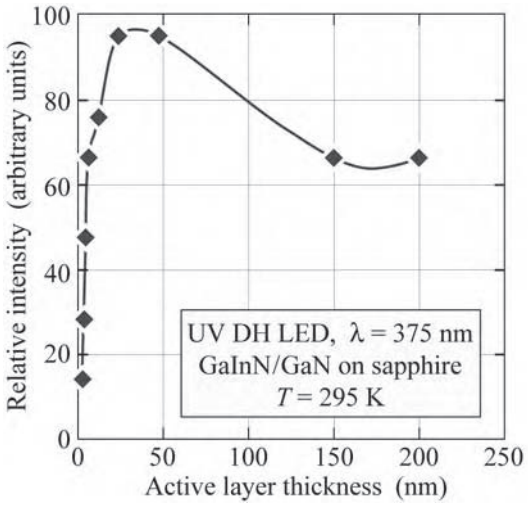


Fig. 13.15. Room temperature emission intensity as a function of GaInN active layer thickness for double heterostructure UV LEDs emitting at 375 nm (after Mukai *et al.*, 1998).



Nichia Exhibit 1014
Page 47

Figure 13.16 shows the dependence of the output power as a function of wavelength. As the emission wavelength decreases, a pronounced drop in the emission intensity is found. This has been attributed to the very positive influence of indium (In) incorporation on the internal quantum efficiency. The positive influence is reduced as less indium is incorporated in the active region with pure GaN active regions ($\lambda \approx 360$ nm) not benefiting at all.

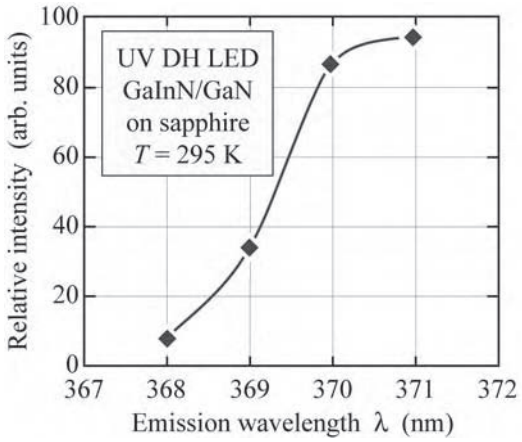


Fig. 13.16. Room temperature intensity as a function of emission wavelength for GaInN double heterostructure UV LEDs (after Mukai *et al.*, 1998).

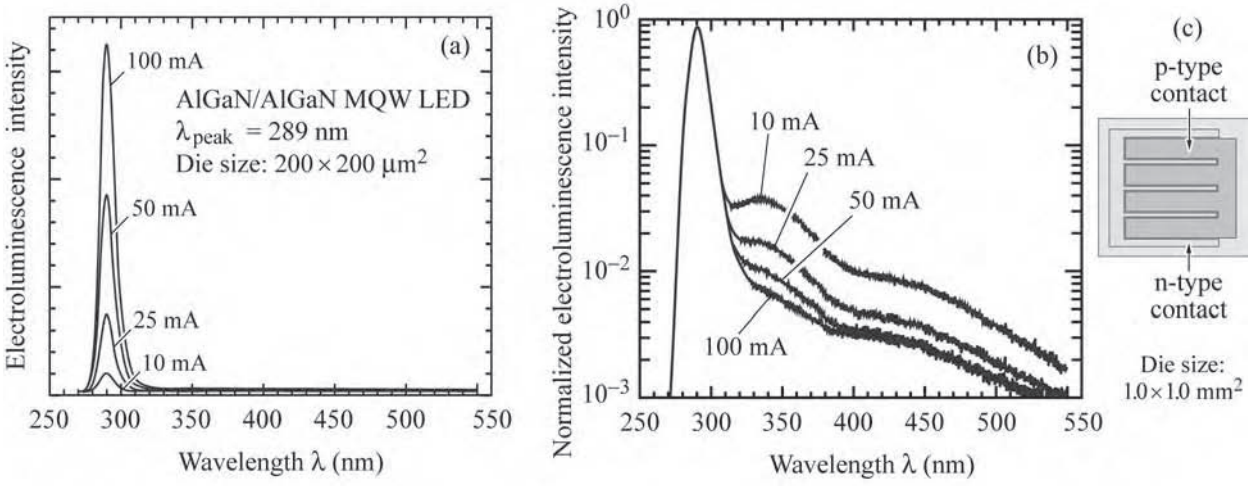


Fig. 13.17. Emission spectrum of deep-UV AlGaN/AlGaN multiple-quantum well LED for different injection currents on (a) linear and (b) logarithmic scales. An interdigitated contact geometry, as shown in (c), was used for large-area dies (after Fischer *et al.*, 2004).

## *13.7 UV devices emitting at wavelengths shorter than 360 nm*

Diodes emitting at wavelengths less than 360 nm have AlGaN active regions or $Al_xGa_{1-x}N$/$Al_yGa_{1-y}N$ multiple-quantum well (MQW) active regions. The power efficiency of these devices is generally low, i.e. less than 1%, although substantial progress has been made in recent years

(Zhang *et al*., 2002a, 2003; Yasan *et al*., 2002; Kipshidze *et al*., 2003; Fischer *et al*., 2004; Kim *et al*., 2004; Oder *et al*., 2004; Razeghi and Henini, 2004; Shakya *et al*., 2004; ).

The emission spectrum of an AlGaN/AlGaN deep-UV LED with interdigitated contact geometry is shown in Fig. 13.17 for different injection currents (Fischer *et al*., 2004). The active region of the device is composed of three $Al_{0.36}Ga_{0.64}N$ quantum wells with $Al_{0.48}Ga_{0.52}N$ barriers for emission at 290 nm. The spectrum displays one clean emission line with a peak wavelength of 289 nm. Some sub-bandgap emission near 330 nm becomes apparent when plotting the spectrum on a logarithmic scale. The forward voltage of the $200 \times 200\ \mu m^2$ and $1 \times 1\ mm^2$ devices was reported to be about 7.0 V and 6.0 V at a forward current of 20 mA, respectively.

The following issues deserve special attention in the field of AlGaN/AlGaN UV LEDs:

- ***Affinity of aluminum to oxygen***: Al has a very high affinity to $O_2$ making the incorporation of oxygen into AlGaN increasingly likely as the Al content increases. Oxygen forms a deep, DX-like level in Al-rich AlGaN (McCluskey *et al*., 1998; Wetzel *et al*., 2001).
- ***Conductivity of AlGaN***: Both the p-type and n-type conductivity of AlGaN decrease as the Al mol fraction increases, particularly for Al mol fractions exceeding 30% (Katsuragawa *et al*., 1998; Goepfert *et al*., 2000; Jiang and Lin, 2002). This leads to a higher resistivity in the confinement layers and higher device series resistances. A particular problem is the p-type conductivity in AlGaN. $Al_xGa_{1-x}N/Al_yGa_{1-y}N$ superlattices have been employed to alleviate the p-type doping problem.
- ***Lateral conductivity***: In devices grown on insulating substrates, with the standard side-by-side contact configuration, the n-type AlGaN layer provides the lateral conductivity. As the resistivity of Si-doped n-type AlGaN increases with the Al content, devices generally become more resistive. To compensate for this effect, the mean distance, which the electron current flows laterally in the n-type AlGaN lateral-conduction layer, needs to be reduced. This can be accomplished by an array of micro-LEDs (Kim *et al*., 2003; Khan, 2004) or by closely spaced fingers in interdigitated-contact geometries.
- ***Contact resistance***: Due to the high bandgap of AlGaN, contact-barrier heights are generally higher, which makes the attainment of low-resistance contacts increasingly difficult as the Al content increases.
- ***Diffusion of acceptors***: During the epitaxial growth of the top cladding layer, Mg acceptors may diffuse back into the active region, thereby lowering its radiative efficiency. Acceptor diffusion and the associated decrease in radiative efficiency may impose a limit on the maximum thickness of the p-type cladding layer.
- ***Heterojunction barriers***: Due to the larger bandgap energies, the conduction- and valence-



Nichia Exhibit 1014
Page 49

band discontinuities of heterojunctions are generally larger than for smaller-bandgap semiconductors. Compositional grading at the heterojunction interfaces reduces the resistance of heterojunction barriers.

- ***Light extraction***: To reduce reabsorption effects, all device layers should have an Al content sufficiently high to be transparent to the emitted light.
- ***Cracking***: AlGaN films grown on relaxed GaN are, due to the smaller lattice constant of AlGaN, under tensile strain. If the films are sufficiently thick, they crack. However, cracking can be strongly reduced or even eliminated by using Al-rich strain-compensating superlattices (Hearne *et al*., 2000; Han *et al*., 2001; Zhang *et al*., 2002b). Such strain-compensating superlattices reduce the lattice constant so that subsequent epitaxial layers have a much reduced tensile strain or are even under compressive strain. Hearne *et al*. (2000) provided a quantitative analysis of the maximum attainable thickness of a crack-free layer under tensile strain.

Optical micrographs of a 0.9 μm thick $Al_{0.15}Ga_{0.85}N$ film are shown in Fig. 13.18 (a) and (b) for growth without and with a strain-compensating superlattice, respectively. Figure 13.18 (b) shows a virtually crack-free AlGaN layer that was grown on a strain-compensating $AlN/Al_{0.45}Ga_{0.55}N$ superlattice with 10 periods and equal well- and barrier-layer thicknesses of 100 Å.

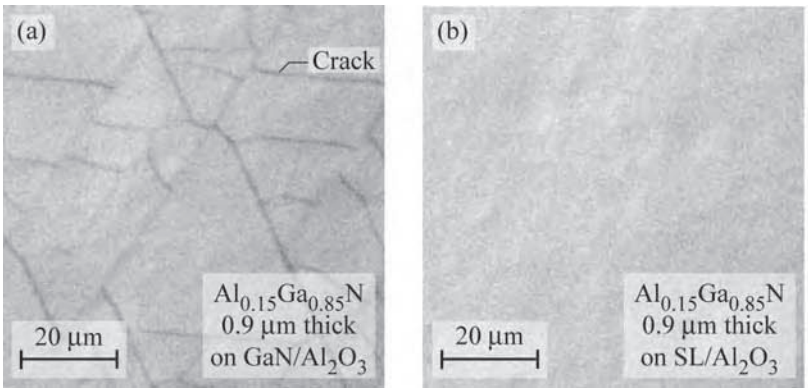


Fig. 13.18. Optical micrographs of $Al_{0.15}Ga_{0.85}N$ layer grown (a) without and (b) with a strain-compensating $AlN/Al_{0.45}Ga_{0.55}N$ superlattice (SL). The SL has 10 periods and equal well and barrier thicknesses of 10 nm. Angles between crack lines frequently are 60° or 120°.

**Exercise**: ***Cracking***. Why does cracking occur in epitaxial layers that are under biaxial tensile strain but not in epilayers that are under biaxial compressive strain?

Solution: Wafer bowing and ultimately cracking of an epitaxial film that is under biaxial tensile strain releases the strain energy stored in the film. For epitaxial layers that are under compressive strain, the strain energy can be released by wafer bowing, film buckling, and film delamination. Due to the compressive strain, there is "no room" for fissures or cracks, so that cracks generally do not form in compressively strained films.

The strain energy stored in a homo-epitaxial film, that is lattice mismatched to the substrate, is proportional to the thickness of the film. As the thickness of a strained film increases, it will at some point become energetically more favorable to reduce the strain energy by creating misfit dislocations and cracks. Thus, at a certain thickness, the film will form misfit dislocations to release the strain energy. The

critical thickness, at which a homo-epitaxial film starts forming misfit dislocations, is given by the ***Matthews–Blakeslee law*** (Matthews and Blakeslee, 1976). As the film thickness increases further, misfit dislocations do not suffice to release the strain energy, so that at some point the film will start to crack. A formula for the critical thickness at which a film under biaxial tensile strain starts to crack was given by Hearne *et al*. (2000).

AlGaN UV LEDs frequently have forward voltages $V_f >> h\nu/e$. Depending on the device structure, the excess forward voltage may originate from the p-type contact, the p-type AlGaN confinement layer, the n-type AlGaN layer providing lateral conduction, or from unipolar heterojunctions.

For devices with low or moderate efficiency as well as for high-power devices, device packages with low thermal resistance are desirable. The heat resulting from an excess forward voltage and low quantum efficiency must be removed to avoid excessively high junction temperatures. Morita *et al*. (2004) reported a particularly well heat-sunk device, namely a structure in which the sapphire substrate was removed by laser lift-off, and, using an AuSn solder, the epilayer was directly bonded to a CuW heat sink.

## *References*


Albrecht M., Strunk H. P., Weyher J. L., Grzegory I., Porowski S., and Wosinski T. "Carrier recombination at single dislocations in GaN measured by cathodoluminescence in a transmission electron microscope" *J. Appl. Phys*. **92**, 2000 (2002)

Amano H., Kito M., Hiramatsu K., and Akasaki I. "P-type conduction in Mg-doped GaN treated with low-energy electron beam irradiation (LEEBI)" *Jpn. J. Appl. Phys*. **28**, L2112 (1989)

Ambacher O., Smart J., Shealy J. R., Weimann N. G., Chu K., Murphy M., Schaff W. J., Eastman L. F. Dimitrov R., Wittmer L., Stutzmann M., Rieger W. and Hilsenbeck J. "Two-dimensional electron gases induced by spontaneous and piezoelectric polarization charges in N- and Ga-face AlGaN/GaN heterostructures" *J. Appl. Phys*. **85**, 3222 (1999)

Ambacher O., Foutz B., Smart J., Shealy J. R., Weimann N. G., Chu K., Murphy M., Sierakowski A. J., Schaff W. J., Eastman L. F., Dimitrov R., Mitchell A., and Stutzmann M. "Two dimensional electron gases induced by spontaneous and piezoelectric polarization in undoped and doped AlGaN/GaN heterostructures" *J. Appl. Phys*. **87**, 334 (2000)

Ambacher O., Majewski J., Miskys C., Link A., Hermann M., Eickhoff M., Stutzmann M., Bernardini F., Fiorentini V., Tilak V., Schaff W. J, and Eastman L. F. "Pyroelectric properties of Al(In)GaN/GaN hetero- and quantum well structures" *J. Phys.: Condens. Matter* **14**, 3399 (2002)

Bernardini F., Fiorentini V., and Vanderbilt D. "Spontaneous polarization and piezoelectric constants of III–V nitrides" *Phys. Rev. B* **56**, R10 024 (1997)

Chichibu S., Azuhata T., Sota T., and Nakamura S. "Spontaneous emission of localized excitons in InGaN single and multiquantum well structures" *Appl. Phys. Lett*. **69**, 4188 (1996)

Fischer A. J., Allerman A. A., Crawford M. H., Bogart K. H. A., Lee S. R., Kaplar R. J., Chow W. W., Kurtz S. R., Fullmer K. W., and Figiel J. J. "Room-temperature direct current operation of 290 nm light-emitting diodes with milliwatt power levels" *Appl. Phys. Lett*. **84**, 3394 (2004)

Gessmann T., Li Y.-L., Waldron E. L., Graff J. W., Schubert E. F., and Sheu J. K. "Ohmic contacts to p-type GaN mediated by polarization fields in thin $In_xGa_{1-x}N$ capping layers" *Appl. Phys. Lett*. **80**, 986 (2002)

Goepfert I. D., Schubert E. F., Osinsky A., and Norris P. E. "Demonstration of efficient p-type doping in AlGaN/GaN superlattice structures" *Electron. Lett.* **35**, 1109 (1999)




Nichia Exhibit 1014
Page 51

Goepfert I. D., Schubert E. F., Osinsky A., Norris P. E., and Faleev N. N. "Experimental and theoretical study of acceptor activation and transport properties in p-type $Al_xGa_{1-x}N$/GaN superlattices" *J. Appl. Phys*. **88**, 2030 (2000)

Hangleiter A., Hitzel F., Netzel C., Fuhrmann D., Rossow U., Ade G., and Hinze P. "Suppression of nonradiative recombination by V-shaped pits in GaInN/GaN quantum wells produces a large increase in the light emission efficiency" *Phys. Rev. Lett*. **95**, 127402 (2005)

Han J., Waldrip K. E., Lee S. R., Figiel J. J., Hearne S. J., Petersen G. A., and Myers S. M. "Control and elimination of cracking of AlGaN using low-temperature AlGaN interlayers" *Appl. Phys. Lett*. **78**, 67 (2001)

Hearne S. J., Han J., Lee S. R., Floro J. A., Follstaedt D., Chason M. E., and Tsong I. S. T. "Brittle-ductile relaxation kinetics of strained AlGaN/GaN heterostructures" *Appl. Phys. Lett*. **76**, 1534 (2000)

International Congress on Light, Copenhagen, Denmark (1932)

Jiang H. X. and Lin J. Y. "AlGaN and InAlGaN alloys – epitaxial growth, optical and electrical properties, and applications" *Opto-Electron. Rev.* **10**, 271 (2002)

Katsuragawa M., Sota S., Komori M., Anbe C., Takeuchi T., Sakai H., Amano H., and Akasaki I. "Thermal ionization energy of Si and Mg in AlGaN" *J. Cryst. Growth* **189/190**, 528 (1998)

Khan M. A. "Deep-ultraviolet LEDs fabricated in AlInGaN using MEMOCVD" *Proc. SPIE* **5530**, 224 (2004)

Kim K. H., Li J., Jin S. X., Lin J. Y., and Jiang H. X. "III-nitride ultraviolet light-emitting diodes with delta doping" *Appl. Phys. Lett*. **83**, 566 (2003)

Kim K. H., Fan Z. Y., Khizar M., Nakarmi M. L., Lin J. Y., and Jiang H. X. "AlGaN-based ultraviolet light-emitting diodes grown on AlN epilayers" *Appl. Phys. Lett*. **85**, 4777 (2004)

Kipshidze G., Kuryatkov V., Borisov B., Holtz M., Nikishin S., and Temkin H. "AlGaInN-based ultraviolet light-emitting diodes grown on Si ⟨111⟩" *Appl. Phys. Lett*. **80**, 3682 (2002)

Kipshidze G., Kuryatkov V., Zhu K., Borisov B., Holtz M., Nikishin S., and Temkin H. "AlN/AlGaInN superlattice light-emitting diodes at 280 nm" *J. Appl. Phys*. **93**, 1363 (2003)

Koleske D. D., Coltrin M. E., Cross K. C., Mitchell C. C., and Allerman A. A. "Understanding GaN nucleation layer evolution on sapphire" *J. Cryst. Growth* **273**, 86 (2004)

Kozodoy P., Hansen M., DenBaars S. P., and Mishra U. K. "Enhanced Mg doping efficiency in $Al_{0.2}Ga_{0.8}N$/GaN superlattices" *Appl. Phys. Lett*. **74**, 3681 (1999a)

Kozodoy P., Smorchkova Y. P., Hansen M., Xing H., DenBaars S. P., Mishra U. K., Saxler A. W., Perrin R., and Mitchel W. C. "Polarization-enhanced Mg doping of AlGaN/GaN superlattices" *Appl. Phys. Lett*. **75**, 2444 (1999b)

Kumakura K., Makimoto T., and Kobayashi N. "Low resistance non-alloy ohmic contact to p-type GaN using Mg-doped InGaN contact layer" *Phys. Stat. Sol. (a)* **188**, 363 (2001)

Kumakura K., Makimoto T., and Kobayashi N. "Ohmic contact to p-GaN using a strained InGaN contact layer and its thermal stability" *Jpn. J. Appl. Phys*. **42**, 2254 (2003)

Lester S. D., Ponce F. A., Craford M. G., and Steigerwald D. A. "High dislocation densities in high efficiency GaN-based light-emitting diodes" *Appl. Phys. Lett*. **66**, 1249 (1995)

Li Y.-L., Schubert E. F., Graff J. W., Osinsky A., and Schaff W. F. "Low-resistance ohmic contacts to p-type GaN" *Appl. Phys. Lett*. **76**, 2728 (2000)

Matthews J. W. and Blakeslee A. E. "Defects in epitaxial multilayers – III. Preparation of almost perfect multilayers" *J. Cryst. Growth* **32**, 265 (1976)

McCluskey M. D., Johnson N. M., Van de Walle C. G., Bour D. P., Kneissl M., and Walukiewicz W. "Metastability of oxygen donors in AlGaN" *Phys. Rev. Lett*. **80**, 4008 (1998)

Morita D., Yamamoto M., Akaishi K., Matoba K., Yasutomo K., Kasai Y., Sano M., Nagahama S.-I., and Mukai T. "Watt-class high-output-power 365 nm ultraviolet light-emitting diodes" *Jpn. J. Appl. Phys*. **43**, 5945 (2004)

Mukai T., Morita D., and Nakamura S. "High-power UV GaInN/AlGaN double-heterostructure LEDs" *J. Cryst. Growth* **189**, 778 (1998)

Nakamura S., Senoh M., and Mukai T. "Highly p-type Mg doped GaN films grown with GaN buffer layers" *Jpn. J. Appl. Phys*. **30**, L1708 (1991)

Nakamura S., Mukai T., Senoh M., and Iwasa N. "Thermal annealing effects on p-type Mg-doped GaN films" *Jpn. J. Appl. Phys*. **31**, L139 (1992)

Nakamura S., Senoh M., and Mukai T. "P-GaN / N-InGaN / N-InGaN double heterostructure blue-light-emitting diodes" *Jpn. J. Appl. Phys*. **32**, L8 (1993a)

Nakamura S., Senoh M., and Mukai T. "High-power InGaN/GaN double-heterostructure violet light emitting diodes" *Appl. Phys. Lett*. **62**, 2390 (1993b)

Nakamura S. "Growth of InGaN compound semiconductors and high-power InGaN/AlGaN double heterostructure violet-light-emitting diode" *Microelectron. J.* **25**, 651 (1994)

Nakamura S. and Fasol G. *The Blue Laser Diode* (Springer, Berlin, 1997). The authors discuss carrier localization effects on page 305 of the book. The authors discuss the initial stages of epitaxial growth on page 13 of the book.

Narukawa Y., Kawakami Y., Fujita S., Fujita S., and Nakamura S. "Recombination dynamics of localized excitons in $In_{0\,20}Ga_{0\,80}N$ - $In_{0\,05}Ga_{0\,95}N$ multiple quantum wells" *Phys. Rev*. **B 55**, R 1938 (1997a)

Narukawa Y., Kawakami Y., Funato M., Fujita S., Fujita S., and Nakamura S. "Role of self-formed InGaN quantum dots for exciton localization in the purple laser diode emitting at 420 nm" *Appl. Phys. Lett*. **70**, 981 (1997b)

Oder T. N., Kim K. H., Lin J. Y., and Jiang H. X. "III-nitride blue and ultraviolet photonic crystal light emitting diodes" *Appl. Phys. Lett*. **84**, 466 (2004)

Razeghi M. and Henini M. "Optoelectronic devices: III–nitrides" (Elsevier, Amsterdam, 2004)

Rosner S. J., Carr E. C., Ludowise M. J., Girolami G., and Erikson H. I. "Correlation of cathodoluminescence inhomogeneity with microstructural defects in epitaxial GaN grown by metal-organic chemical-vapor deposition" *Appl. Phys. Lett*. **70**, 420 (1997)

Schubert E. F., Grieshaber W., and Goepfert I. D. "Enhancement of deep acceptor activation in semiconductors by superlattice doping" *Appl. Phys. Lett.* **69**, 3737 (1996)

Shakya J., Kim K. H., Lin J. Y., and Jiang H. X. "Enhanced light extraction in III-nitride ultraviolet photonic crystal light-emitting diodes" *Appl. Phys. Lett*. **85**, 142 (2004)

Siozade L., Leymarie J., Disseix P., Vasson A., Mihailovic M., Grandjean N., Leroux M., and Massies J. "Modelling of thermally detected optical absorption and luminescence of (In,Ga)N/GaN heterostructures" *Solid State Commun.* **115**, 575 (2000)

Smeeton T. M., Kappers M. J., Barnard J. S., Vickers M. E., and Humphreys C. J. "Electron-beam-induced strain within InGaN quantum wells: False indium "cluster" detection in the transmission electron microscope" *Appl. Phys. Lett*. **83**, 5419 (2003)

Su Y. K., personal communication at the *Second Asia-Pacific Workshop on Widegap Semiconductors* (APWS), Hsinchu, Taiwan, March 7–9 (2005)

Walukiewicz W., Li S. X., Wu J., Yu K. M., Ager III J. W., Haller E. E., Lu K., and Schaff W. J. "Optical properties and electronic structure of InN and In-rich group III-nitride alloys" *J. Cryst. Growth* **269**, 119 (2004)

Wetzel C., Amano H., Akasaki I., Ager III J. W., Grzegory I., and Meyer B. K. "DX-like behavior of oxygen in GaN" *Physica B* **302–303**, 23 (2001)

Wu J., Walukiewicz W., Yu K. M., Ager J. W., Haller E. E., Lu H., and Schaff W. J. "Small band gap bowing in $In_{1-x}Ga_xN$ alloys" *Appl. Phys. Lett.* **80**, 4741 (2002)

Wu J, Walukievicz W., Yu K. M., Ager III J. W., Li S. X., Haller E. E., Lu H., and Schaff W. J. "Universal bandgap bowing in group-III nitride alloys" *Solid State Commun.* **127**, 411 (2003)

Yasan A., McClintock R., Mayes K., Darvish S. R., Kung P., and Razeghi M. "Top-emission ultraviolet light-emitting diodes with peak emission at 280 nm" *Appl. Phys. Lett*. **81**, 801 (2002)

Yun F., Reshchikov M. A., He L., King T., Morkoç H., Novak S. W., and Wei L. "Energy band bowing parameter in $Al_xGa_{1-x}N$ alloys" *J. Appl. Phys*. **92** , 4837 (2002)

Zhang J. P., Chitnis A., Adivarahan V., Wu S., Mandavilli V., Pachipulusu R., Shatalov M., Simin G., Yang J. W., and Khan M. A. "Milliwatt power deep ultraviolet light-emitting diodes over sapphire with emission at 278 nm" *Appl. Phys. Lett*. **81**, 4910 (2002a)

Zhang J. P., Wang H. M., Gaevski M. E., Chen C. Q., Fareed Q., Yang J. W., Simin G., and Khan M. A. "Crack-free thick AlGaN grown on sapphire using AlN/AlGaN superlattices for strain management" *Appl. Phys. Lett*. **80**, 3542 (2002b)

Zhang J. P., Wu S., Rai S., Mandavilli V., Adivarahan V., Chitnis A., Shatalov M., and Khan M. A. "AlGaN multiple-quantum-well-based deep ultraviolet light-emitting diodes with significantly reduced long-wave emission" *Appl. Phys. Lett*. **83**, 3456 (2003)



Nichia Exhibit 1014
Page 53

# 14

## Spontaneous emission from resonant cavities

### *14.1 Modification of spontaneous emission*

Radiative transitions, i.e. transitions of electrons from an initial quantum state to a final state and the simultaneous emission of a light quantum, are one of the most fundamental processes in optoelectronic devices. There are two distinct ways by which the emission of a photon can occur, namely by *spontaneous* and *stimulated* emission. These two processes were first postulated by Einstein (1917).

Stimulated emission is employed in semiconductor lasers and superluminescent LEDs. It was realized in the 1960s that the stimulated emission mode can be used in semiconductors to drastically change the radiative emission characteristics. The efforts to harness stimulated emission resulted in the first room-temperature operation of semiconductor lasers (Hayashi *et al*., 1970) and the first demonstration of a superluminescent LED (Hall *et al*., 1962).

Spontaneous emission implies the notion that the recombination process occurs *spontaneously*, that is without a means to influence this process. In fact, spontaneous emission has long been believed to be uncontrollable. However, research in microscopic optical resonators, where spatial dimensions are of the order of the wavelength of light, showed the possibility of controlling the spontaneous emission properties of a light-emitting medium. The changes of the emission properties include the spontaneous emission rate, spectral purity, and emission pattern. These changes can be employed to make more efficient, faster, and brighter semiconductor devices. The changes in spontaneous emission characteristics in resonant cavity (RC) and photonic crystal (PC) structures were reviewed by Joannopoulos (1995).

Microcavity structures have been demonstrated with different active media and different microcavity structures. The first microcavity structure was proposed by Purcell (1946) for emission frequencies in the radio frequency (rf) regime. Small metallic spheres were proposed as the resonator medium. However, no experimental reports followed Purcell's theoretical publication. In the 1980s and 1990s, several microcavity structures were realized with different

types of optically active media. The emission media included organic dyes (De Martini *et al*., 1987; Suzuki *et al*., 1991), semiconductors (Yablonovitch *et al*., 1988; Yokoyama *et al*., 1990), rare-earth-doped silica (Schubert *et al*., 1992b; Hunt *et al*., 1995b), and organic polymers (Nakayama *et al*., 1993; Dodabalapur *et al*., 1994). In these publications, clear changes in spontaneous emission were demonstrated including changes in spectral, spatial, and temporal emission characteristics.

At the beginning of the 1990s, current-injection ***resonant-cavity light-emitting diodes*** (RCLEDs) were first demonstrated in the GaAs material system (Schubert *et al*., 1992a) and subsequently in organic light-emitting materials (Nakayama *et al*., 1993). Both publications reported an emission line narrowing due to the resonant cavities. RCLEDs have many advantageous properties when compared with conventional LEDs, including higher brightness, increased spectral purity, and higher efficiency. For example, the spectral power density in RCLEDs was shown to be enhanced by more than one order of magnitude (Hunt *et al*., 1992, 1995a).

The changes in optical gain in VCSELs due to the enhancement in spontaneous emission was analyzed by Deppe and Lei (1992). The comparison of a *macro*cavity, in which the cavity is much *longer* than the emission wavelength ($\lambda << L_{cav}$), with a *micro*cavity ($\lambda \approx L_{cav}$) revealed that the gain can be enhanced by factors of 2–4 for typical GaAs emission linewidths at room temperature (50 nm). Thus laser threshold currents can be lower in microcavity structures due to the higher gain.

It is important to distinguish between emission *inside* the cavity and emission *out of* the cavity. The enhancement of the spontaneous emission *inside* the cavity and emission through one of the mirrors *out of* the cavity can be very different. At moderate values of the cavity finesse, the spontaneous emission inside and out of the cavity is enhanced. However, for very high finesse cavities (see, for example, Jewell *et al*., 1988), the overall emission out of the cavity *decreases* (Schubert *et al*., 1996). In the limit of very high reflectivity reflectors ($R_1 = R_2 \rightarrow 100\%$), the emission out of the cavity becomes zero. This effect will be discussed in detail below.

A device in which all the spontaneous emission occurs into a single optical mode has been proposed by Kobayashi *et al*. (1982, 1985). This device has been termed a ***zero-threshold laser*** (Yokoyama, 1992) and a ***single-mode LED*** (Yablonovitch, 1994). In a conventional laser, only a small portion of the spontaneous emission couples into a single state of the electromagnetic field controlled by the laser cavity. The rest is lost to free-space modes that radiate out of the side of



Nichia Exhibit 1014
Page 55

the laser. The idea of a thresholdless laser is simple. It assumes a wavelength-size cavity in which only one optical mode exists. Thus spontaneous as well as stimulated emission couples to this optical mode. The thresholdless laser should lack a threshold, i.e. the clear distinction between the spontaneous and the lasing regime which is observed in the light-output versus current characteristic of conventional lasers. Clearly, the prospects of such a device are intriguing. Even though several attempts to demonstrate a thresholdless laser have been reported (Yokoyama *et al*., 1990; Yokoyama 1992; Numai *et al*., 1993), a thresholdless laser has not yet been demonstrated.

## *14.2 Fabry–Perot resonators*

The simplest form of optical cavity consists of two coplanar mirrors separated by a distance $L_{cav}$. About one century ago, Fabry and Perot (1899) were the first to build and analyze optical cavities with coplanar reflectors. These cavities had a large separation between the two reflectors, i.e. $L_{cav} >> \lambda$. However, if the distance between the two reflectors is of the order of the wavelength of light, new physical phenomena occur, including the enhancement of the optical emission from an active material inside the cavity. Very small cavities, with typical dimensions of $L_{cav} \approx \lambda$, will be denoted as *microcavities*.

Coplanar microcavities are the simplest form of optical microcavities and their properties are summarized below. For a detailed discussion of the optical properties of Fabry–Perot cavities, the reader is referred to the literature (Coldren and Corzine, 1995; Saleh and Teich, 1991). Fabry–Perot cavities with two reflectors of reflectivity $R_1$ and $R_2$ are shown in Figs. 14.1 (a) and (b). Plane waves propagating inside the cavity can interfere constructively and destructively resulting in stable (allowed) optical modes and attenuated (disallowed) optical modes, respectively. (Note that the photon length is much longer than the microcavity length.) For lossless (non-absorbing) reflectors, the transmittance through the two reflectors is given by $T_1 = 1 - R_1$ and $T_2 = 1 - R_2$. Taking into account multiple reflections inside the cavity, the transmittance through a Fabry–Perot cavity can be expressed in terms of a geometric series. The transmitted light intensity (transmittance) is then given by

$$T = \frac{T_1 T_2}{1 + R_1 R_2 - 2\sqrt{R_1 R_2}\cos 2\phi} \tag{14.1}$$

where $\phi$ is the phase change of the optical wave for a single pass between the two reflectors. Phase changes at the reflectors are neglected. The maxima of the transmittance occur if the

condition of constructive interference is fulfilled, i.e. if $2\phi = 0, 2\pi, \ldots$ . Insertion of these values into Eq. (14.1) yields the transmittance maxima as

$$T_{\max} = \frac{T_1 T_2}{\left(1 - \sqrt{R_1 R_2}\right)^2} . \tag{14.2}$$

For asymmetric cavities ($R_1 \neq R_2$), $T_{\max} < 1$. For symmetric cavities ($R_1 = R_2$), the transmittance maxima are unity, $T_{\max} = 1$.

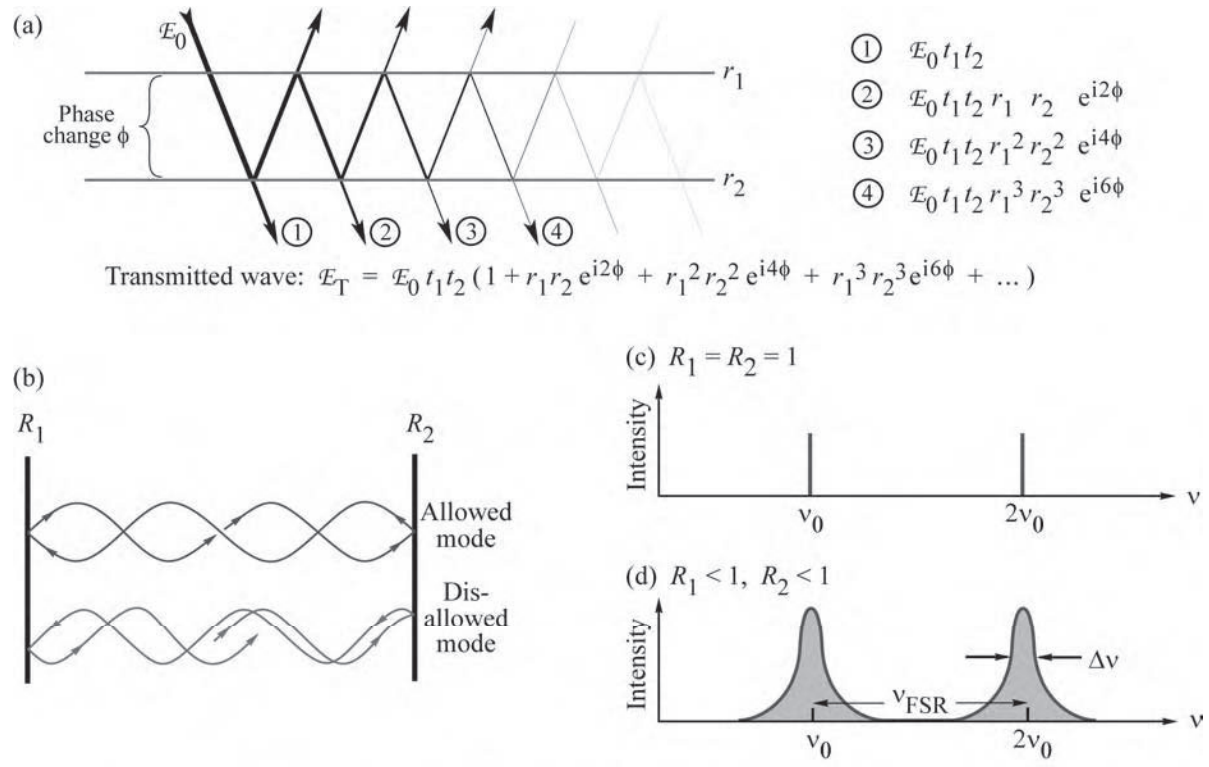


Fig. 14.1. (a) Transmission of a light wave with electric field ampltitude $\mathcal{E}_0$ through a Fabry–Perot resonator. (b) Schematic illustration of allowed and disallowed optical modes in a Fabry–Perot cavity consisting of two coplanar reflectors. Optical mode density for a resonator with (c) no mirror losses ($R_1 = R_2 = 100\%$) and (d) mirror losses.

**Exercise**: ***Transmission through a Fabry–Perot cavity***. Derive Eq. (14.1) by calculating the transmitted wave intensity in terms of a geometric series as illustrated in Fig. 14.1 (a).

Near $\phi = 0, 2\pi, 4\pi \ldots$, the cosine term in Eq. (14.1) can be expanded into a power series ($\cos 2\phi \approx 1 - 2\phi^2$). One obtains



Nichia Exhibit 1014
Page 57

$$T = \frac{T_1 T_2}{\left(1 - \sqrt{R_1 R_2}\right)^2 + \sqrt{R_1 R_2}\, 4\phi^2} . \tag{14.3}$$

Equation (14.3) indicates that near the maxima, the transmittance can be approximated by a lorentzian function. The transmittance $T$ in Eq. (14.3) has a maximum at $\phi = 0$. The transmittance decreases to half of the maximum value at $\phi_{1/2} = [1 - (R_1 R_2)^{1/2}] / [4 (R_1 R_2)^{1/2}]^{1/2}$. For high values of $R_1$ and $R_2$, i.e. $R_1 \approx 1$ and $R_2 \approx 1$, it is $\phi_{1/2} = (1/2) [1 - (R_1 R_2)^{1/2}]$.

The cavity finesse, $F$, is defined as the ratio of the transmittance peak separation to the transmittance full-width at half-maximum, i.e.

$$F = \frac{\text{peak separation}}{\text{peak width}} = \frac{\pi}{2\phi_{1/2}} = \frac{\pi \sqrt[4]{R_1 R_2}}{1 - \sqrt{R_1 R_2}} \approx \frac{\pi}{1 - \sqrt{R_1 R_2}} . \tag{14.4}$$

Inspection of Eq. (14.4) shows that the finesse becomes very large for high values of $R_1$ and $R_2$.

The wavelength and frequency of light are practically more accessible than the phase. Equations (14.1)–(14.4) can be converted to wavelength and frequency using

$$\phi = 2\pi \frac{\bar{n} L_{\text{cav}}}{\lambda} = 2\pi \frac{\bar{n} L_{\text{cav}} \nu}{c} \tag{14.5}$$

where $L_{\text{cav}}$ is the length of the cavity, $\lambda$ is the wavelength of light in vacuum, $\nu$ is the frequency of light, and $\bar{n}$ is the refractive index inside the cavity. Figures 14.1 (c) and (d) show the transmittance through a cavity with $R = 1$ and $R < 1$, respectively. In the frequency domain, the transmittance peak separation is called the *free spectral* range $\nu_{\text{FSR}}$, as shown in Fig. 14.1 (d). The finesse of the cavity in the frequency domain is then given by $F = \nu_{\text{FSR}} / \Delta\nu$.

Frequently the *cavity quality factor Q* rather than the finesse is used. The cavity $Q$ is defined as the ratio of the transmittance peak frequency to the peak width. Using this definition and Eq. (14.4), one obtains

$$Q = \frac{\text{peak frequency}}{\text{peak width}} = \frac{2\bar{n} L_{\text{cav}}}{\lambda} \frac{\pi \sqrt[4]{R_1 R_2}}{1 - \sqrt{R_1 R_2}} \approx \frac{2\bar{n} L_{\text{cav}}}{\lambda} \frac{\pi}{1 - \sqrt{R_1 R_2}} \tag{14.6}$$

where the peak width is measured in units of frequency.

Figure 14.2 shows an example of a reflectance spectrum of a microcavity consisting of a four-pair $Si / SiO_2$ distributed Bragg reflector (DBR) deposited on a Si substrate, a $SiO_2$ center

region, a 2.5-pair $Si/SiO_2$ DBR top reflector. The resonance wavelength of the cavity is approximately 1.0 μm. The reflectance of the cavity does not approach zero at the resonance wavelength due to the unequalness of the reflectivities of the two reflectors.

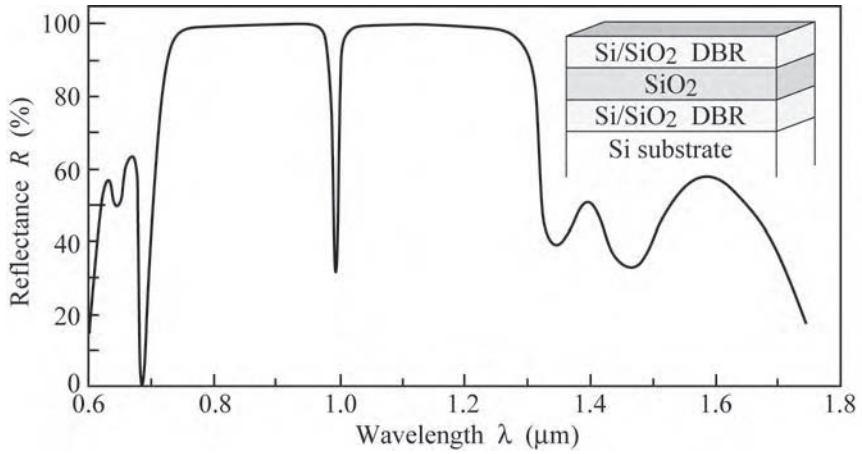


Fig. 14.2. Reflectance of a Fabry–Perot cavity consisting of two $Si/SiO_2$ reflectors and a $SiO_2$ center region. At the resonance wavelength ($\lambda \approx 1000$ nm), the reflectivity has a sharp dip.

### *14.3 Optical mode density in a one-dimensional resonator*

In this section, the enhancement of spontaneous emission will be calculated based on the changes of the *optical mode density* in a one-dimensional (1D) resonator, i.e. a coplanar Fabry–Perot microcavity. We first discuss the basic physics causing the changes of the spontaneous emission from an optically active medium located inside a microcavity and then derive analytical formulas for the spectral and integrated emission enhancement. The spontaneous radiative transition rate in an optically active, homogeneous medium is given by (see, for example, Yariv, 1982)

$$W_{\text{spont}} = \tau_{\text{spont}}^{-1} = \int_0^\infty W_{\text{spont}}^{(\ell)}\, \rho(\nu_\ell)\, d\nu_\ell \tag{14.7}$$

where $W_{\text{spont}}^{(\ell)}$ is the spontaneous transition rate into the optical mode $\ell$ and $\rho(\nu_\ell)$ is the optical mode density. Assuming that the optical medium is homogeneous, the spontaneous emission lifetime, $\tau_{\text{spont}}$, is the inverse of the spontaneous emission rate. However, if the optical mode density in the device depends on the spatial direction, as in the case of a cavity structure, then the emission rate given in Eq. (14.7) depends on the direction. Equation (14.7) can be applied to some small range of solid angle along a certain direction, for example the direction perpendicular to the reflectors of a Fabry–Perot cavity. Thus, Eq. (14.7) can be used to calculate the emission rate along a specific direction, in particular the optical axis of a cavity.



Nichia Exhibit 1014
Page 59

The spontaneous emission rate into the optical mode $\ell$, $W_{\text{spont}}^{(\ell)}$, contains the dipole matrix element of the two electronic states involved in the transition (Yariv, 1982). Thus $W_{\text{spont}}^{(\ell)}$ will *not* be changed by placing the optically active medium inside an optical cavity. However, the optical mode density, $\rho(\nu_\ell)$, is strongly modified by the cavity. Next, the changes in optical mode density will be used to calculate the changes in spontaneous emission rate.

We first compare the optical mode density in free space with the optical mode density in a microcavity. For simplicity, we restrict our considerations to the one-dimensional case, i.e. to the case of a coplanar Fabry–Perot microcavity. Furthermore, we restrict our considerations to the emission along the optical axis of the cavity.

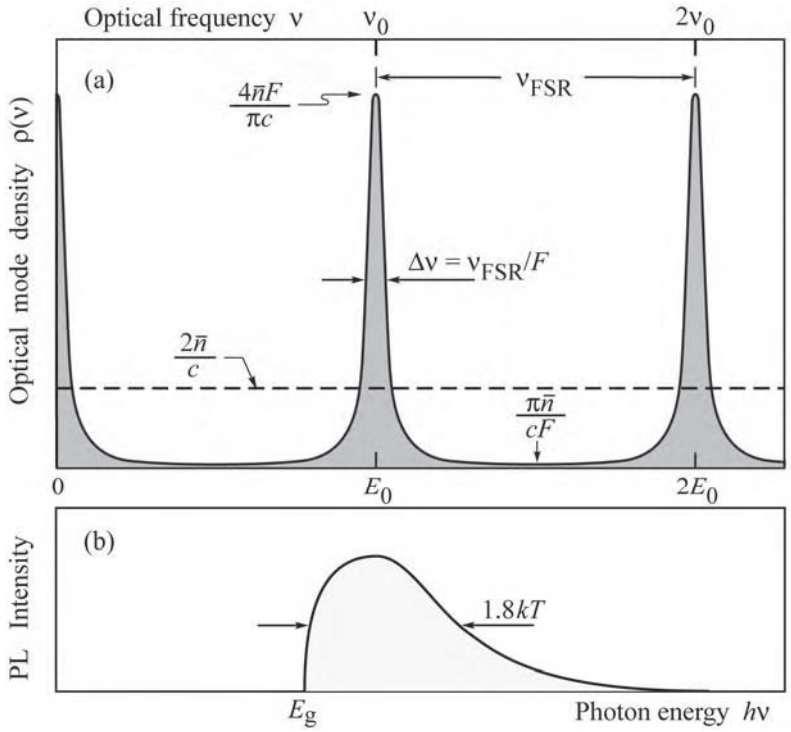


Fig. 14.3. (a) Optical mode density of a one-dimensional planar microcavity (solid line) and of homogeneous one-dimensional space. (b) Theoretical shape of the luminescence spectrum of bulk semiconductors.

In a one-dimensional homogeneous medium, the density of optical modes per unit length per unit frequency is given by

$$\rho^{1D}(\nu) = \frac{2\bar{n}}{c} \tag{14.8}$$

where $\bar{n}$ is the refractive index of the medium. Equation (14.8) can be derived using a similar formalism commonly used for the derivation of the mode density in free space. The constant optical mode density given by Eq. (14.8) is shown in Fig. 14.3 (a).

**Exercise**: ***Optical mode density***. Derive Eq. (14.8), i.e. optical mode density in a 1D space.

In planar microcavities, the optical modes are discrete and the frequencies of these modes are integer multiples of the fundamental mode frequency. The optical mode density of a planar microcavity is shown schematically in Fig. 14.3 (a). The fundamental and first excited mode occur at frequencies of $\nu_0$ and $2\nu_0$, respectively. For a cavity with two metallic reflectors (no distributed Bragg reflectors) and a $\pi$ phase shift of the optical wave upon reflection, the fundamental frequency is given by $\nu_0 = c/(2\,\bar{n}\,L_{\mathrm{cav}})$, where $c$ is the velocity of light in vacuum and $L_{\mathrm{cav}}$ is the length of the cavity. In a *resonant microcavity*, the emission frequency of an optically active medium located inside the cavity equals the frequency of one of the cavity modes.

The optical mode density along the cavity axis can be derived using the relation between the mode density in the cavity and the optical transmittance through the cavity, $T(\nu)$,

$$\rho(\nu) \;=\; K\,T(\nu) \tag{14.9}$$

where $K$ is a constant. The value of this constant will be determined by a normalization condition, i.e. by considering a single optical mode. Using Eq. (14.1), the transmission through a Fabry–Perot cavity can be written as

$$T(\nu) \;=\; \frac{T_1\,T_2}{1 \;+\; R_1\,R_2 \;-\; 2\sqrt{R_1\,R_2}\;\cos(4\pi\,\bar{n}\,L_{\mathrm{cav}}\nu/c)}\;. \tag{14.10}$$

The transmittance has maxima at $\nu = 0,\ \nu_0,\ 2\,\nu_0\ \ldots$ , and minima at $\nu = \nu_0/2,\ \ 3\,\nu_0/2,\ \ 5\,\nu_0/2\ \ldots$ . The lorentzian approximation of a transmittance maximum at $\nu = 0$ is obtained by expanding the cosine term in Eq. (14.10) into a power series using $\cos x \;\approx\; 1 - (x^2/2)$, so that

$$T(\nu) \;=\; \frac{T_1\,T_2\,\left(\sqrt{R_1\,R_2}\;\right)^{-1}\,(4\pi\,\bar{n}\,L_{\mathrm{cav}}/c)^{-2}}{\dfrac{\left(1-\sqrt{R_1\,R_2}\;\right)^2}{\left(\sqrt{R_1\,R_2}\;\right)^{-1}\,(4\pi\,\bar{n}\,L_{\mathrm{cav}}/c)^2} \;+\; \nu^2}\;. \tag{14.11}$$

Integrating $\rho(\nu)$ over all frequencies and the cavity length yields a single optical mode, i.e.

$$K\,\int_0^{L_{\mathrm{c}}}\,\int_{-\infty}^{\infty}\,\rho(\nu)\;\mathrm{d}\nu\;\mathrm{d}L \;=\; 1\;. \tag{14.12}$$



Nichia Exhibit 1014
Page 61

The lower and upper limit of the frequency integration can be chosen to be $\pm\infty$ since the lorentzian approximation of Eq. (14.11) has only one maximum at $\nu = 0$. Using Eqs. (14.9), (14.11), and the integration formula $\int_{-\infty}^{\infty}(a^2 + x^2)^{-1}\mathrm{d}x = \pi / a$ yields

$$K = \frac{(R_1 R_2)^{3/4}}{T_1 T_2} \frac{4\overline{n}}{c} \left(1 - \sqrt{R_1 R_2}\right). \tag{14.13}$$

Using Eq. (14.9), the optical mode density of a one-dimensional cavity for emission along the cavity axis is then given by

$$\boxed{\rho(\nu) = \frac{(R_1 R_2)^{3/4}}{T_1 T_2} \frac{4\overline{n}}{c} \left(1 - \sqrt{R_1 R_2}\right) T(\nu)}. \tag{14.14}$$

Equation (14.14) allows one to calculate the density of optical modes at the maxima and minima. At the *maxima*, the mode density is given by

$$\rho_{\max} = \frac{(R_1 R_2)^{3/4}}{1 - \sqrt{R_1 R_2}} \frac{4\overline{n}}{c}. \tag{14.15}$$

Using $(R_1 R_2)^{3/4} \approx 1$ and the expression derived for the finesse $F$ (see Eq. 14.4), one obtains an approximate expression for the mode density at the maxima

$$\rho_{\max} \approx \frac{4}{\pi} \frac{\overline{n} F}{c}. \tag{14.16}$$

That is, the mode density at the maxima is proportional to the finesse of the cavity. At the *minima*, the mode density is given by

$$\rho_{\min} = \frac{(R_1 R_2)^{3/4} \left(1 - \sqrt{R_1 R_2}\right)}{\left(1 + \sqrt{R_1 R_2}\right)^2} \frac{4\overline{n}}{c}. \tag{14.17}$$

Using $(R_1 R_2)^{3/4} \approx 1$ and the expression derived for the finesse $F$ (see Eq. 14.4), one obtains an approximate expression for the mode density at the minima

$$\rho_{\min} \approx \pi \frac{\overline{n}}{cF}. \tag{14.18}$$

That is, the mode density at the minima is *inversely* proportional to the finesse of the cavity.

The comparison of the optical mode densities of a one-dimensional (1D) free space and a 1D planar cavity is shown in Fig. 14.3. Note that the *mode density is conserved*, i.e. the areas below the 1D mode density and the 1D cavity mode density are the same.

### *14.4 Spectral emission enhancement*

Because the emission rate at a given wavelength is directly proportional to the optical mode density (see Eq. 14.7), the emission rate *enhancement spectrum* is given by the ratio of the 1D cavity mode density to the 1D free space mode density. As calculated earlier, the cavity enhancement spectrum has a lorentzian lineshape. The enhancement factor at the resonance wavelength is thus given by the ratio of the optical mode densities with and without a cavity, i.e.

$$G_e = \frac{\rho_{max}}{\rho^{1D}} \approx \frac{2}{\pi} F \approx \frac{2}{\pi} \frac{\pi (R_1 R_2)^{1/4}}{1 - \sqrt{R_1 R_2}} . \qquad (14.19)$$

The equation shows that a strong enhancement of the spontaneous emission rate along the cavity axis can be achieved with microcavities.

Equation (14.19) represents the *average* emission rate enhancement out of *both* reflectors of the cavity. To find the enhancement in a *single* direction, we multiply the enhancement given by Eq. (14.19) by the fraction of the light exiting the mirror with reflectivity $R_1$ (i.e. $1 - R_1$) divided by the average loss of the two mirrors for one round trip in the cavity (i.e. $(1/2)\,[(1 - R_1) + (1 - R_2)]$ ). For large $R_1$ and $R_2$, this gives for the enhancement of the emission exiting $R_1$

$$G_e \approx \frac{2(1-R_1)}{2-R_1-R_2} \frac{2F}{\pi} \approx \frac{1-R_1}{1-\sqrt{R_1 R_2}} \frac{2F}{\pi} \approx \frac{2}{\pi} \frac{\pi (R_1 R_2)^{1/4} (1-R_1)}{\left(1-\sqrt{R_1 R_2}\right)^2} \qquad (14.20)$$

where we used the approximation $1 - (R_1 R_2)^{1/2} \approx (1/2)(1 - R_1 R_2) \approx (1/2)(2 - R_1 - R_2)$. Equation (14.20) represents the emission rate enhancement from a *single* reflector with reflectivity $R_1$.

Next we take into account the standing wave effect, that is, the distribution of the optically active material relative to the nodes and antinodes of the optical wave. The antinode enhancement factor $\xi$ has a value of 2, if the active region is located exactly at an antinode of the standing wave inside the cavity. The value of $\xi$ is unity if the active region is smeared out over



Nichia Exhibit 1014
Page 63

many periods of the standing optical wave. Finally, $\xi = 0$ if the active material is located at a node.

The emission rate enhancement is then given by

$$G_e = \frac{\xi}{2}\,\frac{2}{\pi}\,\frac{\pi(R_1R_2)^{1/4}\,(1-R_1)}{\left(1-\sqrt{R_1R_2}\right)^2}\,\frac{\tau_{cav}}{\tau} \tag{14.21}$$

where $R_1$ is the reflectivity of the light-exit mirror and therefore $R_1 < R_2$. Equation (14.21) also takes into account changes in the spontaneous emission lifetime in terms of $\tau$, the lifetime without cavity, and $\tau_{cav}$, the lifetime with cavity. The factor of $\tau_{cav}/\tau$ ensures that the enhancement decreases if the cavity lifetime is reduced as a result of the cavity. For planar microcavities, the ratio of the spontaneous lifetime with a cavity, $\tau_{cav}$, and the lifetime without a cavity, $\tau$, is $\tau_{cav}/\tau \geq 0.9$ (Vredenberg *et al.*, 1993). Thus, the emission lifetime is changed by only a minor amount in a planar microcavity.

## *14.5 Integrated emission enhancement*

The total enhancement *integrated over wavelength*, rather than the enhancement at the resonance wavelength, is relevant for many practical devices. *On resonance*, the emission is enhanced along the axis of the cavity. However, sufficiently far *off resonance*, the emission is suppressed. Because the natural emission spectrum of the active medium (without a cavity) can be much broader than the cavity resonance, it is, *a priori*, not clear whether the integrated emission is enhanced at all. To calculate the wavelength-integrated enhancement, the spectral width of the cavity resonance and the spectral width of the natural emission spectrum must be determined. The resonance spectral width can be calculated from the finesse of the cavity or the cavity quality factor.

The theoretical width of the emission spectrum of bulk semiconductors is $1.8kT$ (see, for example, Schubert, 1993), where $k$ is Boltzmann's constant and $T$ is the absolute temperature. At room temperature, $1.8kT$ corresponds to an emission linewidth of $\Delta\lambda_n = 31$ nm for an emission wavelength of 900 nm. For a cavity resonance width of 5–10 nm, one part of the spectrum is strongly enhanced, whereas the rest of the spectrum is suppressed. The integrated enhancement ratio (or suppression ratio) can be calculated analytically by assuming a gaussian natural emission spectrum. For semiconductors at 300 K, the linewidth of the natural emission is, in the case of high-finesse cavities, *larger* than the width of the cavity resonance. The gaussian

emission spectrum has a width of $\Delta\lambda_n = 2\sigma(2\ln 2)^{1/2}$ and a peak value of $(\sigma(2\pi)^{1/2})^{-1}$, where $\sigma$ is the standard deviation of the gaussian function. The integrated enhancement ratio (or suppression ratio) is then given by (Hunt *et al*., 1993)

$$G_{\text{int}} = \frac{\pi}{2} G_e \, \Delta\lambda \frac{1}{\sigma\sqrt{2\pi}} = G_e \sqrt{\pi \ln 2} \frac{\Delta\lambda}{\Delta\lambda_n} \tag{14.22}$$

where the factor of $\pi/2$ is due to the lorentzian lineshape of the enhancement spectrum. Hence, the integrated emission enhancement depends on the natural emission linewidth of the active material. The value of $G_{\text{int}}$ can be quite different for different types of optically active materials. Narrow atomic emission spectra can be enhanced by several orders of magnitude (Schubert *et al*., 1992b). On the other hand, materials having broad emission spectra such as dyes or polymers (de Martini *et al*., 1987; Suzuki *et al*., 1991) may not exhibit any integrated enhancement at all. Equation (14.22) also shows that the width of the resonance has a profound influence on the integrated enhancement. Narrow resonance spectral widths, i.e. high finesse values or long cavities (Hunt *et al*., 1992), reduce the integrated enhancement.

---

**Example**: ***Spectral enhancement and integrated enhancement of a resonant-cavity structure***. As an example, we calculate the spectral and wavelength-integrated enhancement of a semiconductor resonant-cavity structure using Eqs. (14.21) and (14.22). With the reflectivities $R_1 = 90\%$ and $R_2 = 97\%$, an antinode enhancement factor of $\xi = 1.5$ and $\tau_{\text{cav}}/\tau \approx 1$, one obtains a finesse of $F = 46$, and a peak enhancement factor of $G_e = 68$ using Eq. (14.21). Insertion of this value into Eq. (14.22), using a cavity resonance bandwidth of $\Delta\lambda = 6.5$ nm (Schubert *et al*., 1994), and the theoretical 300 K natural emission linewidth of $\Delta\lambda = 31$ nm, one obtains a theoretical integrated enhancement factor of $G_{\text{int}} = 13$. Experimental enhancement factors of 5 have been demonstrated (Schubert *et al*., 1994) for the reflectivity values assumed above. The lower experimental enhancement is in part due to a broader natural emission linewidth, which exceeds the theoretical value of $1.8kT$.

---

The spontaneous emission spectrum of a bulk semiconductor is shown schematically in Fig. 14.3 (b). For maximum enhancement along the cavity axis, the cavity must be in resonance with the natural emission spectrum. Note that additional broadening mechanisms, such as alloy broadening, will broaden the natural emission spectrum over its theoretical value of $1.8kT$. Quantum well structures have inherently narrower spectra ($0.7kT$), due to the step-function-like density of states. Low temperatures and excitonic effects can further narrow the natural emission linewidth. Thus, higher enhancements are expected for low temperatures and quantum well active regions.



Nichia Exhibit 1014
Page 65

### *14.6 Experimental emission enhancement and angular dependence*

Particularly high spontaneous emission enhancements can be attained with emitters that have naturally narrow emission lines. Atomic transitions, as in rare-earth elements, have such narrow emission lines. For this reason, rare-earth doped cavities are a great system to study the emission enhancement. The emission spectrum of a high-finesse $Si/SiO_2$ cavity with an erbium-doped $SiO_2$ active layer is shown in Fig. 14.4 (Schubert *et al*., 1992b). A distinct narrowing of the Er emission spectrum and a giant enhancement of the emission was found. The enhancement factor was greater than 50, when compared to a non-cavity structure.

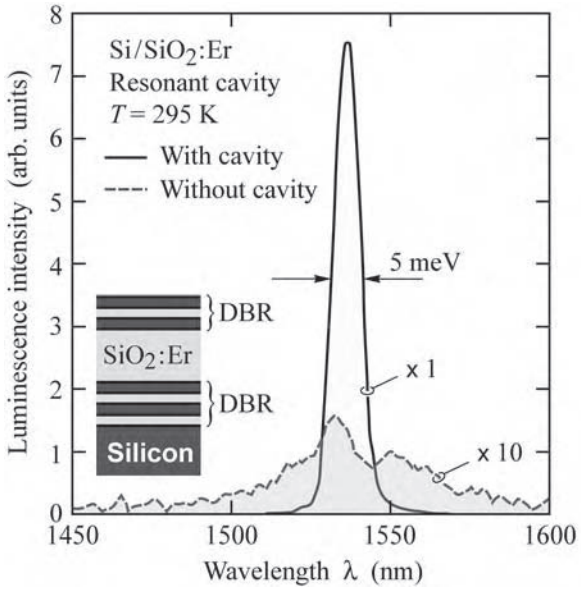


Fig. 14.4. Photoluminescence spectra of Er-doped $SiO_2$. One of the spectra is for Er-doped $SiO_2$ located in a cavity resonant at 1540 nm. The other spectrum is without a cavity. An emission enhancement factor greater than 50 is found (after Schubert *et al*., 1992b).

The cavity consisted of a 4-pair $Si/SiO_2$ bottom DBR with a calculated reflectivity of 99.8%, the Er-doped $\lambda/2$ thick $SiO_2$ active layer, and a 2.5-pair $Si/SiO_2$ top DBR with a calculated reflectivity of 98.5%. The $SiO_2$ active layer was doped with Er of dose $7.7 \times 10^{15}$ cm$^{-2}$. The measured cavity finesse was $F = 310$, slightly lower than the calculated finesse of 370.

The peak emission wavelength depends on the emission angle. The angular dependence can be derived from the condition that the normal wave vector, $k_\perp$, must be constant (in resonance with the cavity), independent of the $k$ propagation direction. This condition can be written as

$$k \cos\theta = k_\perp \tag{14.23}$$

or

$$\frac{2\pi}{\lambda_e(\theta)} \cos\theta = \frac{2\pi}{\lambda_{res}} \tag{14.24}$$

where $\lambda_{res}$ and $\lambda_e$ are the resonance and emission wavelengths, respectively, and $\theta$ is the angle inside the cavity with respect to the surface normal (polar angle), as illustrated in Fig. 14.5.

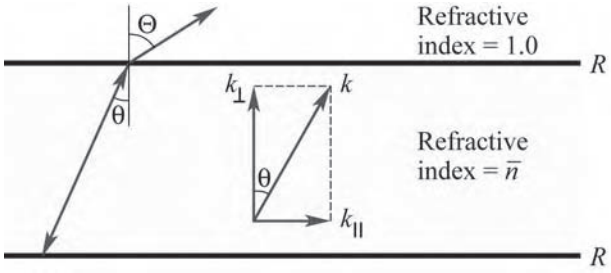


Fig. 14.5. Perpendicular and parallel component of wave vector $k$ for light propagating in a resonant cavity.

Using Eq. (14.24) and Snell's law ($\bar{n}$ sin θ = sin Θ), the emission wavelength is given by

$$\lambda_e = \lambda_{res} \cos\left[\arcsin\left(\frac{1}{\bar{n}}\sin\Theta\right)\right]. \tag{14.25}$$

For small angles, the equation can be approximated by

$$\lambda_e \approx \lambda_{res}\left(1 - \frac{\Theta^2}{2\bar{n}^2}\right). \tag{14.26}$$

The angular dependence of the peak emission wavelength is shown in Fig. 14.6. The solid and dashed lines are the exact (Eq. 14.25) and approximate solutions (Eq. 14.26), respectively. A refractive index of 1.5 is used in the calculation.

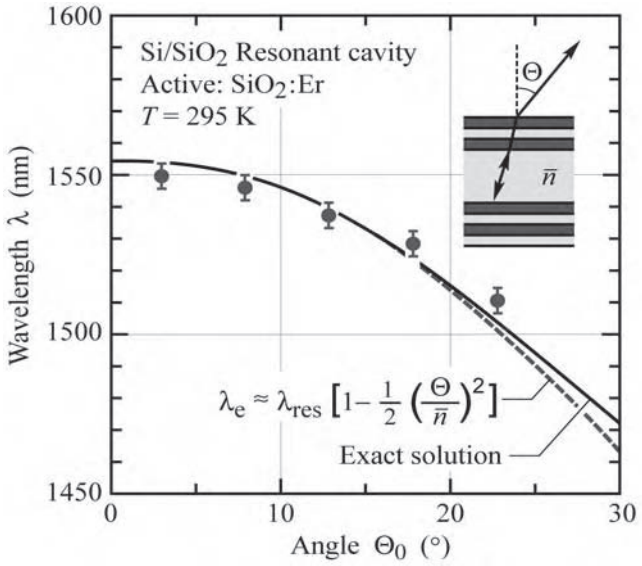


Fig. 14.6. Peak emission wavelength as a function of polar angle for a planar $Si/SiO_2$:Er resonant cavity (after Schubert *et al.*, 1992b).



Nichia Exhibit 1014
Page 67

A similar angular dependence is found for semiconductors. The emission spectra of an AlGaInP cavity are shown in Fig. 14.7 for different emission angles (Streubel *et al*., 2002). Note that the highest intensity is found at an emission angle of 30°, indicating that the resonance wavelength of the cavity is located at the long-wavelength end of the semiconductor natural emission spectrum. This results in the highest angle-integrated emission power (Streubel *et al*., 2002).

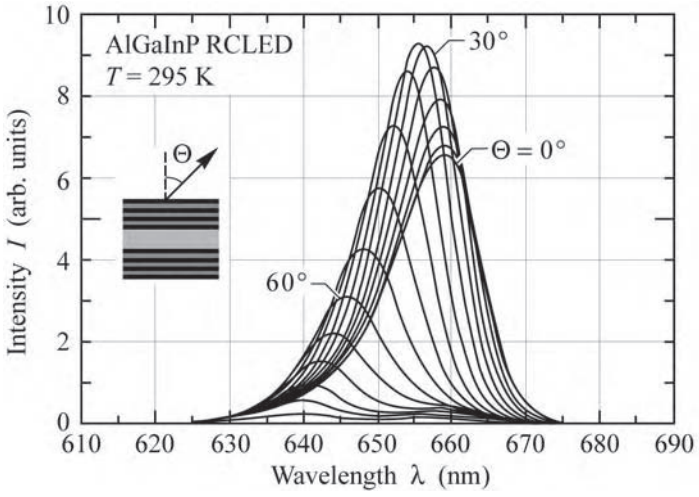


Fig. 14.7. Emission spectra of AlGaInP RCLED for different polar angles. The long-wavelength part of the QW emission is emitted in the forward direction (0°). The shorter wavelengths are emitted off-axis. When measured with an integrating sphere, an 18 nm wide spectrum (FWHM) is found (after Streubel *et al*., 2002).

## *References*


Coldren L. A. and Corzime S. W. *Diode Lasers and Photonic Integrated Circuits* (John Wiley and Sons, New York, 1995)

De Martini F., Innocenti G., Jacobovitz G. R., and Mataloni P. "Anomalous spontaneous emission time in a microscopic optical cavity" *Phys. Rev. Lett*. **59**, 2955 (1987)

Deppe D. G. and Lei C. "Spontaneous emission and optical gain in a Fabry–Perot microcavity" *Appl. Phys. Lett*. **60**, 527 (1992)

Dodabalapur A., Rothberg L. J., and Miller T. M. "Color variation with electroluminescent organic semiconductors in multimode resonant cavities" *Appl. Phys. Lett*. **65**, 2308 (1994)

Einstein A. "On the quantum theory of radiation" (translated from German) *Z. Phys*. **18**, 121 (1917)

Fabry G. and Perot A. "Theory and applications of a new interference method for spectroscopy" (translated from French) *Ann. Chim. Phys*. **16**, 115 (1899)

Hall R. N., Fenner G. E., Kingsley J. D., Soltys T. J., and Carlson R. O. "Coherent light emission from GaAs junctions" *Phys. Rev. Lett*. **9**, 366 (1962)

Hayashi I., Panish M. B., Foy P. W., and Sumski S. "Junction lasers which operate continuously at room temperature" *Appl. Phys. Lett*. **17**, 109 (1970)

Hunt N. E. J., Schubert E. F., Logan R. A., and Zydzik G. J. "Enhanced spectral power density and reduced linewidth at 1.3 μm in an InGaAsP quantum well resonant cavity light emitting diode" *Appl. Phys. Lett*. **61**, 2287 (1992)

Hunt N. E. J., Schubert E. F., Kopf R. F., Sivco D. L., Cho A. Y., and Zydzik G. J. "Increased fiber communications bandwidth from a resonant cavity light emitting diode emitting at λ = 940 nm" *Appl. Phys. Lett*. **63**, 2600 (1993)

Hunt N. E. J., Schubert E. F., Sivco D. L., Cho A. Y., Kopf R. F., Logan R. A., and Zydzik G. J. "High efficiency, narrow spectrum resonant cavity light-emitting diodes" in *Confined Electrons and Photons*

edited by E. Burstein and C. Weisbuch (Plenum Press, New York, 1995a)
Hunt N. E. J., Vredenberg A. M., Schubert E. F., Becker P. C., Jacobson D. C., Poate J. M., and Zydzik G. J. "Spontaneous emission control of $Er^{3+}$ in $Si/SiO_2$ microcavities" in *Confined Electrons and Photons* edited by E. Burstein and C. Weisbuch (Plenum Press, New York, 1995b)
Jewell J. L., Lee Y. H., McCall S. L., Harbison J. P., and Florez L. T. "High-finesse AlGaAs interference filters grown by molecular beam epitaxy" *Appl. Phys. Lett*. **53**, 640 (1988)
Joannopoulos J. D., Meade R. D., and Winn J. N. *Photonic Crystals* (Princeton University Press, Princeton, 1995)
Kobayashi T., Segawa T., Morimoto A., and Sueta T. *Meeting of the Jpn. Soc. of Appl. Phys*. Tokyo (1982); see also Yokoyama (1992)
Kobayashi T., Morimoto A., and Sueta T. *Meeting of the Jpn. Soc. of Appl. Phys*. Tokyo (1985); see also Yokoyama (1992)
Nakayama T., Itoh Y., and Kakuta A. "Organic photo- and electroluminescent devices with double mirrors" *Appl. Phys. Lett*. **63**, 594 (1993)
Numai T., Kosaka H., Ogura I., Kurihara K., Sugimoto M., and Kasahara K. "Indistinct threshold laser operation in a pnpn vertical to surface transmission electrophotonic device with a vertical cavity" *IEEE J. Quantum Electron.* **29**, 403 (1993)
Purcell E. M. "Spontaneous emission probabilities at radio frequencies" *Phys. Rev*. **69**, 681 (1946)
Saleh B. E. A. and Teich M. C. *Fundamentals of Photonics* (John Wiley and Sons, New York, 1991)
Schubert E. F., Wang Y. H., Cho A. Y., Tu L. W., and Zydzik G. J. "Resonant cavity light emitting diode" *Appl. Phys. Lett*. **60**, 921 (1992a)
Schubert E. F., Vredenberg A. M., Hunt N. E. J., Wong Y. H., Becker P. C., Poate J. M., Jacobson D. C., Feldman L. C., and Zydzik G. J. "Giant enhancement in luminescence intensity in Er-doped $Si/SiO_2$ resonant cavities" *Appl. Phys. Lett*. **61**, 1381 (1992b)
Schubert E. F. *Doping in III–V Semiconductors* p. 512 (Cambridge University Press, Cambridge UK, 1993)
Schubert E. F., Hunt N. E. J., Micovic M., Malik R. J., Sivco D. L., Cho A. Y., and Zydzik G. J. *Science* **265**, 943 (1994)
Schubert E. F., Hunt N. E. J., Malik R. J., Micovic M., and Miller D. L. "Temperature and modulation characteristics of resonant cavity light-emitting diodes" *IEEE J. Lightwave Technol.* **14**, 1721 (1996)
Streubel K., Linder N., Wirth R., and Jaeger A. "High brightness AlGaInP light-emitting diodes" *IEEE J. Sel. Top. Quantum Electron*. **8**, 321 (2002)
Suzuki M., Yokoyama H., Brorson S. D., and Ippen E. P. "Observation of spontaneous emission lifetime change of dye-containing Langmuir–Blodgett films in optical microcavities" *Appl. Phys. Lett*. **58**, 998 (1991)
Vredenberg A. M., Hunt N. E. J., Schubert E. F., Jacobson D. C., Poate J. M., and Zydzik G. J. *Phys. Rev, Lett*. **71**, 517 (1993)
Yablonovitch E., Gmitter T. J., and Bhat R. "Inhibited and enhanced spontaneous emission from optically thin AlGaAs / GaAs double heterostructures" *Phys. Rev. Lett*. **61**, 2546 (1988)
Yablonovitch E. personal communication (1994)
Yariv A. *Theory and Applications of Quantum Mechanics* (John Wiley and Sons, New York, 1982) p. 143
Yokoyama H., Nishi K., Anan T., Yamada H., Boorson S.D., and Ippen E. P. "Enhanced spontaneous emission from GaAs quantum wells in monolithic microcavities" *Appl. Phys. Lett*. **57**, 2814 (1990)
Yokoyama H. "Physics and device applications of optical microcavities" *Science* **256**, 66 (1992)



Nichia Exhibit 1014
Page 69

# 15

## Resonant-cavity light-emitting diodes

### *15.1 Introduction and history*

The resonant-cavity light-emitting diode (RCLED) is a light-emitting diode that has a light-emitting region inside an optical cavity. The optical cavity has a thickness of typically one-half or one times the wavelength of the light emitted by the LED, i.e. a fraction of a micrometer for devices emitting in the visible or in the infrared. The resonance wavelength of the cavity coincides or is in resonance with the emission wavelength of the light-emitting active region of the LED. Thus the cavity is a *resonant cavity*. The spontaneous emission properties from a light-emitting region located inside the resonant cavity are enhanced by the resonant-cavity effect. The RCLED is the first practical device making use of spontaneous emission enhancement occurring in microcavities.

The placement of an active region inside a resonant cavity results in multiple improvements of the device characteristics. Firstly, the light intensity emitted from the RCLED along the axis of the cavity, i.e. normal to the semiconductor surface, is higher compared with conventional LEDs. The enhancement factor is typically a factor of 2–10. Secondly, the emission spectrum of the RCLED has a *higher spectral purity* compared with conventional LEDs. In conventional LEDs, the spectral emission linewidth is determined by the thermal energy $kT$. However, in RCLEDs, the emission linewidth is determined by the quality factor ($Q$ factor) of the optical cavity. As a result, the spectral emission width of the RCLED is a factor of 2–5 narrower compared with conventional LEDs. For the same reason, the wavelength shift with temperature is determined by the temperature coefficient of the optical cavity and not by the energy gap of the active material. This results in a significantly higher temperature stability of the RCLED emission wavelength compared with conventional LEDs. Thirdly, the emission far-field pattern of the RCLED is more *directed* compared with conventional LEDs. In conventional LEDs, the emission pattern is lambertian (i.e. cosine-function-like). In an RCLED, the emission pattern is directed mostly along the optical axis of the cavity.

These characteristics of RCLEDs are desirable for local-area, medium bit rate optical communication systems. LEDs play an important role in local-area (< 5 km) medium bit rate (< 1 Gbit/s) optical communication networks. In particular, plastic optical fibers are increasingly used for optical communication over short distances. The higher emission intensity and the more directed emission pattern afforded by the RCLED increase the power coupled into the optical fiber. As a result, the RCLED can transmit data over longer distances. Furthermore, the higher spectral purity of RCLEDs results in less chromatic dispersion allowing for higher bit rates.

Light-emitting diodes are the transmitter device of choice for medium bit rate optical communication over distances less than 5 km. Compared with lasers, LEDs are less expensive, more reliable, and less temperature sensitive. The RCLED has improved characteristics compared with conventional LEDs while maintaining the inherent advantages of LEDs. The reflectivity of the RCLED reflectors is lower compared with vertical-cavity surface-emitting lasers (VCSELs), thereby allowing for a lower RCLED manufacturing cost compared with VCSELs. At 650 nm, the preferred communication wavelength for plastic optical fibers, VCSELs are difficult to manufacture due to the lack of high-reflectivity reflectors.

RCLEDs are also used for high-brightness applications (Streubel *et al*., 1998; Wirth *et al*., 2001, 2002). In these devices, the resonance wavelength is designed to be at the long-wavelength end of the spontaneous emission spectrum of the semiconductor. This ensures that the emission intensity, integrated over all spatial directions, is maximized.

The enhanced spontaneous emission occurring in resonant-cavity structures can be beneficially employed in semiconductor and polymer LEDs. Resonant-cavity light-emitting diodes were first realized in 1992 (Schubert *et al*., 1992a) in the GaAs material system. About a year later, RCLEDs were demonstrated in organic materials (Nakayama *et al*., 1993).

Resonant-cavity structures with enhanced spontaneous emission also include Er-doped microcavities (Schubert *et al*., 1992b). Owing to the inherently narrow luminescence line of intra-atomic Er radiative transitions, there is a very good overlap between the cavity optical mode and the Er luminescence line. At the present time, no Er-doped current-injection devices exist. However, the great potential of Er-doped resonant cavities makes the realization of Er-doped RCLEDs likely in the future.

## *15.2 RCLED design rules*

The basic structure of an RCLED is shown in Fig. 15.1 and comprises two mirrors with reflectivity $R_1$ and $R_2$. The reflectivity of the two mirrors is chosen to be unequal so that the light



Nichia Exhibit 1014
Page 71

exits the cavity predominantly through one of the mirrors. This mirror is called the ***light-exit mirror***. Here we designate the mirror with reflectivity $R_1$ as the light-exit mirror. An active region is located between the mirrors, preferably at the antinode location of the standing optical wave of the cavity, as shown in Fig. 15.1. Metal mirrors are assumed in Fig. 15.1 so that the wave amplitude is zero at the location of the mirrors.

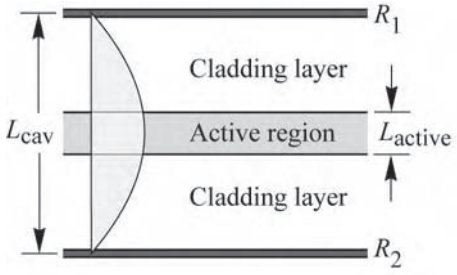


Fig. 15.1. Schematic illustration of a resonant cavity consisting of two metal mirrors with reflectivity $R_1$ and $R_2$. The active region has a thickness $L_{active}$ and an absorption coefficient $\alpha$. Also shown is the standing optical wave. The cavity length $L_{cav}$ is equal to $\lambda/2$.

Next, we summarize several design rules intended to maximize the spontaneous emission enhancement in resonant-cavity structures (Schubert *et al*., 1994, 1996; Hunt *et al*., 1995a, 1995b). These rules will provide further insight into the fundamental operating principles of RCLEDs and the differences of these devices with respect to VCSELs.

The ***first design criterion*** for RCLEDs is that the reflectivity of the light-exit reflector, $R_1$, should be much lower than the reflectivity of the back reflector, i.e.

$$R_1 \ll R_2 \ . \tag{15.1}$$

This condition ensures that light exits the device mainly through the reflector with reflectivity $R_1$. Equation (15.1) applies to the design of communication RCLEDs, where light is emitted into the small core of a multimode fiber, and display RCLEDs, where light should be emitted towards the observer.

The ***second design criterion*** calls for the shortest possible cavity length $L_{cav}$. In order to derive this criterion, the integrated enhancement, discussed in a preceding section, can be rewritten by using the expressions for the cavity finesse $F$ and cavity quality factor $Q$. One obtains

$$G_{int} = \frac{\xi}{2}\frac{2}{\pi}\frac{1-R_1}{1-\sqrt{R_1R_2}}\sqrt{\pi \ln 2}\ \frac{\lambda}{\Delta\lambda_n}\frac{\lambda_{cav}}{L_{cav}}\frac{\tau_{cav}}{\tau} \tag{15.2}$$

where $\lambda$ and $\lambda_{cav}$ are the active region emission wavelengths in vacuum and inside the cavity,

respectively. Since the emission wavelength λ and the natural linewidth of the active medium, $\Delta\lambda_n$, are given quantities, Eq. (15.2) shows that minimization of the cavity length $L_{cav}$ maximizes the integrated intensity.

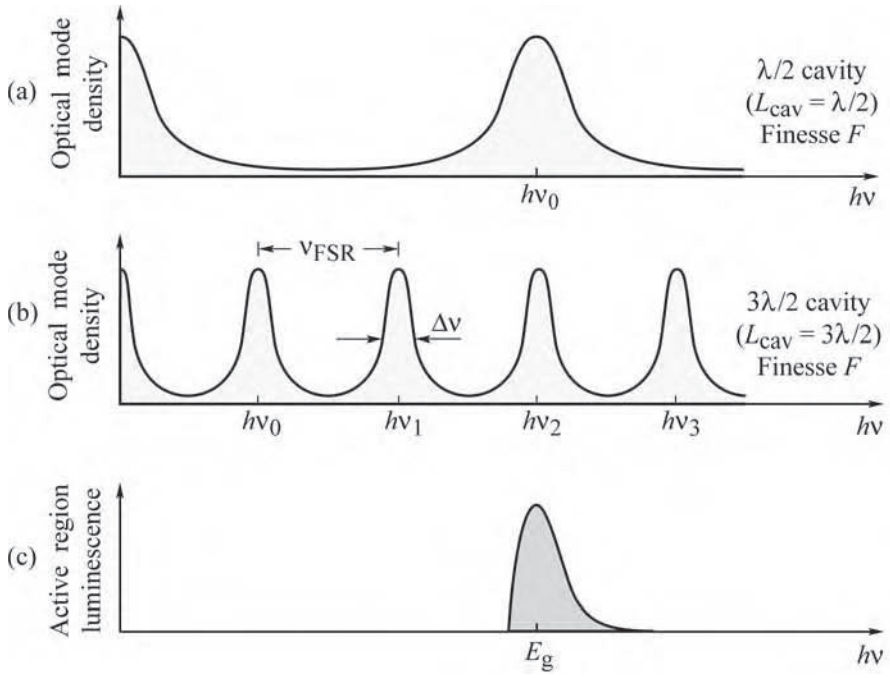


Fig. 15.2. Optical mode density for (a) a short and (b) a long cavity with the same finesse *F*. (c) Spontaneous free-space emission spectrum of an LED active region. The spontaneous emission spectrum has a better overlap with the short-cavity mode spectrum compared with the long-cavity mode spectrum.

The importance of a short cavity length is elucidated by Fig. 15.2. The optical mode densities of two different cavities, namely a short and a long cavity, are shown in Figs. 15.2 (a) and (b), respectively. Both cavities have the same mirror reflectivities and finesse. The natural emission spectrum of the active region is shown in Fig. 15.2 (c). The best overlap between the resonant optical mode and the active region emission spectrum is obtained for the shortest cavity.

The largest enhancements are achieved with the shortest cavities, which in turn are obtained if the *fundamental* cavity mode is in resonance with the emission from the active medium. The cavity length is also reduced by using a DBR with a short penetration depth, i.e. a DBR consisting of two materials with a large difference in the refractive index.

The ***third design criterion*** is the minimization of self-absorption in the active region. This criterion can be stated as follows: the reabsorption probability of photons emitted from the active region into the cavity mode should be much smaller than the escape probability of photons through one of the reflectors. Assuming $R_2 \approx 1$, this criterion can be written as

$$2\xi\alpha L_{active} \quad < \quad (1 - R_1) \tag{15.3}$$



Nichia Exhibit 1014
Page 73

where α and $L_{active}$ are the absorption coefficient and the thickness of the active region, respectively. If the criterion of Eq. (15.3) were not fulfilled, photons would most likely be reabsorbed by the active region. Subsequently, re-emission will, with a certain probability, occur along the lateral direction (waveguided modes), i.e. not into the cavity mode. Another possibility is that the electron–hole pairs generated by reabsorption recombine non-radiatively. In either case, reabsorption processes occurring in high-finesse cavities *reduce the cavity mode emission out of the cavity*. Thus, if the condition of Eq. (15.3) is not fulfilled, the emission intensity of resonant cavities is lowered rather than enhanced.

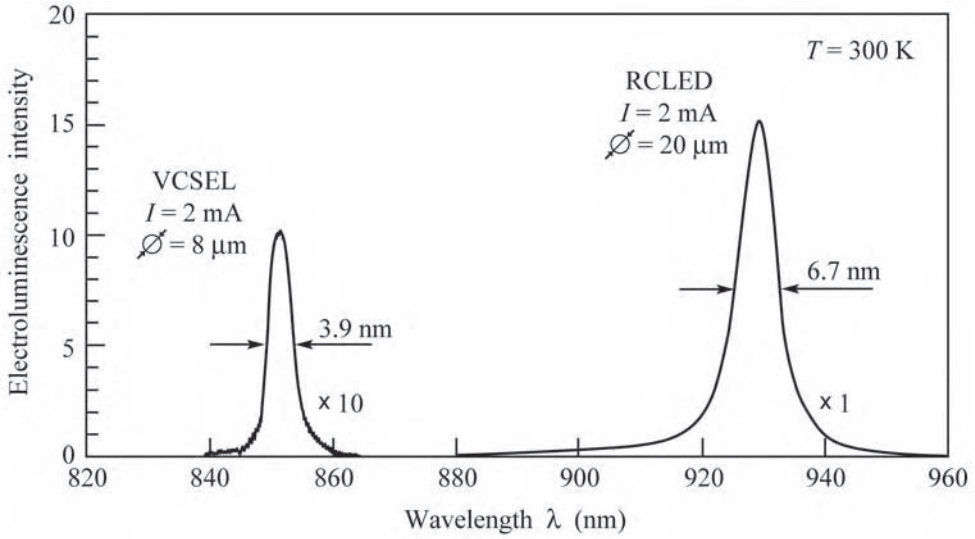


Fig. 15.3. Spontaneous electroluminescence spectrum of a vertical-cavity surface-emitting laser (VCSEL) emitting at 850 nm and of a resonant-cavity light-emitting diode (RCLED) emitting at 930 nm. The drive current for both devices is 2 mA. The VCSEL spectrum is multiplied by a factor of 10. The threshold current of the VCSEL is 7 mA (after Schubert *et al*., 1996).

Whereas the condition of Eq. (15.3) is fulfilled in RCLEDs, it is clearly not fulfilled in VCSELs. The spontaneous emission intensities of RCLEDs and VCSELs were compared by Schubert *et al*. (1996). In this comparison, the VCSEL and the RCLED were driven by an injection current of 2 mA, which is below the threshold current of the VCSEL of $I_{th}$ = 7 mA. The spontaneous emission spectra of an RCLED and a VCSEL are shown in Fig. 15.3. The VCSEL has an AlGaAs/GaAs quantum well active region emitting at 850 nm. Both reflectors of the VCSEL are AlGaAs/AlAs DBRs. Figure 15.3 reveals that the emission intensity of the VCSEL in the *spontaneous* regime is more than a factor of 15 lower than the emission intensity from the RCLED.

Because the magnitude of the maximum gain in semiconductors is always lower than the

magnitude of the absorption coefficient in an unpumped semiconductor ($|g| < |\alpha|$), VCSELs could not lase if the condition of Eq. (15.3) were met. Thus, the spontaneous emission intensity in VCSELs is low and *must be low* in order to enable the device to lase. Figure 15.3 also reveals that the emission spectral linewidth of VCSELs is narrower than that of RCLEDs. The higher spectral purity is due to the higher values of $R_1$ and $R_2$ as required for VCSELs.

The fulfillment of Eq. (15.3) by RCLEDs also implies that these devices *cannot lase*. As stated above, it is always $|g| < |\alpha|$. Consequently, the mirror loss $(1 - R_1)$ is always larger than the maximum achievable round-trip gain ($2\xi g L_{\text{active}}$). The fundamental inability of RCLEDs to lase has been verified experimentally by pulsed injecting currents of large magnitude without finding any evidence for lasing. These considerations show that the device physics of RCLEDs and VCSELs is fundamentally different.

The arguments used above imply that the *spontaneous* emission into the fundamental cavity mode in VCSEL structures is very low due to reabsorption of photons by the active region. A reduction of the threshold current by increasing the reflectivity will be accompanied by a further decrease of the *spontaneous* emission below threshold. We therefore conclude that the so-called zero-threshold laser (Kobayashi *et al*. 1982; Yokoyama, 1992) cannot be realized by a planar resonant-cavity structure.

### *15.3 GaInAs/GaAs RCLEDs emitting at 930 nm*

The structure of an RCLED with a GaInAs active region is shown in Fig. 15.4 (a). The cavity is defined by one distributed Bragg reflector (DBR) and one metallic reflector. Also included are two confinement regions and a four-quantum-well active region. The heavily doped n-type substrate is coated with a $ZrO_2$ anti-reflection layer (Schubert *et al*., 1994). A picture of the first RCLED is shown in Fig. 15.4 (b).

The motivation for the metal reflector is twofold. Firstly, the metallic Ag reflector serves as a non-alloyed ohmic contact to the heavily doped p-type ($N_A \approx 5 \times 10^{19}$ cm$^{-3}$) GaAs top layer, thus effectively confining the pumped region to the area below the contact. Secondly, it was shown in the preceding section that the cavity length must be kept as short as possible for maximizing the emission enhancement. Owing to the lack of a penetration depth, metal reflectors allow for a short cavity length. Cavities with two metallic reflectors have been reported (Wilkinson *et al*., 1995). However, optical absorption losses in the light-exit mirror can be large in a double metal mirror structure, unless very thin metallic reflectors are used (Tu *et al*., 1990). The lack of a p-type DBR also avoids the well-known problem of high resistance in p-type DBRs (Schubert *et*



Nichia Exhibit 1014
Page 75

*al*., 1992c; Lear and Schneider, 1996). It has been shown that parabolic grading yields the lowest ohmic resistance in DBRs. Such parabolic grading is suited to eliminating heterojunction band discontinuities (Schubert *et al.,* 1992c).

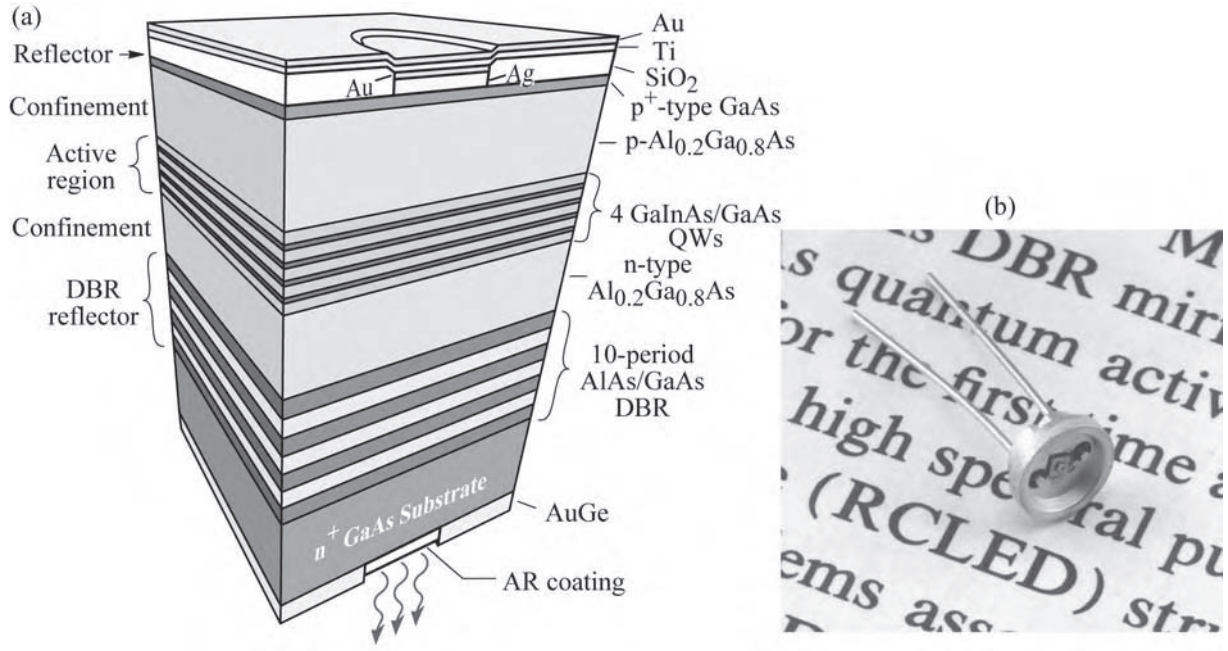


Fig. 15.4. (a) Schematic structure of a substrate-emitting GaInAs/GaAs RCLED consisting of a metal top reflector and a bottom distributed Bragg reflector (DBR). The RCLED emits at 930 nm. The reflectors are an AlAs/GaAs DBR and a Ag top reflector. (b) Picture of the first RCLED (after Schubert *et al*., 1994).

The magnitude of the reflectivity of the DBR needs to be consistent with Eqs. (15.1) and (15.3). The Ag back mirror has a reflectivity of approximately 96%. According to Eq. (15.1), the DBR reflectivity must be < 96%. The second criterion of Eq. (15.3) requires that $2\xi\alpha L_{\text{active}} < 1 - R_1$. Assuming $\xi = 1.3$, $\alpha = 10^4$ cm$^{-1}$, $L_{\text{active}} = 400$ Å, one obtains the condition $R_1 < 90\%$. Thus the mirror reflectivity of RCLEDs must be much lower than that of VCSELs. A high reflectivity would increase self-absorption and decrease the light output of the device as discussed earlier. De Neve *et al*. (1995) used an extensive theoretical model to calculate the mirror reflectivity. The maximum efficiency was calculated at a reflectivity of $R_1 = 50$–$60\%$.

The reflection and emission properties of the RCLED are shown in Figs. 15.5 (a) and (b). The reflection spectrum of the RCLED (Fig. 15.5 (a)) exhibits a highly reflective band for wavelengths > 900 nm and a dip in the reflectivity at the cavity resonance. The spectral width of the cavity resonance is 6.3 nm. The emission spectrum of an electrically pumped device, shown in Fig. 15.5 (b), has nearly the same shape and width as the cavity resonance.

In conventional LEDs, the spectral characteristics of the devices reflect the thermal distribution of electrons and holes in the conduction and valence bands. The spectral characteristics of light emission from microcavities are as intriguing as they are complex. However, restricting our considerations to the optical axis of the cavity simplifies the cavity physics considerably. If we assume that the cavity resonance is much narrower than the natural emission spectrum of the semiconductor, then the on-resonance luminescence is enhanced whereas the off-resonance luminescence is suppressed. The on-axis emission spectrum should therefore reflect the enhancement, that is, the resonance spectrum of the cavity. The experimental results shown in Fig. 15.5 confirm this conjecture.

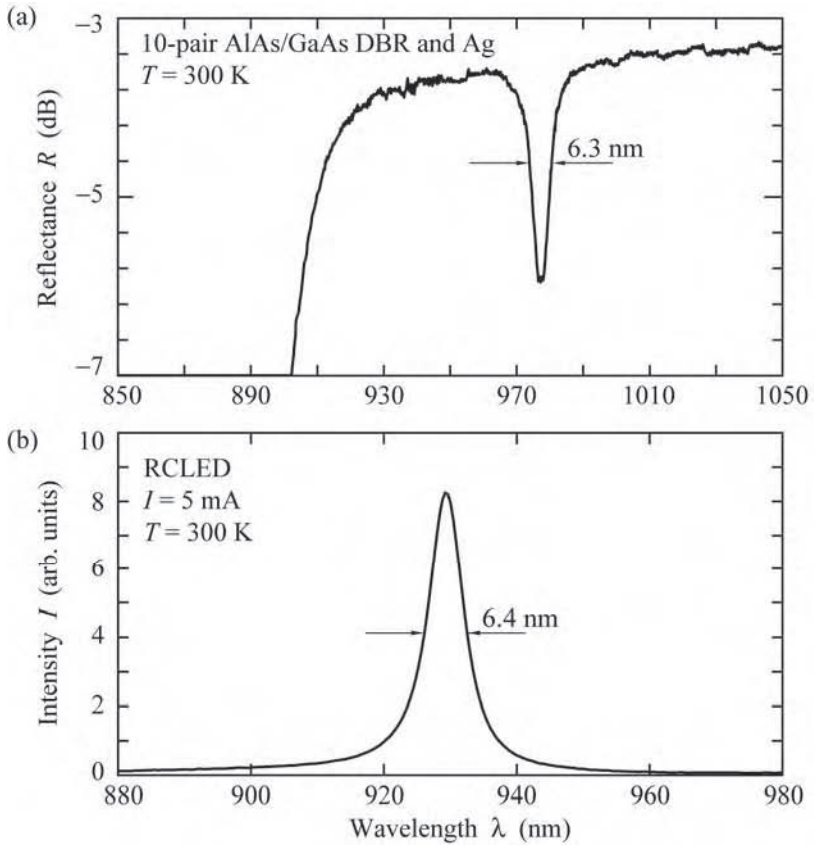


Fig. 15.5. (a) Reflectance of a resonant cavity consisting of a 10-pair AlAs/GaAs distributed Bragg reflector and an Ag reflector. (b) Emission spectrum of an RCLED consisting of a 10-pair AlAs/GaAs distributed Bragg reflector and an Ag reflector (after Schubert *et al*., 1994).

Owing to the cavity, the emission spectrum of an RCLED is much narrower than the emission spectrum of regular LEDs (Schubert *et al*. 1992a; Hunt *et al*., 1992, 1993). The spectral width of the RCLED emitted into a certain direction is given by the optical characteristics of the cavity. In contrast, the spectral width of a regular LED is about $1.8kT$, a value that is much wider than the RCLED emission spectrum. A comparison of a regular GaAs LED and a GaInAs



Nichia Exhibit 1014
Page 77

RCLED emission spectrum is shown in Fig. 15.6. Comparison of the spectra shows that the RCLED emission spectrum is a factor of about 10 narrower than the spectrum of the GaAs LED.

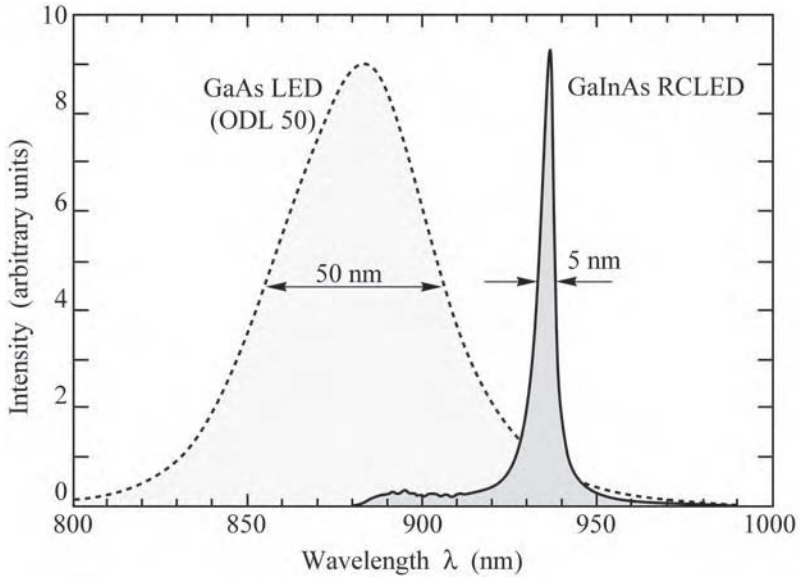


Fig. 15.6. Comparison of the emission spectra of a GaAs LED emitting at 870 nm (AT&T ODL 50 product) and a GaInAs RCLED emitting at 930 nm (after Hunt *et al.*, 1993).

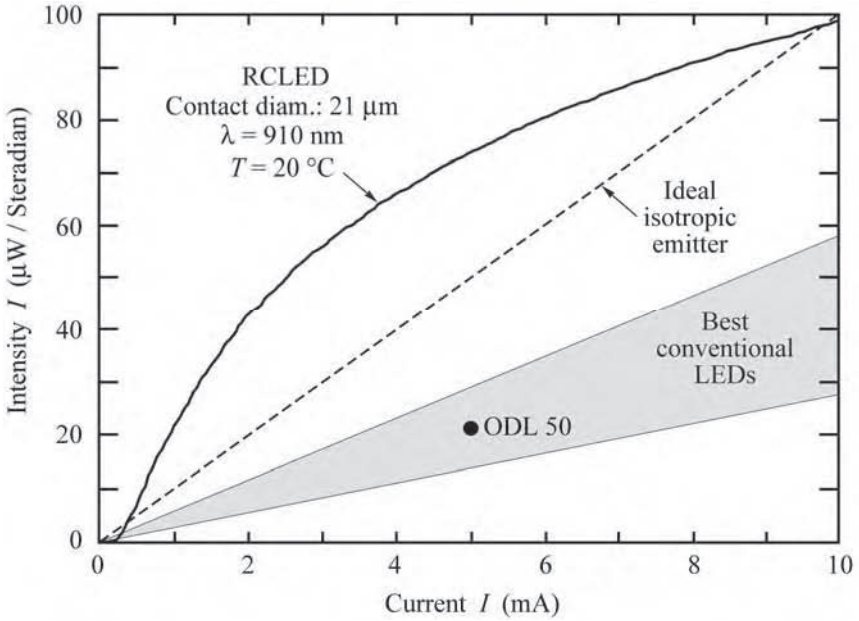


Fig. 15.7. Light-versus-current curves of a GaInAs/GaAs RCLED and of the *ideal isotropic emitter*. The ideal isotropic emitter is a hypothetial device emitting light isotropically with a quantum efficiency of 100%. The shaded region shows the intensity of the best conventional LEDs. The ODL 50 is a commercial LED product (after Schubert *et al.*, 1994).

A regular LED has little or no angle dependence of the emission spectrum. However, the reflective properties of DBRs and of cavities consisting of DBRs are angle-dependent. Consequently, the emission from an RCLED along a certain direction is narrower than that of a regular LED. Integrated over all directions, the RCLED has a broad emission spectrum.

A figure of merit for LEDs used in optical fiber communication systems is the photon flux

density emitted from the diode at a given current, which, for a given wavelength, can be characterized in terms of the unit microwatts per steradian. The optical power coupled into a fiber is directly proportional to the photon flux density.

The intensity of an RCLED as a function of the injection current is shown in Fig. 15.7. For comparison, the calculated intensity of the ***ideal isotropic emitter***, which is a hypothetical device, is also shown. The ideal isotropic emitter is assumed to have an internal quantum efficiency of 100% and the device is assumed to be clad by an anti-reflection coating providing zero reflectivity ($R = 0$) for all wavelengths emitted from the active region. If the photon emission inside the semiconductor is isotropic, then the optical power per unit current per unit solid angle normal to the planar semiconductor surface is given by

$$\frac{P_{\text{optical}}}{\Omega} = \frac{1}{4\pi \bar{n}^2} \frac{hc}{e\lambda} \tag{15.4}$$

where $\Omega$ represents the unit solid angle, $\bar{n}$ is the refractive index of the semiconductor, $c$ is the velocity of light, $e$ is the electronic charge, and $\lambda$ is the emission wavelength in vacuum. Equation (15.4) is represented by the dashed line in Fig. 15.7. Neither the 100% internal quantum efficiency nor the hypothetical anti-reflection coating can be reproduced in practice for fundamental reasons. Therefore, the ideal isotropic emitter represents an upper limit for the intensity attainable with any conventional LED. Of course, even the best conventional LEDs have intensities lower than that of the ideal isotropic emitter. Also included in Fig. 15.7 is the ODL 50 GaAs LED, frequently used for optical fiber communication. All devices shown in Fig. 15.7 have planar light-emitting surfaces, and no lensing is used.

Figure 15.7 reveals that the RCLED provides unprecedented intensities in terms of both absolute values and slope efficiencies. The slope efficiency is 7.3 times the efficiency of the best conventional LEDs and 3.1 times the calculated efficiency of the ideal isotropic emitter. At a current of 5 mA, the intensity of the RCLED is 3.3 times that of the best conventional LEDs including the ODL 50. The high efficiencies make the RCLED well suited for optical interconnect and communication systems.

The higher spectral purity of RCLEDs reduces chromatic dispersion in optical fiber communications (Hunt *et al*., 1993). The chromatic dispersion is directly proportional to the linewidth of the source. Since RCLEDs have linewidths 5–10 times narrower than conventional LEDs, chromatic dispersion effects, which dominate at wavelengths of 800–900 nm, are reduced as well. Hunt *et al*. (1993) showed that the bandwidth of RCLEDs is a factor of 5–10 higher than



Nichia Exhibit 1014
Page 79

that of conventional LEDs. An RCLED-versus-LED comparison in a transmission experiment is shown in Fig. 15.8. The results show the received signal after transmission lengths of 5 m and 3.4 km for the two devices. The fiber used is a graded-index multimode fiber with a core diameter of 62.5 μm. After a transmission length of 5 m, no marked difference is found for the two devices. However, a substantial difference is found after a transmission length of 3.4 km. Inspection of Fig. 15.8 reveals that the RCLED exhibits much less pulse broadening as compared to the conventional LED. This difference is due to reduced material dispersion for the RCLED.

Schubert *et al*. (1996) demonstrated the high-speed modulation capability of RCLEDs. Eye diagram measurements with a random bit pattern generator revealed wide-open eyes at 622 Mbit/s. Due to the small size of the current injected region, the parasitic capacitances of communication RCLEDs are small. It is expected that RCLEDs will be suitable for modulation frequencies exceeding 1 Gbit/s.

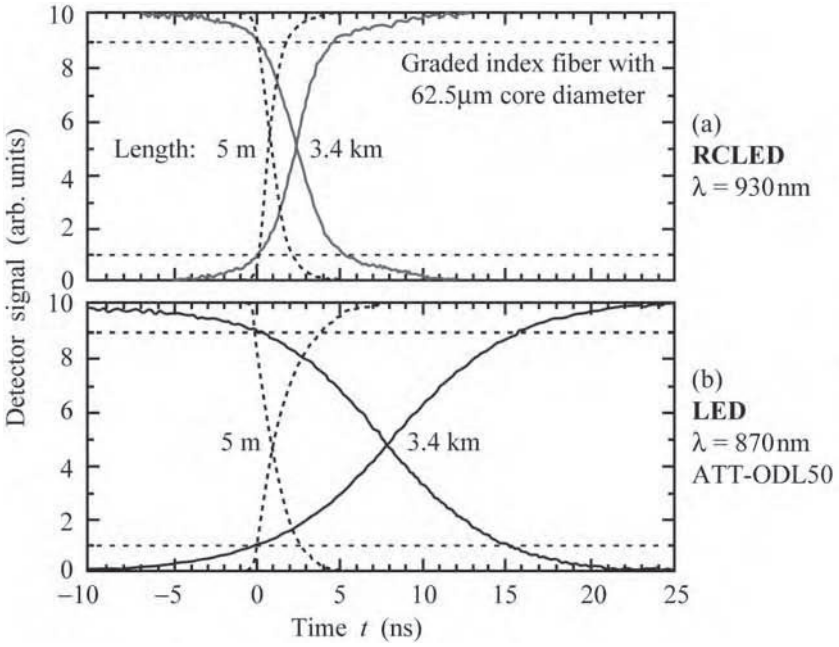


Fig. 15.8. Signal detected at the receiver end of a graded-index multimode fiber with a core diameter of 62.5 μm using (a) a GaInAs RCLED and (b) a GaAs LED source. After a short transmission distance of 5 m, no marked difference is found for the two sources. After a trans-mission distance of 3.4 km, the RCLED exhibits much less pulse broadening than the LED (after Hunt *et al*., 1993).

### *15.4 AlGaInP/GaAs RCLEDs emitting at 650 nm*

RCLEDs have also been demonstrated in the visible wavelength range using the AlGaInP material system (Streubel *et al*., 1998; Whitaker, 1999; Wirth *et al*., 2001, 2002). The AlGaInP material system is commonly used for high-brightness red, orange, and yellow emitters and can be grown lattice matched on GaAs substrates. The active region of RCLEDs is an AlGaInP/GaInP multiple-quantum well structure emitting at 650 nm. The RCLEDs are suited for

use in communication systems using plastic optical fibers. It is difficult to fabricate VCSELs in this wavelength range due to the unavailability of lattice-matched and transparent DBR materials with a large refractive-index contrast.

The basic structure of a top-emitting AlGaInP RCLED emitting at 650 nm is shown in Fig. 15.9. The device consists of an AlGaInP/GaInP MQW active region and AlGaInP cladding layers. The DBRs consist of AlAs/AlGaAs layers. The Al content in the AlGaAs layers of the DBR is chosen to be sufficiently high to make the DBR transparent to the light emitted by the active region. As a result, the index contrast of the AlAs/AlGaAs DBR layers is somewhat low.

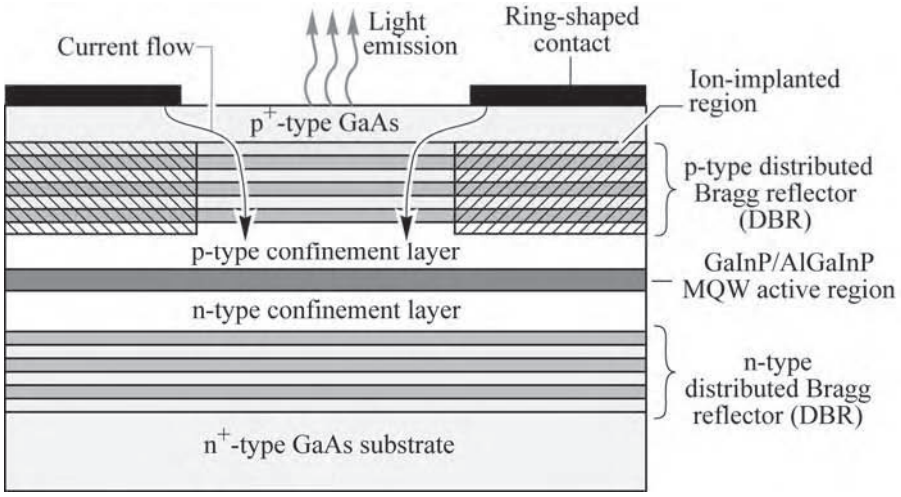


Fig. 15.9. Structure of a GaInP/AlGaInP/GaAs MQW RCLED emitting at 650 nm used for plastic optical fiber applications (after Whitaker, 1999)

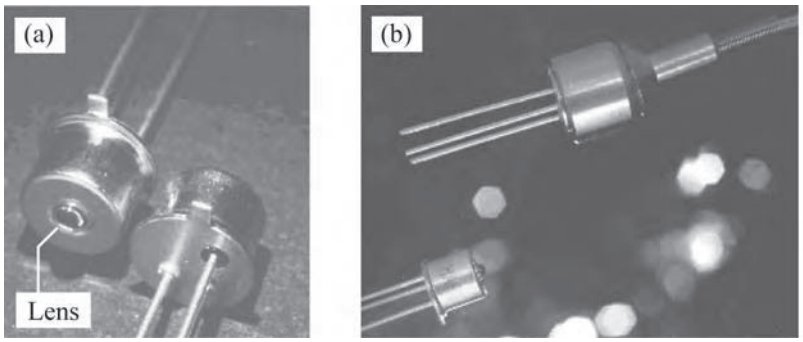


Fig. 15.10. (a) Packaged (TO package) RCLED emitting at 650 nm suited for plastic optical fiber applications. (b) Pig-tailed RCLED (courtesy of Mitel Corporation, Sweden, 1999).

The RCLED has a ring-shaped top contact configuration. The current is funneled into the center region of the ring using ion implantation to create an insulating region under the ring-shaped metalization. Hydrogen and, more frequently, oxygen implantation is used to render the semiconductor highly resistive. Note that the ion-implanted region is located in the p-type region



Nichia Exhibit 1014
Page 81

only and does not extend into the active region, thereby avoiding the creation of defects in the active region where they would act as luminescence killers.

Packaged RCLEDs in a lensed TO package and in a pig-tailed package are shown in Figs. 15.10 (a) and (b) (Mitel Corporation, 1999), respectively. The lens is used for beam collimation, thereby enhancing the coupling efficiency to fibers.

Three RCLEDs under current injection conditions are shown in Fig. 15.11 (Osram Opto Semiconductors Corporation). The picture shows that the emission pattern is directed towards the surface normal of the devices. The emission wavelength is 650 nm.

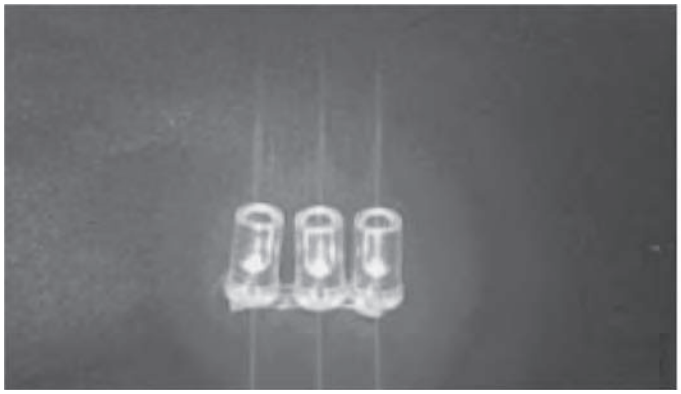

Fig. 15.11. AlGaInP/GaAs RCLEDs emitting at 650 nm. Note the forward-directed emission pattern similar to that of a semiconductor laser (courtesy of Osram Opto Semiconductors Corporation, Germany, 1999).

Optical spectra of a 650 nm RCLED and of a conventional LED injected at different current levels are shown in Fig. 15.12. The spectra are measured after the light is coupled into a plastic optical fiber. Thus, the magnitude of the spectra is a direct measure of the device efficiency *and* of the coupling efficiency. Inspection of the figure reveals several features. Firstly, the RCLED has a higher coupled peak power as well as integrated power than the LED. Secondly, the RCLED has a higher spectral purity than the LED.

Streubel *et al*. (1998) also reported that the emission spectrum was, at room temperature, intentionally blue-shifted with respect to the cavity resonance in order to improve the temperature stability of the RCLED output power. This cavity tuning results in a heart-shaped (double-lobed) emission pattern at room temperature, because the resonance wavelength of the cavity decreases for off-normal emission directions. As the temperature increases, the natural emission spectrum from the active region red-shifts, so that the cavity resonance (along the normal direction) has a better overlap with the natural emission spectrum. As a result, the temperature sensitivity of the RCLED is reduced. The natural emission spectrum red-shifts at a rate of about 0.5 nm/°C, whereas the cavity resonance shifts at only about one-tenth of that rate.

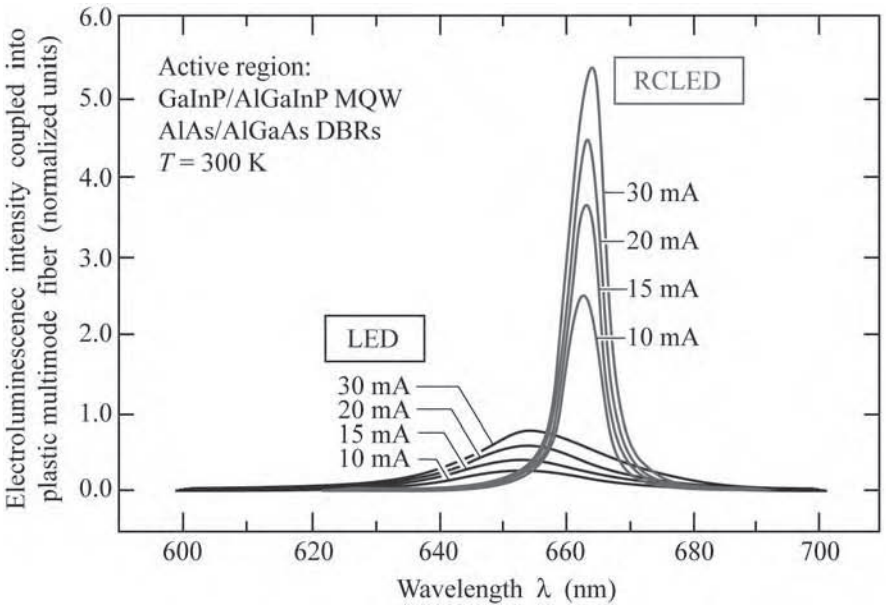


Fig. 15.12. Spectra of light coupled into a plastic optical fiber from a GaInP/AlGaInP MQW RCLED and a conventional GaInP/AlGaInP LED at different drive currents. Note the narrower spectrum and higher coupled power of the RCLED (after Streubel *et al.*, 1998).

### *15.5 Large-area photon recycling LEDs*

Instead of devising ways to *reduce the lateral emission*, one could devise ways to *recycle* lateral emission, thereby redirecting the emission towards the top of the device. By reabsorbing the lateral emission, one can recapture the energy into the active region, giving it another chance to emit along the desired direction. Below, two examples of such devices are discussed.

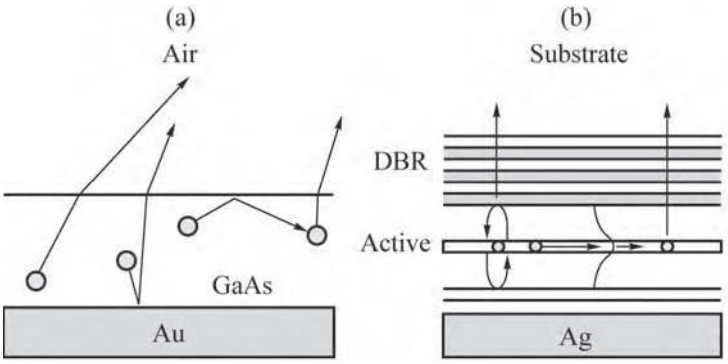


Fig. 15.13. Two approaches to photon recycling LEDs. (a) Bulk epilayer placed on top of gold. Most spontaneous emission that does not escape into air is reabsorbed and has a chance to emit again. (b) Microcavity designed with a waveguiding active region. Waveguided light is reabsorbed after some tens of micrometers, and has a chance to re-emit out of the top of the device.

The first example of such a device is an optically pumped semiconductor structure reported by Schnitzer *et al*. (1993). Consider the structure shown in Fig. 15.13 (a). The backside of a thin semiconductor layer is coated with gold. If one optically pumps the sample at low intensities, the active region remains absorbing. Most of the emission (about 95%) that hits the semiconductor–air interface will totally internally reflect, and stay within the semiconductor. Gold is a good reflector at infrared wavelengths. The semiconductor forming the active region is absorbing at the emission wavelength, so after some average absorption length, $L_{abs}$, the trapped light has a chance to re-emit.



Nichia Exhibit 1014
Page 83

This structure exhibited 72% external efficiency, which required a 99.7% internal quantum efficiency. The fabrication of the structure required the active epilayer to be etched and floated off its substrate. Note that the structure had no electrical contacts. The extraction efficiency of contactless structures is always higher compared with current-injection devices with contacts. An electrical device fabricated in this manner would probably have reliability problems due to the fragile nature of unsupported epitaxial films. A similar but more practical photon-recycling device was made by Blondelle *et al.* (1995).

The concept of photon recycling was used by De Neve *et al*. (1995) in a GaInAs/GaAs/AlGaAs RCLED. A simplified diagram of their structure is shown in Fig. 15.13 (b). If the graded-composition carrier confinement region is thick enough around the quantum wells, it also acts as a graded-index waveguide. De Neve *et al*. calculated that 30% of the light emitted by the active region goes into this waveguide mode. This is reabsorbed after some tens of micrometers, allowing the photons another chance to re-emit out of the top of the structure. In this way, about a 30% increase in external quantum efficiency was attained. The active region of quantum well RCLEDs is not thick enough to support a strongly guided optical mode. One might think that a strong waveguiding mode would take power away from the normal emission, but this does not appear to be the case. The energy tends to be at the expense of other high-angle modes instead, meaning that just modifying the waveguiding mode does little to change the external efficiency. Making use of this high-angle light by achieving photon recycling of the waveguiding emission is an attractive option.

One drawback to photon recycling is that it requires a device with large enough diameter that multiple reabsorption events can occur within the emitting area of the device. This makes such devices less attractive for fiber-optic communications, where small diameters couple better to fibers, especially when coupling lenses are used. Another drawback is that self-absorption necessarily increases the lifetime of the spontaneous emission, thereby slowing down the maximum modulation rate of the devices.

The device reported by De Neve *et al*. (1995) was shown to work with highest efficiency at large diameters. The authors were not targeting this RCLED for fiber communications. At high current densities, the carrier confinement in the quantum wells is reduced, and the efficiency decreases, so larger devices tend to be more efficient. Also, their device was resonant to the long-wavelength side of the natural emission peak, rather than at the peak. This shifts the maximum intensity of the main emission lobe to an off-normal angle, rather than being on axis, but it maximizes the total amount of emission into the main lobe. The Blondelle *et al*. (1995) and De

Neve *et al*. (1995) device is therefore designed for maximization of total emission from the top of the device, rather than for the specific needs of fiber coupling. Display devices and free-space communication devices benefit from this approach. The authors achieved an external quantum efficiency of 16%, compared with the theoretical 2% for an ideal planar emitter of the same index.

### *15.6 Thresholdless lasers*

There have been a number of papers describing a thresholdless laser as a possible communications device (De Martini *et al*., 1987). This would essentially be a light-emitting device that emitted most or all of its light into the fundamental spatial cavity mode. In this way, one can achieve the lasing condition of there being one photon in the cavity almost without gain. Let us denote the probability that light is emitted into the fundamental spatial cavity mode as β. If the β of the LED were almost 1, then the light-versus-current curve of the device would be linear, and *indistinguishable* from a laser with no threshold. A comparison of the light-versus-current for a conventional laser, a high-β laser, and a truly thresholdless laser is given in Fig. 15.14. If one envisions a thresholdless device as fabricated from a resonant-cavity pillar, there are a number of problems besides those of fabrication. Simply having a good sub-threshold intensity, giving only a small kink in the *L–I* curve between sub-threshold and lasing, is not good enough for a thresholdless laser. The output modulation of such a device would be extremely slow below threshold compared to the lasing regime. To enable lasing, there must be some gain, because the β will never be 1. For there to be gain, we must pump the active region past transparency first, since it is absorbing under no-pump conditions. This gain condition requires a certain carrier density, which, in fact, determines the threshold.

One can imagine a device such that all optical modes other than the fundamental are highly suppressed, and the internal quantum efficiency is nearly perfect. In this case, with even a small current, the carrier densities within the device would slowly build until the active region became transparent, and some light could get out through the fundamental optical mode. Such a device would have a very low threshold, but one would have to be careful not to ever drive the device below its threshold even momentarily, because of the long time required to build the necessary space charge inside the device for transparency. Also, if the fundamental emission was suppressed at low carrier densities, it is unlikely that the other modes would be suppressed by an even higher degree, which is what would be required not to lose the injected carriers. In fact, it is the difficulty in suppressing any side emission that makes semiconductor thresholdless lasers difficult if not impractical.



Nichia Exhibit 1014
Page 85

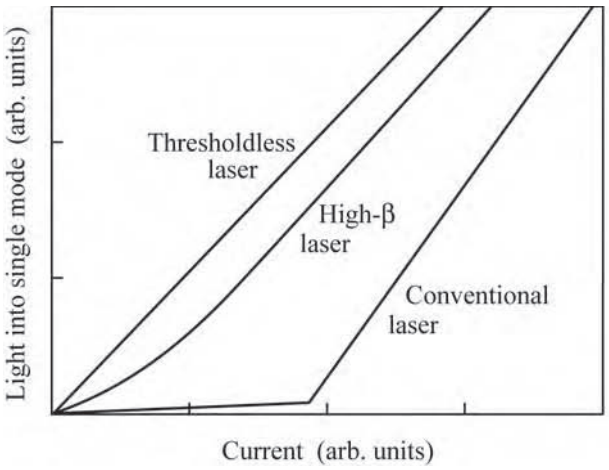


Fig. 15.14. Light-power-versus-current curves for single spatial-mode emission from (*i*) a conventional laser, (*ii*) a high β-factor laser, and (*iii*) a thresholdless laser. The conventional laser has a distinct current threshold. The high β-factor laser has a less distinct threshold. It would be noticeable in the spectrum and device modulation speed, however. A hypothetical thresholdless laser would have a β close to 1, and would somehow suppress all other lossy emission until the carrier density required for gain (or at least transparency) was achieved.

One could, of course, make a laser with a very small threshold by making the laser very small. The problem is that such a device would be capable of only a very small output power. For a hypothetical four-quantum-well single-mode LED, which does not rely on gain, but achieves a β close to 1, the current densities cannot be more than about 50 μA/μm$^2$ or 5 kA/cm$^2$. Using the formulas for β for a dielectric pillar (β > 0.5), and this current density, one can find that less than 2 μW could be emitted into a single mode for an RCLED pillar structure. This is clearly too small for high-speed communications in the 100–650 Mbit/s regime, where 10 μW is considered a minimum for an emitter. An RCLED with a very short carrier lifetime owing to extreme enhancement of the desired emission could have higher pump currents, but no semiconductor design can do this. If the device is a laser, higher powers could be drawn because of the reduced carrier lifetime, but the device sizes are incredibly small for real fabrication, or for any sort of heat dissipation.

In conclusion, semiconductor RCLEDs should remain devices larger than about 5 or 10 μm in diameter, and should remain multimode emitters. Semiconductor vertical-cavity lasers are best fabricated at sizes that make sense technologically, without regard to the β factor of the spontaneous emission. A high-β laser may not be desirable anyway, since the spontaneous emission will introduce excess noise into the emission.

## *15.7 Other RCLED devices*

It is likely that the future of resonant-cavity LEDs and confined-photon emitters will involve new materials and applications from those currently used in communications and display systems. Spontaneously emitting confined-photon devices will always have competition from lasers, conventional LEDs, and other forms of devices. It is only a matter of time, however, before the right

materials combination at the right wavelengths, for the right application, will make commercial devices a reality. It is therefore worthwhile to mention other confined photonic LED material systems.

Wilkinson *et al.* (1995) fabricated an AlGaAs/GaAs thin-film emitter with metal mirrors on a Si substrate, emitting at 880 nm. Pavesi *et al.* (1996) fabricated porous silicon RCLEDs at 750 nm wavelength. Fisher *et al*., (1995) investigated a conjugate polymer RCLED designed for 650 nm. Hadji *et al.* (1995) have realized CdHgTe/HgTe RCLEDs operating at a wavelength of 3.2 μm.

A structure of particular note is a GaAs/$Al_xO_y$ RCLED (Huffaker *et al.*, 1995) operating at 950 nm, where the aluminum oxide in the output mirror was produced from AlAs by oxidation. This composition of output mirror allows the effective cavity length to remain small, maximizing the output enhancement in the RCLED. The back mirror of the structure was Ag. Another particularly interesting device is the broadly tunable RCLED by Larson and Harris (1995). The top mirror is a deformable membrane which can be moved by electrostatic forces. Tunable emission was shown from 938 to 970 nm.

## *15.8 Other novel confined-photon emitters*

A complete discussion of other light-emitting structures that confine photons is beyond the scope of this chapter. It is useful, however, to discuss the properties of some confined-photon emitters. ***Photonic crystal*** or ***photonic bandgap structures*** or involve two- or three-dimensional photon confinement achieved by periodic patterning of the light-emitting active region or the material adjoining the active region. Examples of photonic crystal structures were given by Joannopoulos *et al*. (1995), Baba and Matsuzaki (1996), and Fan *et al*. (1997). Erchak *et al*. (2001) reported very encouraging results on photonic crystal LEDs, namely a six-fold enhancement of light extraction along the surface-normal direction.

Photonic crystal structures can consist of a series of rods or holes arranged in a regular pattern, such as a hexagonal close-packed array. The periodicity of the array can create an optical bandgap for lateral emission at certain emission energies and one or both polarizations. By suppressing the lateral emission, a structure consisting of rods will have a large bandgap for TM emission and a smaller bandgap for TE emission, but not at the same emission energies. However, if the emitting region had a dipole oriented mainly along the rods (such as in quantum well electron-to-light-hole recombination), the lateral emission could be efficiently suppressed. A structure consisting of patterned holes will have a smaller bandgap than that of the rod structure, but it has the advantage that it can have a true optical bandgap for both polarizations of light. Photonic crystal structures


Nichia Exhibit 1014
Page 87

either by themselves, or combined with a planar resonant cavity, enable a strong longitudinal emission enhancement.

Another confined-photon emitter is the ***microdisk laser*** (McCall *et al.*, 1992), which is fabricated as a thin dielectric disk that couples light out the edges of the disk. Lasing modes can be described by a mode number $M$, where $\exp(\mathrm{i}M\phi)$ is the form of the electric field around the cylindrical disk. Because waves can propagate both ways, $M$ can be positive or negative. The disk can be fabricated with a thickness such that the emission perpendicular to the disk is suppressed. Small disks will only support a few modes, and therefore can have a high spontaneous emission factor $\beta$. The $Q$ of these modes are also high enough to achieve lasing. One attractive aspect of such disks is that the lasing emission occurs in the plane of the sample, from a very small device. This could be useful for integration of many photonic devices on a single wafer. However, the output is difficult to efficiently couple into waveguides and fibers, as it only couples evanescently. Advances have been made in improving the longevity, operating temperature range, and active-region passivation of such devices (Mohideen *et al.*, 1993). Room-temperature cw electrical pumping is still a problem, however.

### *References*


Baba T. and Matsuzaki T., "GaInAsP/InP 2-dimensional photonic crystals" in *Microcavities and Photonic Bandgaps* edited by J. Rarity and C. Weisbuch, p. 193 (Kluwer Academic Publishers, Netherlands, 1996)

Blondelle J., De Neve H., Demeester P., Van Daele P., Borghs G., and Baets R. "16% external quantum efficiency from planar microcavity LED's at 940 nm by precise matching of the cavity wavelength" *Electron. Lett.* **31**, 1286 (1995)

De Martini F., Innocenti G., Jacobovitz G. R., and Mataloni P. "Anomalous spontaneous emission time in a microscopic optical cavity" *Phys. Rev. Lett*. **59**, 2955 (1987)

De Neve H., Blondelle J., Baets R., Demeester P., Van Daele P., and Borghs G. "High efficiency planar microcavity LEDs: Comparison of design and experiment" *IEEE Photonics Technol. Lett.* **7**, 287 (1995)

Erchak A. A., Ripin D. J., Fan S., Rakich P., Joannopoulos J. D., Ippen E. P., Petrich G. S., and Kolodziejski L. A. "Enhanced coupling to vertical radiation using a two-dimensional photonic crystal in a semiconductor light-emitting diode" *Appl. Phys. Lett.* **78**, 563 (2001)

Fan S., Villeneuve P. R., Joannopolous J. D., and Schubert E. F. "High extraction efficiency of spontaneous emission from slabs of photonic crystals" *Phys. Rev. Lett*. **78**, 3294 (1997)

Fisher T. A., Lidzey D. G., Pate M. A., Weaver M. S., Whittaker D. M., Skolnick M. S., and Bradley D. D. C. "Electroluminescence from a conjugated polymer microcavity structure" *Appl. Phys. Lett.* **67**, 1355 (1995)

Hadji E., Bleuse J., Magnea N., and Pautrat J. L. "3.2 μm infrared resonant cavity light emitting diode" *Appl. Phys. Lett.* **67**, 2591 (1995)

Huffaker D. L., Lin C. C., Shin J., and Deppe D. G. "Resonant cavity light emitting diode with an $Al_xO_y$/GaAs reflector" *Appl. Phys. Lett.* **66**, 3096 (1995)

Hunt N. E. J., Schubert E. F., Logan R. A., and Zydzik G. J. "Enhanced spectral power density and reduced linewidth at 1.3 μm in an InGaAsP quantum well resonant-cavity light-emitting diode" *Appl. Phys. Lett*. **61**, 2287 (1992)

Hunt N. E. J., Schubert E. F., Kopf R. F., Sivco D. L., Cho A. Y., and Zydzik G. J. "Increased fiber communications bandwidth from a resonant cavity light-emitting diode emitting at λ = 940 nm" *Appl. Phys. Lett*. **63**, 2600 (1993)

Hunt N. E. J., Schubert E. F., Sivco D. L., Cho A. Y., Kopf R. F., Logan R. A., and Zydzik G. J. "High efficiency, narrow spectrum resonant cavity light-emitting diodes" in *Confined Electrons and Photons* edited by E. Burstein and C. Weisbuch (Plenum Press, New York, 1995a)

Hunt N. E. J., Vredenberg A. M., Schubert E. F., Becker P. C., Jacobson D. C., Poate J. M., and Zydzik G. J. "Spontaneous emission control of $Er^{3+}$ in $Si/SiO_2$ microcavities" in *Confined Electrons and Photons* edited by E. Burstein and C. Weisbuch (Plenum Press, New York, 1995b)

Joannopoulos J. D., Meade R. D., and Winn J. N. *Photonic Crystals* (Princeton University Press, Princeton NJ, 1995)

Kobayashi T., Segawa T., Morimoto A., and Sueta T., paper presented at the 43rd fall meeting of the Japanese Society of Applied Physics, Tokyo, Sept. (1982)

Larson M. C. and Harris Jr. J. S. "Broadly tunable resonant-cavity light emission" *Appl. Phys. Lett.* **67**, 590 (1995)

Lear K. L. and Schneider Jr. R. P. "Uniparabolic mirror grading for vertical cavity surface emitting lasers" *Appl. Phys. Lett*. **68**, 605 (1996)

McCall S. L., Levi A. F. J., Slusher R. E., Pearton S. J., and Logan R. A. "Whispering-gallery mode microdisk laser" *Appl. Phys. Lett.* **60**, 289 (1992)

Mitel Corporation, Sweden. Photograph of RCLED is gratefully acknowledged (1999)

Mohideen U., Hobson W. S., Pearton J., Ren F., and Slusher R. E. "GaAs/AlGaAs microdisk lasers" *Appl. Phys. Lett.* **64**, 1911 (1993)

Nakayama T., Itoh Y., and Kakuta A. "Organic photo- and electroluminescent devices with double mirrors" *Appl. Phys. Lett*. **63**, 594 (1993)

Osram Opto Semiconductors Corp., Germany. RCLED photograph is gratefully acknowledged (1999)

Pavesi L., Guardini R., and Mazzoleni C. "Porous silicon resonant cavity light emitting diodes" *Solid State Comm.* **97**, 1051 (1996)

Schnitzer I., Yablonovitch E., Caneau C., and Gmitter T. J. "Ultra-high spontaneous emission quantum efficiency, 99.7% internally and 72% externally, from AlGaAs/GaAs/AlGaAs double heterostructures" *Appl. Phys. Lett.* **62**, 131 (1993)

Schubert E. F., Wang Y.-H., Cho A. Y., Tu L.-W., and Zydzik G. J. "Resonant cavity light-emitting diode" *Appl. Phys. Lett*. **60**, 921 (1992a)

Schubert E. F., Vredenberg A. M., Hunt N. E. J., Wong Y. H., Becker P. C., Poate J. M., Jacobson D. C., Feldman L. C., and Zydzik G. J. "Giant enhancement of luminescence intensity in Er-doped $Si/SiO_2$ resonant cavities" *Appl. Phys. Lett*. **61**, 1381 (1992b)

Schubert E. F., Tu L. W., Zydzik G. J., Kopf R. F., Benvenuti A., and Pinto M. R. "Elimination of heterojunction band discontinuities by modulation doping" *Appl. Phys. Lett*. **60**, 466 (1992c)

Schubert E. F., Hunt N. E. J., Micovic M., Malik R. J., Sivco D. L., Cho A. Y., and Zydzik G. J. "Highly efficient light-emitting diodes with microcavities" *Science* **265**, 943 (1994)

Schubert E. F., Hunt N. E. J., Malik R. J., Micovic M., and Miller D. L. "Temperature and modulation characteristics of resonant cavity light-emitting diodes" *IEEE J. Lightwave Technol.* **14**, 1721 (1996)

Streubel K., Helin U., Oskarsson V., Backlin E., and Johanson A. "High-brightness visible (660 nm) resonant-cavity light-emitting diode" *IEEE Photonics Technol. Lett.* **10**, 1685 (1998)

Tu L. W., Schubert E. F., Zydzik G. J., Kopf R. F., Hong M., Chu S. N. G., and Mannaerts J. P. "Vertical cavity surface emitting lasers with semitransparent metallic mirrors and high quantum efficiencies" *Appl. Phys. Lett*. **57**, 2045 (1990)

Whitaker T. "Resonant cavity LEDs" *Compound Semiconductors* **5**, 32 (1999)

Wilkinson S. T., Jokerst N. M., and Leavitt R. P. "Resonant-cavity-enhanced thin-film AlGaAs/GaAs/AlGaAs LED's with metal mirrors" *Appl. Opt.* **34**, 8298 (1995)

Wirth R., Karnutsch C., Kugler S., and Streubel K. "High-efficiency resonant-cavity LEDs emitting at 650 nm" *IEEE Photonics Technol. Lett*. **13**, 421 (2001)

Wirth R., Huber W., Karnutsch C., and Streubel K. "Resonators provide LEDs with laser-like performance" *Compound Semiconductors* **8**, 49 (2002)

Yokoyama H. "Physics and device applications of optical microcavities" *Science* **256**, 66 (1992)



Nichia Exhibit 1014
Page 89

# 16

## Human eye sensitivity and photometric quantities

The recipient of the light emitted by most visible-spectrum LEDs is the human eye. In this chapter, the characteristics of human vision and of the human eye and are summarized, in particular as these characteristics relate to human eye sensitivity and photometric quantities.

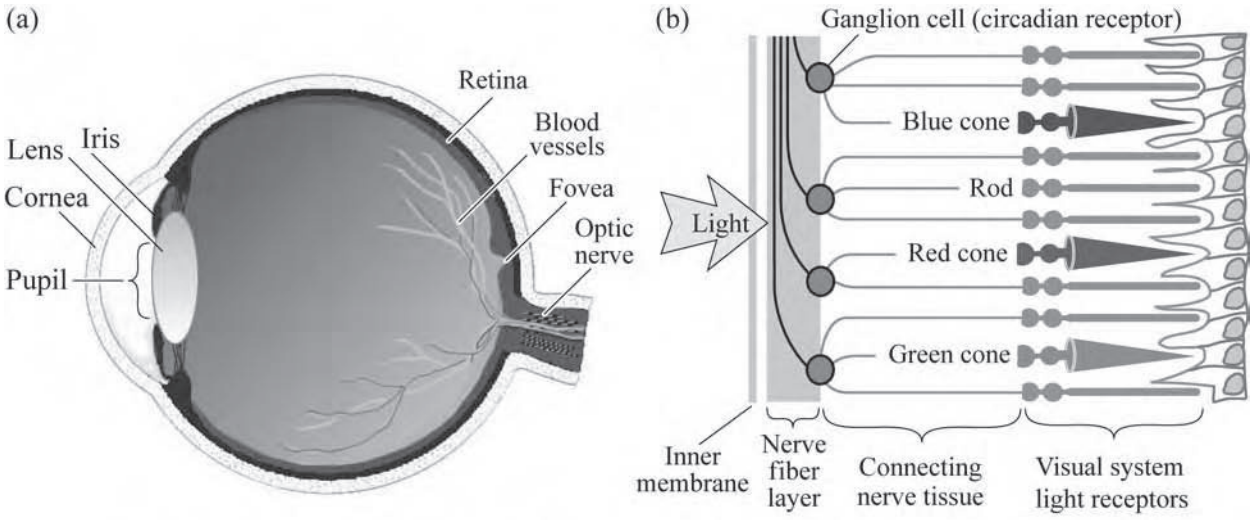


Fig. 16.1. (a) Cross section through a human eye. (b) Schematic view of the retina including rod and cone light receptors (adapted from Encyclopedia Britannica, 1994).

### *16.1 Light receptors of the human eye*

Figure 16.1 (a) shows a schematic illustration of the human eye (Encyclopedia Britannica, 1994). The inside of the eyeball is clad by the retina, which is the light-sensitive part of the eye. The illustration also shows the fovea, a cone-rich central region of the retina which affords the high acuteness of central vision. Figure 16.1 (b) shows the cell structure of the retina including the light-sensitive ***rod cells*** and ***cone cells***. Also shown are the ganglion cells and nerve fibers that transmit the visual information to the brain. Rod cells are more abundant and more light sensitive than cone cells. Rods are sensitive over the entire visible spectrum. There are three types of cone

cells, namely cone cells sensitive in the red, green, and blue spectral range. The cone cells are therefore denoted as the red-sensitive, green-sensitive, and blue-sensitive cones, or simply as the red, green, and blue cones.

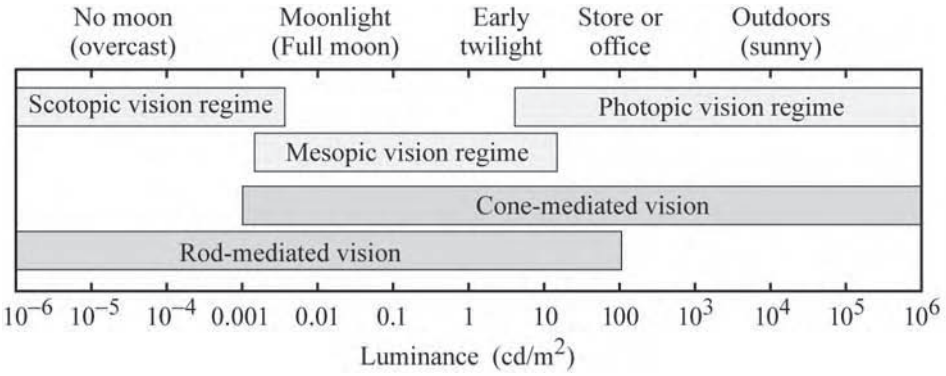


Fig. 16.2. Approximate ranges of vision regimes and receptor regimes (after Osram Sylvania, 2000).

Three different vision regimes are shown in Fig. 16.2 along with the receptors relevant to each of the regimes (Osram Sylvania, 2000). ***Photopic vision*** relates to human vision at high ambient light levels (e.g. during daylight conditions) when vision is mediated by the cones. The photopic vision regime applies to luminance levels > 3 cd/m$^2$. ***Scotopic vision*** relates to human vision at low ambient light levels (e.g. at night) when vision is mediated by rods. Rods have a much higher sensitivity than the cones. However, the sense of color is essentially lost in the scotopic vision regime. At low light levels such as in a moonless night, objects lose their colors and only appear to have different gray levels. The scotopic vision regime applies to luminance levels < 0.003 cd/m$^2$. ***Mesopic vision*** relates to light levels between the photopic and scotopic vision regime (0.003 cd/m$^2$ < mesopic luminance < 3 cd/m$^2$).

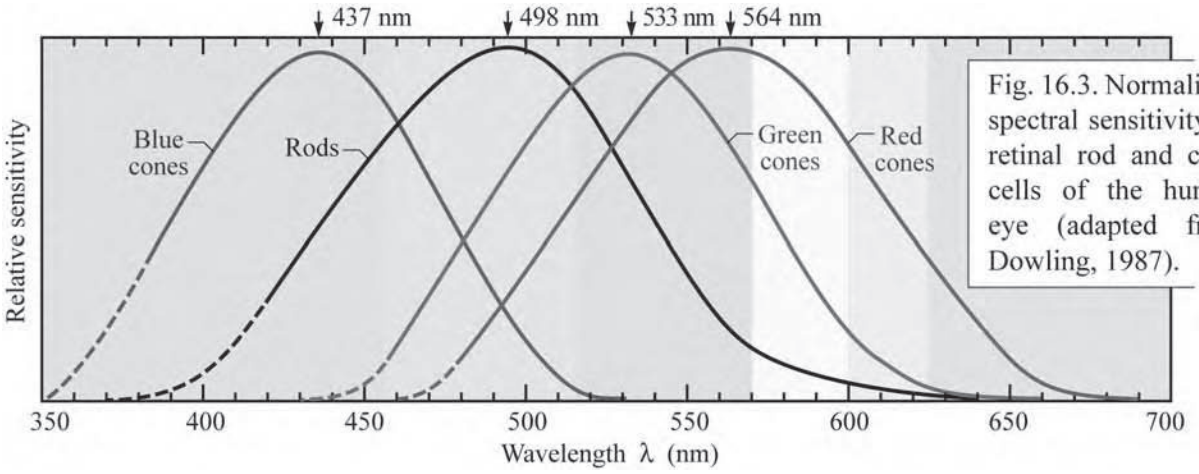


Fig. 16.3. Normalized spectral sensitivity of retinal rod and cone cells of the human eye (adapted from Dowling, 1987).



Nichia Exhibit 1014
Page 91

The approximate spectral sensitivity functions of the rods and three types or cones are shown in Fig. 16.3 (Dowling, 1987). Inspection of the figure reveals that night-time vision (scotopic vision) is weaker in the red spectral range and thus stronger in the blue spectral range as compared to day-time vision (photopic vision). The following discussion mostly relates to the photopic vision regime.

## *16.2 Basic radiometric and photometric units*

The physical properties of electromagnetic radiation are characterized by ***radiometric units***. Using radiometric units, we can characterize light in terms of physical quantities; for example, the number of photons, photon energy, and ***optical power*** (in the lighting community frequently called the ***radiant flux***). However, the radiometric units are irrelevant when it comes to light perception by a human being. For example, infrared radiation causes no luminous sensation in the eye. To characterize the light and color sensation by the human eye, different types of units are needed. These units are called ***photometric units***.

The ***luminous intensity***, which is a photometric quantity, represents the light intensity of an optical source, as perceived by the human eye. The luminous intensity is measured in units of ***candela*** (cd), which is a base unit of the International System of Units (SI unit). The present definition of luminous intensity is as follows: *a monochromatic light source emitting an optical power of (1/683) watt at 555 nm into the solid angle of 1 steradian (sr) has a luminous intensity of 1 candela (cd)*.

The unit *candela* has great historical significance. All light intensity measurements can be traced back to the candela. It evolved from an older unit, the ***candlepower***, or simply, the ***candle***. The original, now obsolete, definition of one candela was the light intensity emitted by a plumber's candle, as shown in Fig. 16.4, which had a specified construction and dimensions:

| one standardized candle emits a luminous intensity of 1.0 cd |
|---|

.

Fig. 16.4. Plumber's candle, as used by plumbers in the nineteenth century to melt lead solder when joining water pipes.

The luminous intensity of a light source can thus be characterized by giving the number of standardized candles that, when combined, would emit the same luminous intensity. Note that *candlepower* and *candle* are non-SI units that are no longer current and rarely used at the present time.

The ***luminous flux***, which is also a photometric quantity, represents the light power of a source as perceived by the human eye. The unit of luminous flux is the ***lumen*** (lm). It is defined as follows: *a monochromatic light source emitting an optical power of (1/683) watt at 555 nm has a luminous flux of 1 lumen (lm)*. The lumen is an SI unit.

A comparison of the definitions for the candela and lumen reveals that 1 candela equals 1 lumen per steradian or cd = lm/sr. Thus, an isotropically emitting light source with luminous intensity of 1 cd has a luminous flux of $4\pi$ lm = 12.57 lm.

The ***illuminance*** is the luminous flux incident per unit area. The illuminance measured in ***lux*** (lux = lm/m$^2$). It is an SI unit used when characterizing illumination conditions. Table 16.1 gives typical values of the illuminance in different environments.

Table 16.1. Typical illuminance in different environments.

| **Illumination condition** | **Illuminance** |
|---|---|
| Full moon | 1 lux |
| Street lighting | 10 lux |
| Home lighting | 30 to 300 lux |
| Office desk lighting | 100 to 1 000 lux |
| Surgery lighting | 10 000 lux |
| Direct sunlight | 100 000 lux |

The ***luminance*** of a ***surface source*** (i.e. a source with a non-zero light-emitting surface area such as a display or an LED) is the ratio of the luminous intensity emitted in a certain direction (measured in cd) divided by the *projected surface area* in that direction (measured in m$^2$). The luminance is measured in units of cd/m$^2$. In most cases, the direction of interest is normal to the chip surface. In this case, the luminance is the luminous intensity emitted along the chip-normal direction divided by the chip area.

The *projected surface area* mentioned above follows a cosine law, i.e. the projected area is given by $A_{\text{projected}} = A_{\text{surface}} \cos\Theta$ , where $\Theta$ is the angle between the direction considered and the surface normal. The light-emitting surface area and the projected area are shown in Fig. 16.5. The luminous intensity of LEDs with lambertian emission pattern also depends on the angle $\Theta$



Nichia Exhibit 1014
Page 93

according to a cosine law. Thus the luminance of lambertian LEDs is a constant, independent of angle.

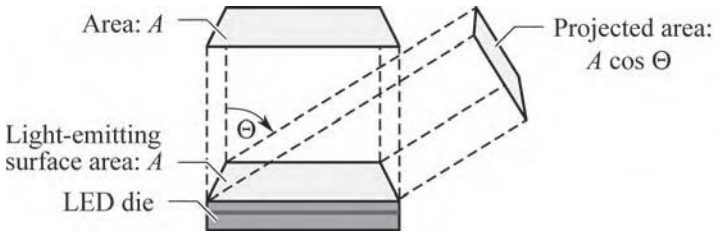


Fig. 16.5. Area of LED, $A$, and projected area, $A \cos \Theta$, used for the definition of the luminance of an LED.

For LEDs, it is desirable to maximize luminous intensity and luminous flux while keeping the LED chip area minimal. Thus the luminance is a measure of how efficiently the valuable semiconductor wafer area is used to attain, at a given injection current, a certain luminous intensity.

There are several units that are used to characterize the luminance of a source. The names of these common units are given in Table 16.2.

Typical luminances of displays, organic LEDs, and inorganic LEDs are given in Table 16.3. The table reveals that displays require a comparatively low luminance because the observer directly views the display from a close distance. This is not the case for high-power inorganic LEDs used for example in traffic light and illumination applications.

Photometric and the corresponding radiometric units are summarized in Table 16.4.

Table 16.2. Conversion between common SI and non-SI units for luminance.

| **Unit** | **Common name** |
|---|---|
| 1 cd/cm$^2$ | 1 stilb |
| (1/π) cd/cm$^2$ | 1 lambert |
| 1 cd/m$^2$ | 1 nit |

| **Unit** | **Common name** |
|---|---|
| (1/π) cd/m$^2$ | 1 apostilb |
| (1/π) cd/ft$^2$ | 1 foot-lambert |

Table 16.3. Typical values for the luminance of displays, LEDs fabricated from organic materials, and inorganic LEDs.

| **Device** | **Luminance** (cd/m$^2$) |
|---|---|
| Display | 100 (operation) |
| Display | 250–750 (max. value) |

| **Device** | **Luminance** (cd/m$^2$) |
|---|---|
| Organic LED | 100–10 000 |
| III–V LED | 1 000 000–10 000 000 |

Table 16.4. Photometric and corresponding radiometric units.

| Photometric unit | Dimension | Radiometric unit | Dimension |
|---|---|---|---|
| Luminous flux | lm | Radiant flux (optical power) | W |
| Luminous intensity | lm / sr = cd | Radiant intensity | W / sr |
| Illuminance | lm / $m^2$ = lux | Irradiance (power density) | W / $m^2$ |
| Luminance | lm / (sr $m^2$) = cd / $m^2$ | Radiance | W / (sr $m^2$) |

**Exercise**: ***Photometric units***. A 60 W incandescent light bulb has a luminous flux of 1000 lm. Assume that light is emitted isotropically from the bulb.

(a) What is the luminous efficiency (i.e. the number of lumens emitted per watt of electrical input power) of the light bulb?
(b) What number of standardized candles emit the same luminous intensity?
(c) What is the illuminance, $E_{lum}$, in units of lux, on a desk located 1.5 m below the bulb?
(d) Is the illuminance level obtained under (c) sufficiently high for reading?
(e) What is the luminous intensity, $I_{lum}$, in units of candela, of the light bulb?
(f) Derive the relationship between the illuminance at a distance $r$ from the light bulb, measured in *lux*, and the luminous intensity, measured in *candela*.
(g) Derive the relationship between the illuminance at a distance $r$ from the light bulb, measured in *lux*, and the luminous flux, measured in *lumen*.
(h) The definition of the cd involves the optical power of (1/683) W. What, do you suppose, is the origin of this particular power level?

Solution: (a) 16.7 lm/W. (b) 80 candles. (c) $E_{lum}$ = 35.4 lm/$m^2$ = 35.4 lux. (d) Yes.
(e) 79.6 lm/sr = 79.6 cd. (f) $E_{lum}\, r^2 = I_{lum}$. (g) $E_{lum}\, 4\pi r^2 = \Phi_{lum}$.
(h) Originally, the unit of luminous intensity had been defined as the intensity emitted by a real candle. Subsequently the unit was defined as the intensity of a light source with specified wavelength and optical power. When the power of that light source is (1/683) W, it has the same intensity as the candle. Thus this particular power level has a historical origin and results from the effort to maintain continuity.

### *16.3 Eye sensitivity function*

The conversion between radiometric and photometric units is provided by the ***luminous efficiency function*** or ***eye sensitivity function***, $V(\lambda)$. In 1924, the CIE introduced the photopic eye sensitivity function $V(\lambda)$ for point-like light sources where the viewer angle is 2° (CIE, 1931). This function is referred to as the ***CIE 1931 V(λ) function***. It is the current photometric standard in the United States.

A *modified* $V(\lambda)$ function was introduced by Judd and Vos in 1978 (Vos, 1978; Wyszecki and Stiles, 1982, 2000) and this modified function is here referred to as the ***CIE 1978 V(λ) function***. The modification was motivated by the underestimation of the human eye sensitivity in the blue and violet spectral region by the CIE 1931 $V(\lambda)$ function. The modified function $V(\lambda)$ has higher values in the spectral region below 460 nm. The CIE has endorsed the CIE 1978 $V(\lambda)$


Nichia Exhibit 1014
Page 95

function by stating "the spectral luminous efficiency function for a point source may be adequately represented by the Judd modified $V(\lambda)$ function" (CIE, 1988) and "the Judd modified $V(\lambda)$ function would be the preferred function in those conditions where luminance measurements of short wavelengths consistent with color normal observers is desired" (CIE, 1990).

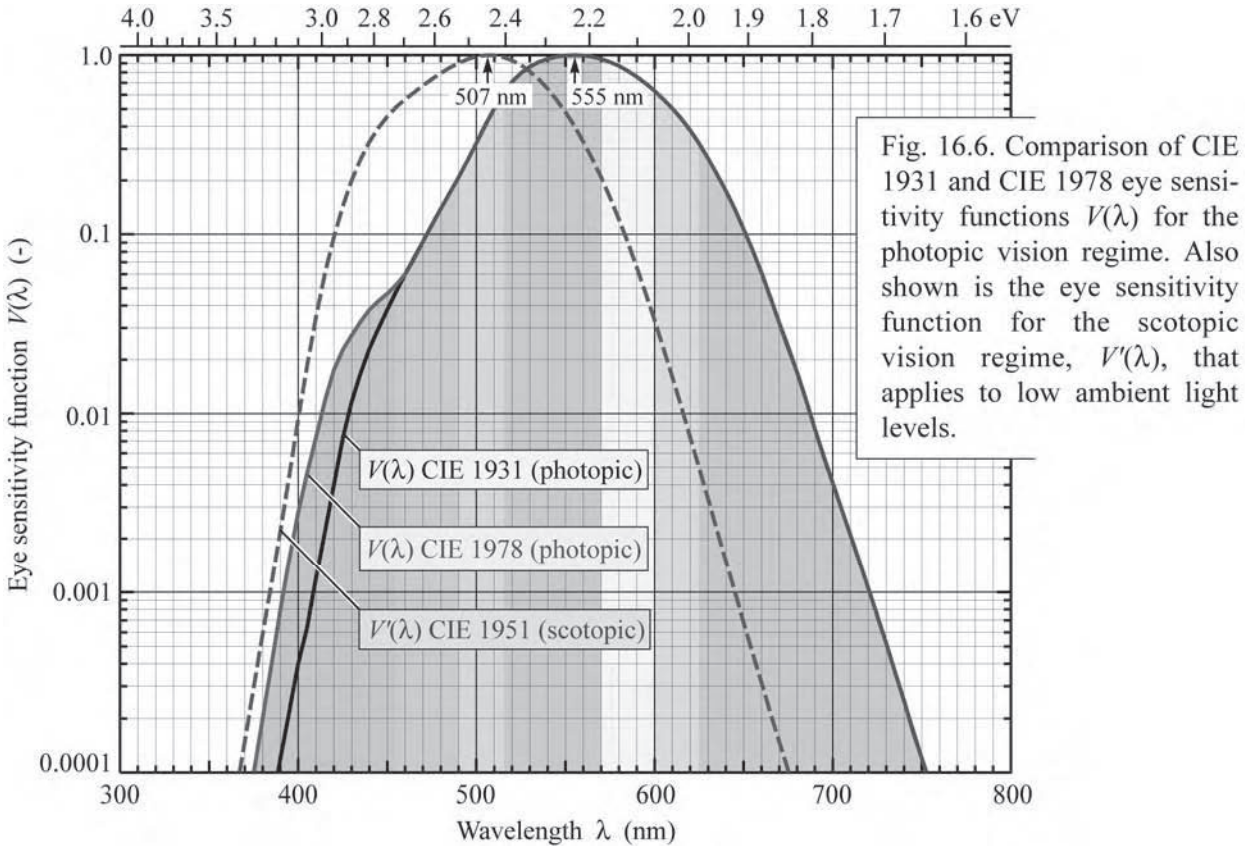


Fig. 16.6. Comparison of CIE 1931 and CIE 1978 eye sensitivity functions $V(\lambda)$ for the photopic vision regime. Also shown is the eye sensitivity function for the scotopic vision regime, $V'(\lambda)$, that applies to low ambient light levels.

The CIE 1931 $V(\lambda)$ function and the CIE 1978 $V(\lambda)$ function are shown in Fig. 16.6. The photopic eye sensitivity function has maximum sensitivity in the green spectral range at 555 nm, where $V(\lambda)$ has a value of unity, i.e. $V(555\text{ nm}) = 1$. Inspection of the figure also reveals that the CIE 1931 $V(\lambda)$ function underestimated the eye sensitivity in the blue spectral range ($\lambda < 460$ nm). Numerical values of the CIE 1931 and CIE 1978 $V(\lambda)$ function are tabulated in Appendix 16.1.

Also shown in Fig. 16.6 is the scotopic eye sensitivity function $V'(\lambda)$. The peak sensitivity in the scotopic vision regime occurs at 507 nm. This value is markedly shorter than the peak sensitivity in the photopic vision regime. Numerical values of the CIE 1951 $V'(\lambda)$ function are tabulated in Appendix 16.2.

Note that even though the CIE 1978 $V(\lambda)$ function is preferable, it is not the standard, mostly for practical reasons such as possible ambiguities created by changing standards. Wyszecki and Stiles (2000) note that even though the CIE 1978 $V(\lambda)$ function is not a standard, it has been used in several visual studies. The CIE 1978 $V(\lambda)$ function, which can be considered the most accurate description of the eye sensitivity in the photopic vision regime, is shown in Fig. 16.7.

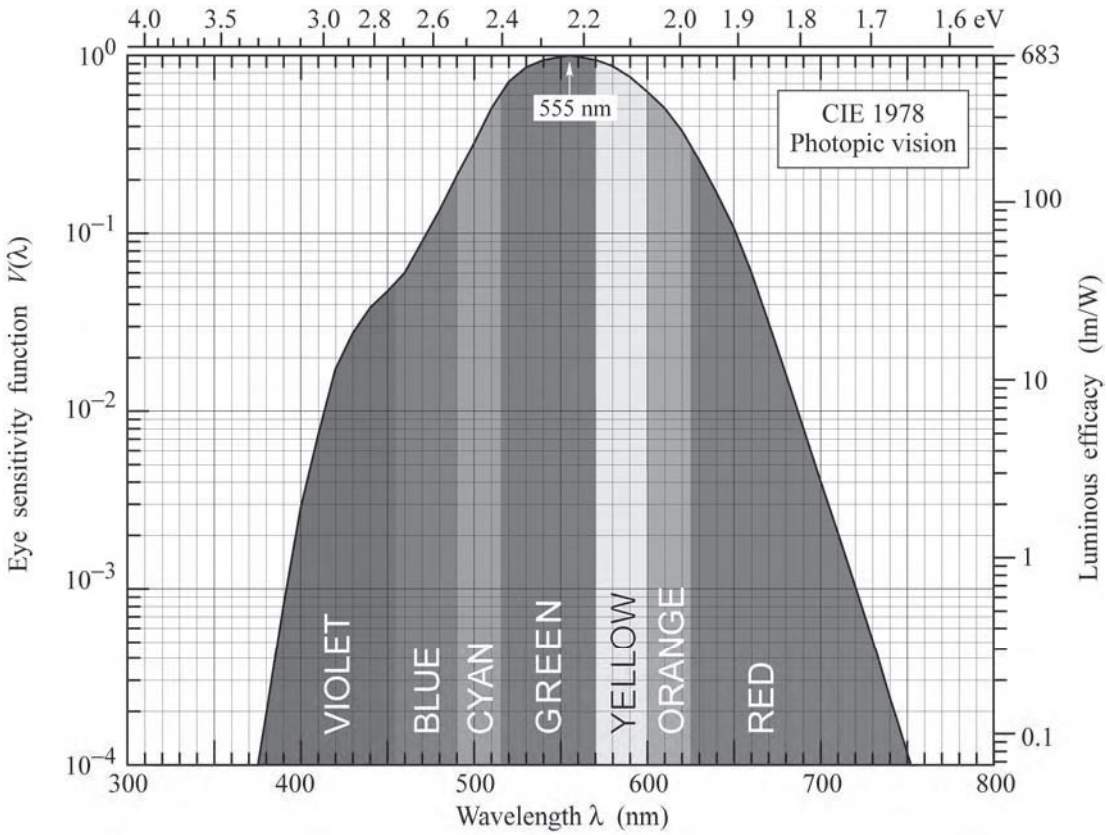


Fig. 16.7. Eye sensitivity function, $V(\lambda)$, (left-hand ordinate) and luminous efficacy, measured in lumens per watt of optical power (right-hand ordinate). $V(\lambda)$ is maximum at 555 nm (after 1978 CIE data).

The eye sensitivity function has been determined by the ***minimum flicker method***, which is the classic method for luminance comparison and for the determination of $V(\lambda)$. The stimulus is a light-emitting small circular area, alternatingly illuminated (with a frequency of 15 Hz) with the standard color and the comparison color. Since the hue-fusion frequency is lower than 15 Hz, the hues fuse. However, the brightness-fusion frequency is higher than 15 Hz and thus if the two colors differ in brightness, then there will be visible flicker. The human subject's task is to adjust the target color until the flicker is minimal.

Any desired chromaticity can be obtained with an infinite variety of spectral power



Nichia Exhibit 1014
Page 97

distributions $P(\lambda)$. One of these distributions has the greatest possible luminous efficacy. This limit can be obtained in only one way, namely by the mixture of suitable intensities emitted by two monochromatic sources (MacAdam, 1950). The maximum attainable luminous efficacy obtained with a single monochromatic pair of emitters is shown in Fig. 16.8. The maximum luminous efficacy of *white* light depends on the color temperature; it is about 420 lm/W for a color temperature of 6500 K and can exceed 500 lm/W for lower color temperatures. The exact value depends on the exact location within the white area of the chromaticity diagram.

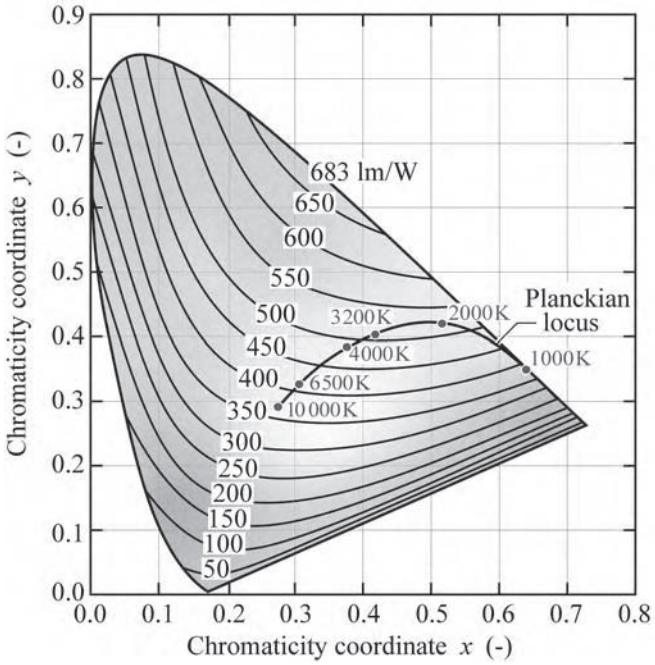


Fig. 16.8. Relation of maximum possible luminous efficacy (lumens per optical watt) and chromaticity in the CIE 1931 *x*, *y* chromaticity diagram (adapted from MacAdam, 1950).

### *16.4 Colors of near-monochromatic emitters*

For wavelengths ranging from 390 to 720 nm, the eye sensitivity function $V(\lambda)$ is greater than $10^{-3}$. Although the human eye is sensitive to light with wavelengths < 390 nm and > 720 nm, the sensitivity at these wavelengths is extremely low. Therefore, the wavelength range $390\ \text{nm} \le \lambda \le 720\ \text{nm}$ can be considered the *visible wavelength range*. The relationship between color and wavelength within the visible wavelength range is given in Table 16.5. This relationship is valid for monochromatic or near-monochromatic light sources such as LEDs. Note that color is, to some extent, a subjective quantity. Also note that the transition between different colors is continuous.

Table 16.5. Colors and associated typical LED peak wavelength ranges

| Color | Wavelength |
|---|---|
| Ultraviolet | < 390 nm |
| Violet | 390–455 nm |
| Blue | 455–490 nm |
| Cyan | 490–515 nm |
| Green | 515–570 nm |

| Color | Wavelength |
|---|---|
| Yellow | 570–600 nm |
| Amber | 590–600 nm |
| Orange | 600–625 nm |
| Red | 625–720 nm |
| Infrared | > 720 nm |

.

### *16.5 Luminous efficacy and luminous efficiency*

The ***luminous flux***, $\Phi_{\text{lum}}$, is obtained from the radiometric light power using the equation

$$\Phi_{\text{lum}} = 683 \frac{\text{lm}}{\text{W}} \int_{\lambda} V(\lambda)\, P(\lambda)\, \mathrm{d}\lambda \tag{16.1}$$

where $P(\lambda)$ is the power spectral density, i.e. the light power emitted per unit wavelength, and the prefactor 683 lm/W is a normalization factor. The optical power emitted by a light source is then given by

$$P = \int_{\lambda} P(\lambda)\, \mathrm{d}\lambda \ . \tag{16.2}$$

High-performance single-chip visible-spectrum LEDs can have a luminous flux of about 10–100 lm at an injection current of 100–1 000 mA.

The ***luminous efficacy of optical radiation*** (also called the ***luminosity function***), measured in units of lumens per watt of optical power, is the conversion efficiency from optical power to luminous flux. The luminous efficacy is defined as

$$\text{Luminous efficacy} = \frac{\Phi_{\text{lum}}}{P} = \left[ 683 \frac{\text{lm}}{\text{W}} \int_{\lambda} V(\lambda)\, P(\lambda)\, \mathrm{d}\lambda \right] \Big/ \left[ \int_{\lambda} P(\lambda)\, \mathrm{d}\lambda \right] \ . \tag{16.3}$$

For strictly monochromatic light sources ($\Delta\lambda \to 0$), the luminous efficacy is equal to the eye sensitivity function $V(\lambda)$ multiplied by 683 lm/W. However, for multicolor light sources and especially for white light sources, the luminous efficacy needs to be calculated by integration over all wavelengths. The luminous efficacy is shown on the right-hand ordinate of Fig. 16.4.

The ***luminous efficiency of a light source***, also measured in units of lm/W, is the luminous



Nichia Exhibit 1014
Page 99

flux of the light source divided by the electrical input power.

$$\text{Luminous efficiency} = \Phi_{\text{lum}} / (I\,V) \tag{16.4}$$

where the product $(I\,V)$ is the electrical input power of the device. Note that in the lighting community, luminous efficiency is often referred to as *luminous efficacy of the source*.

Inspection of Eqs. (16.3) and (16.4) reveals that the luminous efficiency is the product of the luminous efficacy and the electrical-to-optical power conversion efficiency. The luminous efficiency of common light sources is given in Table 16.6.

Table 16.6. Luminous efficiencies of different light sources. (a) Incandescent sources. (b) Fluorescent sources. (c) High-intensity discharge (HID) sources.

| Light source | | Luminous efficiency |
|---|---|---|
| Edison's first light bulb (with C filament) | (a) | 1.4 lm/W |
| Tungsten filament light bulbs | (a) | 15–20 lm/W |
| Quartz halogen light bulbs | (a) | 20–25 lm/W |
| Fluorescent light tubes and compact bulbs | (b) | 50–80 lm/W |
| Mercury vapor light bulbs | (c) | 50–60 lm/W |
| Metal halide light bulbs | (c) | 80–125 lm/W |
| High-pressure sodium vapor light bulbs | (c) | 100–140 lm/W |

The luminous efficiency is a highly relevant figure of merit for visible-spectrum LEDs. It is a measure of the perceived light power normalized to the electrical power expended to operate the LED. For light sources with a perfect electrical-power-to-optical-power conversion, the luminous source efficiency is equal to the luminous efficacy of radiation.

---

**Exercise**: ***Luminous efficacy and luminous efficiency of LEDs***. Consider a red and an amber LED emitting at 625 and 590 nm, respectively. For simplicity, assume that the emission spectra are monochromatic ($\Delta\lambda \to 0$). What is the luminous efficacy of the two light sources? Calculate the luminous efficiency of the LEDs, assuming that the red and amber LEDs have an external quantum efficiency of 50%. Assume that the LED voltage is given by $V = E_g / e = h\nu / e$.

Assume next that the LED spectra are thermally broadened and have a gaussian lineshape with a linewidth of $1.8\,kT$. Again calculate the luminous efficacy and luminous efficiency of the two light sources. How accurate are the results obtained with the approximation of monochromaticity?

---

Some LED structures attain excellent power efficiency by using small light-emitting areas (current injection in a small area of chip) and advanced light-output-coupling structures (see, for example, Schmid *et al*., 2002). However, such devices have low luminance because only a small

fraction of the chip area is injected with current. Table 16.7 summarizes frequently used figures of merit for light-emitting diodes.

Table 16.7. Summary of photometric, radiometric, and quantum performance measures for LEDs.

| Figure of merit | Explanation | Unit |
|---|---|---|
| Luminous efficacy | Luminous flux per optical unit power | lm/W |
| Luminous efficiency | Luminous flux per input electrical unit power | lm/W |
| Luminous intensity efficiency | Luminous flux per sr per input electrical unit power | cd/W |
| Luminance | Luminous flux per sr per chip unit area | $cd/m^2$ |
| Power efficiency | Optical output power per input electrical unit power | % |
| Internal quantum efficiency | Photons emitted in active region per electron injected | % |
| External quantum efficiency | Photons emitted from LED per electron injected | % |
| Extraction efficiency | Escape probability of photons emitted in active region | % |

### *16.6 Brightness and linearity of human vision*

Although the term ***brightness*** is frequently used, it lacks a standardized scientific definition. The frequent usage is due to the fact that the general public can more easily relate to the term *brightness* than to photometric terms such as *luminance* or *luminous intensity*. Brightness is an attribute of visual perception and is frequently used as synonym for *luminance* and (incorrectly) for the radiometric term *radiance*.

To quantify the brightness of a source, it is useful to differentiate between point and surface area sources. For *point sources*, brightness (in the photopic vision regime) can be approximated by the luminous intensity (measured in cd). For *surface sources*, brightness (in the photopic vision regime) can be approximated by the luminance (measured in $cd/m^2$). However, due to the lack of a formal standardized definition of the term brightness, it is frequently avoided in technical publications.

Standard CIE photometry assumes human vision to be ***linear*** within the photopic regime. It is clear that an isotropically emitting blue point source and an isotropically emitting red point source each having a luminous flux of, e.g., 5 lm, have the same luminous intensity. Assuming *linearity* of photopic vision, both sources still have the same luminous intensity as the luminous fluxes of the sources are increased from 5 to, e.g., 5000 lm.

However, if the luminous fluxes of the two sources are reduced so that the mesopic or scotopic vision regime is entered, the blue source will appear brighter than the red source due to



Nichia Exhibit 1014
Page 101

the shift of the eye sensitivity function to shorter wavelengths in the scotopic regime.

It is important to keep in mind that the linearity of human vision within the photopic regime is an *approximation*. Linearity clearly simplifies photometry. However, human subjects may feel discrepancies between the experience of brightness and measured luminance of a light source, especially for colored light sources if the luminous flux is changed over orders of magnitude.

## *16.7 Circadian rhythm and circadian sensitivity*

The human wake-sleep rhythm has a period of approximately 24 hours and the rhythm therefore is referred to as the ***circadian rhythm*** or ***circadian cycle***, with the name being derived from the Latin words *circa* and *dies* (and its declination *diem*), meaning *approximately* and *day*, respectively. Light has been known for a long time to be the synchronizing clock (*zeitgeber*) of the human circadian rhythm. For reviews on the development of the understanding of the circadian rhythm including the identification of light as the dominant trigger for the endogenous *zeitgeber*, see Pittendrigh (1993) and Sehgal (2004).

The wake-sleep rhythm of humans is synchronized by the intensity and spectral composition of light. Sunlight is the natural *zeitgeber*. During mid-day hours sunlight has high intensity, a high color temperature, and a high content of blue light. During evening hours, intensity, color temperature, and blue content of sunlight strongly decrease. Humans have adapted to this variation and the circadian rhythm is most likely synchronized by the following three factors: intensity, color temperature, and blue content.

Exposure to inappropriately high intensities of light in the late afternoon or evening can upset the regular wake-seep rhythm and lead to sleeplessness and even serious illnesses such as cancer (Brainard *et al*., 2001; Blask *et al*, 2003). It is therefore highly advisable to limit exposure to high intensity light in the late afternoon and evening hours, to not be counterproductive to the natural circadian rhythm (Schubert, 1997).

It was believed for a long time that rod cells and the three types of cone cells are the only optically sensitive cells in the human eye. However, Brainard *et al*. (2001) postulated that an unknown photoreceptor in the human eye would control the circadian rhythm. Evidence presented by Berson *et al*. (2002) and Hattar *et al*., (2002) indicates that retinal ganglion cells have an optical sensitivity as well. For a schematic illustration of ganglion cells, see Fig. 16.1. The spectral sensitivity of mammalian ganglion cells was measured and the responsivity curve is shown in Fig. 16.9. Inspection of the figure reveals a ganglion-cell peak-sensitivity at 484 nm, i.e. in the blue spectral range.

Berson *et al*. (2002) presented evidence that the photosensitive ganglion cells are instrumental in the control of the circadian rhythm. Due to their sensitivity in the blue spectral range, it can be hypothesized that the blue sky occurring near mid-day is a strong factor in synchronizing the endogenous circadian rhythm. The photosensitive ganglion cells have therefore been referred to as *blue-sky receptors*.

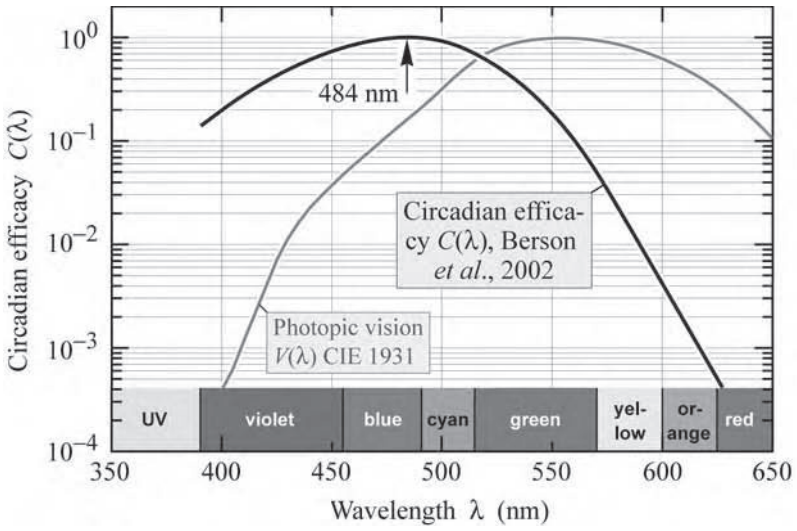


Fig. 16.9. Circadian efficacy curve derived from retinal ganglion cell photoresponse measurements. The ganglion cells on which the measurements were performed originated from mammals. The figure reveals the significant difference between circadian and visual sensitivity (adapted from Berson *et al*., 2002).

Inspection of the spectral sensitivity of the ganglion cells shown in Fig. 16.9 reveals the huge difference of red light and blue light for circadian efficacy: The efficacy of blue light in synchronizing the circadian rhythm can be three orders of magnitude greater than the efficacy of red light. This particular role of blue light should be taken into account in lighting design and the use of artificial lighting by consumers.

### *References*

Berson D. M., Dunn F. A., and Takao M. "Phototransduction by retinal ganglion cells that set the circadian clock" *Science* **295**, 1070 (2002)

Brainard G. C., Hanifin J. P., Greeson J. M., Byrne B., Glickman G., Gerner E., and Rollag M. D. "Action spectrum for melatonin regulation in humans: Evidence for a novel circadian photoreceptor" *J. Neuroscience* **21,** 6405 (2001)

Blask D. E., Dauchy R. T., Sauer L. A., Krause J. A., Brainard G. C. "Growth and fatty acid metabolism of human breast cancer (MCF-7) xenografts in nude rats: Impact of constant light-induced nocturnal melatonin suppression" *Breast Cancer Research and Treatment* **79**, 313 (2003)

CIE *Commission Internationale de l'Eclairage Proceedings* (Cambridge University Press, Cambridge, 1931)

CIE *Proceedings* **1**, Sec. 4; **3**, p. 37; Bureau Central de la CIE, Paris (1951)

CIE data of 1931 and 1978 available at http://cvision.ucsd.edu and http://www.cvrl.org (1978). The CIE 1931 $V(\lambda)$ data were modified by D. B. Judd and J. J. Vos in 1978. The Judd–Vos-modified eye-sensitivity function is frequently referred to as $V_M(\lambda)$; *see* J. J. Vos "Colorimetric and photometric properties of a 2-deg fundamental observer" *Color Res. Appl.* **3**, 125 (1978)



Nichia Exhibit 1014
Page 103

CIE publication 75-1988 *Spectral Luminous Efficiency Functions Based Upon Brightness Matching for Monochromatic Point Sources with 2° and 10° Fields* ISBN 3900734119 (1988)

CIE publication 86-1990 *CIE 1988 2° Spectral Luminous Efficiency Function for Photopic Vision* ISBN 3900734232 (1990)

Dowling J. E. *The retina: An Approachable Part of the Brain* (Harvard University Press, Cambridge, Massachusetts, 1987)

Encyclopedia Britannica, Inc. Illustration of human eye adopted from 1994 edition of the encyclopedia (1994)

Hattar S., Liao H.-W., Takao M., Berson D. M., and Yau K.-W. "Melanopsin-containing retinal ganglion cells: Architecture, projections, and intrinsic photosensitivity" *Science* **295**, 1065 (2002)

MacAdam D. L. "Maximum attainable luminous efficiency of various chromaticities" *J. Opt. Soc. Am.* **40**, 120 (1950)

Osram Sylvania Corporation *Lumens and mesopic vision* Application Note FAQ0016-0297 (2000)

Pittendrigh C. S. "Temporal organization: Reflections of a Darwinian clock-watcher" *Ann. Rev. Physiol.* **55**, 17 (1993)

Schmid W., Scherer M., Karnutsch C., Plobl A., Wegleiter W., Schad S., Neubert B., and Streubel K. "High-efficiency red and infrared light-emitting diodes using radial outcoupling taper" *IEEE J. Sel. Top. Quantum Electron.* **8**, 256 (2002)

Schubert E. F. The author of this book noticed in 1997 that working after 8 PM under bright illumination conditions in the office allowed him to fall asleep only very late, typically after midnight. The origin of sleeplessness was traced back to high-intensity office lighting conditions. Once the high intensity of the office lighting was reduced, the sleeplessness vanished (1997)

Sehgal A., editor *Molecular Biology of Circadian Rhythms* (John Wiley and Sons, New York, 2004)

Vos J. J. "Colorimetric and photometric properties of a 2-deg fundamental observer" *Color Res. Appl.* **3**, 125 (1978)

Wyszecki G. and Stiles W. S. *Color Science – Concepts and Methods, Quantitative Data and Formulae* 2nd edition (John Wiley and Sons, New York, 1982)

Wyszecki G. and Stiles W. S. *Color Science – Concepts and Methods, Quantitative Data and Formulae* 2nd edition (John Wiley and Sons, New York, 2000)

## Appendix 16.1

Tabulated values of the 2º degree CIE 1931 photopic eye sensitivity function and the CIE 1978 Judd–Vos-modified photopic eye sensitivity function for point sources (after CIE, 1931 and CIE, 1978).

| λ (nm) | CIE 1931 $V(\lambda)$ | CIE 1978 $V(\lambda)$ |
|---|---|---|
| 360 | 3.9170 E–6 | 0.0000E–4 |
| 365 | 6.9650 E–6 | 0.0000E–4 |
| 370 | 1.2390 E–5 | 0.0000E–4 |
| 375 | 2.2020 E–5 | 0.0000E–4 |
| 380 | 3.9000 E–5 | 2.0000E–4 |
| 385 | 6.4000 E–5 | 3.9556E–4 |
| 390 | 1.2000 E–4 | 8.0000E–4 |
| 395 | 2.1700 E–4 | 1.5457E–3 |
| 400 | 3.9600 E–4 | 2.8000E–3 |
| 405 | 6.4000 E–4 | 4.6562E–3 |
| 410 | 1.2100 E–3 | 7.4000E–3 |
| 415 | 2.1800 E–3 | 1.1779E–2 |
| 420 | 4.0000 E–3 | 1.7500E–2 |
| 425 | 7.3000 E–3 | 2.2678E–2 |
| 430 | 1.1600 E–2 | 2.7300E–2 |
| 435 | 1.6840 E–2 | 3.2584E–2 |
| 440 | 2.3000 E–2 | 3.7900E–2 |
| 445 | 2.9800 E–2 | 4.2391E–2 |
| 450 | 3.8000 E–2 | 4.6800E–2 |
| 455 | 4.8000 E–2 | 5.2122E–2 |
| 460 | 6.0000 E–2 | 6.0000E–2 |
| 465 | 7.3900 E–2 | 7.2942E–2 |
| 470 | 9.0980 E–2 | 9.0980E–2 |
| 475 | 0.11260 | 0.11284 |
| 480 | 0.13902 | 0.13902 |
| 485 | 0.16930 | 0.16987 |
| 490 | 0.20802 | 0.20802 |
| 495 | 0.25860 | 0.25808 |
| 500 | 0.32300 | 0.32300 |
| 505 | 0.40730 | 0.40540 |
| 510 | 0.50300 | 0.50300 |
| 515 | 0.60820 | 0.60811 |
| 520 | 0.71000 | 0.71000 |
| 525 | 0.79320 | 0.79510 |
| 530 | 0.86200 | 0.86200 |
| 535 | 0.91485 | 0.91505 |
| 540 | 0.95400 | 0.95400 |
| 545 | 0.98030 | 0.98004 |
| 550 | 0.99495 | 0.99495 |
| 555 | 1.00000 | 1.00000 |
| 560 | 0.99500 | 0.99500 |
| 565 | 0.97860 | 0.97875 |
| 570 | 0.95200 | 0.95200 |
| 575 | 0.91540 | 0.91558 |
| 580 | 0.87000 | 0.87000 |
| 585 | 0.81630 | 0.81623 |
| 590 | 0.75700 | 0.75700 |
| 595 | 0.69490 | 0.69483 |
| 600 | 0.63100 | 0.63100 |
| 605 | 0.56680 | 0.56654 |
| 610 | 0.50300 | 0.50300 |
| 615 | 0.44120 | 0.44172 |
| 620 | 0.38100 | 0.38100 |
| 625 | 0.32100 | 0.32052 |
| 630 | 0.26500 | 0.26500 |
| 635 | 0.21700 | 0.21702 |
| 640 | 0.17500 | 0.17500 |
| 645 | 0.13820 | 0.13812 |
| 650 | 0.10700 | 0.1.0700 |
| 655 | 8.1600 E–2 | 8.1652E–2 |
| 660 | 6.1000 E–2 | 6.1000E–2 |
| 665 | 4.4580 E–2 | 4.4327E–2 |
| 670 | 3.2000 E–2 | 3.2000E–2 |
| 675 | 2.3200 E–2 | 2.3454E–2 |
| 680 | 1.7000 E–2 | 1.7000E–2 |
| 685 | 1.1920 E–2 | 1.1872E–2 |
| 690 | 8.2100 E–3 | 8.2100E–3 |
| 695 | 5.7230 E–3 | 5.7723E–3 |
| 700 | 4.1020 E–3 | 4.1020E–3 |
| 705 | 2.9290 E–3 | 2.9291E–3 |
| 710 | 2.0910 E–3 | 2.0910E–3 |
| 715 | 1.4840 E–3 | 1.4822E–3 |
| 720 | 1.0470 E–3 | 1.0470E–3 |
| 725 | 7.4000 E–4 | 7.4015E–4 |
| 730 | 5.2000 E–4 | 5.2000E–4 |
| 735 | 3.6110 E–4 | 3.6093E–4 |
| 740 | 2.4920 E–4 | 2.4920E–4 |
| 745 | 1.7190 E–4 | 1.7231E–4 |
| 750 | 1.2000 E–4 | 1.2000E–4 |
| 755 | 8.4800 E–5 | 8.4620E–5 |
| 760 | 6.0000 E–5 | 6.0000E–5 |
| 765 | 4.2400 E–5 | 4.2446E–5 |
| 770 | 3.0000 E–5 | 3.0000E–5 |
| 775 | 2.1200 E–5 | 2.1210E–5 |
| 780 | 1.4990 E–5 | 1.4989E–5 |
| 785 | 1.0600 E–5 | 1.0584E–5 |
| 790 | 7.4657 E–6 | 7.4656E–6 |
| 795 | 5.2578 E–6 | 5.2592E–6 |
| 800 | 3.7029 E–6 | 3.7028E–6 |
| 805 | 2.6078 E–6 | 2.6076E–6 |
| 810 | 1.8366 E–6 | 1.8365E–6 |
| 815 | 1.2934 E–6 | 1.2950E–6 |
| 820 | 9.1093 E–7 | 9.1092E–7 |
| 825 | 6.4153 E–7 | 6.3564E–7 |



Nichia Exhibit 1014
Page 105

## Appendix 16.2

Tabulated values of the CIE 1951 eye sensitivity function of the scotopic vision regime, $V'(\lambda)$ (after CIE, 1951).

| λ (nm) | CIE 1951 $V'(\lambda)$ | λ (nm) | CIE 1951 $V'(\lambda)$ |
|---|---|---|---|
| 380 | 5.890e-004 | 585 | 8.990e-002 |
| 385 | 1.108e-003 | 590 | 6.550e-002 |
| 390 | 2.209e-003 | 595 | 4.690e-002 |
| 395 | 4.530e-003 | 600 | 3.315e-002 |
| 400 | 9.290e-003 | 605 | 2.312e-002 |
| 405 | 1.852e-002 | 610 | 1.593e-002 |
| 410 | 3.484e-002 | 615 | 1.088e-002 |
| 415 | 6.040e-002 | 620 | 7.370e-003 |
| 420 | 9.660e-002 | 625 | 4.970e-003 |
| 425 | 1.436e-001 | 630 | 3.335e-003 |
| 430 | 1.998e-001 | 635 | 2.235e-003 |
| 435 | 2.625e-001 | 640 | 1.497e-003 |
| 440 | 3.281e-001 | 645 | 1.005e-003 |
| 445 | 3.931e-001 | 650 | 6.770e-004 |
| 450 | 4.550e-001 | 655 | 4.590e-004 |
| 455 | 5.130e-001 | 660 | 3.129e-004 |
| 460 | 5.670e-001 | 665 | 2.146e-004 |
| 465 | 6.200e-001 | 670 | 1.480e-004 |
| 470 | 6.760e-001 | 675 | 1.026e-004 |
| 475 | 7.340e-001 | 680 | 7.150e-005 |
| 480 | 7.930e-001 | 685 | 5.010e-005 |
| 485 | 8.510e-001 | 690 | 3.533e-005 |
| 490 | 9.040e-001 | 695 | 2.501e-005 |
| 495 | 9.490e-001 | 700 | 1.780e-005 |
| 500 | 9.820e-001 | 705 | 1.273e-005 |
| 505 | 9.980e-001 | 710 | 9.140e-006 |
| 510 | 9.970e-001 | 715 | 6.600e-006 |
| 515 | 9.750e-001 | 720 | 4.780e-006 |
| 520 | 9.350e-001 | 725 | 3.482e-006 |
| 525 | 8.800e-001 | 730 | 2.546e-006 |
| 530 | 8.110e-001 | 735 | 1.870e-006 |
| 535 | 7.330e-001 | 740 | 1.379e-006 |
| 540 | 6.500e-001 | 745 | 1.022e-006 |
| 545 | 5.640e-001 | 750 | 7.600e-007 |
| 550 | 4.810e-001 | 755 | 5.670e-007 |
| 555 | 4.020e-001 | 760 | 4.250e-007 |
| 560 | 3.288e-001 | 765 | 3.196e-007 |
| 565 | 2.639e-001 | 770 | 2.413e-007 |
| 570 | 2.076e-001 | 775 | 1.829e-007 |
| 575 | 1.602e-001 | 780 | 1.390e-007 |
| 580 | 1.212e-001 | | |

# 17

## Colorimetry

The assessment and quantification of color is referred to as ***colorimetry*** or the "science of color". Colorimetry is closely associated with human color vision. Both colorimetry and human vision have attracted a great deal of interest that spans many centuries. For a thorough and entertaining review of the history of colorimetry including early attempts to understand color, we recommended the collection of historical reprints complied by MacAdam (1993).

The human sense of vision is very different from the human sense of hearing. If we hear two frequencies simultaneously, e.g. two frequencies generated by a musical instrument, we will be able to recognize the musical tone as having two distinct frequencies. This is not the case for optical signals and the sense of vision. Mixing two monochromatic optical signals will appear to us as one color and we are unable to recognize the original dichromatic composition of that color.

### *17.1 Color-matching functions and chromaticity diagram*

Light causes different levels of excitation of the red, green, and blue cones. However, the sensation of color and luminous flux caused a particular light source varies slightly among different individuals. Furthermore, the sensation of color is, to some extent, a subjective quantity. For these reasons, *The International Commission for Illumination* (*Commission Internationale de l'Eclairage*, CIE) has *standardized the measurement of color* by means of ***color-matching functions*** and the ***chromaticity diagram*** (CIE, 1931).

How are color-matching functions obtained? Consider two lights lying side by side: One being monochromatic and the other one being a mixture of three primary lights with color red, green, and blue, as shown in Fig. 17.1. A human subject will be able to make the two lights appear identical (i.e. "match" them) by adjusting the relative intensities of the red, green, and blue light. The three color-matching functions are obtained from a series of such matches, in which the subject sets the intensities of the three primary lights required to match a series of monochromatic lights across the visible spectrum.



Nichia Exhibit 1014
Page 107

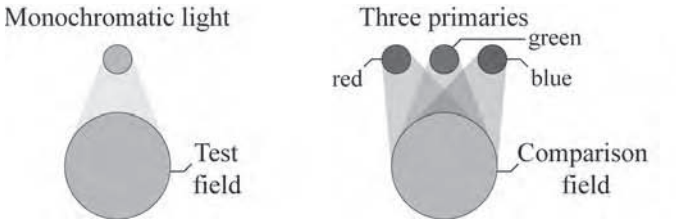


Fig. 17.1. Principle of color matching: A monochromatic test light (imaged on the "test field") is color-matched by mixing three adjustable primary lights, red, green, and blue (imaged on the "comparison field").

Subsequently, the measured set of color-matching functions is mathematically transformed into a new set of color-matching functions for which the green color-matching function, $\bar{y}(\lambda)$, is chosen to be identical to the eye sensitivity function, $V(\lambda)$, i.e.

$$\boxed{\bar{y}(\lambda) = V(\lambda)} \,. \tag{17.1}$$

The CIE 1931 and CIE 1978 color-matching functions $\bar{x}(\lambda)$, $\bar{y}(\lambda)$, and $\bar{z}(\lambda)$ are shown in Fig. 17.2. The numerical values of these color-matching functions are tabulated in Appendices 17.1 and 17.2, respectively. The three color-matching functions reflect the fact that human color vision possesses ***trichromacy***, that is, the color of any light source can be described by just three variables. Note that $\bar{x}(\lambda)$, $\bar{y}(\lambda)$, and $\bar{z}(\lambda)$ are dimensionless quantities. Also note that neither the color-matching functions nor the chromaticity diagram is unique (see, for example, Judd, 1951 or Vos, 1978). In fact there have been several different versions of the color-matching functions and of the chromaticity diagram.

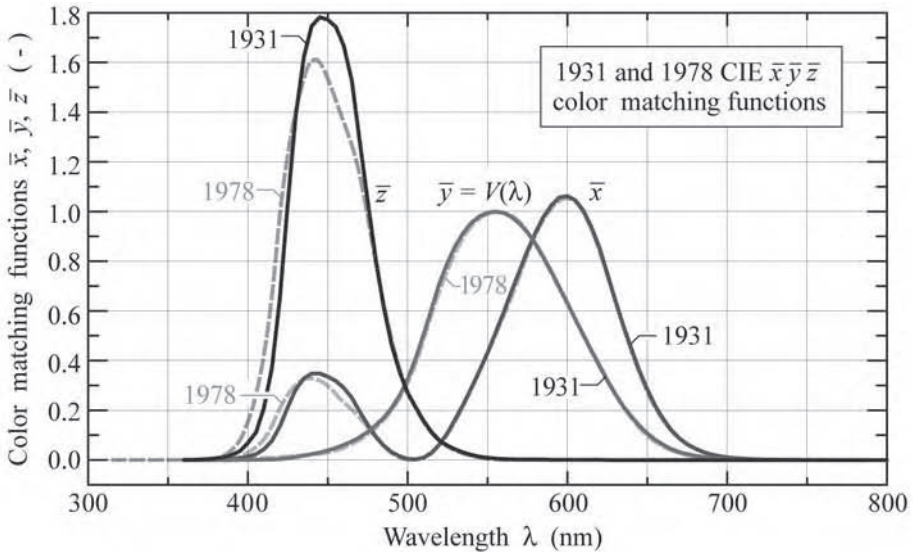


Fig. 17.2. CIE (1931) and CIE (1978) $\bar{x}\bar{y}\bar{z}$ color-matching functions. The $\bar{y}$ color-matching function is identical to the eye sensitivity function $V(\lambda)$. Note that the CIE 1931 color-matching functions are the currently valid official standard in the United States.

For a given power-spectral density $P(\lambda)$, the degree of stimulation required to match the color of $P(\lambda)$ is given by

$$X = \int_{\lambda} \bar{x}(\lambda)\, P(\lambda)\, \mathrm{d}\lambda \tag{17.2}$$

$$Y = \int_{\lambda} \bar{y}(\lambda)\, P(\lambda)\, \mathrm{d}\lambda \tag{17.3}$$

$$Z = \int_{\lambda} \bar{z}(\lambda)\, P(\lambda)\, \mathrm{d}\lambda \tag{17.4}$$

where $X$, $Y$, and $Z$ are the ***tristimulus values*** that give the stimulation (i.e. power) of each of the three primary red, green, and blue lights needed to match the color of $P(\lambda)$. Large values of $X$, $Y$, and $Z$ indicate red, green, and blue colors of the spectrum $P(\lambda)$, respectively.

Because of the distinct similarity of the three retinal-cone-sensitivity functions on one hand, and the color-matching functions on the other hand (both groups of functions have three peaks), each tristimulus value represents the *approximate* (but not *exact*) degree of stimulation that each type of retinal cone experiences when illuminated by a light source with spectrum $P(\lambda)$.

Inspection of Eqs. (17.2)–(17.4) suggests that the unit of the tristimulus values is "watt". However, the tristimulus values are usually given as dimensionless quantities. The prefactor "watt$^{-1}$" in front of the integral can be included so that the tristimulus values become dimensionless. If only *ratios* of tristimulus values are employed, as below, the prefactors and units cancel and thus become irrelevant.

The ***chromaticity coordinates*** $x$ and $y$ are calculated from the tristimulus values according to

$$x = \frac{X}{X + Y + Z} \tag{17.5}$$

$$y = \frac{Y}{X + Y + Z} \,. \tag{17.6}$$

Thus, the value of a chromaticity coordinate is the stimulation of each primary light (or of each type of retinal cone) divided by the entire stimulation ($X + Y + Z$). The value of the $z$ chromaticity coordinate is calculated analogously, that is

$$z = \frac{Z}{X + Y + Z} = 1 - x - y \,. \tag{17.7}$$

Note that the $z$ chromaticity value can be obtained from $x$ and $y$, so that there is no new information provided by the $z$ chromaticity coordinate. Therefore, the $z$ coordinate is redundant



Nichia Exhibit 1014
Page 109

and, for this reason, does not need to be used.

The $(x, y)$ chromaticity diagram is shown in Fig. 17.3. Reddish and greenish colors are found for large values of $x$ and $y$, respectively. Bluish colors are found for large values of $z$, which is, according to Eq. (17.7), for low values of $x$ and $y$, or near the origin of the chromaticity diagram.

The chromaticity diagram of Fig. 17.4 shows a detailed attribution of colors to their locations in the chromaticity diagram. The assignment of colors was given by Gage *et al*. (1977).

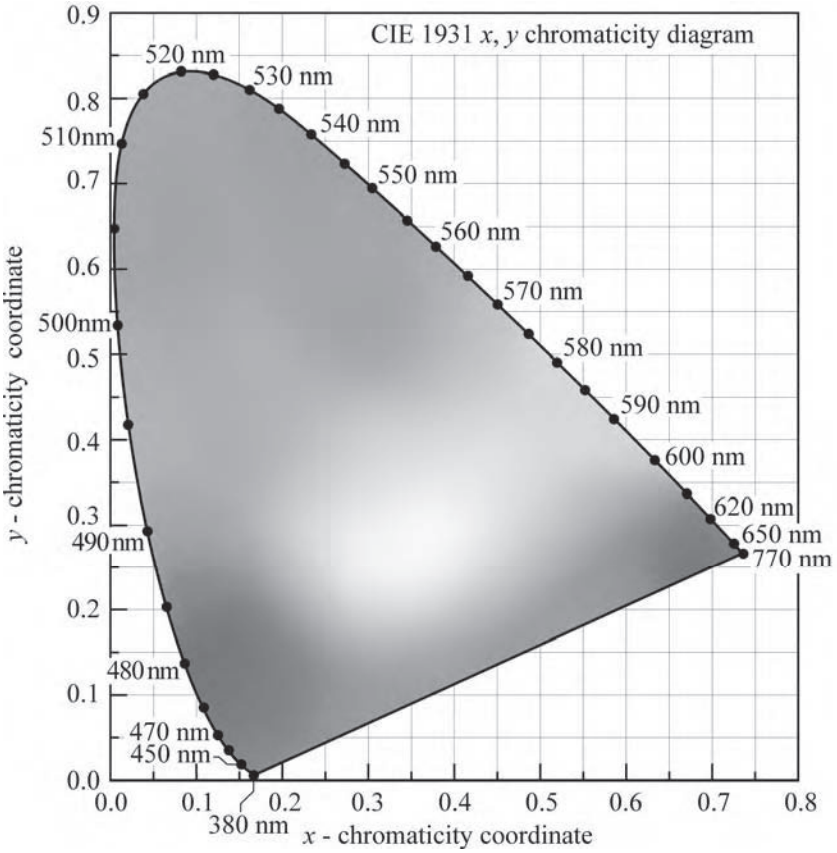


Fig. 17.3. CIE 1931 $(x, y)$ chromaticity diagram. Monochromatic colors are located on the perimeter and white light is located in the center of the diagram.

An assignment of common colors in the chromaticity diagram is given in Fig. 17.5. The figure also shows the ***equal-energy point*** located in the center of the chromaticity diagram at $(x, y, z) = (1/3,\ 1/3,\ 1/3)$. The optical spectrum corresponding to the equal-energy point has a constant spectral distribution, i.e. the optical energy per wavelength interval $d\lambda$ is constant across the visible spectrum. Such a spectrum also results in equal tristimulus values, i.e. $X = Y = Z$.

Monochromatic or pure colors are found on the perimeter of the chromaticity diagram. White light is found in the center of the chromaticity diagram. All colors can be characterized in terms of their location in the chromaticity diagram.

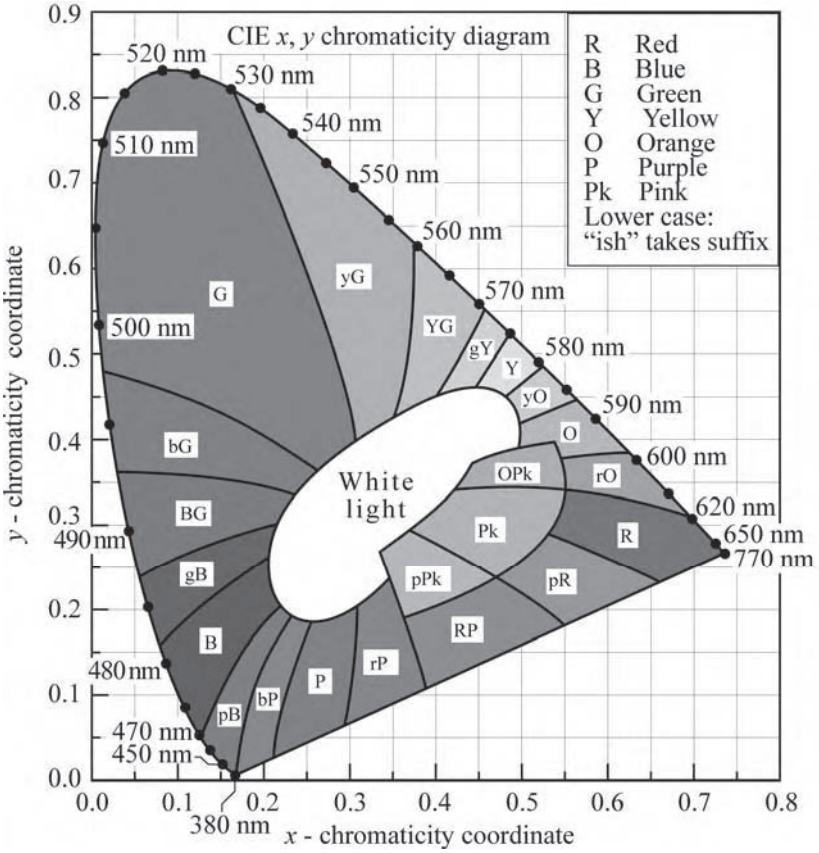


Fig. 17.4. 1931 CIE chromaticity diagram with areas attributed to distinct colors (after Gage *et al.*, 1977).

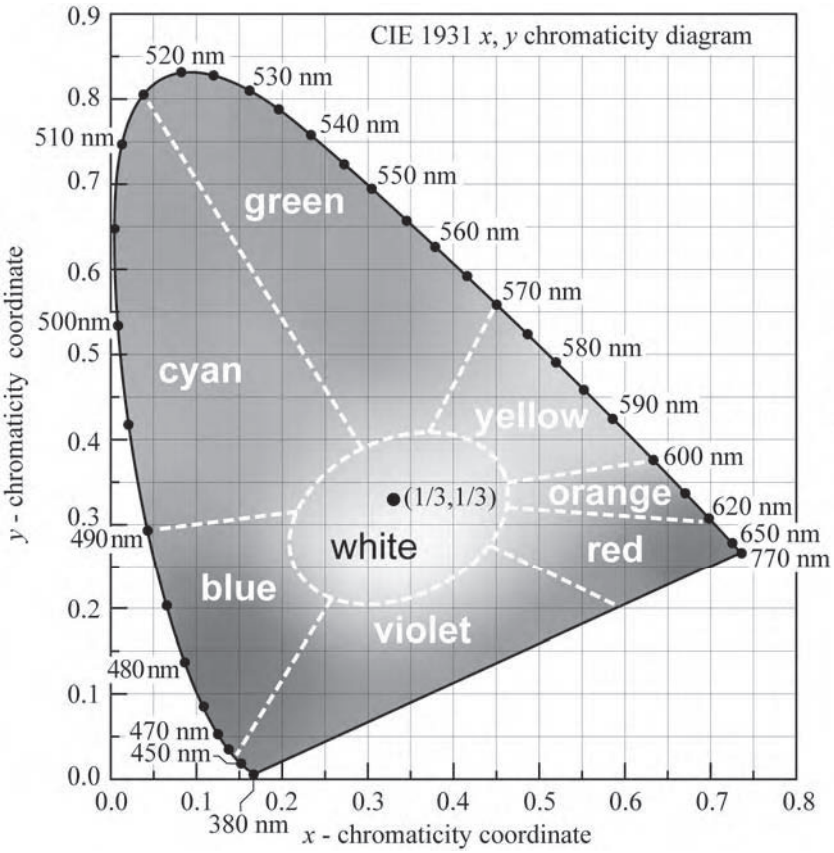


Fig. 17.5. CIE 1931 ($x$, $y$) chromaticity diagram. Monochromatic colors are located on the perimeter. Color saturation decreases towards the center of the diagram. White light is located in the center. Also shown are the regions of distinct colors. The equal-energy point is located at the center and has the coordinates ($x$, $y$) = (1/3, 1/3).



Nichia Exhibit 1014
Page 111

MacAdam (1943) analyzed the color differences of closely spaced points in the chromaticity diagram. The author found that two chromaticity points must have a *minimum geometrical distance* to yield a perceptible difference in color. Colors within a certain small region in the chromaticity diagram appear identical to human subjects. MacAdam showed that these regions have the shape of an ellipses. Such ellipses, now known as the ***MacAdam ellipses***, are shown in Fig. 17.6 (MacAdam, 1943, 1993; Wright, 1943). Inspection of the figure shows that ellipses in the blue and green regions are very different in size. Thus, the geometric distance between two points in the ($x$, $y$) chromaticity diagram does *not* scale linearly with the color difference.

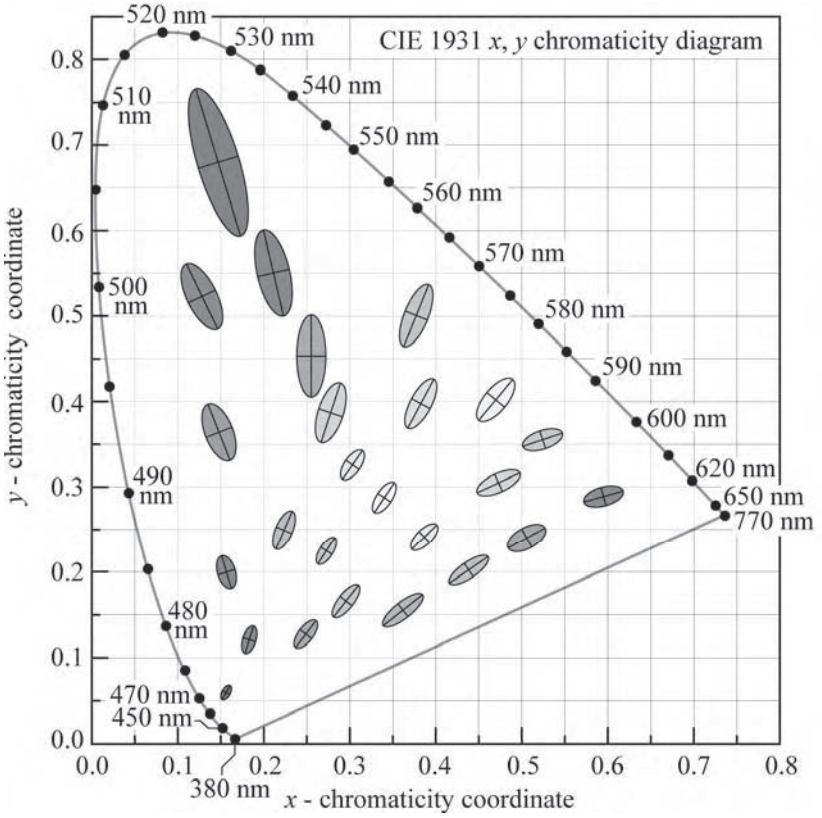


Fig. 17.6. MacAdam ellipses plotted in the CIE 1931 ($x$, $y$) chromaticity diagram. The axes of the ellipses are ten times their actual lengths (after MacAdam, 1943; Wright, 1943; MacAdam, 1993).

The total number of differentiable chromaticities can be obtained by dividing the area of the chromaticity diagram through the average area of the MacAdam ellipses. This calculation yields the result that humans can discern approximately 50 000 distinct chromaticities. If possible variations in luminance (brightness) are taken into account, the number of differentiable colors increases to a value greater than $10^6$.

In the chromaticity diagram, it is very desirable for the color difference to be proportional to the geometric difference. This has motivated the *uniform* chromaticity diagram. In 1960, the CIE introduced the ($u$, $v$) and in 1976 the ($u'$, $v'$) ***uniform chromaticity coordinates*** (Wyszecki and

Stiles, 2000). These coordinates form the ***uniform chromaticity diagram***. The uniform chromaticity coordinates are calculated from the tristimulus values according to

$$u = \frac{4X}{X + 15Y + 3Z} \qquad v = \frac{6Y}{X + 15Y + 3Z} \qquad \text{(CIE, 1960)} \qquad (17.8)$$

and

$$u' = \frac{4X}{X + 15Y + 3Z} \qquad v' = \frac{9Y}{X + 15Y + 3Z} \qquad \text{(CIE, 1976)}. \qquad (17.9)$$

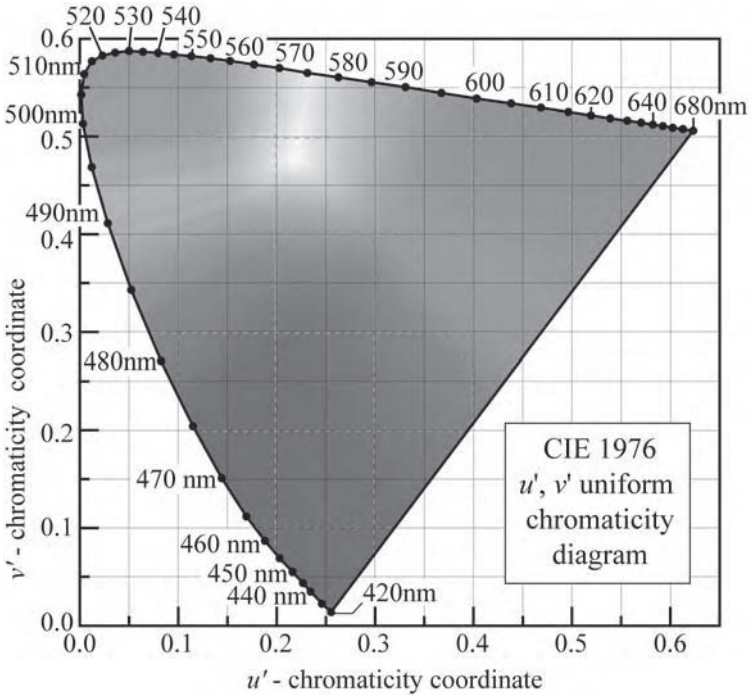


Fig. 17.7. CIE 1976 $(u', v')$ uniform chromaticity diagram calculated using the CIE 1931 2° standard observer.

The CIE 1976 $(u', v')$ uniform chromaticity diagram is shown in Fig. 17.7. The $(u, v)$ and $(u', v')$ uniform chromaticity coordinates can be calculated from the $(x, y)$ chromaticity coordinates according to

$$u = u' = \frac{4x}{-2x + 12y + 3} \qquad (17.10)$$

and

$$v = \frac{6y}{-2x + 12y + 3} \qquad v' = \frac{9y}{-2x + 12y + 3}. \qquad (17.11)$$



Nichia Exhibit 1014
Page 113

Conversely, one obtains

$$x = \frac{9u'}{6u' - 16v' + 12} \qquad y = \frac{2v'}{3u' - 8v' + 6} \tag{17.12}$$

and

$$x = \frac{3u}{2u - 8v + 4} \qquad y = \frac{2v}{2u - 8v + 4} \,. \tag{17.13}$$

The color differences between two points in the $(x, y)$ chromaticity diagram are spatially very non-uniform, that is, the color changes much more rapidly in one direction, e.g. the $x$-direction, compared with the other direction, e.g. the $y$-direction. This deficiency of the $(x, y)$ chromaticity diagram is strongly reduced, although not eliminated, in the $(u, v)$ and $(u', v')$ uniform chromaticity diagrams. As a result, the *color difference* between two locations in the uniform chromaticity diagram is (approximately) directly proportional to the *geometrical distance* between these points.

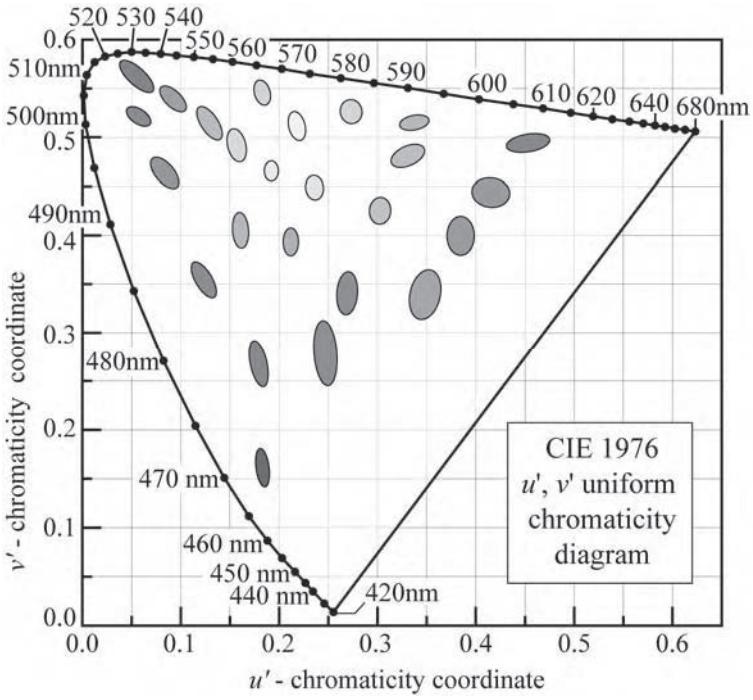


Fig. 17.8. MacAdam ellipses transformed to uniform CIE 1976 $(u', v')$ chromaticity coordinates. For clarity, the axes of the transformed ellipses are ten times their actual lengths. Transformed ellipses are not ellipses in a strict mathematical sense, but their shapes closesly resemble those of ellipses. The areas of the transformed ellipses in the $(u', v')$ diagram are much more similar than the MacAdam ellipses in the $(x, y)$ diagram.

The 1943 MacAdam ellipses in the $(x, y)$ chromaticity diagram can be transformed to the uniform $(u', v')$ chromaticity diagram. This transformation is shown in Fig. 17.8, which reveals that the areas of non-discernable colors are much more uniform in shape and area than the

MacAdam ellipses in the ($x$, $y$) chromaticity diagram.

Note that the transformation from the ($x$, $y$) to the ($u'$, $v'$) coordinate system is mathematically *non-linear*, and thus ellipses in the ($x$, $y$) chromaticity diagram do *not* transform into ellipses in the ($u'$, $v'$) coordinate system. However, if the ellipses in the ($x$, $y$) chromaticity diagram are sufficiently small in size, non-linear distortions are small as well, so that the transformed regions are very close to ellipses.

### *17.2 Color purity*

Monochromatic sources ($\Delta\lambda \to 0$) are located on the perimeter of the chromaticity diagram. However, as the spectral linewidth of a light source gets broader, the color location in the chromaticity diagram moves towards the center of the chromaticity diagram. If the spectral width of a light source becomes comparable to the entire visible range, the light source is *white* and thus located near the center of the chromaticity diagram.

The ***dominant wavelength*** of a test light source is defined as the wavelength (i.e. monochromatic color) located on the perimeter of the chromaticity diagram that appears to be closest to the color of the test light source. The dominant wavelength is determined by drawing a straight line from the equal-energy point to the ($x$, $y$) chromaticity coordinate of the test light source, and by extending the straight line to the perimeter of the chromaticity diagram. The intersection point is the dominant wavelength of the light source. The procedure is schematically shown in Fig. 17.9.

The ***color purity*** or ***color saturation*** of a light source is the distance in the chromaticity diagram between the ($x$, $y$) color-coordinate point of the test source and the coordinate of the equal-energy point divided by the distance between the equal-energy point and the dominant-wavelength point. The color purity is thus given by

$$\text{color purity} \;=\; \frac{a}{a \;+\; b} \;=\; \frac{\sqrt{(x - x_{ee})^2 \;+\; (y - y_{ee})^2}}{\sqrt{(x_d - x_{ee})^2 \;+\; (y_d - y_{ee})^2}} \tag{17.14}$$

where $a$ and $b$ are shown in Fig. 17.9 and ($x$, $y$), ($x_{ee}$, $y_{ee}$), and ($x_d$, $y_d$) represent the chromaticity coordinates of the light source under test, of the equal-energy reference illuminant, and of the dominant-wavelength point, respectively. Thus the color purity is the relative distance of a light source under test from the center of the chromaticity diagram. Generally, the color purity is 100% for monochromatic light sources ($\Delta\lambda \to 0$) located on the perimeter of the chromaticity



Nichia Exhibit 1014
Page 115

diagram and near 0% for white illuminants.

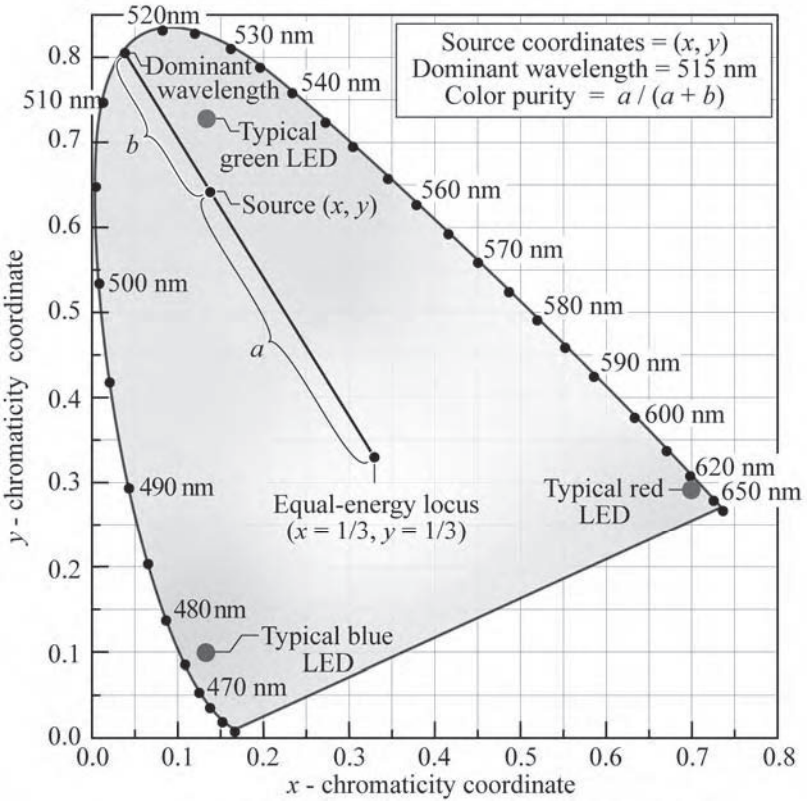


Fig. 17.9. Chromaticity diagram showing the determination of the *dominant wavelength* and *color purity* of a light source with chromaticity coordinates $(x, y)$ using the equal-energy locus $(x = 1/3, y = 1/3)$ as the white-light reference. Also shown are typical locations of blue, green, and red LEDs.

Note that the dominant wavelength and color purity are an alternative way to uniquely characterize the location of an emitter on the chromaticity diagram. Dominant wavelength and color purity are quite intuitive quantities (more so than the numerical $(x, y)$ chromaticity coordinates) and they are therefore frequently preferred.

### *17.3 LEDs in the chromaticity diagram*

Monochromatic light sources ($\Delta\lambda \to 0$) are located on the perimeter of the chromaticity diagram. Light emission from LEDs is monochromatic (single color) to the eye but LEDs are not monochromatic in the strict physical sense since LEDs have a spectral linewidth of about 1.8 $kT$. Owing to the finite spectral linewidth of LEDs, they are not located on the very perimeter of the chromaticity diagram but are located *close* to the perimeter. When a source emits light distributed over a range of wavelengths, then the chromaticity location moves towards the center of the diagram.

The location of different LEDs on the chromaticity diagram is shown in Fig. 17.10. Inspection of the figure reveals that the location of red and blue LEDs is on the perimeter of the

chromaticity diagram. That is, their color purity is very high, close to 100%. However, blue–green and green LEDs are located off the perimeter closer to the center of the diagram due to the finite linewidth of the emission spectrum and the strong curvature of the chromaticity diagram in the green wavelength range.

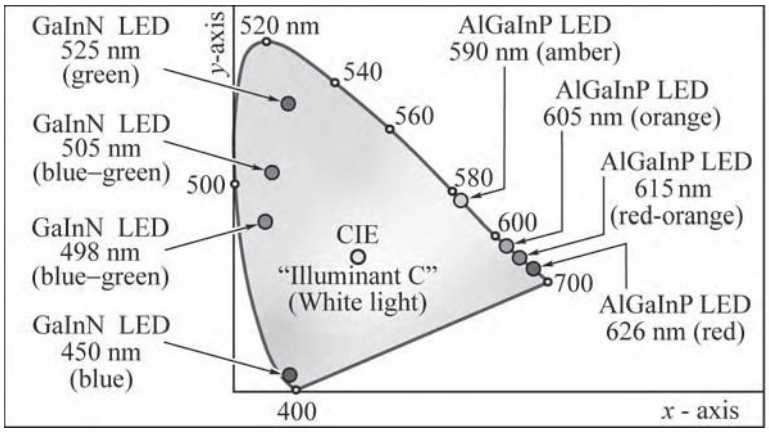


Fig. 17.10. Location of LED light emission on the chromaticity diagram (adapted from Schubert and Miller, 1999).

### *17.4 Relationship between chromaticity and color*

Having completed the discussion of *chromaticity* allows us to revisit the question: What is *color*? One could certainly define a color by its location in the chromaticity diagram (i.e. by its chromaticity). However, the CIE (1986) adopted a more general definition of the term "color" that goes beyond the location in the chromaticity diagram. The CIE's broader definition of color includes ***chromaticity*** as well as ***brightness***. That is, we can keep the chromaticity of a light source the same but change its luminous intensity (brightness); this, according to the CIE definition, changes the color of the source. If, on the other hand, we restrict our considerations to a single brightness level, the terms "chromaticity" and "color" can be used synonymously.

The location of a chromaticity point can be expressed by the *dominant wavelength* and *saturation* (or, alternatively, by *hue* and *saturation*). Thus, the CIE definition of the *color of light* is given by the *dominant wavelength*, *saturation*, *and* ***bright****ness*. The *color of an object* is given by the *dominant wavelength*, *saturation*, *and* ***light****ness*.

### *References*

CIE *Commission Internationale de l'Eclairage Proceedings* (Cambridge University Press, Cambridge, 1931)
CIE data of 1931 and 1978 available at http://cvision.ucsd.edu and http://www.cvrl.org (1978)
CIE data of 1960 relating to the ($u$, $v$) chromaticity coordinates can be found in CIE, 1986
CIE data of 1976 relating to the ($u'$, $v'$) chromaticity coordinates can be found in CIE, 1986



Nichia Exhibit 1014
Page 117

CIE publication No. 15 (E.1.3.1) 1971: *Colorimetry*; this publication was updated in 1986 to CIE Publication 15.2 *Colorimetry* (CIE, Vienna, Austria, 1986)

Gage S., Evans D., Hodapp M. W., and Sorensen H. *Optoelectronics Applications Manual* 1st edition (McGraw Hill, New York, 1977)

Judd D. B. "Report of US Secretariat Committee on Colorimetry and Artificial Daylight" in *Proceedings of the 12th Session of the CIE* **1**, p. 11 (Bureau Central de la CIE, Paris, 1951)

MacAdam D. L. "Specification of small chromaticity differences" *J. Opt. Soc. Am.* **33**, 18 (1943)

MacAdam D. L. (Editor) *Colorimetry – Fundamentals* (SPIE Optical Engineering Press, Bellingham, Washington, 1993)

Schubert E. F. and Miller J. N "Light-emitting diodes - An introduction" *Encyclopedia of Electrical Engineering*, edited by John G. Webster, Vol. **11**, p. 326 (John Wiley and Sons, New York, March 1999)

Vos J. J. "Colorimetric and photometric properties of a 2-degree fundamental observer" *Color Res. Appl.* **3**, 125 (1978)

Wyszecki G. and Stiles W. S. *Color Science – Concepts and Methods, Quantitative Data and Formulae* 2nd edition (John Wiley and Sons, New York, 2000)

Wright W. D. "The graphical representation of small color differences" *J. Opt. Soc. Am.* **33**, 632 (1943)

## Appendix 17.1

Tabulated values of the CIE 1931 two-degree color-matching functions and eye sensitivity function for point sources (after CIE, 1931).

| λ (nm) | $\bar{x}(\lambda)$ ***red*** | $\bar{y} = V(\lambda)$ ***green*** | $\bar{z}(\lambda)$ ***blue*** |
|---|---|---|---|
| 360 | 1.2990 E–4 | 3.9170 E–6 | 6.0610 E–4 |
| 365 | 2.3210 E–4 | 6.9650 E–6 | 1.0860 E–3 |
| 370 | 4.1490 E–4 | 1.2390 E–5 | 1.9460 E–3 |
| 375 | 7.4160 E–4 | 2.2020 E–5 | 3.4860 E–3 |
| 380 | 1.3680 E–3 | 3.9000 E–5 | 6.4500 E–3 |
| 385 | 2.2360 E–3 | 6.4000 E–5 | 1.0550 E–2 |
| 390 | 4.2430 E–3 | 1.2000 E–4 | 2.0050 E–2 |
| 395 | 7.6500 E–3 | 2.1700 E–4 | 3.6210 E–2 |
| 400 | 1.4310 E–2 | 3.9600 E–4 | 6.7850 E–2 |
| 405 | 2.3190 E–2 | 6.4000 E–4 | 0.11020 |
| 410 | 4.3510 E–2 | 1.2100 E–3 | 0.20740 |
| 415 | 7.7630 E–2 | 2.1800 E–3 | 0.37130 |
| 420 | 0.13438 | 4.0000 E–3 | 0.64560 |
| 425 | 0.21477 | 7.3000 E–3 | 1.03905 |
| 430 | 0.28390 | 1.1600 E–2 | 1.38560 |
| 435 | 0.32850 | 1.6840 E–2 | 1.62296 |
| 440 | 0.34828 | 2.3000 E–2 | 1.74706 |
| 445 | 0.34806 | 2.9800 E–2 | 1.78260 |
| 450 | 0.33620 | 3.8000 E–2 | 1.77211 |
| 455 | 0.31870 | 4.8000 E–2 | 1.74410 |
| 460 | 0.29080 | 6.0000 E–2 | 1.66920 |
| 465 | 0.25110 | 7.3900 E–2 | 1.52810 |
| 470 | 0.19536 | 9.0980 E–2 | 1.28764 |
| 475 | 0.14210 | 0.11260 | 1.04190 |
| 480 | 9.5640 E–2 | 0.13902 | 0.81295 |
| 485 | 5.7950 E–2 | 0.16930 | 0.61620 |
| 490 | 3.2010 E–2 | 0.20802 | 0.46518 |
| 495 | 1.4700 E–2 | 0.25860 | 0.35330 |
| 500 | 4.9000 E–3 | 0.32300 | 0.27200 |
| 505 | 2.4000 E–3 | 0.40730 | 0.21230 |
| 510 | 9.3000 E–3 | 0.50300 | 0.15820 |
| 515 | 2.9100 E–2 | 0.60820 | 0.11170 |
| 520 | 6.3270 E–2 | 0.71000 | 7.8250 E–2 |
| 525 | 0.10960 | 0.79320 | 5.7250 E–2 |
| 530 | 0.16550 | 0.86200 | 4.2160 E–2 |
| 535 | 0.22575 | 0.91485 | 2.9840 E–2 |
| 540 | 0.29040 | 0.95400 | 2.0300 E–2 |
| 545 | 0.35970 | 0.98030 | 1.3400 E–2 |
| 550 | 0.43345 | 0.99495 | 8.7500 E–3 |
| 555 | 0.51205 | 1.00000 | 5.7500 E–3 |
| 560 | 0.59450 | 0.99500 | 3.9000 E–3 |
| 565 | 0.67840 | 0.97860 | 2.7500 E–3 |
| 570 | 0.76210 | 0.95200 | 2.1000 E–3 |
| 575 | 0.84250 | 0.91540 | 1.8000 E–3 |
| 580 | 0.91630 | 0.87000 | 1.6500 E–3 |
| 585 | 0.97860 | 0.81630 | 1.4000 E–3 |
| 590 | 1.02630 | 0.75700 | 1.1000 E–3 |
| 595 | 1.05670 | 0.69490 | 1.0000 E–3 |
| 600 | 1.06220 | 0.63100 | 8.0000 E–4 |
| 605 | 1.04560 | 0.56680 | 6.0000 E–4 |
| 610 | 1.00260 | 0.50300 | 3.4000 E–4 |
| 615 | 0.93840 | 0.44120 | 2.4000 E–4 |
| 620 | 0.85445 | 0.38100 | 1.9000 E–4 |
| 625 | 0.75140 | 0.32100 | 1.0000 E–4 |
| 630 | 0.64240 | 0.26500 | 5.0000 E–5 |
| 635 | 0.54190 | 0.21700 | 3.0000 E–5 |
| 640 | 0.44790 | 0.17500 | 2.0000 E–5 |
| 645 | 0.36080 | 0.13820 | 1.0000 E–5 |
| 650 | 0.28350 | 0.10700 | 0.0000 E–5 |
| 655 | 0.21870 | 8.1600 E–2 | 0.0000 E–5 |
| 660 | 0.16490 | 6.1000 E–2 | 0.0000 E–5 |
| 665 | 0.12120 | 4.4580 E–2 | 0.0000 E–5 |
| 670 | 8.7400 E–2 | 3.2000 E–2 | 0.0000 E–5 |
| 675 | 6.3600 E–2 | 2.3200 E–2 | 0.0000 E–5 |
| 680 | 4.6770 E–2 | 1.7000 E–2 | 0.0000 E–5 |
| 685 | 3.2900 E–2 | 1.1920 E–2 | 0.0000 E–5 |
| 690 | 2.2700 E–2 | 8.2100 E–3 | 0.0000 E–5 |
| 695 | 1.5840 E–2 | 5.7230 E–3 | 0.0000 E–5 |
| 700 | 1.1359 E–2 | 4.1020 E–3 | 0.0000 E–5 |
| 705 | 8.1109 E–3 | 2.9290 E–3 | 0.0000 E–5 |
| 710 | 5.7903 E–3 | 2.0910 E–3 | 0.0000 E–5 |
| 715 | 4.1065 E–3 | 1.4840 E–3 | 0.0000 E–5 |
| 720 | 2.8993 E–3 | 1.0470 E–3 | 0.0000 E–5 |
| 725 | 2.0492 E–3 | 7.4000 E–4 | 0.0000 E–5 |
| 730 | 1.4400 E–3 | 5.2000 E–4 | 0.0000 E–5 |
| 735 | 9.9995 E–4 | 3.6110 E–4 | 0.0000 E–5 |
| 740 | 6.9008 E–4 | 2.4920 E–4 | 0.0000 E–5 |
| 745 | 4.7602 E–4 | 1.7190 E–4 | 0.0000 E–5 |
| 750 | 3.3230 E–4 | 1.2000 E–4 | 0.0000 E–5 |
| 755 | 2.3483 E–4 | 8.4800 E–5 | 0.0000 E–5 |
| 760 | 1.6615 E–4 | 6.0000 E–5 | 0.0000 E–5 |
| 765 | 1.1741 E–4 | 4.2400 E–5 | 0.0000 E–5 |
| 770 | 8.3075 E–5 | 3.0000 E–5 | 0.0000 E–5 |
| 775 | 5.8707 E–5 | 2.1200 E–5 | 0.0000 E–5 |
| 780 | 4.1510 E–5 | 1.4990 E–5 | 0.0000 E–5 |
| 785 | 2.9353 E–5 | 1.0600 E–5 | 0.0000 E–5 |
| 790 | 2.0674 E–5 | 7.4657 E–6 | 0.0000 E–5 |
| 795 | 1.4560 E–5 | 5.2578 E–6 | 0.0000 E–5 |
| 800 | 1.0254 E–5 | 3.7029 E–6 | 0.0000 E–5 |
| 805 | 7.2215 E–6 | 2.6078 E–6 | 0.0000 E–5 |
| 810 | 5.0859 E–6 | 1.8366 E–6 | 0.0000 E–5 |
| 815 | 3.5817 E–6 | 1.2934 E–6 | 0.0000 E–5 |
| 820 | 2.5225 E–6 | 9.1093 E–7 | 0.0000 E–5 |
| 825 | 1.7765 E–6 | 6.4153 E–7 | 0.0000 E–5 |



Nichia Exhibit 1014
Page 119

## Appendix 17.2

Tabulated values of the CIE 1978 two-degree color-matching functions and eye sensitivity function for point sources (after CIE, 1978). The functions are also called the Judd–Vos-modified color-matching functions.

| λ (nm) | $\bar{x}(\lambda)$ ***red*** | $\bar{y} = V(\lambda)$ ***green*** | $\bar{z}(\lambda)$ ***blue*** |
|---|---|---|---|
| 380 | 2.6899E–3 | 2.0000E–4 | 1.2260E–2 |
| 385 | 5.3105E–3 | 3.9556E–4 | 2.4222E–2 |
| 390 | 1.0781E–2 | 8.0000E–4 | 4.9250E–2 |
| 395 | 2.0792E–2 | 1.5457E–3 | 9.5135E–2 |
| 400 | 3.7981E–2 | 2.8000E–3 | 1.7409E–1 |
| 405 | 6.3157E–2 | 4.6562E–3 | 2.9013E–1 |
| 410 | 9.9941E–2 | 7.4000E–3 | 4.6053E–1 |
| 415 | 1.5824E–1 | 1.1779E–2 | 7.3166E–1 |
| 420 | 2.2948E–1 | 1.7500E–2 | 1.0658 |
| 425 | 2.8108E–1 | 2.2678E–2 | 1.3146 |
| 430 | 3.1095E–1 | 2.7300E–2 | 1.4672 |
| 435 | 3.3072E–1 | 3.2584E–2 | 1.5796 |
| 440 | 3.3336E–1 | 3.7900E–2 | 1.6166 |
| 445 | 3.1672E–1 | 4.2391E–2 | 1.5682 |
| 450 | 2.8882E–1 | 4.6800E–2 | 1.4717 |
| 455 | 2.5969E–1 | 5.2122E–2 | 1.3740 |
| 460 | 2.3276E–1 | 6.0000E–2 | 1.2917 |
| 465 | 2.0999E–1 | 7.2942E–2 | 1.2356 |
| 470 | 1.7476E–1 | 9.0980E–2 | 1.1138 |
| 475 | 1.3287E–1 | 1.1284E–1 | 9.4220E–1 |
| 480 | 9.1944E–2 | 1.3902E–1 | 7.5596E–1 |
| 485 | 5.6985E–2 | 1.6987E–1 | 5.8640E–1 |
| 490 | 3.1731E–2 | 2.0802E–1 | 4.4669E–1 |
| 495 | 1.4613E–2 | 2.5808E–1 | 3.4116E–1 |
| 500 | 4.8491E–3 | 3.2300E–1 | 2.6437E–1 |
| 505 | 2.3215E–3 | 4.0540E–1 | 2.0594E–1 |
| 510 | 9.2899E–3 | 5.0300E–1 | 1.5445E–1 |
| 515 | 2.9278E–2 | 6.0811E–1 | 1.0918E–1 |
| 520 | 6.3791E–2 | 7.1000E–1 | 7.6585E–2 |
| 525 | 1.1081E–1 | 7.9510E–1 | 5.6227E–2 |
| 530 | 1.6692E–1 | 8.6200E–1 | 4.1366E–2 |
| 535 | 2.2768E–1 | 9.1505E–1 | 2.9353E–2 |
| 540 | 2.9269E–1 | 9.5400E–1 | 2.0042E–2 |
| 545 | 3.6225E–1 | 9.8004E–1 | 1.3312E–2 |
| 550 | 4.3635E–1 | 9.9495E–1 | 8.7823E–3 |
| 555 | 5.1513E–1 | 1.0000 | 5.8573E–3 |
| 560 | 5.9748E–1 | 9.9500E–1 | 4.0493E–3 |
| 565 | 6.8121E–1 | 9.7875E–1 | 2.9217E–3 |
| 570 | 7.6425E–1 | 9.5200E–1 | 2.2771E–3 |
| 575 | 8.4394E–1 | 9.1558E–1 | 1.9706E–3 |
| 580 | 9.1635E–1 | 8.7000E–1 | 1.8066E–3 |
| 585 | 9.7703E–1 | 8.1623E–1 | 1.5449E–3 |
| 590 | 1.0230 | 7.5700E–1 | 1.2348E–3 |
| 595 | 1.0513 | 6.9483E–1 | 1.1177E–3 |
| 600 | 1.0550 | 6.3100E–1 | 9.0564E–4 |
| 605 | 1.0362 | 5.6654E–1 | 6.9467E–4 |
| 610 | 9.9239E–1 | 5.0300E–1 | 4.2885E–4 |
| 615 | 9.2861E–1 | 4.4172E–1 | 3.1817E–4 |
| 620 | 8.4346E–1 | 3.8100E–1 | 2.5598E–4 |
| 625 | 7.3983E–1 | 3.2052E–1 | 1.5679E–4 |
| 630 | 6.3289E–1 | 2.6500E–1 | 9.7694E–5 |
| 635 | 5.3351E–1 | 2.1702E–1 | 6.8944E–5 |
| 640 | 4.4062E–1 | 1.7500E–1 | 5.1165E–5 |
| 645 | 3.5453E–1 | 1.3812E–1 | 3.6016E–5 |
| 650 | 2.7862E–1 | 1.0700E–1 | 2.4238E–5 |
| 655 | 2.1485E–1 | 8.1652E–2 | 1.6915E–5 |
| 660 | 1.6161E–1 | 6.1000E–2 | 1.1906E–5 |
| 665 | 1.1820E–1 | 4.4327E–2 | 8.1489E–6 |
| 670 | 8.5753E–2 | 3.2000E–2 | 5.6006E–6 |
| 675 | 6.3077E–2 | 2.3454E–2 | 3.9544E–6 |
| 680 | 4.5834E–2 | 1.7000E–2 | 2.7912E–6 |
| 685 | 3.2057E–2 | 1.1872E–2 | 1.9176E–6 |
| 690 | 2.2187E–2 | 8.2100E–3 | 1.3135E–6 |
| 695 | 1.5612E–2 | 5.7723E–3 | 9.1519E–7 |
| 700 | 1.1098E–2 | 4.1020E–3 | 6.4767E–7 |
| 705 | 7.9233E–3 | 2.9291E–3 | 4.6352E–7 |
| 710 | 5.6531E–3 | 2.0910E–3 | 3.3304E–7 |
| 715 | 4.0039E–3 | 1.4822E–3 | 2.3823E–7 |
| 720 | 2.8253E–3 | 1.0470E–3 | 1.7026E–7 |
| 725 | 1.9947E–3 | 7.4015E–4 | 1.2207E–7 |
| 730 | 1.3994E–3 | 5.2000E–4 | 8.7107E–8 |
| 735 | 9.6980E–4 | 3.6093E–4 | 6.1455E–8 |
| 740 | 6.6847E–4 | 2.4920E–4 | 4.3162E–8 |
| 745 | 4.6141E–4 | 1.7231E–4 | 3.0379E–8 |
| 750 | 3.2073E–4 | 1.2000E–4 | 2.1554E–8 |
| 755 | 2.2573E–4 | 8.4620E–5 | 1.5493E–8 |
| 760 | 1.5973E–4 | 6.0000E–5 | 1.1204E–8 |
| 765 | 1.1275E–4 | 4.2446E–5 | 8.0873E–9 |
| 770 | 7.9513E–5 | 3.0000E–5 | 5.8340E–9 |
| 775 | 5.6087E–5 | 2.1210E–5 | 4.2110E–9 |
| 780 | 3.9541E–5 | 1.4989E–5 | 3.0383E–9 |
| 785 | 2.7852E–5 | 1.0584E–5 | 2.1907E–9 |
| 790 | 1.9597E–5 | 7.4656E–6 | 1.5778E–9 |
| 795 | 1.3770E–5 | 5.2592E–6 | 1.1348E–9 |
| 800 | 9.6700E–6 | 3.7028E–6 | 8.1565E–10 |
| 805 | 6.7918E–6 | 2.6076E–6 | 5.8626E–10 |
| 810 | 4.7706E–6 | 1.8365E–6 | 4.2138E–10 |
| 815 | 3.3550E–6 | 1.2950E–6 | 3.0319E–10 |
| 820 | 2.3534E–6 | 9.1092E–7 | 2.1753E–10 |
| 825 | 1.6377E–6 | 6.3564E–7 | 1.5476E–10 |

# 18

## Planckian sources and color temperature

White light is a unique color. There are a very large number of optical spectra that can be used to generate white light. Among these spectra, the planckian black-body radiation spectrum forms a unique and very useful standard because it allows us to describe the spectrum with only one parameter, namely the color temperature. Furthermore, natural daylight closely resembles the planckian spectrum.

### *18.1 The solar spectrum*

White light usually has a broad spectrum extending over the entire visible range. An instructive model for white light is sunlight. The sun's optical spectrum is shown in Fig. 18.1, including the spectrum at sea level with the sun at zenith, incident above the earth's atmosphere, and at sunset and sunrise (Jackson, 1975). The spectrum of sunlight extends over the entire visible region. However, the sun's spectrum depends on the time of day, season, altitude, weather, and other factors.

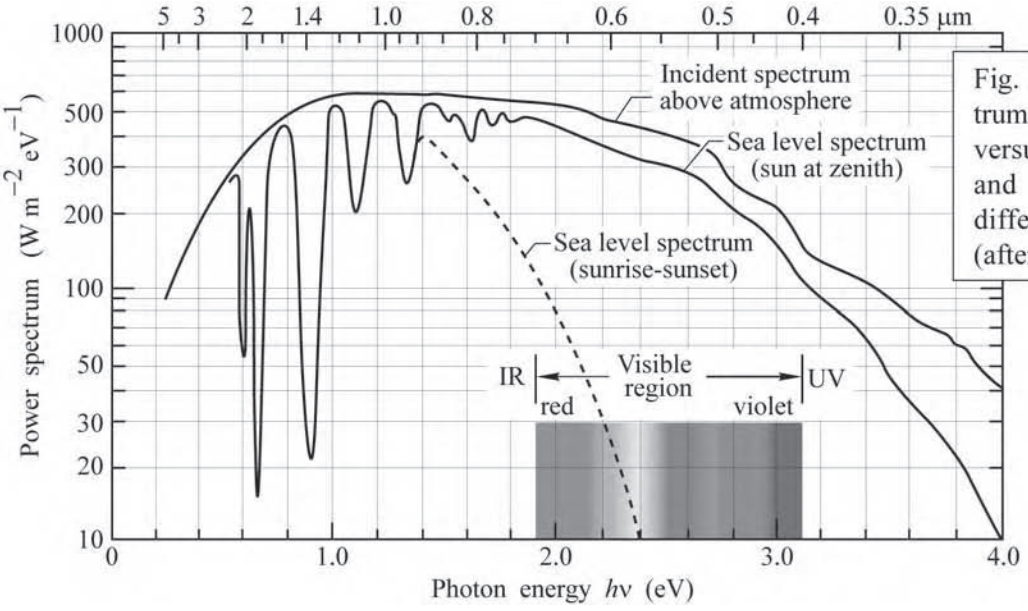


Fig. 18.1. Power spectrum of solar radiation versus photon energy and wavelength for different conditions (after Jackson, 1975).



Nichia Exhibit 1014
Page 121

Exact replication of the solar spectrum for white-light illumination sources would not yield an efficient source due to the large infrared (IR) and ultraviolet (UV) components of the solar spectrum. Thus, "mother nature" does not serve as a good example for an efficient white source. Even if the IR and UV components of the spectrum were to be eliminated, the solar spectrum still would not be optimum, due to the high intensity at the visible-IR and visible-UV boundaries.

### *18.2 The planckian spectrum*

It is desirable to define an independent standard for white light. The ***planckian black-body radiation spectrum*** is used as one such standard. The black-body spectrum is characterized by only one parameter, the temperature of the body. The black-body spectrum was first derived by Max Planck (1900) and is given by

$$I(\lambda) = \frac{2hc^2}{\lambda^5\left[\exp\left(\frac{hc}{\lambda kT}\right) - 1\right]}. \qquad (18.1)$$

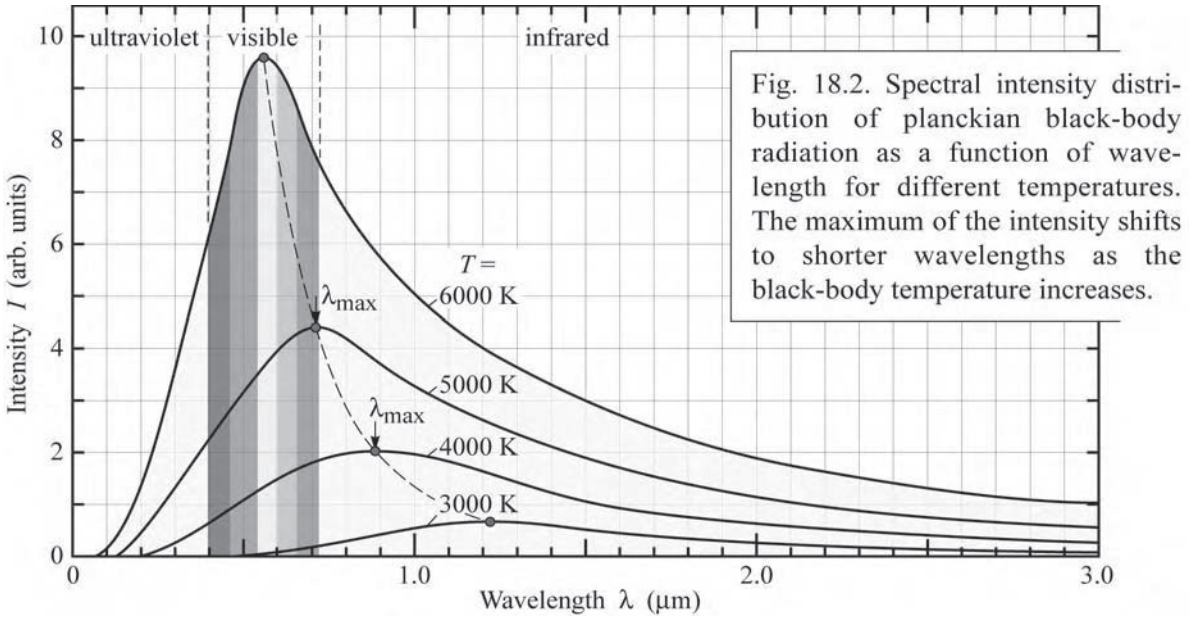


Fig. 18.2. Spectral intensity distribution of planckian black-body radiation as a function of wavelength for different temperatures. The maximum of the intensity shifts to shorter wavelengths as the black-body temperature increases.

The planckian spectrum is shown for different black-body temperatures in Fig. 18.2. The maximum intensity of radiation emanating from a black body of temperature $T$ occurs at a specific wavelength which is given by ***Wien's law***

$$\lambda_{max} = \frac{2880\ \mu m\ K}{T} . \qquad (18.2)$$

At "low" black-body temperatures, e.g. 3 000 K, the radiation occurs mostly in the infrared. As the temperature increases, the maximum of the radiation shifts into the visible wavelength range.

The location of the black-body radiation in the ($x$, $y$) chromaticity diagram (called planckian locus) is shown in Fig. 18.3. As the temperature of the black body increases, the chromaticity location moves from the red wavelength range towards the center of the diagram. Typical black-body temperatures in the white region of the chromaticity diagram range between 2 500 and 10 000 K. Also shown in Fig. 18.3 are the locations of several illuminants standardized by the CIE. These standard illuminants include Illuminants A, B, C, $D_{65}$, and E. The planckian locus and the locations of the black-body temperatures in the ($u'$, $v'$) uniform chromaticity diagram are shown in Fig. 18.4. The ($x$, $y$) and in ($u'$, $v'$) chromaticity coordinates of the planckian radiator are tabulated in Appendix 18.1.

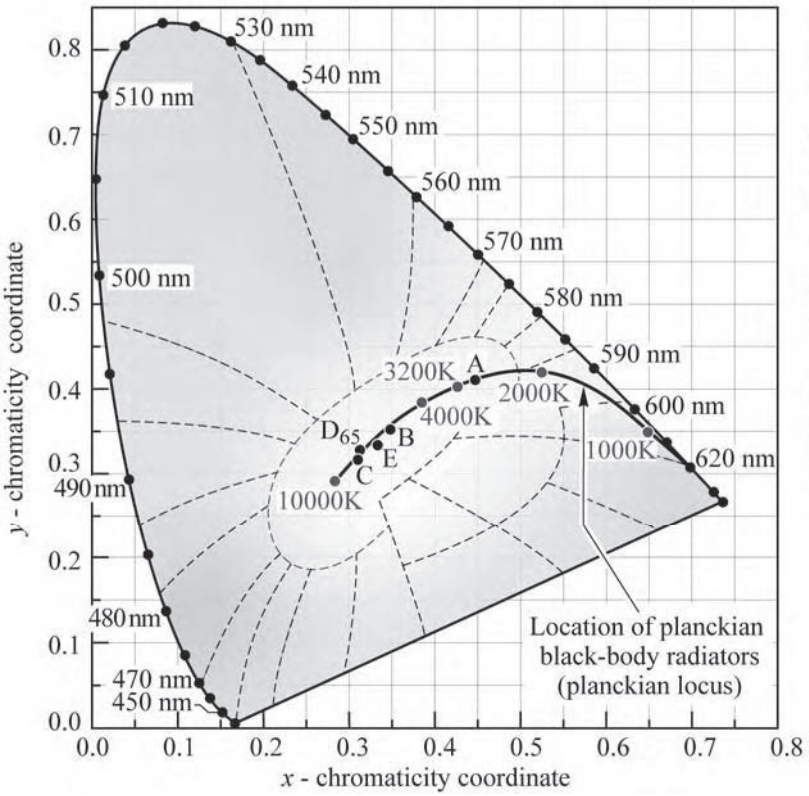


Illuminant A
($x$, $y$) = (0.4476, 0.4074)
(Incandescent source, $T$ = 2856 K)

Illuminant B
($x$, $y$) = (0.3484, 0.3516)
(Direct sunlight, $T$ = 4870 K)

Illuminant C
($x$, $y$) = (0.3101, 0.3162)
(Overcast source, $T$ = 6770 K)

Illuminant $D_{65}$
($x$, $y$) = (0.3128, 0.3292)
(Daylight, $T$ = 6500 K)

Illuminant E (equal-energy point)
($x$, $y$) = (0.3333, 0.3333)

Fig. 18.3. Chromaticity diagram showing planckian locus, the standardized white Illuminants A, B, C, $D_{65}$, and E, and their color temperatures (after CIE, 1978).

In both the ($x$, $y$) and the ($u'$, $v'$) chromaticity diagrams, the planckian locus starts out in the red, then moves through the orange and yellow, to finally the white region. This sequence of colors is reminiscent of the colors of a real object (e.g. a piece of metal) heated to high



Nichia Exhibit 1014
Page 123

temperatures, indicating that real objects closely follow the chromaticity of Planck's idealized black bodies.

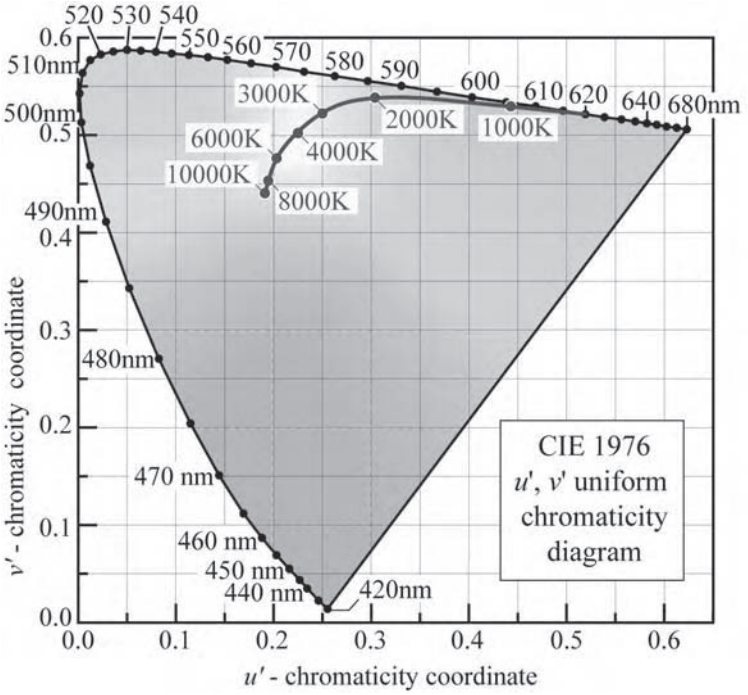


Fig. 18.4. CIE 1976 ($u'$, $v'$) uniform chromaticity diagram calculated using the CIE 1931 2° standard observer and planckian locus.

### *18.3 Color temperature and correlated color temperature*

*Color temperature* may appear to be a somewhat surprising quantity as *color* and *temperature* don't seem to have a direct relationship with each other. However, the relationship is derived from Planck's black-body radiator. With increasing temperatures, it glows in the red, orange, yellowish white, white, and ultimately bluish white. The ***color temperature*** (CT) of a white light source, given in units of kelvin, is the temperature of a planckian black-body radiator that has the same chromaticity location as the white light source considered.

If the color of a white light source does not fall on the planckian locus, the ***correlated color temperature*** (CCT), also given in units of kelvin, is used. The correlated color temperature of a white light source is defined as the temperature of a planckian black-body radiator whose color is closest to the color of the white light source.

The correlated color temperature of a light source is determined as follows. On the ($u'$, $v'$) uniform chromaticity diagram, the point on the planckian locus that is *closest* to the chromaticity location of the light source is determined (i.e. shortest geometrical distance). The correlated color temperature is the temperature of the planckian black-body radiator at that point. The

determination of the correlated color temperature was discussed in CIE publication No. 17.4 (1987) and by Robertson (1968).

On the ($x$, $y$) chromaticity diagram, the correlated color temperature *cannot* be determined by using the shortest distance to the planckian locus due to the non-uniformity of the ($x$, $y$) chromaticity diagram. The lines of constant correlated color temperature in the ($x$, $y$) chromaticity diagram are shown in Fig. 18.5 (Duggal, 2005).

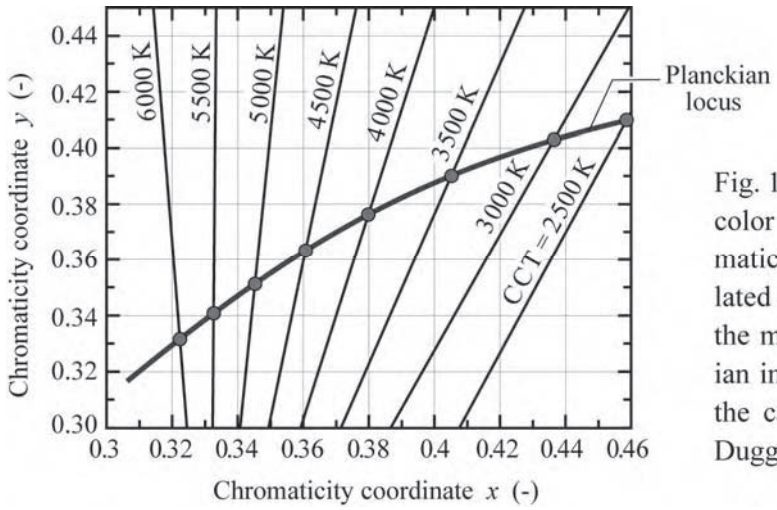


Fig. 18.5. Lines of constant correlated color temperature in the ($x$, $y$) chromaticity diagram. Whereas the correlated color temperature follows from the minimum distance to the planckian in the ($u'$, $v'$) diagram, this is not the case in the ($x$, $y$) diagram (after Duggal, 2005).

Table 18.1. Correlated color temperatures of common artificial and natural light sources.

| **Light source** | **Correlated color temperature (K)** |
|---|---|
| Wax candle flame / CIE standard candle flame | 1 500 to 2 000 / 2 000 |
| W filament household lamp: 60 W / 100 W | 2 800 / 2 850 |
| W filament halogen lamp | 2 800 to 3 200 |
| “Warm white” fluorescent tube | 3 000 |
| “Cool daylight white” fluorescent tube | 4 300 |
| “True daylight” color match fluorescent tube | 6 500 |
| Carbon arc white flame | 5 000 |
| Xenon arc (unfiltered) | 6 000 |
| Summer sunlight (before 9.00 or after 15.00 h) | 4 900 to 5 600 |
| Summer sunlight (9.00 to 15.00 h) | 5 400 to 5 700 |
| Direct sun | 5 700 to 6 500 |
| Overcast daylight | 6 500 to 7 200 |
| Clear blue sky | 8 000 to 27 000 |



Nichia Exhibit 1014
Page 125

The chromaticity locations of incandescent light sources are very close to, although not exactly on the planckian locus (Ohno, 2001). For such incandescent light sources, the *color temperature* can be specified. Standard incandescents have color temperatures ranging from 2 000 to 2 900 K. The common warm incandescent light source has a color temperature of 2 800 K. Quartz halogen incandescent lamps have a color temperature ranging from 2 800 to 3 200 K (Ohno, 1997). Other light sources, such as metal-halide sources, are further removed from the planckian locus. For such light sources, the *correlated color temperature* should be used. Bluish white lights have a correlated color temperature of about 8 000 K. Color temperatures and correlated color temperatures of common artificial and natural light sources are given in Table 18.1.

## *References*

CIE publication No. 17.4 *International Lighting Vocabulary* see http://www.cie.co.at (CIE, Vienna, Austria, 1987)

Duggal A. R. "Organic electroluminescent devices for solid-state lighting" in *Organic Electroluminescence* edited by Z. H. Kafafi (Taylor & Francis Group, Boca Raton, Florida, 2005)

Jackson J. D. *Classical Electrodynamics* (John Wiley and Sons, New York, 1975)

Ohno Y. "Photometric standards" Chapter 3 in *OSA/AIP Handbook of Applied Photometry*, 55 (Optical Society of America, Washington DC, 1997)

Ohno Y. "Photometry and radiometry" Chapter 14 in *OSA Handbook of Optics*, *Volume III Review for Vision Optics, Part 2, Vision Optics* (McGraw-Hill, New York, 2001)

Planck M. "On the theory of the law on energy distribution in the normal spectrum (translated from German)" *Verhandlungen der Deutschen Physikalischen Gesellschaft* **2**, 237 (1900)

Robertson R. "Computation of correlated color temperature and distribution temperature" *J. Opt. Soc. Am*. **58**, 1528 (1968)

**Appendix 18.1**

Color temperature $T$ and $(x, y)$ and $(u', v')$ chromaticity coordinates of a planckian emitter.

| $T$ | $x$ | $y$ | $u'$ | $v'$ |
|---|---|---|---|---|
| 1 000 K | 0.649 | 0.347 | 0.443 | 0.533 |
| 1 200 K | 0.623 | 0.370 | 0.402 | 0.538 |
| 1 400 K | 0.597 | 0.389 | 0.369 | 0.541 |
| 1 600 K | 0.572 | 0.402 | 0.342 | 0.542 |
| 1 800 K | 0.549 | 0.412 | 0.321 | 0.542 |
| 2 000 K | 0.527 | 0.417 | 0.303 | 0.540 |
| 2 200 K | 0.506 | 0.420 | 0.288 | 0.538 |
| 2 400 K | 0.487 | 0.419 | 0.276 | 0.535 |
| 2 600 K | 0.470 | 0.417 | 0.266 | 0.531 |
| 2 800 K | 0.454 | 0.414 | 0.257 | 0.528 |
| 3 000 K | 0.439 | 0.409 | 0.250 | 0.524 |
| 3 200 K | 0.425 | 0.404 | 0.243 | 0.520 |
| 3 400 K | 0.413 | 0.399 | 0.237 | 0.516 |
| 3 600 K | 0.402 | 0.393 | 0.233 | 0.512 |
| 3 800 K | 0.392 | 0.388 | 0.228 | 0.508 |
| 4 000 K | 0.383 | 0.382 | 0.225 | 0.504 |
| 4 200 K | 0.374 | 0.376 | 0.221 | 0.500 |
| 4 400 K | 0.367 | 0.371 | 0.218 | 0.497 |
| 4 600 K | 0.360 | 0.366 | 0.216 | 0.494 |
| 4 800 K | 0.353 | 0.361 | 0.213 | 0.490 |
| 5 000 K | 0.347 | 0.356 | 0.211 | 0.487 |
| 5 200 K | 0.342 | 0.351 | 0.209 | 0.484 |
| 5 400 K | 0.337 | 0.347 | 0.208 | 0.481 |
| 5 600 K | 0.332 | 0.343 | 0.206 | 0.479 |
| 5 800 K | 0.328 | 0.339 | 0.205 | 0.476 |
| 6 000 K | 0.324 | 0.335 | 0.203 | 0.473 |
| 6 200 K | 0.321 | 0.332 | 0.202 | 0.471 |
| 6 400 K | 0.317 | 0.328 | 0.201 | 0.469 |
| 6 500 K | 0.315 | 0.327 | 0.201 | 0.468 |
| 6 600 K | 0.314 | 0.325 | 0.200 | 0.466 |
| 6 800 K | 0.311 | 0.322 | 0.199 | 0.464 |
| 7 000 K | 0.308 | 0.319 | 0.198 | 0.462 |
| 7 200 K | 0.306 | 0.317 | 0.198 | 0.460 |
| 7 400 K | 0.303 | 0.314 | 0.197 | 0.459 |
| 7 600 K | 0.301 | 0.312 | 0.196 | 0.457 |
| 7 800 K | 0.299 | 0.309 | 0.196 | 0.455 |
| 8 000 K | 0.297 | 0.307 | 0.195 | 0.454 |
| 8 500 K | 0.292 | 0.301 | 0.194 | 0.450 |
| 9 000 K | 0.289 | 0.297 | 0.193 | 0.447 |
| 9 500 K | 0.285 | 0.293 | 0.192 | 0.444 |
| 10 000 K | 0.282 | 0.290 | 0.191 | 0.441 |



Nichia Exhibit 1014
Page 127

# 19

## Color mixing and color rendering

### *19.1 Additive color mixing*

The *combination* or *additive mixing* of two or more light sources is employed in a number of applications. In LED displays, three different types of LEDs, usually emitting in the red, green, and blue, are used. The three colors are mixed so that the observer can experience a wide range of colors. Another useful application of color mixing is the generation of white light by two, three, or more complementary colors. A schematic of additive color mixing and a corresponding experiment are shown in Fig. 19.1.

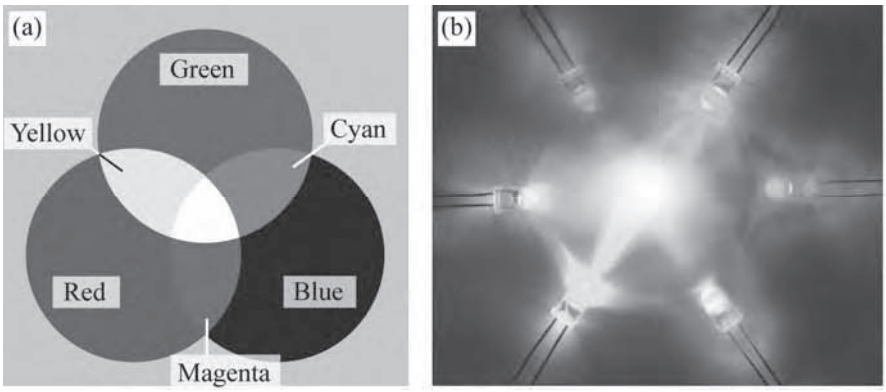


Fig. 19.1. (a) Schematic of additive color mixing of three primary colors. (b) Additive color mixing using LEDs.

Next, we determine the chromaticity coordinates of the mixture of three discrete emission bands. Assume that the three emission bands have spectral power densities $P_1(\lambda)$, $P_2(\lambda)$, and $P_3(\lambda)$ with peak wavelengths of $\lambda_1$, $\lambda_2$, $\lambda_3$, respectively. We assume that each emission band is much narrower than any of the three color-matching functions. We further assume that the three light sources have the chromaticity coordinates $(x_1, y_1)$, $(x_2, y_2)$, and $(x_3, y_3)$. Then the tristimulus values are given by

$$X = \int_\lambda \bar{x}(\lambda) P_1(\lambda)\,\mathrm{d}\lambda + \int_\lambda \bar{x}(\lambda) P_2(\lambda)\,\mathrm{d}\lambda + \int_\lambda \bar{x}(\lambda) P_3(\lambda)\,\mathrm{d}\lambda \approx \bar{x}(\lambda_1) P_1 + \bar{x}(\lambda_2) P_2 + \bar{x}(\lambda_3) P_3 \quad (19.1)$$

$$Y = \int_\lambda \bar{y}(\lambda)\, P_1(\lambda)\, \mathrm{d}\lambda + \int_\lambda \bar{y}(\lambda)\, P_2(\lambda)\, \mathrm{d}\lambda + \int_\lambda \bar{y}(\lambda)\, P_3(\lambda)\, \mathrm{d}\lambda \approx \bar{y}(\lambda_1)\, P_1 + \bar{y}(\lambda_2)\, P_2 + \bar{y}(\lambda_3)\, P_3 \quad (19.2)$$

$$Z = \int_\lambda \bar{z}(\lambda)\, P_1(\lambda)\, \mathrm{d}\lambda + \int_\lambda \bar{z}(\lambda)\, P_2(\lambda)\, \mathrm{d}\lambda + \int_\lambda \bar{z}(\lambda)\, P_3(\lambda)\, \mathrm{d}\lambda \approx \bar{z}(\lambda_1)\, P_1 + \bar{z}(\lambda_2)\, P_2 + \bar{z}(\lambda_3)\, P_3 \quad (19.3)$$

where $P_1$, $P_2$, and $P_3$ are the optical powers emitted by the three sources. Using the abbreviations

$$L_1 = \bar{x}(\lambda_1)\, P_1 + \bar{y}(\lambda_1)\, P_1 + \bar{z}(\lambda_1)\, P_1 \quad (19.4)$$

$$L_2 = \bar{x}(\lambda_2)\, P_2 + \bar{y}(\lambda_2)\, P_2 + \bar{z}(\lambda_2)\, P_2 \quad (19.5)$$

$$L_3 = \bar{x}(\lambda_3)\, P_3 + \bar{y}(\lambda_3)\, P_3 + \bar{z}(\lambda_3)\, P_3 \quad (19.6)$$

the chromaticity coordinates of the mixed light can be calculated from the tristimulus values to yield

$$x = \frac{x_1 L_1 + x_2 L_2 + x_3 L_3}{L_1 + L_2 + L_3} \quad (19.7)$$

$$y = \frac{y_1 L_1 + y_2 L_2 + y_3 L_3}{L_1 + L_2 + L_3}\,. \quad (19.8)$$

Thus, the chromaticity coordinate of the multi-component light *is a linear combination of the individual chromaticity coordinates* weighted by the $L_i$ factors.

The principle of color mixing in the chromaticity diagram is shown in Fig. 19.2. The figure shows the mixing of *two* colors with chromaticity coordinates $(x_1, y_1)$ and $(x_2, y_2)$. For the case of two colors, $L_3 = P_3 = 0$. The mixed color will be located on the straight line connecting the chromaticity coordinates of the two light sources. Thus *any* color (including white) located between the two chromaticity points can be created by mixing the two colors.

Figure 19.2 also shows the mixing of *three* colors, located in the red, green, and blue regions of the chromaticity diagram. The three chromaticity points, connected by a dashed line, are typical points for red, green, and blue LEDs. The area located within the dashed line, called the ***color gamut***, represents all colors that can be created by mixing the three primary colors red, green, and blue. The ability to create a great variety of colors is an important quality for displays. It is desirable that the color gamut provided by the three light sources is as large as possible to create displays able to show brilliant, saturated colors.

The color gamut represents the entire range of colors that can be created from a set of



Nichia Exhibit 1014
Page 129

primary sources. Color gamuts are polygons positioned within the perimeter of the chromaticity diagram. For the case of *three* primary colors, the color gamut is a *triangle*, as shown in Fig. 19.2. All colors created by additive mixtures of the vertex points (primary colors) of a gamut, are necessarily located inside the gamut.

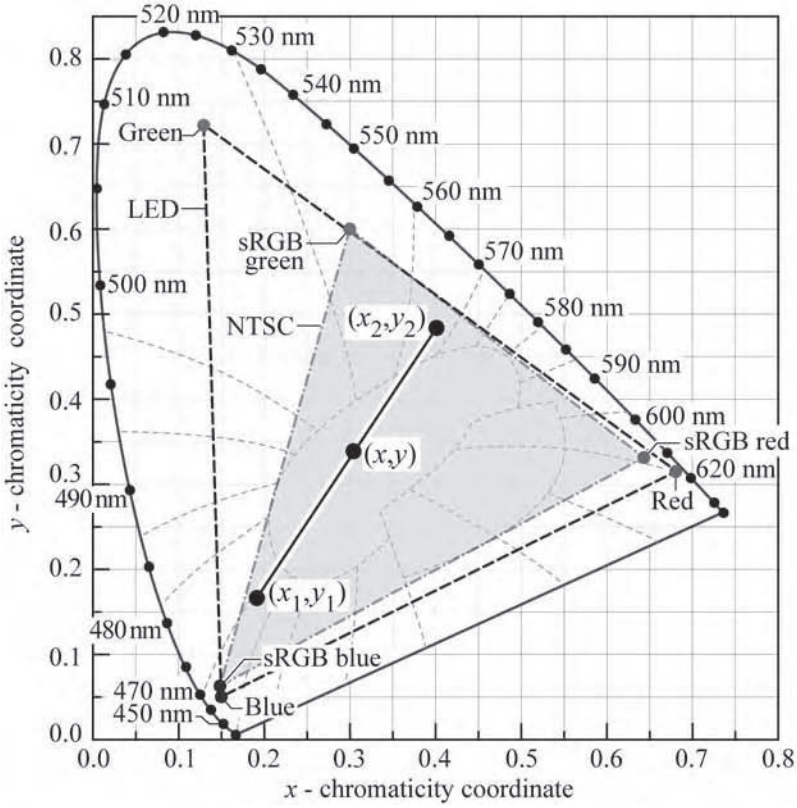


Fig. 19.2. Principle of color mixing illustrated with two light sources with chromaticity coordinates $(x_1, y_1)$ and $(x_2, y_2)$. The resulting color has the coordinates $(x, y)$. Also shown is the triangular area of the chromaticity diagram (color gamut) accessible by additive mixing of a red, green, and blue LED. The locations of the red, green, and blue phosphors of the sRGB display standard ($x_r = 0.64$, $y_r = 0.33$, $x_g = 0.30$, $y_g = 0.60$, $x_b = 0.15$, $y_b = 0.06$) are also shown. The sRGB standard is similar to the NTSC standard.

The insight now gained on color mixing allows one to understand the location of different LEDs in the chromaticity diagram. The perimeter of the chromaticity diagram in the red spectral region is approximately a *straight line*, so that red LEDs, despite their thermal broadening, are located directly on the perimeter of the chromaticity diagram. In contrast, the perimeter is strongly curved in the green region, so that green LEDs, due to their spectral broadening, are displaced from the perimeter towards the center of the chromaticity diagram.

## *19.2 Color rendering*

Another important characteristic of a white light source is its ability to show (i.e. render) the true colors of physical objects, e.g. fruits, plants, or toys, that are being illuminated by the source. The ability to render the colors of an object is measured in terms of the ***color-rendering index*** or ***CRI*** (Wyszecki and Stiles, 1982, 2000; MacAdam, 1993; Berger-Schunn, 1994; CIE, 1995). It is

a measure of the ability of the *illuminant* (i.e. a white illumination source) to faithfully render the colors of physical objects illuminated by the source.

Figure 19.3 shows an example of a physical object (here a painting by the impressionist Auguste Renoir) under illumination with a high-CRI source and with a low-CRI source. Colors appear richer and more vivid under illumination with a high-CRI source. Whereas high color rendering is important in locations such as museums, homes, and offices, it is less so in locations such as streets and parking lots. Finally, the color-rendering index is irrelevant for white light sources used in indicator lamp and signage applications.

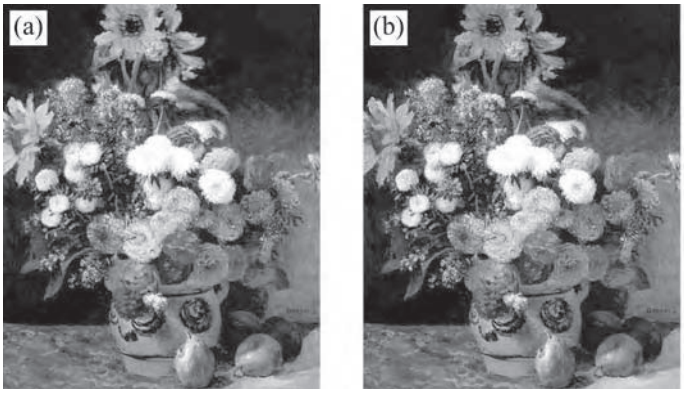


Fig. 19.3. Artwork entitled "Fleurs dans un vase" illuminated with (a) high-CRI source and (b) low-CRI source (Auguste Renoir, French impressionist, 1841–1919) .

The color-rendering ability of a ***test light source*** (to be abbreviated as ***test source***) is evaluated by comparing it with the color-rendering ability of a ***reference light source*** (to be abbreviated as ***reference source***). For the calculation of the CRI, the reference source is chosen as follows (CIE, 1995): (*i*) If the chromaticity point of the test source is located *on* the planckian locus, the reference source is a planckian black-body radiator with the same color temperature as the test source. (*ii*) If the chromaticity point of the test source is located *off* the planckian locus, the reference source is a planckian black-body radiator with the same *correlated* color temperature as the test source. (*iii*) Alternatively, one of the standardized CIE illuminants (e.g. Illuminant $D_{65}$) can be used as a reference source (CIE, 1995). Ideally, the test source and the reference source have the same chromaticity coordinates and luminous flux.

By convention, the planckian black-body reference source is assumed to have perfect color-rendering properties and thus its color-rendering index is CRI = 100. This convention was agreed upon because natural daylight closely resembles a planckian black-body source and thus rightfully deserves to be established as the standard reference source. Illuminants other than the reference source necessarily have a color-rendering index lower than 100. Because the CRI depends sensitively on the choice of the reference source, the selection of the reference source is



Nichia Exhibit 1014
Page 131

of critical importance when calculating the CRIs of test sources.

Because the emission spectrum of an incandescent lamp closely follows that of a planckian black-body radiator, such lamps have the highest possible CRI and thus the best color-rendering properties of all artificial light sources. Incandescent quartz-halogen lamps are used in locations where color rendering is of prime importance, such as in museums, art galleries, and clothing shops. The drawback of quartz-halogen lamps is high power consumption.

In addition to the test source and the reference source, ***test-color samples*** are instrumental in determining the CRI of a test source. Test-color samples could be derived from real objects, e.g. fruit, flowers, wood, furniture, and clothes. However, in the interest of international standardization, a specific set of 14 test-color samples has been agreed upon for the purpose of determining the CRI. These 14 test-color samples are a subset of a larger collection of test-color samples initially introduced by Albert H. Munsell, a professor who taught at Rochester Institute of Technology (Rochester, NY) in the late 1800s and early 1900s (Munsell, 1905; 2005; Billmeyer, 1987; Long and Luke, 2001). Munsell introduced a color notation – the ***Munsell color system*** – which is a notation for defining a very wide range of colors.

The CRI calculation has been discussed in detail by Wyszecki and Stiles (1982; 2000) and by CIE (1995). The ***CIE general CRI*** is an average calculated according to

$$\mathrm{CRI}_{\mathrm{general}} \;=\; \frac{1}{8}\,\sum_{i=1}^{8}\,\mathrm{CRI}_i \tag{19.9}$$

where the $\mathrm{CRI}_i$ are the ***special CRIs*** for a set of eight test-color samples. The special color-rendering indices are calculated according to

$$\mathrm{CRI}_i \;=\; 100 \;-\; 4.6\,\Delta E_i^* \tag{19.10}$$

where $\Delta E_i^*$ represents the quantitative color change that occurs when a test-color sample is illuminated with, first, the reference illumination source ("reference source"), and subsequently with the test illumination source ("test source"). The special color-rendering indices are calculated in such a way that they have a value of 100 if there is no difference in color appearance. The quantitative color change, $\Delta E_i^*$, plays a key role in the calculation of the CRI and the determination of $\Delta E_i^*$ will be discussed in detail in the two subsequent sections where we will differentiate between on-planckian-locus and off-planckian-locus test sources.

At the time Eq. (19.10) was established, the pre-factor 4.6 had been chosen in such a way

that the general CRI equals 60 when a "standard warm white" fluorescent lamp was used as a test source and a planckian black-body radiator was used as a reference source. Current fluorescent light sources have higher CRIs, typically in the range 60–85 (Kendall and Scholand, 2001).

The test-color samples mentioned above are defined in terms of their spectral reflectivity. The reflectivity curves of eight internationally agreed-upon test-color samples are shown in Fig. 19.4. The numerical values of the reflectivity of the eight test-color samples are listed in Appendix 19.1. The general color-rendering index is calculated from these eight test-color samples ($i$ = 1–8).

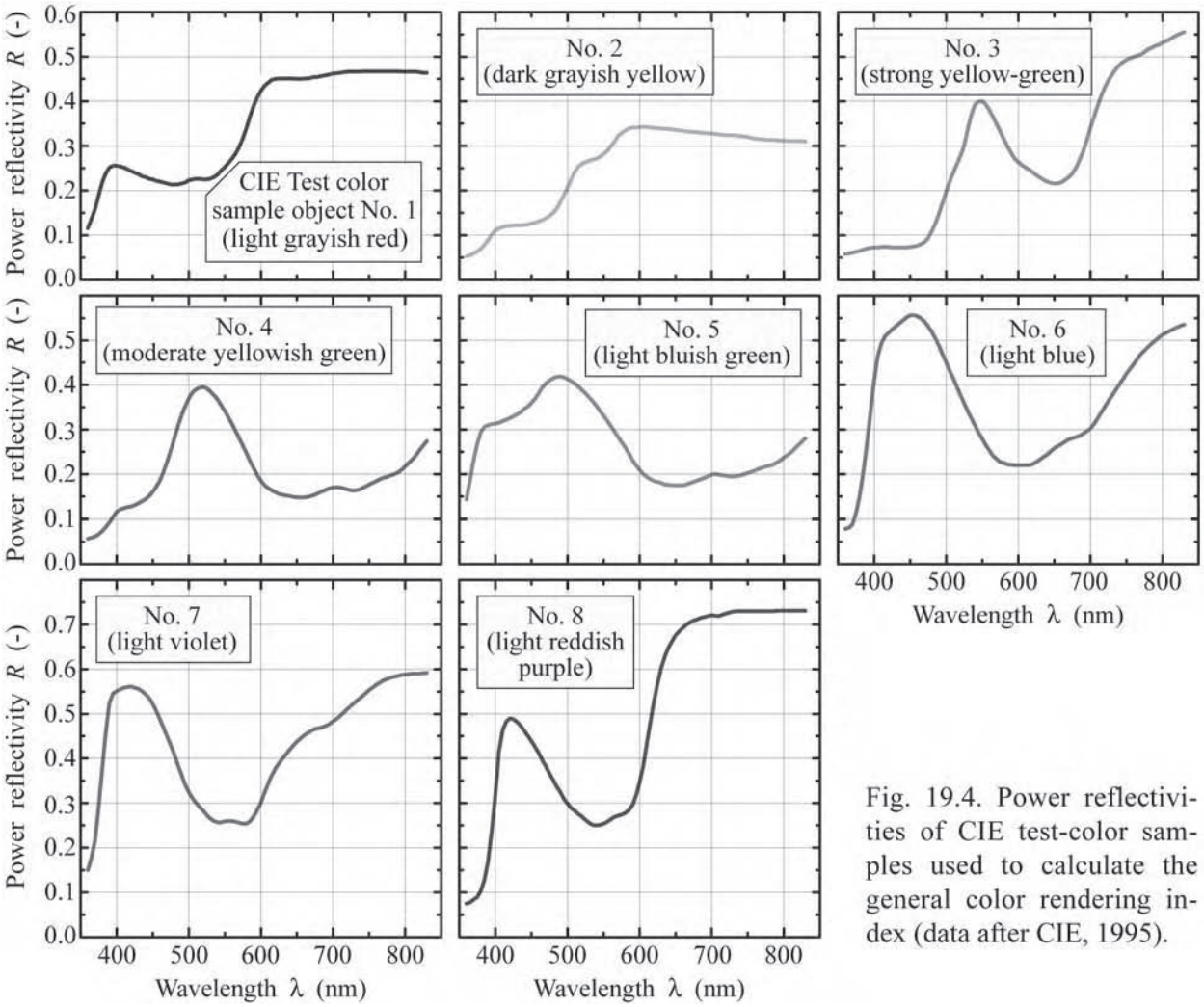


Fig. 19.4. Power reflectivities of CIE test-color samples used to calculate the general color rendering index (data after CIE, 1995).

In addition to the test-color samples (with numbers 1–8) used to calculate the *general* color rendering index, six supplemental test-color samples (with numbers 9–14) are used to further assess the color rendering capabilities of test sources. These supplemental test-color samples



Nichia Exhibit 1014
Page 133

have the following colors: 9 – strong red; 10 – strong yellow; 11 – strong green; 12 – strong purplish blue; 13 – complexion of white person; 14 – leaf of tree. The reflectivity spectra and the numerical values of the reflectivity of the supplemental test-color samples are given in Fig. 19.5 and in Appendix 19.2, respectively. Inspection of the reflectivity curves reveals that the colors of the test-color samples 9–14 have particularly strong colors with relatively narrow peaks. $CRI_9$ to $CRI_{14}$ are referred to as the ***special color-rendering indices 9–14***.

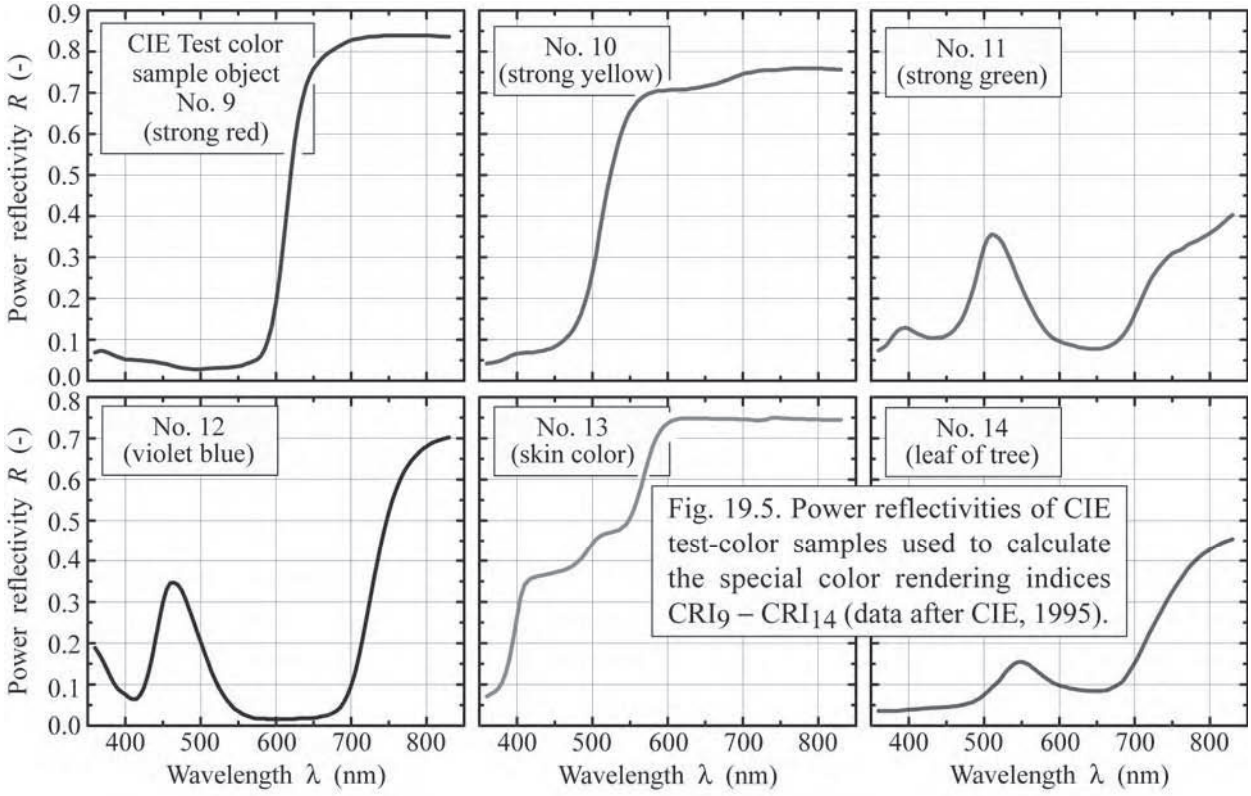


Fig. 19.5. Power reflectivities of CIE test-color samples used to calculate the special color rendering indices $CRI_9 - CRI_{14}$ (data after CIE, 1995).

The meaning of *chromaticity difference* of a test and a reference illumination source and the rendered colors of a test-color sample, when illuminated with the test and reference illumination sources, is illustrated in Fig. 19.6. In the example shown in the figure, the test source is located slightly off the planckian locus. The reference source is a planckian source with the least possible distance from the test-source chromaticity point. As a result, the color temperature of the reference source is equal to the correlated color temperature of the test source. The four chromaticity points shown in Fig. 19.6 enter the calculation of the CRI.

Note, however, that the term “color” as used by the CIE, is not equal to “chromaticity”. The broad CIE definition for color includes hue, saturation, and additionally, brightness (for light) or lightness (for physical objects). Whereas hue and saturation are fully defined by location in the

chromaticity coordinate system, brightness and lightness are not. To allow for a graphical representation of object lightness (or source brightness) a third axis could be added to the chromaticity diagram, as done for illustrative purposes in Fig. 19.7. The *color difference* of a physical object when illuminated with, first, a reference source, and subsequently with a test source, thus consists of the *chromaticity difference* and the *lightness difference*, as represented by the geometrical distance of the two points shown in Fig. 19.7. The reader is cautioned that the representation shown in Fig. 19.7 is for educational purposes and not a standardized CIE representation.

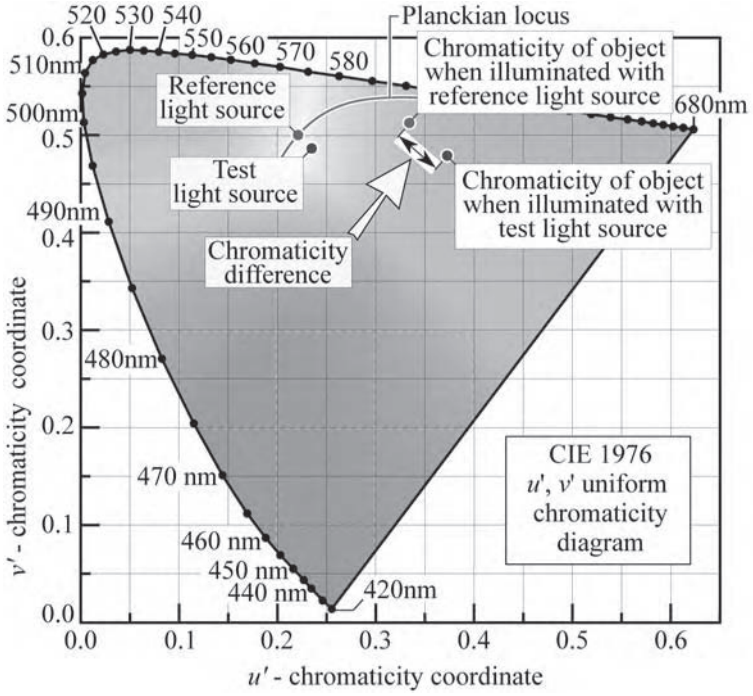


Fig. 19.6. Chromaticity difference resulting from the illumination of an object with a reference and a test light source. In the CIE 1976 $u'$, $v'$ uniform chromaticity diagram, the chromaticity difference is directly proportional to the geometric distance. The reference light source is located on the planckian locus at the correlated color temperature of the test light source.

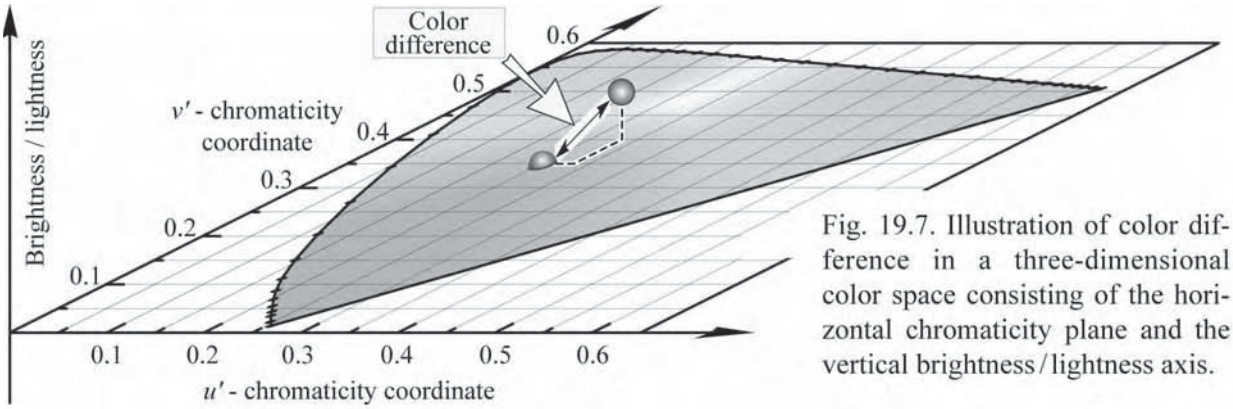


Fig. 19.7. Illustration of color difference in a three-dimensional color space consisting of the horizontal chromaticity plane and the vertical brightness/lightness axis.



Nichia Exhibit 1014
Page 135

A ***uniform color space*** (CIE, 1986) is motivated by the need for a quantitative color space that includes chromaticity and brightness/lightness. This uniform color space provides direct proportionality between color difference and geometrical distance. Thus color differences can be directly related to geometric distances between two points in the uniform color space. The CIE has introduced two three-dimensional uniform color spaces, namely the ($L^*$, $u^*$, $v^*$) and ($L^*$, $a^*$, $b^*$) spaces (CIE, 1986; Wyszecki and Stiles, 2000). For our purposes, it will be sufficient to consider the ($L^*$, $u^*$, $v^*$) uniform color space and we will therefore restrict our considerations to this space. The CIE ($L^*$, $u^*$, $v^*$) uniform color space is a three-dimensional space with cartesian coordinates, two coordinates being associated primarily with the chromaticity ($u^*$, $v^*$), and the third coordinate, $L^*$, representing the brightness (of a source) or lightness (of a physical object). The uniform color space is particularly suited to quantify color *differences*.

As an example and to become familiar with the CIE ($L^*$, $u^*$, $v^*$) color space, we consider a test-color sample $i$ illuminated with a white *reference source*. The coordinates, $L^*$, $u^*$, and $v^*$, which give the color difference between object color and reference-source color, are defined as

$$L^*\big|_{\text{ref}} = 116(Y_{\text{ref},i}/Y_{\text{ref}})^{1/3} - 16 \tag{19.11a}$$

$$u^*\big|_{\text{ref}} = 13L^*(u_{\text{ref},i} - u_{\text{ref}}) \tag{19.11b}$$

$$v^*\big|_{\text{ref}} = 13L^*(v_{\text{ref},i} - v_{\text{ref}}) \tag{19.11c}$$

where $Y_{\text{ref},i}$, $u_{\text{ref},i}$, and $v_{\text{ref},i}$ describe the color stimulus of the test-color sample $i$ when illuminated with the *reference source*, and $Y_{\text{ref}}$, $u_{\text{ref}}$, and $v_{\text{ref}}$ describe the color stimulus of the white reference illuminant.

Next consider the test-color sample illuminated with a white *test source*. The coordinates, $L^*$, $u^*$, and $v^*$, which give the color difference between object color and test-source color, are then given by

$$L^*\big|_{\text{test}} = 116(Y_{\text{test},i}/Y_{\text{test}})^{1/3} - 16 \tag{19.12a}$$

$$u^*\big|_{\text{test}} = 13L^*(u_{\text{test},i} - u_{\text{test}}) \tag{19.12b}$$

$$v^*\big|_{\text{test}} = 13L^*(v_{\text{test},i} - v_{\text{test}}) \tag{19.12c}$$

where $Y_{\text{test},\,i}$, $u_{\text{test},\,i}$, and $v_{\text{test},\,i}$ describe the color stimulus of the test-color sample $i$ when illuminated with the *test source*, and $Y_{\text{test}}$, $u_{\text{test}}$, and $v_{\text{test}}$ describe the color of the white test illuminant.

The difference in color between the two points located in the ($L^*$, $u^*$, $v^*$) space given by Eqs. (19.11) and (19.12) is equal to the euclidean distance between the points, that is

$$\Delta E^* = \sqrt{(\Delta L^*)^2 + (\Delta u^*)^2 + (\Delta v^*)^2} \tag{19.13}$$

where

$$\Delta L^* = L^*\big|_{\text{test}} - L^*\big|_{\text{ref}} \tag{19.14a}$$

$$\Delta u^* = u^*\big|_{\text{test}} - u^*\big|_{\text{ref}} \tag{19.14b}$$

$$\Delta v^* = v^*\big|_{\text{test}} - v^*\big|_{\text{ref}} \,. \tag{19.14c}$$

The calculation of the CRI will be detailed in the two subsequent sections.

Table 19.1. General color-rendering indices (CRIs) of different light sources. (a) Using sunlight as reference source. (b) Using incandescent light with the same correlated color temperature as the reference source. (c) Using Illuminant $D_{65}$ as the reference source (some data after Kendall and Scholand, 2001).

| **Light source** | **Color-rendering index** | |
|---|---|---|
| Sunlight | 100 | (a) |
| Quartz halogen W filament incandescent light | 100 | (b) |
| W filament incandescent light | 100 | (b) |
| Fluorescent light | 60–95 | (b) |
| Trichromatic white LED | 60–95 | (b, c) |
| Tetrachromatic white LED | 70–95 | (b, c) |
| Phosphor-based LED | 55–95 | (b, c) |
| Broadened dichromatic white LED | 10–60 | (b, c) |
| Hg vapor light coated with phosphor | 50 | (b) |
| Hg vapor light | 33 | (b) |
| Low and high-pressure Na vapor light | 10 and 22 | (b) |
| Green monochromatic light | –50 | (c) |

An overview of the general color-rendering indices of common light sources is given in



Nichia Exhibit 1014
Page 137

Table 19.1. The table includes several types of LED sources including dichromatic white LEDs, trichromatic white LEDs, and phosphor-based white LEDs. A CRI between 90 and 100 is suitable for virtually all illumination applications. A CRI between 70 and 90 is suitable for many standard illumination applications. Light sources with a CRI below 70 are considered to be of lower quality.

### *19.3 Color-rendering index for planckian-locus illumination sources*

The following calculation gives the value of the quantity $\Delta E_i^*$, which, according to Eq. (19.10), is needed to determine the CRI of a test source. The calculation is suited for test sources that are located on the planckian locus or extremely close to the planckian locus. The calculation described here follows Wyszecki and Stiles (1982, 2000) and CIE (1995). $\Delta E_i^*$, which is the difference in appearance of a test-color sample when illuminated with the test and reference sources, is calculated according to

$$\Delta E_i^* = \sqrt{(\Delta L^*)^2 + (\Delta u^*)^2 + (\Delta v^*)^2} \tag{19.15}$$

where

$$\Delta L^* = L^*_{\text{ref}} - L^*_{\text{test}} = \left[116\left(\frac{Y_{\text{ref},i}}{Y_{\text{ref}}}\right)^{1/3} - 16\right] - \left[116\left(\frac{Y_{\text{test},i}}{Y_{\text{ref}}}\right)^{1/3} - 16\right] \tag{19.16}$$

$$\Delta u^* = u^*_{\text{ref}} - u^*_{\text{test}} = 13L^*_{\text{ref}}\left(u_{\text{ref},i} - u_{\text{ref}}\right) - 13L^*_{\text{test}}\left(u_{\text{test},i} - u_{\text{ref}}\right) \tag{19.17}$$

$$\Delta v^* = v^*_{\text{ref}} - v^*_{\text{test}} = 13L^*_{\text{ref}}\left(v_{\text{ref},i} - v_{\text{ref}}\right) - 13L^*_{\text{test}}\left(v_{\text{test},i} - v_{\text{ref}}\right) \tag{19.18}$$

and

$$u = \frac{4X}{X + 15Y + 3Z} \quad \text{and} \quad v = \frac{6Y}{X + 15Y + 3Z}\,. \tag{19.19}$$

Note that $u$ and $v$ are calculated from the tristimulus values of the reference source spectrum (subscript "ref"), from the reference source spectrum reflected off the test-color samples (subscript "ref, $i$"), and from the test source spectrum reflected off the test-color samples (subscript "test, $i$").

When calculating the CRI using the equations given above, the chromaticity coordinates and

luminous flux of the test and reference sources should be identical in order to get the highest possible CRI for the test source. That is, the conditions $u_{test} = u_{ref}$, $v_{test} = v_{ref}$, and $Y_{test} = Y_{ref}$ should be satisfied.

The calculation of the color-rendering index in terms of Eqs. (19.9)–(19.19) illustrates that it is calculated from the ability of a test source to render the chromaticity of physical objects (taken into account by $\Delta u^*$ and $\Delta v^*$) but also from the ability of the test source to render the lightnesses of the physical objects (taken into account by $\Delta L^*$). The CRI calculation is based on the premise that the reference source renders the true chromaticity and lightness, i.e. the true color, of physical objects.

The choice of the numerical prefactors in Eqs. (19.16)–(19.19) is somewhat arbitrary. These prefactors have been determined in extensive experiments with human subjects. Evidence exists, however, that the current prefactors may not be optimal (Wyszecki and Stiles, 1982, 2000).

### *19.4 Color-rendering index for non-planckian-locus illumination sources*

The following calculation of $\Delta E_i^*$ is suited for test sources that are located *off the planckian* locus. The calculation described here follows the procedure developed by CIE (1995) and takes into account the ***adaptive color shift*** that follows from the human ability of ***chromatic adaptation***.

Chromatic adaptation is the well-known ability of humans to adapt to certain illumination environments without a substantial loss of color perception. For example, the yellow illumination sources used in semiconductor clean rooms provide a low-quality light. Such yellow sources do not contain short-wavelength light (violet, blue and cyan) and they are located clearly off the planckian locus. However, after having adapted to the clean-room illumination conditions (which typically takes several tens of minutes), colors appear quite natural, certainly much more natural than before the chromatic adaptation.

When calculating the CRI for off-planckian-locus sources according to the method described in the previous section, the CRI is very low. However, such low CRI values are not supported by experiments with human subjects: Due to chromatic adaptation, colors can appear vivid and natural, even for illumination sources slightly off the planckian locus. To overcome this discrepancy and to allow for a more realistic calculation of the CRI, the CIE (1995) introduced an alternative method to calculate the CRI. This alternative method takes into account the human ability of chromatic adaptation by introducing an adaptive color shift of the test source towards the planckian reference source.



Nichia Exhibit 1014
Page 139

As a rule of thumb, the pleasantness and quality of white illumination sources decreases rapidly if the chromaticity point of the illumination source deviates from the planckian locus by a distance greater than 0.01 in the $x$, $y$ chromaticity system. This corresponds to the distance of about 4 MacAdam ellipses, a standard employed by the lighting industry (Duggal, 2005). Note however, that the 0.01-rule-of-thumb is a necessary but not a sufficient condition for high quality of illumination sources.

The calculation starts with the uniform chromaticity coordinates of the reference and test sources and the chromaticity coordinates of the test-color samples when illuminated with the reference and test sources, i.e. $(u_{ref}, v_{ref})$, $(u_{test}, v_{test})$, $(u_{ref,i}, v_{ref,i})$, and $(u_{test,i}, v_{test,i})$.

To account for the adaptive color shift, the $(u, v)$ coordinates of $(u_{ref}, v_{ref})$, $(u_{test}, v_{test})$, and $(u_{test,i}, v_{test,i})$ are transformed into $(c, d)$ coordinates using the formulae

$$c = (4 - u - 10\,v) / v \tag{19.20}$$

$$d = (1.708\,v + 0.404 - 1.481\,u) / v\ . \tag{19.21}$$

Note that these two equations correspond to six equations when transforming $(u_{ref}, v_{ref})$, $(u_{test}, v_{test})$, and $(u_{test,i}, v_{test,i})$ into $(c_{ref}, d_{ref})$, $(c_{test}, d_{test})$, and $(c_{test,i}, d_{test,i})$, respectively. Subsequently the adaptive-color-shifted chromaticity coordinates of the test-color samples are calculated according to

$$u^{**}_{test,i} = \frac{10.872 + 0.404\,\frac{c_{ref}}{c_{test}}\,c_{test,i} - 4\,\frac{d_{ref}}{d_{test}}\,d_{test,i}}{16.518 + 1.481\,\frac{c_{ref}}{c_{test}}\,c_{test,i} - \frac{d_{ref}}{d_{test}}\,d_{test,i}} \tag{19.22}$$

$$v^{**}_{test,i} = \frac{5.520}{16.518 + 1.481\,\frac{c_{ref}}{c_{test}}\,c_{test,i} - \frac{d_{ref}}{d_{test}}\,d_{test,i}}\ . \tag{19.23}$$

Correspondingly, the adaptive-color-shifted chromaticity coordinates of the test source are calculated according to

$$u^{**}_{test} = \frac{10.872 + 0.404\,c_{ref} - 4\,d_{ref}}{16.518 + 1.481\,c_{ref} - d_{ref}} = u_{ref} \tag{19.24}$$

$$v_{\text{test}}^{**} = \frac{5.520}{16.518 + 1.481\,c_{\text{ref}} - d_{\text{ref}}} = v_{\text{ref}} \,. \tag{19.25}$$

The values of $u_{\text{test}}$** and $v_{\text{test}}$** are the chromaticity coordinates of the light source to be tested after the adaptive color shift has been performed (note that $u_{\text{test}}$** = $u_{\text{ref}}$ and $v_{\text{test}}$** = $v_{\text{ref}}$). Finally the color difference is calculated in terms of the uniform color space coordinates

$$\Delta E_i^* = \sqrt{(\Delta L^{**})^2 + (\Delta u^{**})^2 + (\Delta v^{**})^2} \tag{19.26}$$

where

$$\Delta L^{**} = L_{\text{ref},i}^{**} - L_{\text{test},i}^{**} = \left[25\left(Y_{\text{ref},i}\right)^{1/3} - 17\right] - \left[25\left(Y_{\text{test},i}\right)^{1/3} - 17\right] \tag{19.27}$$

$$\Delta u^{**} = u_{\text{ref}}^{***} - u_{\text{test}}^{***} = 13L_{\text{ref},i}^{**}\left(u_{\text{ref},i} - u_{\text{ref}}\right) - 13L_{\text{test},i}^{**}\left(u_{\text{test},i}^{**} - u_{\text{test}}^{**}\right) \tag{19.28}$$

$$\Delta v^{**} = v_{\text{ref}}^{***} - v_{\text{test}}^{***} = 13L_{\text{ref},i}^{**}\left(v_{\text{ref},i} - v_{\text{ref}}\right) - 13L_{\text{test},i}^{**}\left(v_{\text{test},i}^{**} - v_{\text{test}}^{**}\right). \tag{19.29}$$

Note that the calculation requires that $Y_{\text{ref}} = Y_{\text{test}} = 100$ (CIE, 1995). Using the calculated values of $\Delta E_i$*, the general CRI is calculated using Eqs. (19.9) and (19.10). The special $\text{CRI}_i$ for $i = 9$ to 14 may be of interest for a complete assessment of the color rendering properties of an illumination source.

---

**Exercise**: ***Color rendering***. The color of a physical object, as seen by a human being, is not just a function of the object but also a function of the light source illuminating the object! In fact, the color of an object can depend very strongly on the light source illuminating the object. Some light sources do render the natural colors of an object (true color rendering) while some light sources do not (false color rendering).

(a) What is the color of a yellow banana when illuminated with a red LED?
(b) What is the color of a green banana when illuminated with a yellow LED?
(c) Could it be advantageous for a grocer to illuminate meat with red LEDs, bananas with yellow LEDs, and oranges with orange LEDs?
(d) Is it possible for two physical objects of different colors to appear to have the same color under certain illumination conditions?
(e) Why are low-pressure Na vapor lights used despite their low color-rendering index?
(f) What would be the advantage and disadvantage of using green LEDs for illumination?

Solution:

(a) Red. (b) Yellow. (c) Yes – but his truthfulness in displaying fruit could be questioned. (d) Yes. (e) Because of their high luminous efficiency (and thus low electricity consumption). (f) High luminous efficacy would be an advantage but low color-rendering properties would be a disadvantage.

---



Nichia Exhibit 1014
Page 141

## *References*

Berger-Schunn A. *Practical Color Measurement* (John Wiley and Sons, New York, 1994)

Billmeyer Jr. F. W. "Survey of color order systems" *Color Res. Appl.* **12**, 173 (1987)

CIE publication No. 15 (E.1.3.1) 1971: *Colorimetry* this publication was updated in 1986 to CIE Publication 15.2 *Colorimetry* (CIE, Vienna, Austria, 1986)

CIE publication No. 13.3 *Method of Measuring and Specifying Color-Rendering of Light Sources* (see also www.cie.co.at) (CIE, Vienna, Austria, 1995)

Duggal A. R. "Organic electroluminescent devices for solid-state lighting" in *Organic Electroluminescence* edited by Z. H. Kafafi (Taylor and Francis Group, Boca Raton, Florida, 2005)

Kendall M. and Scholand M. *Energy Savings Potential of Solid State Lighting in General Lighting Applications* available to the public from National Technical Information Service (NTIS), US Department of Commerce, 5285 Port Royal Road, Springfield, Virginia 22161 (2001)

Long J. and Luke J. T. *The New Munsell Student Color Set* 2nd ring-bound edition (Fairchild Books and Visuals, New York, 2001)

MacAdam D. L. (Editor) *Colorimetry – Fundamentals* (SPIE Optical Engineering Press, Bellingham, Washington, 1993)

Munsell A. H. *A Color Notation – An Illustrated System Defining All Colors and Their Relations by Measured Scales of Hue, Value, and Chroma* (G. H. Ellis, Boston, 1905)

Munsell *Munsell Book of Color, Matte Edition* is available through GretagMacbeth Corporation, gretagmacbeth.com and munsell.com (Regensdorf, Switzerland, 2005)

Wyszecki G. and Stiles W. S. *Color Science – Concepts and Methods, Quantitative Data and Formulae* 2nd edition (John Wiley and Sons, New York, 1982)

Wyszecki G. and Stiles W. S. *Color Science – Concepts and Methods, Quantitative Data and Formulae* 2nd edition "Wiley Classics Library" (John Wiley and Sons, New York, 2000)

## Appendix 19.1

Spectral reflectivity $R_i(\lambda)$ of the CIE 1974 Test-Color Samples (TCS) Nos. 1–8 to be used in calculating the General Color-Rendering Index (General CRI) (after CIE, 1995)

| λ (nm) | $R_1$ (-) | $R_2$ (-) | $R_3$ (-) | $R_4$ (-) | $R_5$ (-) | $R_6$ (-) | $R_7$ (-) | $R_8$ (-) |
|---|---|---|---|---|---|---|---|---|
| 360 | 0.116 | 0.053 | 0.058 | 0.057 | 0.143 | 0.079 | 0.150 | 0.075 |
| 365 | 0.136 | 0.055 | 0.059 | 0.059 | 0.187 | 0.081 | 0.177 | 0.078 |
| 370 | 0.159 | 0.059 | 0.061 | 0.062 | 0.233 | 0.089 | 0.218 | 0.084 |
| 375 | 0.190 | 0.064 | 0.063 | 0.067 | 0.269 | 0.113 | 0.293 | 0.090 |
| 380 | 0.219 | 0.070 | 0.065 | 0.074 | 0.295 | 0.151 | 0.378 | 0.104 |
| 385 | 0.239 | 0.079 | 0.068 | 0.083 | 0.306 | 0.203 | 0.459 | 0.129 |
| 390 | 0.252 | 0.089 | 0.070 | 0.093 | 0.310 | 0.265 | 0.524 | 0.170 |
| 395 | 0.256 | 0.101 | 0.072 | 0.105 | 0.312 | 0.339 | 0.546 | 0.240 |
| 400 | 0.256 | 0.111 | 0.073 | 0.116 | 0.313 | 0.410 | 0.551 | 0.319 |
| 405 | 0.254 | 0.116 | 0.073 | 0.121 | 0.315 | 0.464 | 0.555 | 0.416 |
| 410 | 0.252 | 0.118 | 0.074 | 0.124 | 0.319 | 0.492 | 0.559 | 0.462 |
| 415 | 0.248 | 0.120 | 0.074 | 0.126 | 0.322 | 0.508 | 0.560 | 0.482 |
| 420 | 0.244 | 0.121 | 0.074 | 0.128 | 0.326 | 0.517 | 0.561 | 0.490 |
| 425 | 0.240 | 0.122 | 0.073 | 0.131 | 0.330 | 0.524 | 0.558 | 0.488 |
| 430 | 0.237 | 0.122 | 0.073 | 0.135 | 0.334 | 0.531 | 0.556 | 0.482 |
| 435 | 0.232 | 0.122 | 0.073 | 0.139 | 0.339 | 0.538 | 0.551 | 0.473 |
| 440 | 0.230 | 0.123 | 0.073 | 0.144 | 0.346 | 0.544 | 0.544 | 0.462 |
| 445 | 0.226 | 0.124 | 0.073 | 0.151 | 0.352 | 0.551 | 0.535 | 0.450 |
| 450 | 0.225 | 0.127 | 0.074 | 0.161 | 0.360 | 0.556 | 0.522 | 0.439 |
| 455 | 0.222 | 0.128 | 0.075 | 0.172 | 0.369 | 0.556 | 0.506 | 0.426 |
| 460 | 0.220 | 0.131 | 0.077 | 0.186 | 0.381 | 0.554 | 0.488 | 0.413 |
| 465 | 0.218 | 0.134 | 0.080 | 0.205 | 0.394 | 0.549 | 0.469 | 0.397 |
| 470 | 0.216 | 0.138 | 0.085 | 0.229 | 0.403 | 0.541 | 0.448 | 0.382 |
| 475 | 0.214 | 0.143 | 0.094 | 0.254 | 0.410 | 0.531 | 0.429 | 0.366 |
| 480 | 0.214 | 0.150 | 0.109 | 0.281 | 0.415 | 0.519 | 0.408 | 0.352 |
| 485 | 0.214 | 0.159 | 0.126 | 0.308 | 0.418 | 0.504 | 0.385 | 0.337 |
| 490 | 0.216 | 0.174 | 0.148 | 0.332 | 0.419 | 0.488 | 0.363 | 0.325 |
| 495 | 0.218 | 0.190 | 0.172 | 0.352 | 0.417 | 0.469 | 0.341 | 0.310 |
| 500 | 0.223 | 0.207 | 0.198 | 0.370 | 0.413 | 0.450 | 0.324 | 0.299 |
| 505 | 0.225 | 0.225 | 0.221 | 0.383 | 0.409 | 0.431 | 0.311 | 0.289 |
| 510 | 0.226 | 0.242 | 0.241 | 0.390 | 0.403 | 0.414 | 0.301 | 0.283 |
| 515 | 0.226 | 0.253 | 0.260 | 0.394 | 0.396 | 0.395 | 0.291 | 0.276 |
| 520 | 0.225 | 0.260 | 0.278 | 0.395 | 0.389 | 0.377 | 0.283 | 0.270 |
| 525 | 0.225 | 0.264 | 0.302 | 0.392 | 0.381 | 0.358 | 0.273 | 0.262 |
| 530 | 0.227 | 0.267 | 0.339 | 0.385 | 0.372 | 0.341 | 0.265 | 0.256 |
| 535 | 0.230 | 0.269 | 0.370 | 0.377 | 0.363 | 0.325 | 0.260 | 0.251 |
| 540 | 0.236 | 0.272 | 0.392 | 0.367 | 0.353 | 0.309 | 0.257 | 0.250 |
| 545 | 0.245 | 0.276 | 0.399 | 0.354 | 0.342 | 0.293 | 0.257 | 0.251 |
| 550 | 0.253 | 0.282 | 0.400 | 0.341 | 0.331 | 0.279 | 0.259 | 0.254 |
| 555 | 0.262 | 0.289 | 0.393 | 0.327 | 0.320 | 0.265 | 0.260 | 0.258 |
| 560 | 0.272 | 0.299 | 0.380 | 0.312 | 0.308 | 0.253 | 0.260 | 0.264 |
| 565 | 0.283 | 0.309 | 0.365 | 0.296 | 0.296 | 0.241 | 0.258 | 0.269 |
| 570 | 0.298 | 0.322 | 0.349 | 0.280 | 0.284 | 0.234 | 0.256 | 0.272 |
| 575 | 0.318 | 0.329 | 0.332 | 0.263 | 0.271 | 0.227 | 0.254 | 0.274 |
| 580 | 0.341 | 0.335 | 0.315 | 0.247 | 0.260 | 0.225 | 0.254 | 0.278 |
| 585 | 0.367 | 0.339 | 0.299 | 0.229 | 0.247 | 0.222 | 0.259 | 0.284 |
| 590 | 0.390 | 0.341 | 0.285 | 0.214 | 0.232 | 0.221 | 0.270 | 0.295 |
| 595 | 0.409 | 0.341 | 0.272 | 0.198 | 0.220 | 0.220 | 0.284 | 0.316 |



Nichia Exhibit 1014
Page 143

| | | | | | | | | |
|---|---|---|---|---|---|---|---|---|
| 600 | 0.424 | 0.342 | 0.264 | 0.185 | 0.210 | 0.220 | 0.302 | 0.348 |
| 605 | 0.435 | 0.342 | 0.257 | 0.175 | 0.200 | 0.220 | 0.324 | 0.384 |
| 610 | 0.442 | 0.342 | 0.252 | 0.169 | 0.194 | 0.220 | 0.344 | 0.434 |
| 615 | 0.448 | 0.341 | 0.247 | 0.164 | 0.189 | 0.220 | 0.362 | 0.482 |
| 620 | 0.450 | 0.341 | 0.241 | 0.160 | 0.185 | 0.223 | 0.377 | 0.528 |
| 625 | 0.451 | 0.339 | 0.235 | 0.156 | 0.183 | 0.227 | 0.389 | 0.568 |
| 630 | 0.451 | 0.339 | 0.229 | 0.154 | 0.180 | 0.233 | 0.400 | 0.604 |
| 635 | 0.451 | 0.338 | 0.224 | 0.152 | 0.177 | 0.239 | 0.410 | 0.629 |
| 640 | 0.451 | 0.338 | 0.220 | 0.151 | 0.176 | 0.244 | 0.420 | 0.648 |
| 645 | 0.451 | 0.337 | 0.217 | 0.149 | 0.175 | 0.251 | 0.429 | 0.663 |
| 650 | 0.450 | 0.336 | 0.216 | 0.148 | 0.175 | 0.258 | 0.438 | 0.676 |
| 655 | 0.450 | 0.335 | 0.216 | 0.148 | 0.175 | 0.263 | 0.445 | 0.685 |
| 660 | 0.451 | 0.334 | 0.219 | 0.148 | 0.175 | 0.268 | 0.452 | 0.693 |
| 665 | 0.451 | 0.332 | 0.224 | 0.149 | 0.177 | 0.273 | 0.457 | 0.700 |
| 670 | 0.453 | 0.332 | 0.230 | 0.151 | 0.180 | 0.278 | 0.462 | 0.705 |
| 675 | 0.454 | 0.331 | 0.238 | 0.154 | 0.183 | 0.281 | 0.466 | 0.709 |
| 680 | 0.455 | 0.331 | 0.251 | 0.158 | 0.186 | 0.283 | 0.468 | 0.712 |
| 685 | 0.457 | 0.330 | 0.269 | 0.162 | 0.189 | 0.286 | 0.470 | 0.715 |
| 690 | 0.458 | 0.329 | 0.288 | 0.165 | 0.192 | 0.291 | 0.473 | 0.717 |
| 695 | 0.460 | 0.328 | 0.312 | 0.168 | 0.195 | 0.296 | 0.477 | 0.719 |
| 700 | 0.462 | 0.328 | 0.340 | 0.170 | 0.199 | 0.302 | 0.483 | 0.721 |
| 705 | 0.463 | 0.327 | 0.366 | 0.171 | 0.200 | 0.313 | 0.489 | 0.720 |
| 710 | 0.464 | 0.326 | 0.390 | 0.170 | 0.199 | 0.325 | 0.496 | 0.719 |
| 715 | 0.465 | 0.325 | 0.412 | 0.168 | 0.198 | 0.338 | 0.503 | 0.722 |
| 720 | 0.466 | 0.324 | 0.431 | 0.166 | 0.196 | 0.351 | 0.511 | 0.725 |
| 725 | 0.466 | 0.324 | 0.447 | 0.164 | 0.195 | 0.364 | 0.518 | 0.727 |
| 730 | 0.466 | 0.324 | 0.460 | 0.164 | 0.195 | 0.376 | 0.525 | 0.729 |
| 735 | 0.466 | 0.323 | 0.472 | 0.165 | 0.196 | 0.389 | 0.532 | 0.730 |
| 740 | 0.467 | 0.322 | 0.481 | 0.168 | 0.197 | 0.401 | 0.539 | 0.730 |
| 745 | 0.467 | 0.321 | 0.488 | 0.172 | 0.200 | 0.413 | 0.546 | 0.730 |
| 750 | 0.467 | 0.320 | 0.493 | 0.177 | 0.203 | 0.425 | 0.553 | 0.730 |
| 755 | 0.467 | 0.318 | 0.497 | 0.181 | 0.205 | 0.436 | 0.559 | 0.730 |
| 760 | 0.467 | 0.316 | 0.500 | 0.185 | 0.208 | 0.447 | 0.565 | 0.730 |
| 765 | 0.467 | 0.315 | 0.502 | 0.189 | 0.212 | 0.458 | 0.570 | 0.730 |
| 770 | 0.467 | 0.315 | 0.505 | 0.192 | 0.215 | 0.469 | 0.575 | 0.730 |
| 775 | 0.467 | 0.314 | 0.510 | 0.194 | 0.217 | 0.477 | 0.578 | 0.730 |
| 780 | 0.467 | 0.314 | 0.516 | 0.197 | 0.219 | 0.485 | 0.581 | 0.730 |
| 785 | 0.467 | 0.313 | 0.520 | 0.200 | 0.222 | 0.493 | 0.583 | 0.730 |
| 790 | 0.467 | 0.313 | 0.524 | 0.204 | 0.226 | 0.500 | 0.585 | 0.731 |
| 795 | 0.466 | 0.312 | 0.527 | 0.210 | 0.231 | 0.506 | 0.587 | 0.731 |
| 800 | 0.466 | 0.312 | 0.531 | 0.218 | 0.237 | 0.512 | 0.588 | 0.731 |
| 805 | 0.466 | 0.311 | 0.535 | 0.225 | 0.243 | 0.517 | 0.589 | 0.731 |
| 810 | 0.466 | 0.311 | 0.539 | 0.233 | 0.249 | 0.521 | 0.590 | 0.731 |
| 815 | 0.466 | 0.311 | 0.544 | 0.243 | 0.257 | 0.525 | 0.590 | 0.731 |
| 820 | 0.465 | 0.311 | 0.548 | 0.254 | 0.265 | 0.529 | 0.590 | 0.731 |
| 825 | 0.464 | 0.311 | 0.552 | 0.264 | 0.273 | 0.532 | 0.591 | 0.731 |
| 830 | 0.464 | 0.310 | 0.555 | 0.274 | 0.280 | 0.535 | 0.592 | 0.731 |

## Appendix 19.2

Spectral reflectivity $R_i(\lambda)$ of the CIE 1974 Test-Color Samples (TCS) Nos. 9–14 (after CIE, 1995)

| λ (nm) | $R_9$ (-) | $R_{10}$ (-) | $R_{11}$ (-) | $R_{12}$ (-) | $R_{13}$ (-) | $R_{14}$ (-) |
|---|---|---|---|---|---|---|
| 360 | 0.069 | 0.042 | 0.074 | 0.189 | 0.071 | 0.036 |
| 365 | 0.072 | 0.043 | 0.079 | 0.175 | 0.076 | 0.036 |
| 370 | 0.073 | 0.045 | 0.086 | 0.158 | 0.082 | 0.036 |
| 375 | 0.070 | 0.047 | 0.098 | 0.139 | 0.090 | 0.036 |
| 380 | 0.066 | 0.050 | 0.111 | 0.120 | 0.104 | 0.036 |
| 385 | 0.062 | 0.054 | 0.121 | 0.103 | 0.127 | 0.036 |
| 390 | 0.058 | 0.059 | 0.127 | 0.090 | 0.161 | 0.037 |
| 395 | 0.055 | 0.063 | 0.129 | 0.082 | 0.211 | 0.038 |
| 400 | 0.052 | 0.066 | 0.127 | 0.076 | 0.264 | 0.039 |
| 405 | 0.052 | 0.067 | 0.121 | 0.068 | 0.313 | 0.039 |
| 410 | 0.051 | 0.068 | 0.116 | 0.064 | 0.341 | 0.040 |
| 415 | 0.050 | 0.069 | 0.112 | 0.065 | 0.352 | 0.041 |
| 420 | 0.050 | 0.069 | 0.108 | 0.075 | 0.359 | 0.042 |
| 425 | 0.049 | 0.070 | 0.105 | 0.093 | 0.361 | 0.042 |
| 430 | 0.048 | 0.072 | 0.104 | 0.123 | 0.364 | 0.043 |
| 435 | 0.047 | 0.073 | 0.104 | 0.160 | 0.365 | 0.044 |
| 440 | 0.046 | 0.076 | 0.105 | 0.207 | 0.367 | 0.044 |
| 445 | 0.044 | 0.078 | 0.106 | 0.256 | 0.369 | 0.045 |
| 450 | 0.042 | 0.083 | 0.110 | 0.300 | 0.372 | 0.045 |
| 455 | 0.041 | 0.088 | 0.115 | 0.331 | 0.374 | 0.046 |
| 460 | 0.038 | 0.095 | 0.123 | 0.346 | 0.376 | 0.047 |
| 465 | 0.035 | 0.103 | 0.134 | 0.347 | 0.379 | 0.048 |
| 470 | 0.033 | 0.113 | 0.148 | 0.341 | 0.384 | 0.050 |
| 475 | 0.031 | 0.125 | 0.167 | 0.328 | 0.389 | 0.052 |
| 480 | 0.030 | 0.142 | 0.192 | 0.307 | 0.397 | 0.055 |
| 485 | 0.029 | 0.162 | 0.219 | 0.282 | 0.405 | 0.057 |
| 490 | 0.028 | 0.189 | 0.252 | 0.257 | 0.416 | 0.062 |
| 495 | 0.028 | 0.219 | 0.291 | 0.230 | 0.429 | 0.067 |
| 500 | 0.028 | 0.262 | 0.325 | 0.204 | 0.443 | 0.075 |
| 505 | 0.029 | 0.305 | 0.347 | 0.178 | 0.454 | 0.083 |
| 510 | 0.030 | 0.365 | 0.356 | 0.154 | 0.461 | 0.092 |
| 515 | 0.030 | 0.416 | 0.353 | 0.129 | 0.466 | 0.100 |
| 520 | 0.031 | 0.465 | 0.346 | 0.109 | 0.469 | 0.108 |
| 525 | 0.031 | 0.509 | 0.333 | 0.090 | 0.471 | 0.121 |
| 530 | 0.032 | 0.546 | 0.314 | 0.075 | 0.474 | 0.133 |
| 535 | 0.032 | 0.581 | 0.294 | 0.062 | 0.476 | 0.142 |
| 540 | 0.033 | 0.610 | 0.271 | 0.051 | 0.483 | 0.150 |
| 545 | 0.034 | 0.634 | 0.248 | 0.041 | 0.490 | 0.154 |
| 550 | 0.035 | 0.653 | 0.227 | 0.035 | 0.506 | 0.155 |
| 555 | 0.037 | 0.666 | 0.206 | 0.029 | 0.526 | 0.152 |
| 560 | 0.041 | 0.678 | 0.188 | 0.025 | 0.553 | 0.147 |
| 565 | 0.044 | 0.687 | 0.170 | 0.022 | 0.582 | 0.140 |
| 570 | 0.048 | 0.693 | 0.153 | 0.019 | 0.618 | 0.133 |
| 575 | 0.052 | 0.698 | 0.138 | 0.017 | 0.651 | 0.125 |
| 580 | 0.060 | 0.701 | 0.125 | 0.017 | 0.680 | 0.118 |
| 585 | 0.076 | 0.704 | 0.114 | 0.017 | 0.701 | 0.112 |
| 590 | 0.102 | 0.705 | 0.106 | 0.016 | 0.717 | 0.106 |
| 595 | 0.136 | 0.705 | 0.100 | 0.016 | 0.729 | 0.101 |
| 600 | 0.190 | 0.706 | 0.096 | 0.016 | 0.736 | 0.098 |



Nichia Exhibit 1014
Page 145

| | | | | | | |
|---|---|---|---|---|---|---|
| 605 | 0.256 | 0.707 | 0.092 | 0.016 | 0.742 | 0.095 |
| 610 | 0.336 | 0.707 | 0.090 | 0.016 | 0.745 | 0.093 |
| 615 | 0.418 | 0.707 | 0.087 | 0.016 | 0.747 | 0.090 |
| 620 | 0.505 | 0.708 | 0.085 | 0.016 | 0.748 | 0.089 |
| 625 | 0.581 | 0.708 | 0.082 | 0.016 | 0.748 | 0.087 |
| 630 | 0.641 | 0.710 | 0.080 | 0.018 | 0.748 | 0.086 |
| 635 | 0.682 | 0.711 | 0.079 | 0.018 | 0.748 | 0.085 |
| 640 | 0.717 | 0.712 | 0.078 | 0.018 | 0.748 | 0.084 |
| 645 | 0.740 | 0.714 | 0.078 | 0.018 | 0.748 | 0.084 |
| 650 | 0.758 | 0.716 | 0.078 | 0.019 | 0.748 | 0.084 |
| 655 | 0.770 | 0.718 | 0.078 | 0.020 | 0.748 | 0.084 |
| 660 | 0.781 | 0.720 | 0.081 | 0.023 | 0.747 | 0.085 |
| 665 | 0.790 | 0.722 | 0.083 | 0.024 | 0.747 | 0.087 |
| 670 | 0.797 | 0.725 | 0.088 | 0.026 | 0.747 | 0.092 |
| 675 | 0.803 | 0.729 | 0.093 | 0.030 | 0.747 | 0.096 |
| 680 | 0.809 | 0.731 | 0.102 | 0.035 | 0.747 | 0.102 |
| 685 | 0.814 | 0.735 | 0.112 | 0.043 | 0.747 | 0.110 |
| 690 | 0.819 | 0.739 | 0.125 | 0.056 | 0.747 | 0.123 |
| 695 | 0.824 | 0.742 | 0.141 | 0.074 | 0.746 | 0.137 |
| 700 | 0.828 | 0.746 | 0.161 | 0.097 | 0.746 | 0.152 |
| 705 | 0.830 | 0.748 | 0.182 | 0.128 | 0.746 | 0.169 |
| 710 | 0.831 | 0.749 | 0.203 | 0.166 | 0.745 | 0.188 |
| 715 | 0.833 | 0.751 | 0.223 | 0.210 | 0.744 | 0.207 |
| 720 | 0.835 | 0.753 | 0.242 | 0.257 | 0.743 | 0.226 |
| 725 | 0.836 | 0.754 | 0.257 | 0.305 | 0.744 | 0.243 |
| 730 | 0.836 | 0.755 | 0.270 | 0.354 | 0.745 | 0.260 |
| 735 | 0.837 | 0.755 | 0.282 | 0.401 | 0.748 | 0.277 |
| 740 | 0.838 | 0.755 | 0.292 | 0.446 | 0.750 | 0.294 |
| 745 | 0.839 | 0.755 | 0.302 | 0.485 | 0.750 | 0.310 |
| 750 | 0.839 | 0.756 | 0.310 | 0.520 | 0.749 | 0.325 |
| 755 | 0.839 | 0.757 | 0.314 | 0.551 | 0.748 | 0.339 |
| 760 | 0.839 | 0.758 | 0.317 | 0.577 | 0.748 | 0.353 |
| 765 | 0.839 | 0.759 | 0.323 | 0.599 | 0.747 | 0.366 |
| 770 | 0.839 | 0.759 | 0.330 | 0.618 | 0.747 | 0.379 |
| 775 | 0.839 | 0.759 | 0.334 | 0.633 | 0.747 | 0.390 |
| 780 | 0.839 | 0.759 | 0.338 | 0.645 | 0.747 | 0.399 |
| 785 | 0.839 | 0.759 | 0.343 | 0.656 | 0.746 | 0.408 |
| 790 | 0.839 | 0.759 | 0.348 | 0.666 | 0.746 | 0.416 |
| 795 | 0.839 | 0.759 | 0.353 | 0.674 | 0.746 | 0.422 |
| 800 | 0.839 | 0.759 | 0.359 | 0.680 | 0.746 | 0.428 |
| 805 | 0.839 | 0.759 | 0.365 | 0.686 | 0.745 | 0.434 |
| 810 | 0.838 | 0.758 | 0.372 | 0.691 | 0.745 | 0.439 |
| 815 | 0.837 | 0.757 | 0.380 | 0.694 | 0.745 | 0.444 |
| 820 | 0.837 | 0.757 | 0.388 | 0.697 | 0.745 | 0.448 |
| 825 | 0.836 | 0.756 | 0.396 | 0.700 | 0.745 | 0.451 |
| 830 | 0.836 | 0.756 | 0.403 | 0.702 | 0.745 | 0.454 |

# 20

## White-light sources based on LEDs

As the trend of higher efficiencies in LEDs continues, the number of possible applications increases as well. A highly interesting application with a very large potential market size is *general daylight illumination* in homes and offices. The field of ***solid-state lighting*** (SSL) is concerned with the development of solid-state sources for illumination applications. LEDs are inherently monochromatic emitters. However, there are several ways to generate white light using LEDs. Approaches to white-light generation based on LEDs will be covered in the current chapter, whereas approaches based on LEDs and wavelength-converting materials will be discussed in the following chapter. A pivotal discussion of the promise of solid-state lighting was given by Bergh *et al*. (2001). A comprehensive introduction to lighting technology using solid-state sources was given by Zukauskas *et al*. (2002a).

In the field of general daylight illumination, devices should have the following properties (*i*) high efficiency, (*ii*) high power capability, (*iii*) good color-rendering capabilities (*iv*) high reliability, (*v*) low-cost manufacturability, and (*vi*) environmental benignity. Such properties would allow LEDs to compete with conventional illumination sources, in particular incandescent and fluorescent lamps.

### *20.1 Generation of white light with LEDs*

Light is perceived as *white* light if the three types of cones located on the retina of the human eye are excited in a certain ratio, namely with similar intensity. For the case of white light, the tristimulus values are such that the location of the chromaticity point is near the center of the chromaticity diagram.

The generation of white light can be accomplished with a huge number of possible spectra. The creation of white light out of monochromatic visible-spectrum emitters can be based on dichromatic, trichromatic, or tetrachromatic approaches, as shown in Fig. 20.1, or on approaches of higher chromaticity. The optical sources can be classified in terms of their luminous efficacy


Nichia Exhibit 1014
Page 147

of radiation, luminous source efficiency, and color-rendering properties.

Whereas high luminous efficacy and high luminous efficiency are always desirable properties of high-power light sources, color rendering depends strongly on the application. Generally, high-quality daylight illumination applications, e.g. illumination in museums, homes, offices, and stores, require a high color-rendering capability.

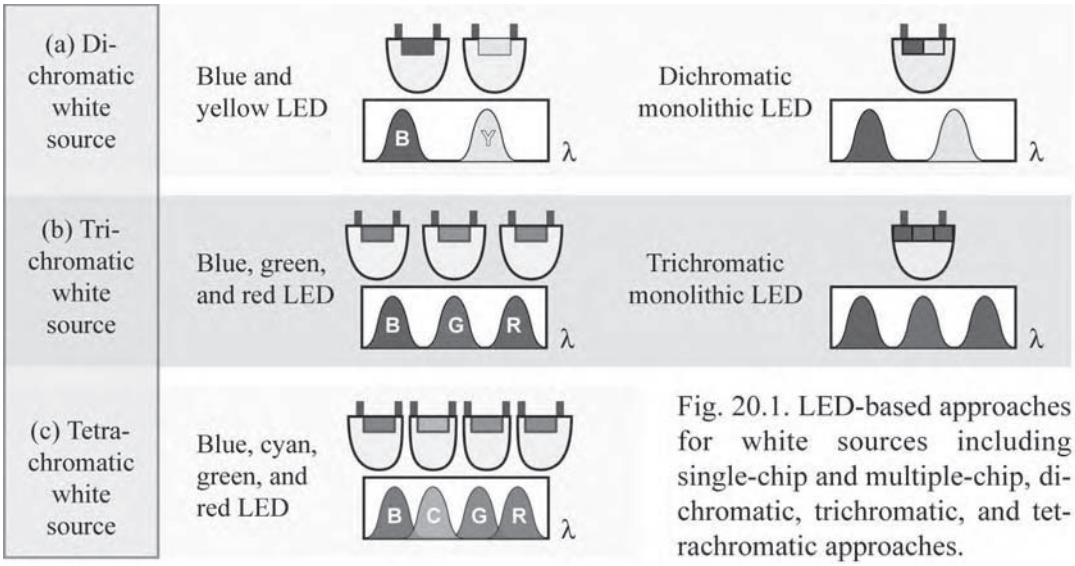


Fig. 20.1. LED-based approaches for white sources including single-chip and multiple-chip, di-chromatic, trichromatic, and tet-rachromatic approaches.

However, there are numerous applications where the color rendering capability is of lower priority, for example in the illumination of streets, parking garages, and stairwells. Finally, in signage applications, color rendering is irrelevant. Such signage applications include white pedestrian traffic lights, displays, and indicator lights.

There is a fundamental trade-off between the luminous efficacy of radiation and color rendering capability of a light source. Generally, dichromatic white light has the highest luminous efficacy and the poorest color-rendering capabilities. A trichromatic white source can have very acceptable color-rendering properties (CRI > 80) and luminous efficacies greater than 300 lm/W. Tetrachromatic sources can have color-rendering indices greater than 90.

## *20.2 Generation of white light by dichromatic sources*

White light can be generated in several different ways. One way of generating white light is the use of two narrow emission bands, called ***complementary wavelengths*** or ***complementary colors***. Two complementary colors, at a certain power ratio, result in tristimulus values that are perceived as white light. The wavelengths of complementary colors are shown in Fig. 20.2.

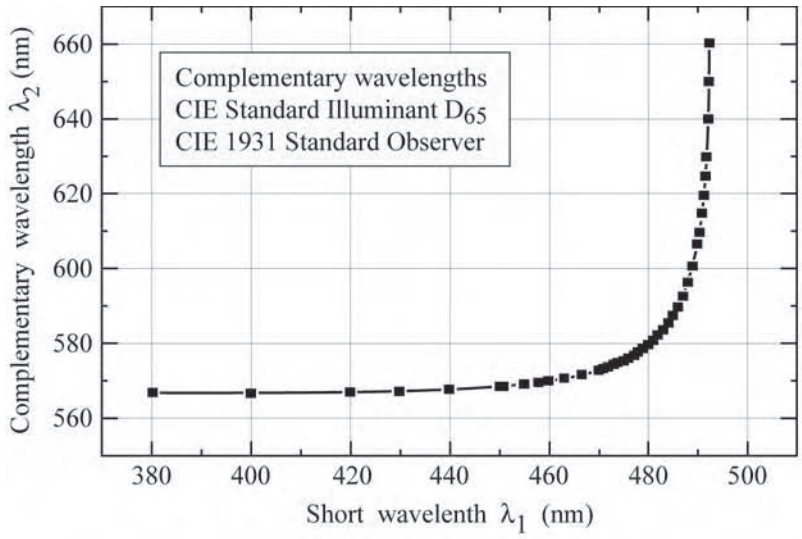


Fig. 20.2. Monochromatic complementary wavelengths resulting in the perception of white light at a certain power ratio (after Wyszecki and Stiles, 1982).

The numerical values for monochromatic complementary wavelengths are given in Table 20.1. The table also gives the power ratio required to attain the same chromaticity coordinate as Illuminant $D_{65}$.

Table 20.1. Wavelengths $\lambda_1$ and $\lambda_2$ of monochromatic complementary colors with respect to CIE Illuminant $D_{65}$ and the CIE 1964 Standard Observer. Also given is the required power ratio. Illuminant $D_{65}$ has chromaticity coordinates $x_{D65} = 0.3138$ and $y_{D65} = 0.3310$ (after Wyszecki and Stiles, 1982).

| **Complementary wavelengths** | | **Power ratio** | **Complementary wavelengths** | | **Power ratio** |
|---|---|---|---|---|---|
| $\lambda_1$ (nm) | $\lambda_2$ (nm) | $P(\lambda_2) / P(\lambda_1)$ | $\lambda_1$ (nm) | $\lambda_2$ (nm) | $P(\lambda_2) / P(\lambda_1)$ |
| 380 | 560.9 | 0.000642 | 460 | 565.9 | 1.53 |
| 390 | 560.9 | 0.00955 | 470 | 570.4 | 1.09 |
| 400 | 561.1 | 0.0785 | 475 | 575.5 | 0.812 |
| 410 | 561.3 | 0.356 | 480 | 584.6 | 0.562 |
| 420 | 561.7 | 0.891 | 482 | 591.1 | 0.482 |
| 430 | 562.2 | 1.42 | 484 | 602.1 | 0.440 |
| 440 | 562.9 | 1.79 | 485 | 611.3 | 0.457 |
| 450 | 564.0 | 1.79 | 486 | 629.6 | 0.668 |

Next we analyze the luminous efficacy of radiation of a source with two complementary emission lines. It is assumed that the two lines are thermally broadened to a full-width at half-maximum of $\Delta E$. Emission lines of $\Delta E = 2\,kT$ to $10\,kT$ have been found experimentally for the GaInN system at room temperature ($kT$ = 25.9 meV at 300 K). A ***gaussian distribution*** is assumed for the two emission lines, so that the spectral power density is given by



Nichia Exhibit 1014
Page 149

$$P(\lambda) = P_1 \frac{1}{\sigma_1\sqrt{2\pi}} e^{-\frac{1}{2}\left(\frac{\lambda-\lambda_1}{\sigma_1}\right)^2} + P_2 \frac{1}{\sigma_2\sqrt{2\pi}} e^{-\frac{1}{2}\left(\frac{\lambda-\lambda_2}{\sigma_2}\right)^2} \quad (20.1)$$

where $P_1$ and $P_2$ are the optical powers of the two emission lines, and $\lambda_1$ and $\lambda_2$ are the peak wavelengths of the source. The gaussian standard deviation $\sigma$ is related to the full-width at half-maximum of an emission spectrum, $\Delta\lambda$, by

$$\sigma = \Delta\lambda \Big/ \left[ 2\sqrt{2\ln 2} \right] = \Delta\lambda / 2.355 \ . \quad (20.2)$$

The peak emission wavelengths $\lambda_1$ and $\lambda_2$ are chosen from Table 20.1. The table also gives the required power ratio of the two light sources. Although the table applies to strictly monochromatic sources ($\Delta\lambda \to 0$), the data can be used, as an excellent approximation, for sources exhibiting moderate spectral broadening such as LEDs.

The luminous efficacy of radiation of a dichromatic source is shown in Fig. 20.3. The figure reveals that the highest luminous efficacy of 440 lm/W occurs at a primary wavelength of $\lambda_1 = 445$ nm for $\Delta E = 2kT$. The very high value of the efficacy shows the great potential of dichromatic sources.

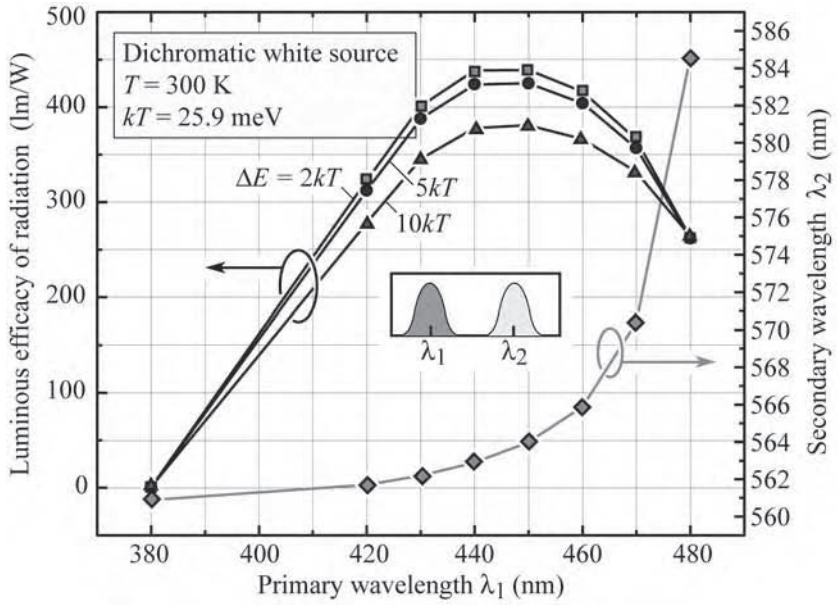


Fig. 20.3. Calculated luminous efficacy of dichromatic white-light source (with chromaticity point at $D_{65}$ standard illuminant) for different linewidths $\Delta E$ as a function of the primary wavelength. Also shown is the complementary secondary wavelength (after Li *et al.*, 2003).

Several approaches for the generation of white light by mixing two complementary colors have been demonstrated (Guo *et al.,* 1999; Sheu *et al*., 2002; Dalmasso *et al*., 2002; Li *et al*.,

2003). One possibility uses the mixing of light emitted by two LEDs, one emitting in the blue and the other one in the yellow spectral region. Another possibility, demonstrated by Guo *et al.* (1999), generates white light by using a GaN-based blue LED and a second semiconductor, AlGaInP, as a wavelength converter. Sheu *et al*. (2002) demonstrated a codoped single active region quantum well white LED. The active region is doped with both Si and Zn. Blue light emission originates from quantum well band-to-band transitions, whereas a wide yellowish emission originates from donor-acceptor-pair (D-A) transitions. Because the D-A transition is spectrally wide, the codoped approach has the advantage of good color rendering. A dichromatic monolithic LED has also been reported by Dalmasso *et al*. (2002), who employed two closely spaced GaInN active regions within the pn-junction region. A strong dependence of the emission spectrum on the injection current was found.

Li *et al*. (2003) reported a monolithic GaInN based LED with two active regions separated by a thin GaN layer. The device was designed for emission at 465 nm and 525 nm. The device structure is shown in Fig. 20.4.

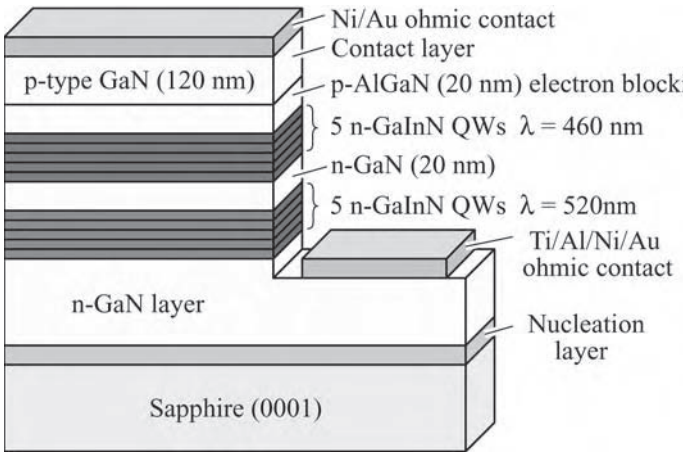


Fig. 20.4. Structure of a monolithic dichromatic LED with two active regions (after Li *et al*., 2003).

Photoluminescence results are shown in Fig. 20.5 (a). The spectra exhibit two emission bands one centered at about 465 nm and one at 525 nm. As the excitation density is varied, the two peak positions do not change. However, the ratio of the two peak intensities changes with the excitation power density of the laser. The excitation-density-dependent emission ratio can be explained by the competition of different recombination paths (Li *et al*., 2003). Neglecting non-radiative recombination, possible recombination paths of an electron in the blue quantum well (QW) are either direct radiative recombination in the blue QW or tunneling to the green QW with subsequent radiative recombination. Electrons and holes can tunnel from the blue QW to



Nichia Exhibit 1014
Page 151

the green QW and recombine there radiatively. However, once in the green QW, carriers cannot tunnel back to the blue QW due to the higher energy of this QW.

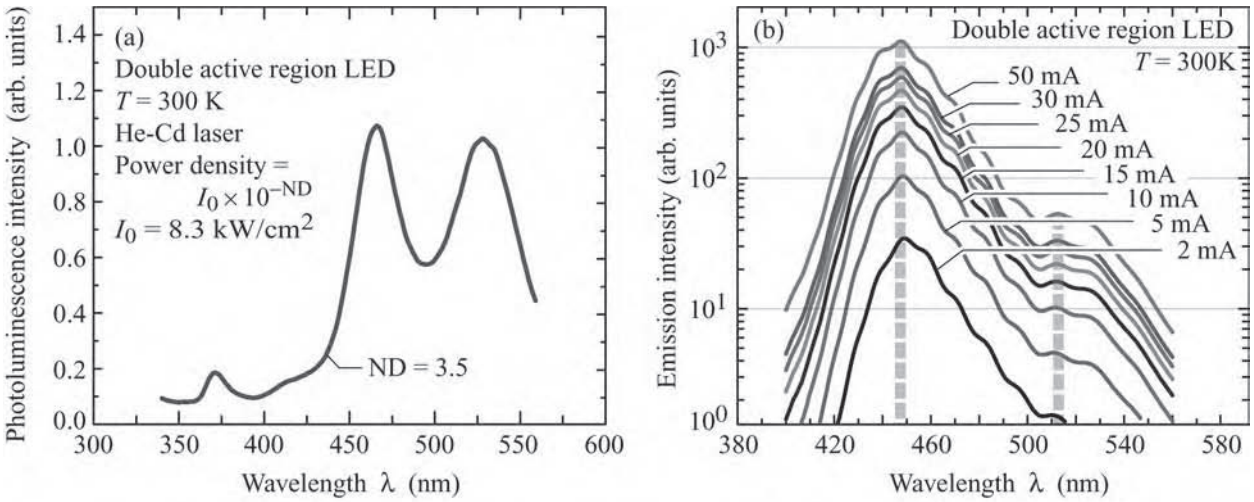


Fig. 20.5. Room temperature (a) photoluminescence and (b) electroluminescence spectra of monolithic dichromatic LED with two active regions (after Li *et al*., 2003).

Electroluminescence (EL) spectra of the device are shown in Fig. 20.5 (b). Two emission peaks are clearly observed with center wavelengths at about 450 nm and 520 nm. The blue peak is more intense than the green peak which can be attributed to the higher quantum efficiency of blue QWs compared with green QWs. In addition, holes are injected from the blue side (i.e. the side of the high-energy, blue-emitting QWs), whereas electrons are injected from the green side. As holes have a lower mobility and a higher effective mass, they are less likely to reach the green QWs, which can explain the higher intensity of the blue emission.

For current injection, holes are injected into the blue QWs, whereas electrons are injected into the green QWs. This is very different from optical excitation, where both types of carriers are injected from both sides of the active region. For the structure discussed here, the optical absorption length is longer than the distance between the active regions and the surface. This can explain the marked difference between the results for photoluminescence and electroluminescence (Li *et al*., 2003).

Room temperature *I–V* curves of the double-active region LED exhibit excellent forward voltages < 3.0 V at small contact diameters of 100 μm indicating high-quality ohmic contacts. The increase in forward voltage for contacts with larger diameters was attributed to an increased voltage drop in the n-type buffer layer, because, at a given current density, the current in the buffer layer scales with the area of the contact *A*, but the access resistance through the n-type

buffer layer scales with the circumference $A^{-1/2}$. In addition, the current crowding effect leads to non-uniform current injection particularly in large-diameter contacts and thus to an increased forward voltage.

### *20.3 Generation of white light by trichromatic sources*

Whereas high-quality white light suitable for illumination applications cannot be generated by additive mixing of *two* complementary colors, such high-quality white light can be generated by mixing of *three* primary colors or more than three colors. In a detailed analysis, Thornton (1971) showed that mixing of discrete emission bands with peak wavelengths near 450 nm, 540 nm, and 610 nm resulted in a high-quality source. Thornton (1971) reported experiments with 60 human subjects who judged the quality of a trichromatic source in terms of its color rendition capability of meat, vegetables, flowers, and complexion, to be "very good, if not excellent". Thornton (1971) also reported that, for high-quality color rendition of trichromatic sources, the use of emitters near 500 nm and 580 nm should be avoided.

Although Thornton (1971) established that trichromatic sources can have high quality, the individual emission bands used in the experiments had a broad spectral width: The full-widths at half-maximum of the phosphor emitters employed in the study exceeded 50 nm. Semiconductors, with typical spectral widths < 50 nm, have much narrower emission lines than phosphors.

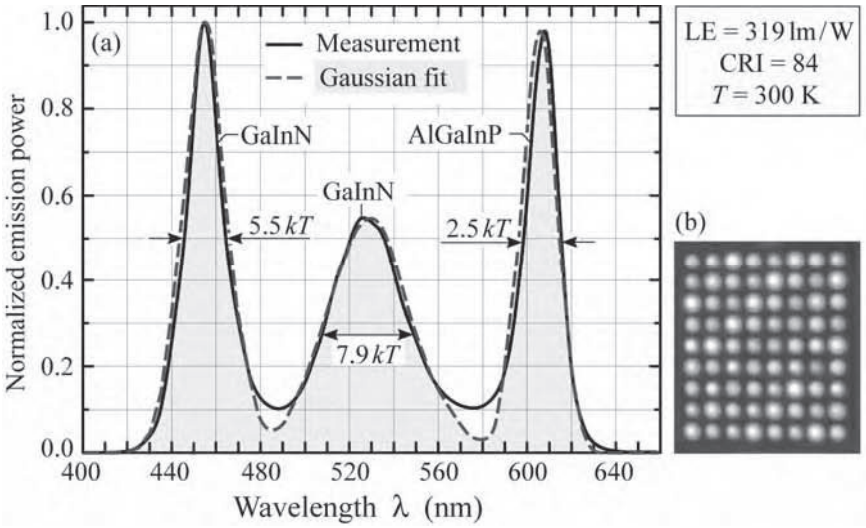


Fig. 20.6. (a) Emission spectrum of trichromatic white multi-LED source with color temperature of 6500 K (solid line) and gaussian fit (dashed line). The source has a luminous efficacy of radiation of 319 lm/W and a color rendering index of 84. (b) Photograph of source assembled from standard commercial devices (after Chhajed *et al.*, 2005).

The trichromatic emission spectrum of a white-light source made out of three types of LEDs emitting at 455 nm, 525 nm, and 605 nm is shown in Fig. 20.6 (a). The experimentally determined full-width at half-maximum of the spectra at room temperature (20 °C) is 5.5 $kT$,



Nichia Exhibit 1014
Page 153

7.9 $kT$, and 2.5 $kT$ for the GaInN blue, GaInN green, and AlGaInP orange emitter, respectively, where $kT = 25.25$ meV. The expression of the full-width at half-maximum in terms of $kT$ is very useful, as it can be easily related to the theoretical full-width at half-maximum of a thermally broadened emission band of a semiconductor, which is 1.8 $kT$. Using the full-width at half-maximum given in the figure and

$$\Delta\lambda \quad = \quad \frac{\lambda^2}{hc}\ \Delta E \quad = \quad \frac{(\lambda / \mathrm{nm})^2}{1239.8}\ (\Delta E / \mathrm{eV}) \ , \tag{20.3}$$

the full-widths at half-maximum of the blue, green, and orange sources are 23.2 nm, 44.3 nm, and 18.6 nm, respectively. Note that the green emission line is particularly broad, which can be attributed to alloy broadening and the formation of quantum-dot-like InN-rich regions within the high-In-content GaInN.

Also shown in the figure are gaussian fits to the experimental spectra. The gaussian fits match the experimental spectra well. Note that the gaussian curves (equations were given earlier in this chapter) are symmetric in terms of wavelength. *Asymmetric gaussian distributions*, which have a more pronounced long-wavelength tail, have been employed for phosphors (Ivey, 1963). The use of such asymmetric gaussian distributions does not appear to be warranted for semiconductors as their spectral power distribution is quite symmetric when plotted versus wavelength.

A photograph of the light source assembled from a large number of LEDs is shown in Fig. 20.6 (b). The power ratio of the orange, green, and blue emitters is adjusted to match the chromaticity of a planckian radiator with color temperature 6500 K. The LED source, assembled from standard commercial devices, has a luminous efficacy of radiation of 319 lm/W, a luminous source efficiency of 32 lm/W, and a color-rendering index of 84 (Chhajed *et al*., 2005).

There are a large number of possible wavelength combinations for trichromatic sources. To attain a high efficacy of radiation, sources near the fringes of the visible spectrum (deep red and deep violet) should be avoided. Contour plots of the luminous efficacy of radiation and of the color rendering index of a trichromatic source with color temperature of 6500 K are shown in Fig. 20.7 for a full-width at half-maximum for each emission line of 5 $kT$. Inspection of the figure reveals that $\lambda_1 = 455$ nm, $\lambda_2 = 530$ nm, and $\lambda_3 = 605$ nm are particularly favorable in terms of the color-rendering index. The CIE general CRI is about 85 for this wavelength combination with the luminous efficacy of radiation being 320 lm/W.

The figure also reveals that the CRI depends very sensitively on the exact peak positions. For

example, changing the red peak wavelength from 605 nm to 620 nm decreases the CRI from 85 to 65. Similarly, changing the green wavelength from 530 nm to 550 nm decreases the CRI to values less than 60.

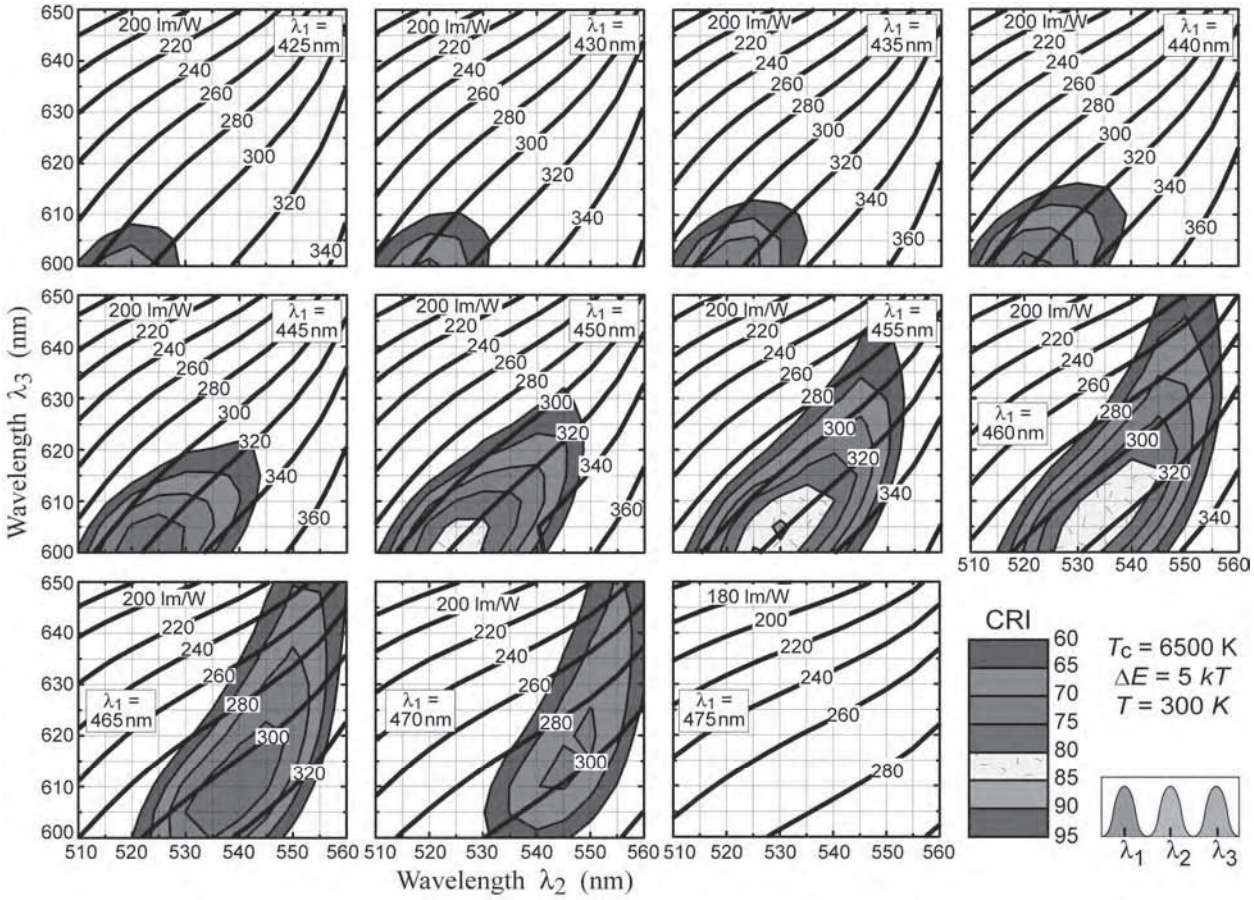


Fig. 20.7. Contour plot of luminous efficacy of radiation and CIE color-rendering index of white trichromatic LED source with color temperature 6500 K as a function of the three wavelengths for a linewidth (FWHM) of $5kT$ (after Chhajed *et al.*, 2005).

Contour plots of the luminous efficacy of radiation and of the color-rendering index of a trichromatic source with color temperature of 6500 K are shown in Fig. 20.8 for a full-width at half-maximum for each emission line of $8kT$. A higher CRI results from the broader emission lines. A very favorable combination in terms of a high CRI is obtained for $\lambda_1$ = 450–455 nm, $\lambda_2$ = 525–535 nm, and $\lambda_3$ = 600–615 nm, where a CRI in the range 90–95 is obtained.

### *20.4 Temperature dependence of trichromatic LED-based white-light source*

The relatively small range of wavelengths that enables a high color-rendering capability raises the question as to the stability of trichromatic sources with respect to junction and ambient



Nichia Exhibit 1014
Page 155

temperature. It is known that emission power ($P$), peak wavelength ($\lambda_{peak}$), and spectral width ($\Delta\lambda$) depend on temperature, each of these quantities having a different temperature coefficient.

The optical output power of LEDs is temperature dependent in a manner that can be described by an exponential function and a characteristic temperature, $T_1$. The light output power of an LED is then given by

$$P = P\big|_{300\,\mathrm{K}} \exp \frac{T - 300\,\mathrm{K}}{T_1} . \tag{20.4}$$

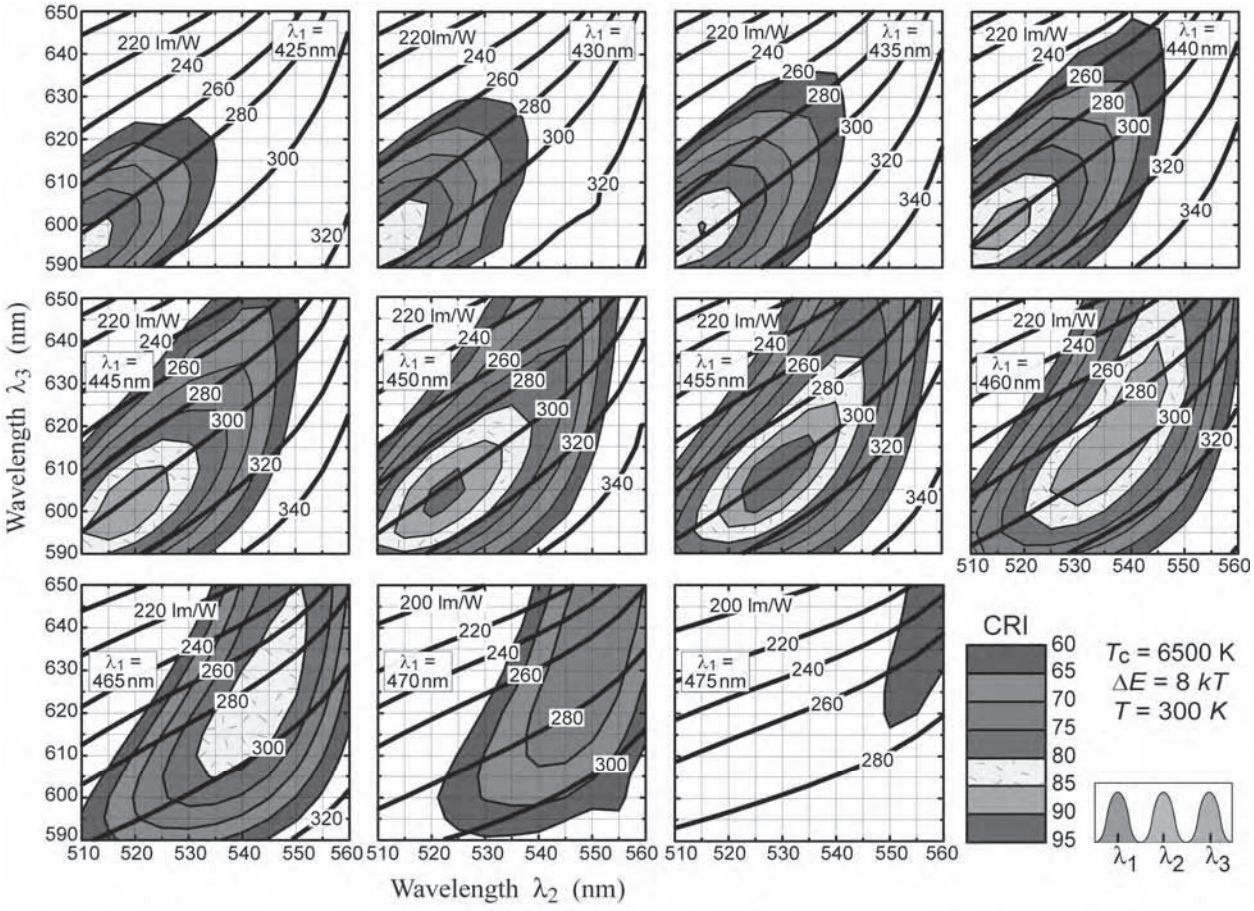


Fig. 20.8. Contour plot of luminous efficacy of radiation and CIE color-rendering index of white trichromatic LED source with color temperature 6500 K as a function of the three wavelengths for a linewidth (FWHM) of $8kT$ (after Chhajed *et al*., 2005).

As a result of these temperature dependences, the chromaticity point of a multi-LED white-light source changes with temperature. Consider a white-light source consisting of three types of emitters emitting in the red, green, and blue. For such LEDs, the temperature coefficients of the peak emission wavelength, spectral width, and emission power have been measured and are

given in Table 20.2 (Chhajed *et al*., 2005).

Table 20.2. Experimentally determined temperature coefficients for peak wavelength, spectral width, and emission power for blue, green, and red LEDs.

| | **Blue** | **Green** | **Red** |
|---|---|---|---|
| $d\lambda_{peak}/dT$ | 0.0389 nm / °C | 0.0308 nm / °C | 0.156 nm / °C |
| $d\Delta\lambda/dT$ | 0.0466 nm / °C | 0.0625 nm / °C | 0.181 nm / °C |
| $T_{characteristic}$ | 493 K | 379 K | 209 K |

Consider further that the three currents feeding the red, green, and blue LEDs are adjusted in such a way that the resulting chromaticity point equals that of Illuminant $D_{65}$ when the device temperature is 20 °C. The optical spectrum of such a trichromatic white source is shown in Fig. 20.9.

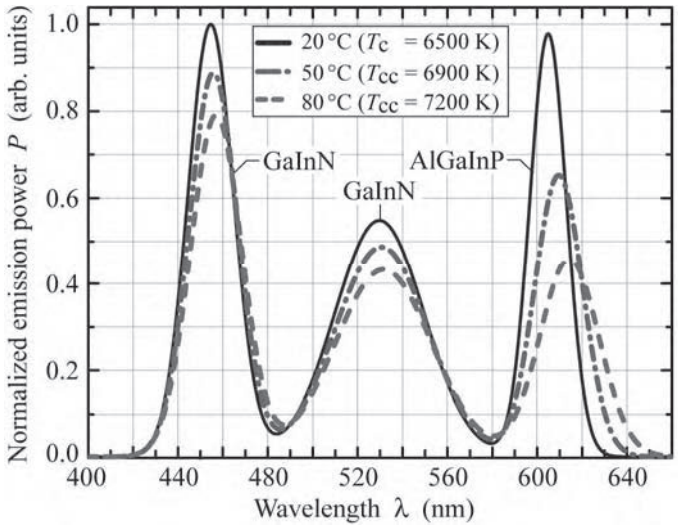


Fig. 20.9. Emission spectrum of trichromatic white LED source for different ambient temperatures (junction heating neglected). Optical power, linewidth, and peak wavelength change with temperature. As a result of these changes, the color temperature of the source increases (after Chhajed *et al*., 2005).

However, as the device temperature increases, the chromaticity point of the trichromatic source changes due to the temperature dependences of the emission power, peak wavelength, and spectral width. This shift of the chromaticity point is shown in Fig. 20.10. Inspection of the figure reveals that the chromaticity point shifts towards higher color temperatures. This can be explained by the stronger temperature dependence of the red LED emission power. At high temperatures, the red component of the light source decreases more strongly (due to low $T_1$ value) than the green component, and the blue component, which is particularly stable.

Figure 20.11 shows the chromaticity shift of the trichromatic source on a magnified scale in the CIE 1931 ($x$, $y$) chromaticity coordinate system as well as in the CIE 1976 ($u'$, $v'$) uniform



Nichia Exhibit 1014
Page 157

chromaticity coordinate system along with the planckian locus. At $T_j$ = 50 °C, the chromaticity point is 0.009 units away from the original point, and at 80 °C, it is shifted 0.02 units from the original point. This shift causes a clearly noticeable change in color appearance and exceeds the deviation limit of 0.01 units ("***0.01 rule***") commonly used in the lighting industry (Duggal, 2005).

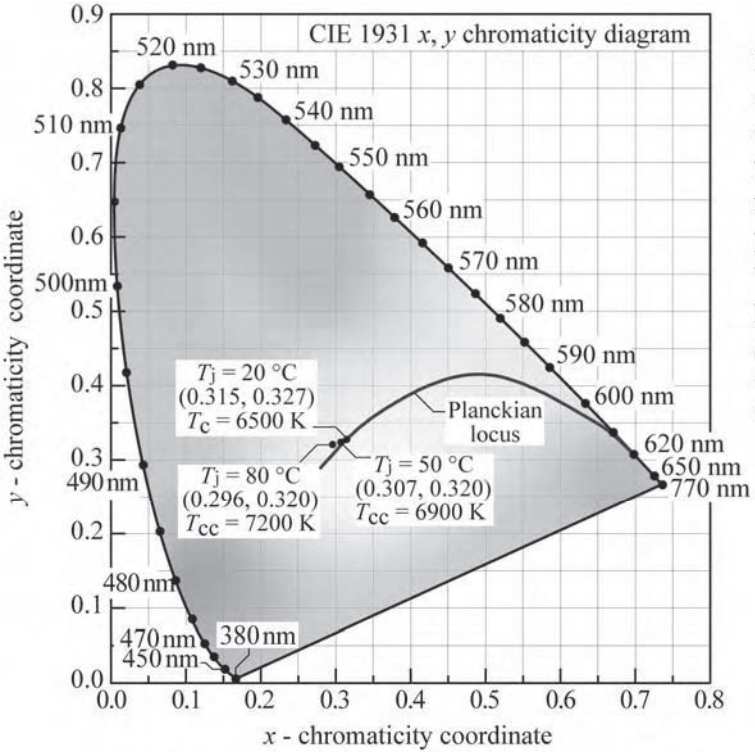


Fig. 20.10. Change in chromaticity of trichromatic white LED-based source. The source color temperature is 6500 K when devices are at room temperature. Due to the dependence of emission power, peak wavelength, and linewidth on temperature, the chromaticity point migrates off the planckian locus as the device temperature increases (after Chhajed *et al*., 2005).

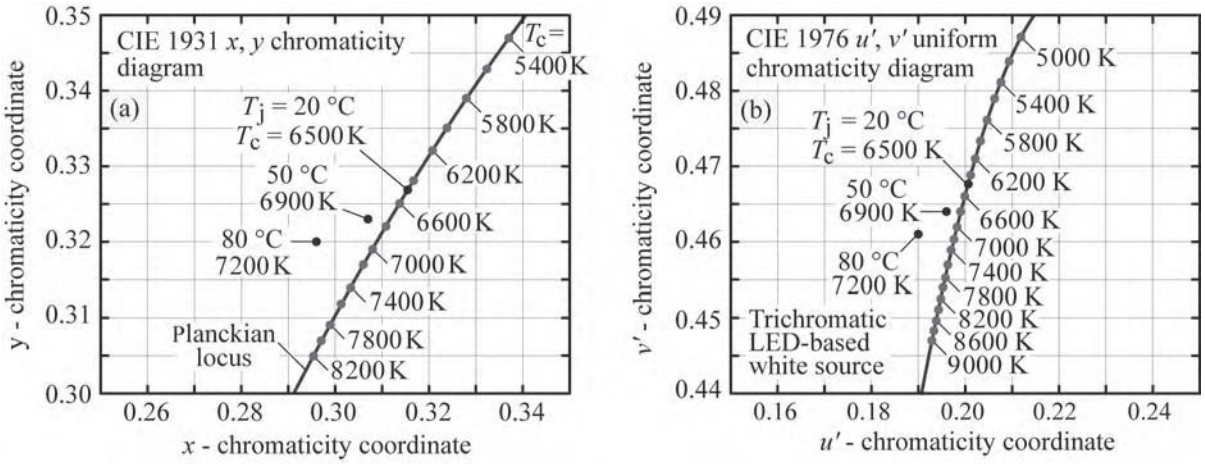


Fig. 20.11. Change in (a) $x$, $y$ and (b) $u'$, $v'$ chromaticity of trichromatic white LED source. $T_c$ = 6500 K when p-n junctions are at room temperature (after Chhajed *et al*., 2005).

The shift in chromaticity can be eliminated by adjusting the relative power ratio of the three LED sources. There are two possible implementations for adjusting the power ratio. In one implementation, the spectrum of the light source is constantly measured and a feedback control is used to adjust the optical power of the three components. In an alternative implementation, the device temperature is monitored and the optical power of the three components is adjusted using the known temperature dependence of the different types of emitters. The second method is easier due to the simplicity of a temperature measurement. However, the second method does not enable a compensation for device-aging effects.

### *20.5 Generation of white light by tetrachromatic and pentachromatic sources*

Tetrachromatic and pentachromatic white sources use four and five types of LEDs, respectively (Zukauskas *et al*., 2002a; Schubert and Kim, 2005). The color-rendering index of polychromatic sources generally increases with the number of sources. However, the luminous efficacy generally decreases with increasing number of sources. Thus, the color-rendering index and the luminous efficacy of tetrachromatic sources are generally higher and lower than those of trichromatic sources, respectively. However, the specifics depend on the exact choice of the emission wavelengths. Due to the greater number of wavelength choices, the color temperatures of such sources can be adjusted more liberally without compromising the color-rendering capability of the source.

### *References*

Bergh A., Craford G., Duggal A., and Haitz R. "The promise and challenges of solid-state lighting" *Physics Today* p. 42 (December 2001)

Chhajed S., Xi Y., Li Y.-L., Gessmann Th., and Schubert E. F. "Influence of junction temperature on chromaticity and color rendering properties of trichromatic white light sources based on light-emitting diodes" *J. Appl. Phys*. **97**, 054506 (2005)

Duggal A. R. "Organic electroluminescent devices for solid-state lighting" in *Organic Electroluminescence* edited by Z. H. Kafafi (Taylor & Francis Group, Boca Raton, Florida, 2005)

Dalmasso S., Damilano B., Pernot C., Dussaigne A., Byrne D., Grandjean N., Leroux M., and Massies J. "Injection dependence of the electroluminescence spectra of phosphor free GaN-based white light emitting diodes" *Phys. Stat. Sol. (a)* **192,** 139 (2002)

Guo X., Graff J. W., and Schubert E. F. "Photon-recycling semiconductor light-emitting diodes" *IEDM Technol. Dig.*, **IEDM-99**, 600 (1999)

Ivey H. F. "Color and efficiency of luminescent light sources" *J. Opt. Soc. Am.* **53**, 1185 (1963)

Li Y.-L., Gessmann Th., Schubert E. F., and Sheu J. K. "Carrier dynamics in nitride-based light-emitting p-n junction diodes with two active regions emitting at different wavelengths" *J. Appl. Phys.* **94**, 2167 (2003)

Schubert E. F. and Kim J. K. "Solid-state light sources becoming smart" *Science* **308**, 1274 (2005)



Nichia Exhibit 1014
Page 159

# 21

## White-light sources based on wavelength converters

The generation of white light by a semiconductor LED whose light is partially or fully used to optically excite one or several phosphors, is a viable and common method to generate white light for general illumination applications. There are several different approaches to generate white light based on phosphors excited by semiconductor LEDs, which are shown in Fig. 21.1. They can be classified in dichromatic, trichromatic, and tetrachromatic approaches. These approaches use either UV-excitation sources or visible-spectrum-excitation sources (mostly blue semiconductor LEDs).

Generally, the luminous source efficiency decreases with increasing multi-chromaticity of the source. Thus, dichromatic sources have the highest luminous efficacy of radiation and also the highest potential luminous source efficiency. On the other hand, the color-rendering capability is lowest for dichromatic sources and it increases with the multi-chromaticity of the source. The color-rendering index can reach values very close to CRI = 100 for tetrachromatic sources.

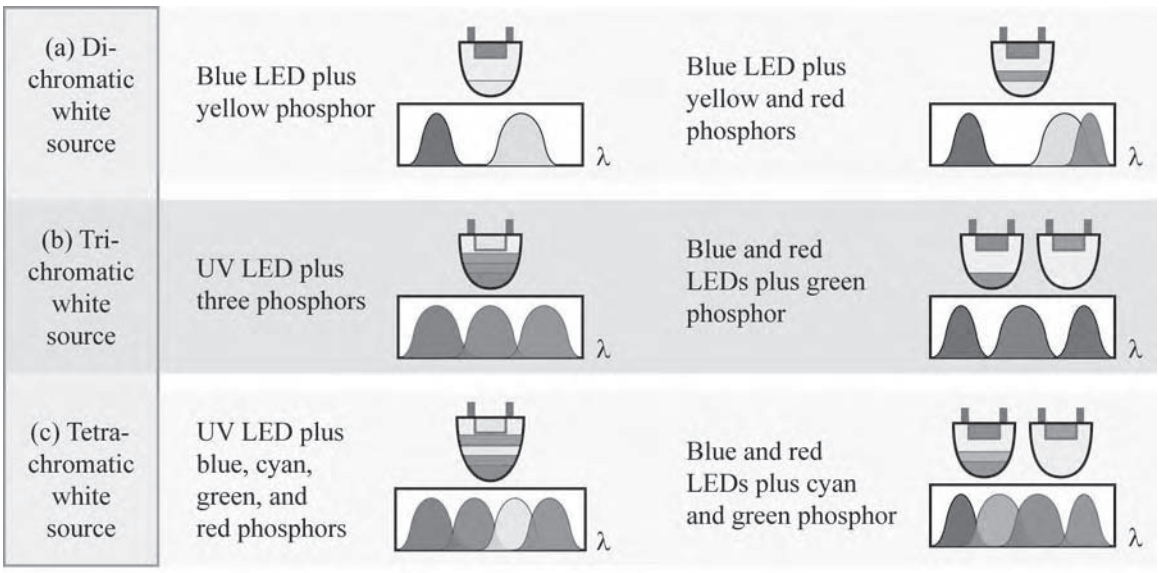


Fig. 21.1. White sources using phosphors that are optically excited by UV or blue LEDs.



Nichia Exhibit 1014
Page 160

## 21.1 Efficiency of wavelength-converter materials

The conversion efficiency of short-wavelength light to long-wavelength light by a ***wavelength-converter*** (λ-converter) material is determined by two distinct factors, namely (*i*) the external quantum efficiency of the λ-converter and (*ii*) the inherent quantum-mechanical-energy loss incurred in wavelength conversion.

The ***external quantum efficiency*** of the converter material, $\eta_{ext}$, is given by

$$\eta_{ext} = \frac{\text{number of photons emitted into free space by } \lambda\text{-converter per second}}{\text{number of photons absorbed by } \lambda\text{-converter per second}} . \qquad (21.1)$$

The external efficiency originates in the *internal efficiency* and the *extraction efficiency* of the converter material according to $\eta_{ext} = \eta_{internal}\ \eta_{extraction}$. Note that the internal quantum efficiency depends on the inherent efficiency of the material whereas the extraction efficiency depends on the spatial distribution of the λ-converter material. Generally, thin films have high extraction efficiencies whereas lumpy aggregations of converter materials have lower extraction efficiency due to reabsorption. It is therefore desirable to employ λ-converter materials in the form of thin layers.

The inherent ***wavelength-conversion loss*** (sometimes called ***quantum deficit*** or ***Stokes shift***) incurred when converting a photon with wavelength $\lambda_1$ to a photon with wavelength $\lambda_2$ ($\lambda_1 < \lambda_2$) is given by

$$\Delta E = h\nu_1 - h\nu_2 = \frac{hc}{\lambda_1} - \frac{hc}{\lambda_2} . \qquad (21.2)$$

Thus the wavelength-conversion efficiency is given by

$$\eta_{\lambda\text{-conversion}} = \frac{h\nu_2}{h\nu_1} = \frac{\lambda_1}{\lambda_2} \qquad (21.3)$$

where $\lambda_1$ is the wavelength of the photon absorbed by the phosphor and $\lambda_2$ is the wavelength of the photon emitted by the phosphor. Note that wavelength-conversion loss is fundamental in nature. The loss cannot be overcome with conventional λ-converter materials.

However, ***quantum-splitting phosphors*** allow one to convert one short-wavelength photon into two longer-wavelength photons so that $h\nu_1 = h\nu_2 + h\nu_3$, where $h\nu_1$ is the energy of the photon absorbed by the phosphor and $h\nu_2$ and $h\nu_3$ are the energies of the photons emitted by the

phosphors. Several quantum-splitting phosphors have been reported (Justel *et al*., 1998; Wegh *et al*., 1999; Srivastava and Ronda, 2003; Srivastava, 2004). The possibility of quantum efficiencies approaching 200% for $Eu^{3+}$-doped $LiGdF_4$ has been proposed (Wegh *et al.*, 1999). The quantum-splitting phosphor $YF_3:Pr^{3+}$ at room temperature has a quantum efficiency of about 140% for 185 nm excitation (Justel *et al.*, 1998). However, viable quantum phosphors suitable for commercial applications have not yet been demonstrated.

The power-conversion efficiency of a wavelength converter is the product of Eqs. (21.1) and (21.3)

$$\eta_{\lambda\text{-converter}} = \eta_{\lambda\text{-conversion}}\, \eta_{\text{ext}} \,. \tag{21.4}$$

The inherent wavelength-conversion loss is the reason that λ-converter-based white LEDs such as phosphor-based white LEDs have a fundamentally lower efficiency limit than white-light sources based on multiple LEDs.

The wavelength-conversion loss is highest for wavelength conversion from the UV to the red. For example, the conversion from UV (405 nm) to red (625 nm) can have a λ-conversion efficiency of at most 65%. The low λ-conversion efficiency represents a strong driving force to employ red LEDs (rather than red phosphors) in highly efficient lighting systems.

Most white-light emitters use an LED emitting at short wavelength (e.g. blue) and a ***wavelength converter***. Some of the light emitted by the blue LED is absorbed in the converter material and then re-emitted as light with a longer wavelength. As a result, the lamp emits at least two different wavelengths. The types and characteristics of wavelength-converter materials will be discussed below.

The possibility that white light can be generated in different ways raises the question as to which is the optimum way to generate white light? There are two parameters that need to be considered: Firstly, the luminous efficiency and, secondly, the color-rendering index. For *signage applications*, the luminous efficiency is of primary importance and the color-rendering index is irrelevant. For *illumination applications*, both the luminous efficiency and the color-rendering index are important.

White-light sources employing two monochromatic complementary colors result in the highest possible luminous efficacy. However, the color-rendering index of such a dichromatic light source is lower than that of broad-band emitters.

The maximum luminous efficacy of radiation, attainable for white light created by two complementary monochromatic colors was calculated by MacAdam (1950). MacAdam showed



Nichia Exhibit 1014
Page 162

that luminous efficacies exceeding 400 lm/W can be attained using a dichromatic source for white-light generation. The work of MacAdam (1950) was further refined by Ivey (1963) and Thornton (1971). These authors showed that dichromatic white-light sources have high luminous efficacy but low color-rendering properties, making them perfectly suitable for display applications but unsuitable for daylight illumination applications. In addition, Thornton (1971) showed that trichromatic white-light sources, i.e. sources creating white light by additive mixing of three discrete colors, have a color-rendering index suited for most applications. Thornton reported on an experiment in which 60 observers judged the color rendition of meat, vegetables, flowers, complexions, etc., when illuminated with a trichromatic light source with peak wavelengths at 450, 540, and 610 nm. The color rendition in this experiment was found to be "very good, if not excellent" illustrating the suitability of trichromatic white-light sources as potent daylight illumination sources.

A white-light source duplicating the sun's spectrum would have good color-rendering capability. However, the radiation efficacy of such a light source would be lower than what is possible with other spectral distributions, e.g. a trichromatic distribution. The sun's spectrum has strong emission near the boundaries of the visible spectrum (390 and 720 nm) where the eye sensitivity is very low. Thus exact duplication of the sun's spectrum is not a viable strategy for high-efficiency light sources.

## *21.2 Wavelength-converter materials*

There are several types of converter materials including ***phosphors***, ***semiconductors***, and ***dyes***. Converter materials have several parameters of interest, including the absorption wavelength, the emission wavelength, and the quantum efficiency. A good converter has near 100% quantum efficiency. The overall power-conversion efficiency of a wavelength converter is given by

$$\eta = \eta_{ext}\,(\lambda_1 / \lambda_2) \tag{21.5}$$

where $\eta_{ext}$ is the external quantum efficiency of the converter, $\lambda_1$ is the wavelength of photons absorbed by the phosphor, and $\lambda_2$ is the wavelength of photons emitted by the phosphor. Even if the external quantum efficiency is unity, there is always energy loss associated with the wavelength-conversion process, so that the power-conversion efficiency of a wavelength converter is always less than unity.

The most common wavelength-converter materials are ***phosphors*** and they will be discussed in greater detail in the following section. The optical absorption and emission spectrum of a

commercial phosphor is shown in Fig. 21.2. The phosphor displays an absorption band and a lower-energy emission band. The emission band is rather broad, making this particular phosphor suitable for white-light emission. Phosphors are very stable materials and can have quantum efficiencies close to 100%. A common phosphor used for white LEDs is cerium-doped (Ce-doped) YAG phosphor (Nakamura and Fasol, 1997). For Ce-doped phosphors, quantum efficiencies of 75% have been reported (Schlotter *et al.*, 1999).

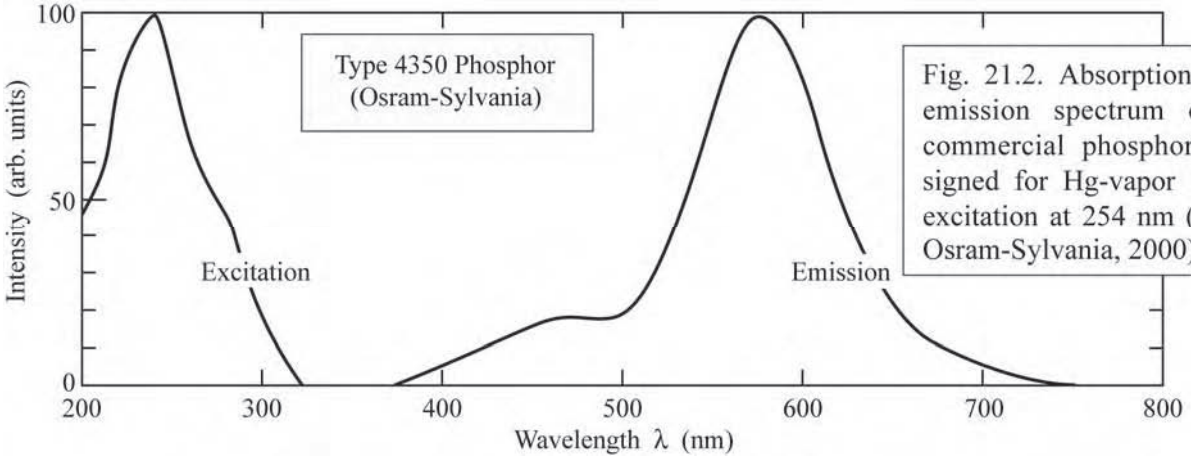


Fig. 21.2. Absorption and emission spectrum of a commercial phosphor designed for Hg-vapor lamp excitation at 254 nm (after Osram-Sylvania, 2000).

***Dyes*** are another type of wavelength converter. Many different dyes are commercially available. An example of a dye optical absorption and emission spectrum is shown in Fig. 21.3. Dyes can have quantum efficiencies close to 100%. However, dyes, as organic molecules, lack the long-term stability afforded by phosphors and semiconductors.

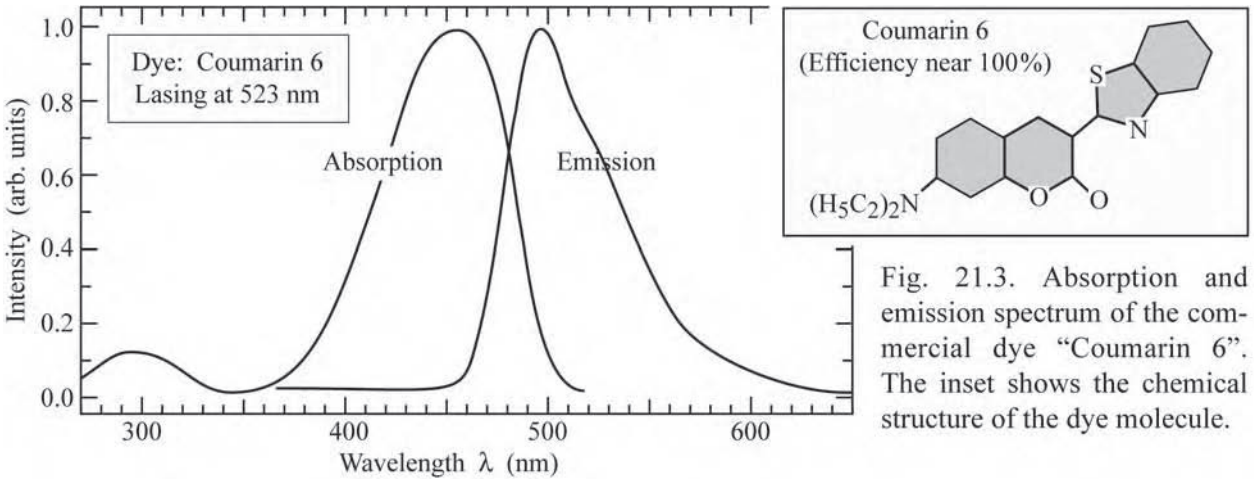


Fig. 21.3. Absorption and emission spectrum of the commercial dye "Coumarin 6". The inset shows the chemical structure of the dye molecule.

Finally, ***semiconductors*** are another type of wavelength converter. Semiconductors are



Nichia Exhibit 1014
Page 164

characterized by narrow emission lines with linewidths of the order of $2kT$. The spectral emission linewidth of semiconductors is narrower than the linewidth of many phosphors and dyes. Thus, semiconductors allow one to tailor the emission spectrum of a semiconductor wavelength converter with good precision.

As for phosphors and dyes, semiconductors can have internal quantum efficiencies near 100%. The light escape problem in semiconductor converters is less severe than it is in LEDs due to the fact that semiconductor converters do not need electrical contacts that could block the light.

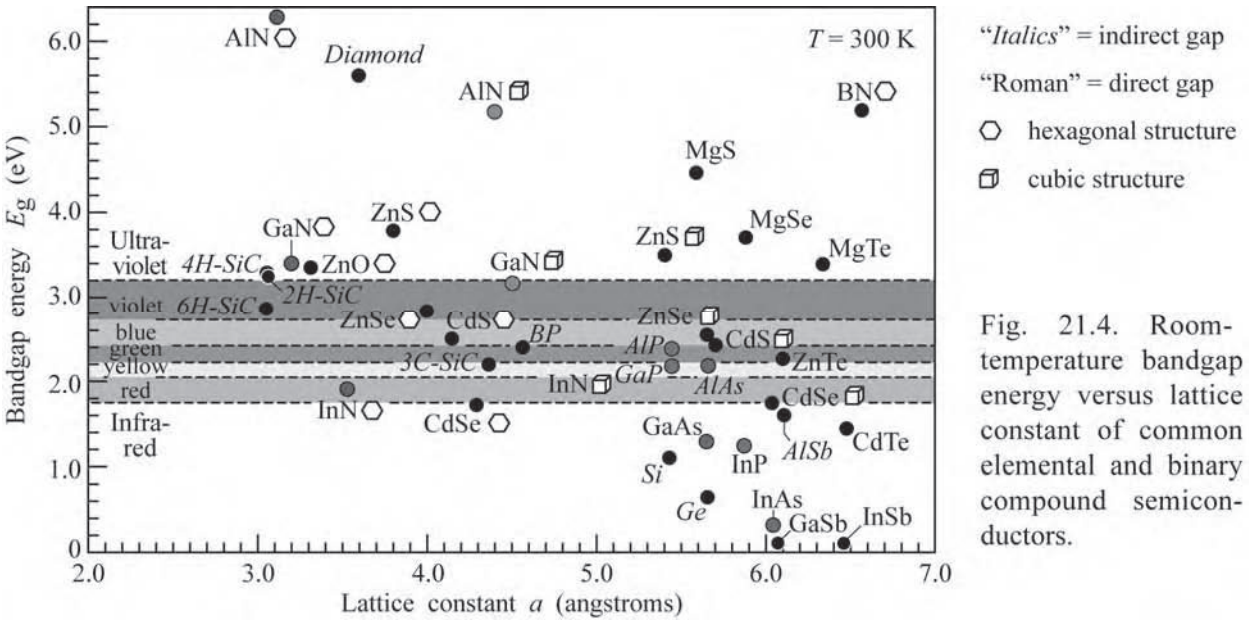


Fig. 21.4. Room-temperature bandgap energy versus lattice constant of common elemental and binary compound semiconductors.

Similar to phosphors and dyes, a great variety of semiconductors is available. Figure 21.4 shows elemental and binary compound semiconductors versus the semiconductor lattice constant. Using ternary or quaternary alloys, wavelength converters operating at virtually any visible wavelength can be fabricated.

## *21.3 Phosphors*

Phosphors consist of an inorganic host material doped with an optically active element. Common hosts are ***garnets***, which have the chemical formula $A_3B_5O_{12}$ where A and B are chemical elements and O is oxygen. Among the large group of garnets, yttrium aluminum garnet (YAG), $Y_3Al_5O_{12}$, is a particularly common host material. Phosphors having YAG as a host material are called ***YAG phosphors***. The optically active dopant is a rare-earth element, a rare-earth oxide, or

another rare-earth compound. Most rare-earth elements are optically active. Rare-earth light-emitting elements include cerium (Ce) used in white-light YAG phosphors, neodymium (Nd) used in lasers (Nd-doped YAG lasers), erbium (Er) used in optical amplifiers, and thorium (Th) oxide used in the mantle of gas lights.

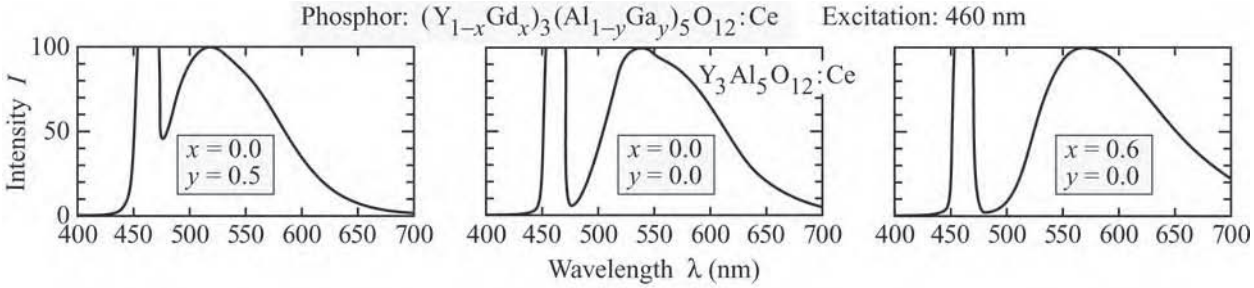


Fig. 21.5. Emssion spectrum of Ce-doped yttrium aluminum garnet (YAG:Ce) phosphor for different chemical compositions. The excitation wavelength is 460 nm (after Nakamura and Fasol, 1997).

The optical characteristics of YAG phosphors can be modified by partially substituting Gd for Y and Ga for Al so that the phosphor host has the composition $(Y_{1-x}Gd_x)_3(Al_{1-y}Ga_y)_5O_{12}$. The emission spectra for a Ce-doped $(Y_{1-x}Gd_x)_3(Al_{1-y}Ga_y)_5O_{12}$ phosphor with different compositions are shown in Fig. 21.5 (Nakamura and Fasol, 1997). The figure reveals that the addition of Gd shifts the emission spectrum to longer wavelengths whereas the addition of Ga shifts the emission spectrum to shorter wavelengths.

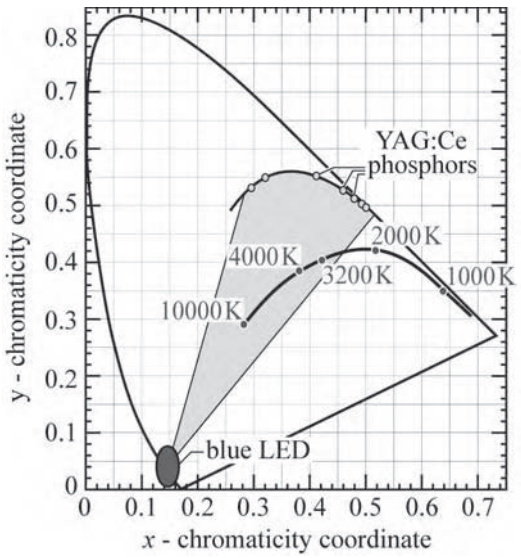


Fig. 21.6. Chromaticity points of YAG:Ce phosphor, and the general area (shaded) accessible to white emitters consisting of a blue LED and YAG:Ce phosphor (adapted from Nakamura and Fasol, 1997). Also shown is the planckian locus with color temperatures.

The chromaticity points of the YAG:Ce phosphors are shown in Fig. 21.6. The shaded region


Nichia Exhibit 1014
Page 166

reveals the chromaticities that can be attained by mixing light from a blue LED source with the light of YAG:Ce. The figure reveals that such white emitters can have a very high color temperature.

An alternative to YAG phosphor is ***TAG phosphor***, which is based on terbium aluminum garnet, $Tb_3Al_5O_{12}$. Both YAG and TAG crystallize with the garnet structure. Additionally, the $Y^{3+}$ and $Tb^{3+}$ ionic radii are very close ($r_{Y3+}$ = 1.02 Å and $r_{Tb3+}$ = 1.04 Å). Consequently, the X-ray diffraction pattern of YAG does not strongly change as Y in YAG is substituted with Tb, even for Tb mol fractions of 30% (Potdevin *et al*., 2005). Although TAG phosphors may have slightly lower radiative efficiency than YAG phosphors, TAG phosphors represent a viable alternative to YAG phosphors (Kim, 2005).

## *21.4 White LEDs based on phosphor converters*

A white LED lamp using a phosphor wavelength converter and a blue GaInN/GaN optical excitation LED was first reported by Bando *et al.* (1996) and reviewed by Nakamura and Fasol (1997). The GaInN/GaN LED used for optical excitation ("optical pumping") was a device reported by Nakamura *et al.* (1995). The phosphor used as a wavelength converter was Ce-doped YAG with chemical formula $(Y_{1-a}Gd_a)_3\,(Al_{1-b}Ga_b)_5\,O_{12}$ : Ce. The exact chemical composition of the host (YAG) and the dopants (e.g. Ce) is usually proprietary and not publicly available.

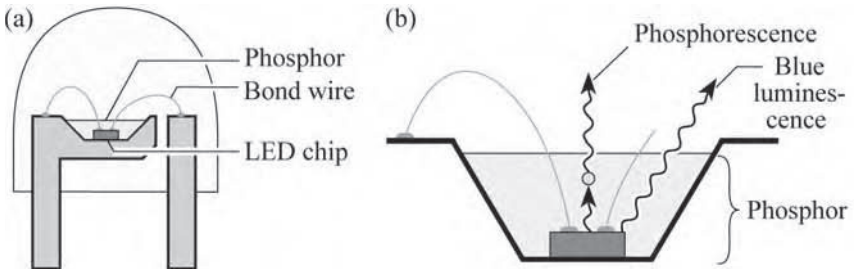


Fig. 21.7. (a) Structure of white LED lamp consisting of a GaInN blue LED chip and a phosphor. (b) Wavelength-converting phosphorescence and blue luminescence (after Nakamura and Fasol, 1997).

The cross-sectional structure of a white LED lamp is shown in Fig. 21.7 (a). The figure shows the LED die emitting in the blue and the YAG phosphor surrounding the die. The YAG phosphor can be made as a powder and suspended in epoxy resin. During the manufacturing process, a droplet of the YAG phosphor suspended in the epoxy is deposited on the LED die, so that the resin fills the cup-shaped depression in which the LED die is located, as shown in Fig. 21.7 (b). As indicated in the figure, a fraction of the blue light is absorbed by the phosphor and re-emitted as longer-wavelength light.

The emission spectrum of the phosphor-based white lamp thus consists of the blue emission

band originating from the semiconductor LED and longer-wavelength phosphorescence, as shown in Fig. 21.8. The thickness of the phosphor-containing epoxy and the concentration of the phosphor suspended in the epoxy determine the relative strengths of the two emission bands. The two bands can thus be adjusted to optimize the luminous efficiency and the color-rendering characteristics of the LED.

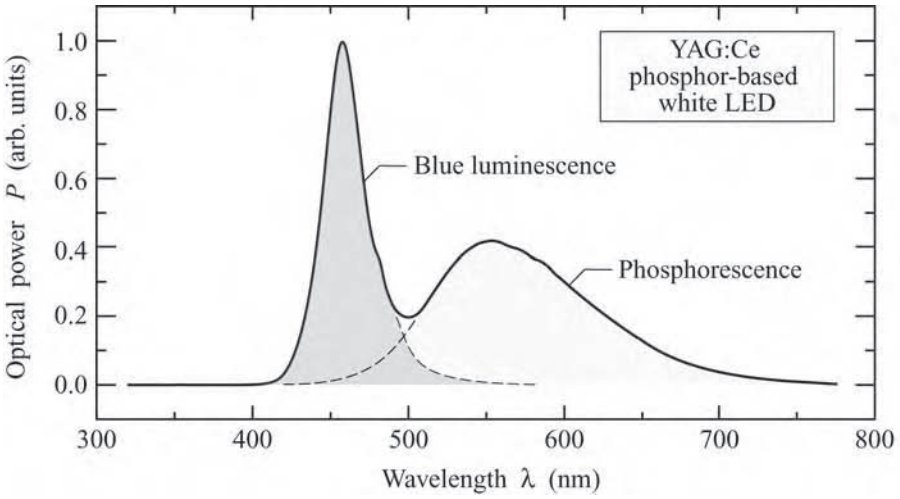


Fig. 21.8. Emission spectrum of a phophor-based white LED manufactured by Nichia Corporation (Anan, Tokushima, Japan).

The location of the white lamp in the chromaticity diagram is shown in Fig. 21.9. The location suggests that the emission color is white with a bluish tint. A bluish white is indeed confirmed when looking at the lamp.

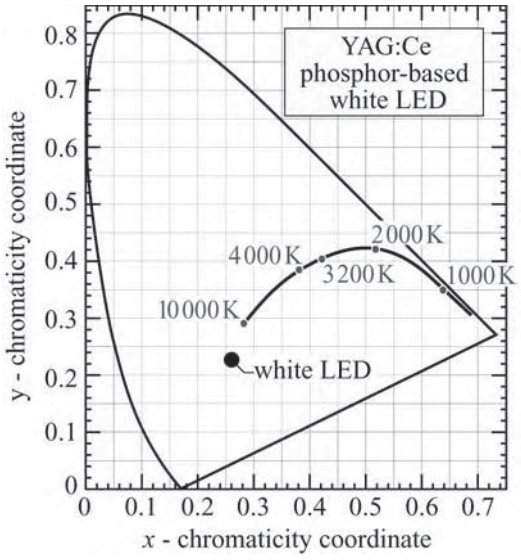


Fig. 21.9. Chromaticity coordinates of a commercial phophor-based white LED manufactured in 2001 by Nichia Corporation (Anan, Tokushima, Japan). Also shown is the planckian locus and associated color temperatures.

First-generation white LEDs from Nichia Corporation were improved in terms of their color



Nichia Exhibit 1014
Page 168

rendering capability by adding an additional phosphor that, when excited by 460 nm blue light, has a peak emission wavelength of 655 nm and a full-width at half-maximum of 110 nm (Narukawa, 2004). As a result, the emission can be enhanced in the red range, as shown in Fig. 21.10. Furthermore, by using an optimized phosphor mix, the pronounced notch in the first-generation white LED is reduced. The second-generation white LED lamps from Nichia Corporation (Narukawa, 2004) render red colors better than the first-generation and have a lower color temperature that can range between 2800 K (warm white) and 4700 K depending on the phosphor mix.

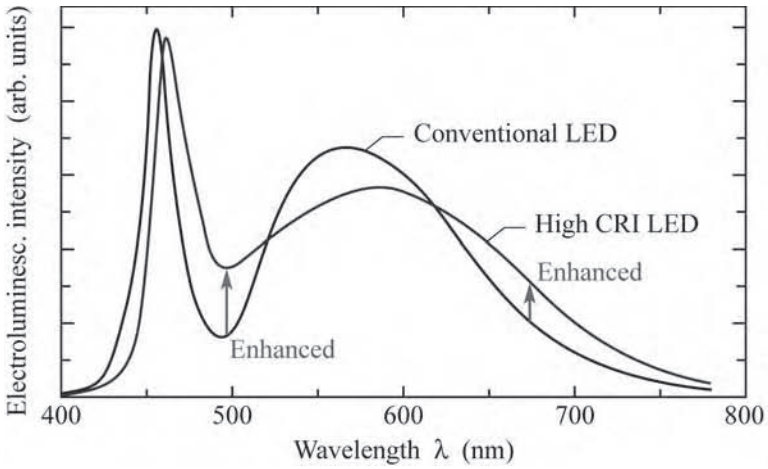


Fig. 21.10. Electroluminescence spectrum of conventional white LED and of high-color-rendering-index white LED. The high CRI results from the broader emission spectrum and the reduction of the notch in the spectrum (after Narukawa, 2004).

Note that the downside of adding red phosphors is a reduced luminous efficiency: The large Stokes shift of red phosphors reduces the efficiency (excitation 460 nm; emission 655 nm) Furthermore, it is well known that red phosphors excitable at 460 nm are comparatively inefficient. Thus, although color rendering capabilities are improved, they are improved at the expense of luminous efficiency.

A concern with white sources is spatial ***color uniformity***. The chromaticity of the white source should not depend on the emission direction. Color uniformity can be attained by a phosphor distribution that provides an ***equal optical path length*** in the phosphor material independent of the emission direction (Reeh *et al*., 2003).

Spatial uniformity can also be attained by adding ***mineral diffusers*** to the encapsulant (Reeh *et al*., 2003). Such mineral diffusers are optically transparent substances, such as $TiO_2$, $CaF_2$, $SiO_2$, $CaCO_3$, and $BaSO_4$, with a refractive index different from the encapsulant. The diffuser will cause light to reflect, refract, and scatter, thereby randomizing the propagation direction and uniformizing the far-field distribution in terms of chromaticity (i.e. spectral composition).

### *21.5 Spatial phosphor distributions*

The ***spatial phosphor distribution*** in white LED lamps strongly influences the color uniformity and efficiency of the lamp. One can distinguish between ***proximate*** and ***remote phosphor distributions*** (Goetz, 2003; Holcomb *et al*., 2003; Kim *et al*., 2005; Luo *et al*., 2005; Narendran *et al*., 2005). In proximate phosphor distributions, the phosphor is located in close proximity to the semiconductor chip. Proximate phosphor distributions are shown in Fig. 21.11(a) and (b). In remote phosphor distributions, the phosphor is spatially removed from the semiconductor chip. A remote phosphor distribution is shown in Fig. 21.11(c).

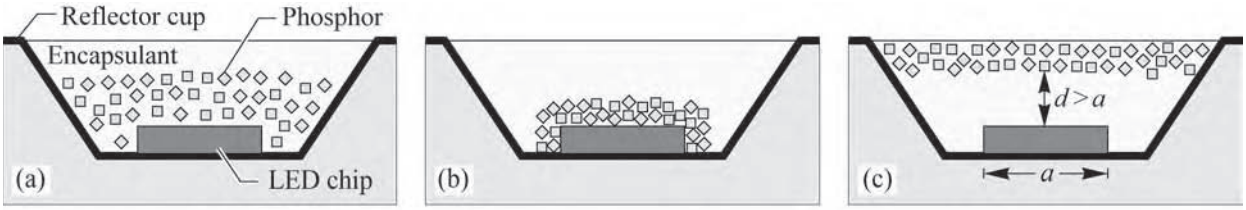


Fig. 21.11. (a) Proximate phosphor distribution, (b) proximate conformal phosphor distribution, and (c) remote phosphor distribution in which phosphor and chip are separated by at least one times the lateral dimension of the chip (after Kim *et al*., 2005).

Photographs of the different phosphor distributions are shown in Fig. 21.12. The proximate phosphor distribution shown in Fig. 21.12(a) was introduced by Nichia Corporation during the 1990s. The phosphor particles are dissolved in the encapsulation material that is dispensed into the reflector cup. Gravity, buoyancy, and friction generally lead to a distribution of phosphor particles that favors larger phosphor particles to move downward, thereby bringing them closer to the chip surface.

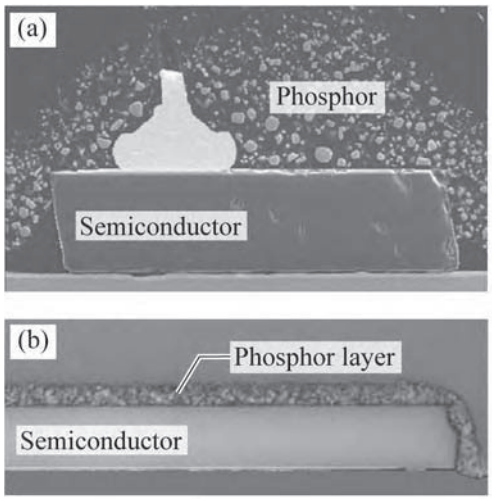


Fig. 21.12. Phosphor distributions in white LEDs: (a) Proximate phosphor distribution. (b) Proximate conformal phosphor distribution. (c) Remote phosphor distribution ((a) and (b) adopted from Goetz, 2003; (c) after Kim *et al*., 2005).

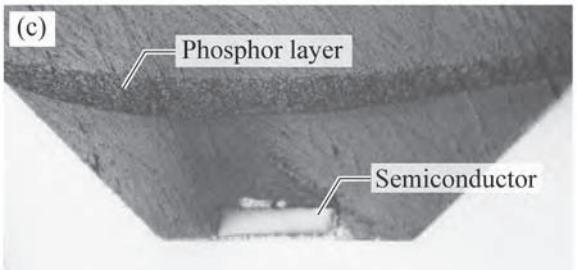




Nichia Exhibit 1014
Page 170

Another proximate phosphor distribution, called the ***conformal phosphor distribution***, is shown in Fig. 21.12 (b). Conformal phosphor distributions are accomplished by wafer-level phosphor dispensation thereby lowering the manufacturing cost as compared with a lamp-level phosphor dispensation. Conformal phosphor distributions provide a small emission area and high luminance, which is particularly relevant for imaging-optics applications. Imaging-optics applications (e.g. automotive headlights) frequently require the use of lenses. Optical design considerations show that point-like sources, i.e. sources with a small emission area, are desirable for these applications.

A general drawback of proximate phosphor distributions is the absorption of phosphorescence by the semiconductor chip. Phosphorescence emitted toward the semiconductor chip can be absorbed by the chip, e.g. by the metal contacts covering the chip. The reflectivity of the semiconductor chip and metal contacts is generally not very high.

This drawback can be avoided by remote phosphor distributions in which the phosphor is spatially distanced from the semiconductor chip (Kim *et al*., 2005; Luo *et al*., 2005; Narendran *et al*., 2005). In such remote phosphor structures, it is less likely that phosphorescence impinges on the low-reflectance semiconductor chip due to the spatial separation between the primary emitter (semiconductor chip) and the secondary emitter (phosphor). The probability that phosphorescence impinges on the semiconductor chip is greatly diminished if the distance between chip and phosphor is equal to or greater than the chip's lateral dimension, i.e. $d > a$, as shown in Fig. 21.11(c). As a result, higher phosphorescence efficiency is enabled. Ray-tracing simulations and experiments using a remote blue phosphor pumped by a GaInN emitter have indeed demonstrated phosphorescence efficiency improvements of 75% and 27%, respectively (Kim *et al*., 2005; Luo *et al*., 2005). Narendran *et al*. (2005) reported an average of 61% improvement in light output by using the "scattered photon extraction" (SPE) method. At low currents, the SPE packages exceeded 80 lm/W, compared to 54 lm/W for a typical conventional package.

## *21.6 UV-pumped phosphor-based white LEDs*

White LEDs can also be fabricated with optical excitation of phosphor in the ultraviolet (UV) wavelength range (Karlicek, 1999). Semiconductor sources emitting in the near-UV (320–390 nm) and in the violet, close the edge of the visible spectrum (390–410 nm) are frequently used for such white sources. Semiconductor diodes emitting near 400 nm with remarkably high efficiencies have been reported (Morita *et al*., 2004).

For deep-UV semiconductor sources (200–320 nm), conventional phosphors, as used in fluorescent lighting, can be used for wavelength conversion. However, the large Stokes shift associated with deep-UV sources is a significant drawback for such sources. Furthermore the development of deep-UV LEDs is challenging due to the low p-type and n-type doping efficiency in AlGaN with high Al content and the difficulties encountered in epitaxially growing high-quality AlGaN with low dislocation and defect densities.

In UV-pumped white LEDs, the entire visible emission originates in the phosphor. Phosphors excited in the deep UV have been used since the 1950s in fluorescent light tubes and since the 1980s in compact fluorescent lamps (CFLs). Phosphors in fluorescent light sources are pumped by the UV emission coming from the low-pressure mercury-vapor discharge occurring inside the tube. The dominant emission of low-pressure mercury-vapor discharge lamps (***Hg lamps***) occurs in the UV at 254 nm. Phosphors with strong absorption in this wavelength range are readily available. The color rendering properties of such phosphors are very suitable for most applications.

A white LED using a UV AlGaInN LED pump source and a tricolor phosphor blend was reported by Kaufmann *et al*. (2001). The LED pump source emitted at 380–400 nm, that is, near the boundary between the visible and UV spectrum. The phosphor blend consisted of three phosphors emitting in the red, green, and blue parts of the spectrum. A color-rendering index of 78 was reported for the lamp.

The color-rendering index (CRI) of UV-excited phosphor mixes ranges between 60 and 100. Excellent CRIs as high as 97 were reported by Radkov *et al*. (2003) for phosphor blends excited near 400 nm. Furthermore, such UV-LED based sources exhibit independence of the phosphor-emission spectrum on the exact UV-LED excitation wavelength, because the visible emission is solely due to the phosphor. Consequently, UV-pumped white lamps are expected to have a highly reproducible optical spectrum so that “binning” will likely not be required. Monte Carlo simulations reported by Radkov *et al*. (2004) indeed showed a very low chromaticity point variation (entirely within the first MacAdam ellipse) for phosphor sources excited with a variety of LEDs coming from chip bins with peak wavelengths ranging between 400 nm and 410 nm. The chromaticity variation was shown to be much lower for UV-LED/phosphor sources than for blue-LED/phosphor sources.

A fundamental drawback of UV-pumped white LEDs is the energy loss (Stokes shift) incurred when converting UV light to white light. The potential luminous efficiency of UV-pumped white LED lamps is therefore markedly lower than that of white sources based on a blue



Nichia Exhibit 1014
Page 172

LED exciting a yellow phosphor.

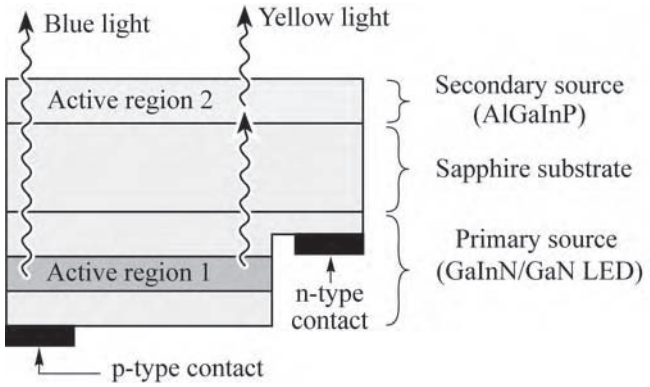


Fig. 21.13. Schematic structure of a photon-recycling semiconductor LED with one current-injected active region (Active region 1) and one optically excited active region (Active region 2) (after Guo *et al*., 1999).

### *21.7 White LEDs based on semiconductor converters (PRS-LED)*

Light-emitting diodes using semiconductor wavelength converters have been demonstrated by Guo *et al*. (1999). The schematic structure of the photon-recycling semiconductor LED (PRS-LED) is shown in Fig. 21.13. The figure indicates that a fraction of the light emitted by the blue GaInN LED is absorbed by a AlGaInP secondary active region and re-emitted (or "recycled") as lower-energy photons. In order to obtain white light, the intensity of the two light sources must have a certain ratio that will be calculated below. The schematic power budget of the device is shown in Fig. 21.14. It is assumed that the electrical input power is $P_0$, and the output powers in the blue and amber spectral range are $P_1$ and $P_2$, respectively. The power-conversion efficiency of the blue LED and the photon-recycling semiconductor are assumed to be $\eta_1$ and $\eta_2$, respectively. The efficiency and luminous efficiency of the device are calculated below.

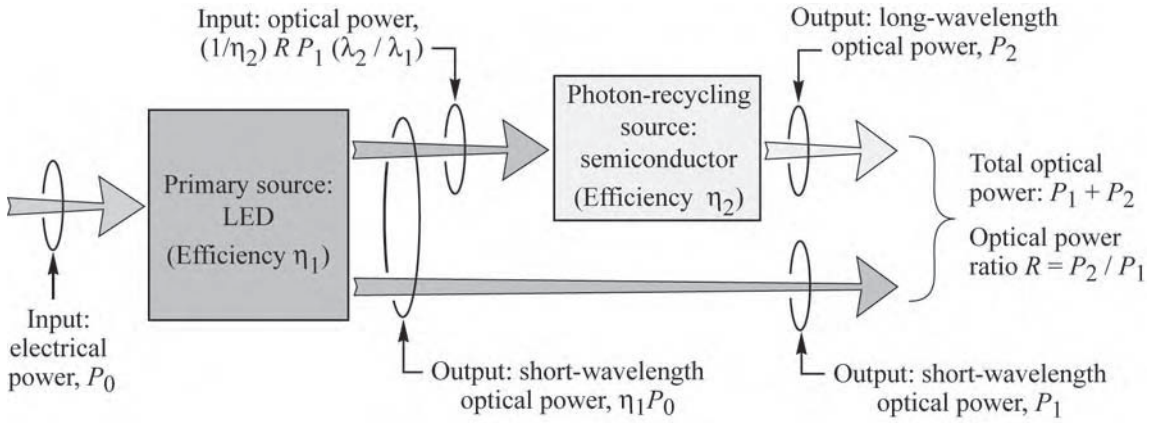


Fig. 21.14. Photon-recycling semiconductor LED power budget with electrical input power $P_0$ and optical output power $P_1$ and $P_2$.

The energy loss occurring in the photon-recycling process must be taken into account when determining the optimum choice of wavelengths for highest efficiency. Note that energy is lost even if the recycling process occurs with unit quantum efficiency. To calculate the optimum wavelength of operation, we represent white light by the Illuminant C standard, for which the chromaticity coordinates are $x_c = 0.3101$, $y_c = 0.3163$, $z_c = 0.3736$. Using these chromaticity coordinates, the pairs of complementary wavelengths can be determined.

### *21.8 Calculation of the power ratio of PRS-LED*

Next, we calculate the light-power ratio between two sources required for the emission of white light and the luminous efficiency of the photon-recycling semiconductor LED. We refer to $\lambda_1$ and $\lambda_2$ as the primary (short) and secondary (long) wavelength, respectively. For white light, $\lambda_1$ and $\lambda_2$ are pairs of complementary wavelengths. We define the color masses of the two light sources as

$$m_1 = \bar{x}_1 + \bar{y}_1 + \bar{z}_1 \qquad \text{and} \qquad m_2 = \bar{x}_2 + \bar{y}_2 + \bar{z}_2 \tag{21.6}$$

where $\bar{x}_1$, $\bar{y}_1$, $\bar{z}_1$, $\bar{x}_2$, $\bar{y}_2$, and $\bar{z}_2$ are color-matching functions at the two emission wavelengths $\lambda_1$ and $\lambda_2$, respectively (Judd, 1951; Vos, 1978; MacAdam, 1950, 1985). We define the power ratio of the two light sources as

$$R = P_2 / P_1 \tag{21.7}$$

where $P_1$ and $P_2$ are the optical powers of the short-wavelength source ($\lambda_1$) and the long-wavelength source ($\lambda_2$), respectively. The chromaticity coordinates of the newly generated color are then given by

$$y_{\text{new}} = \frac{P_1 \bar{y}_1 + P_2 \bar{y}_2}{P_1 m_1 + P_2 m_2} = \frac{\bar{y}_1 + R \bar{y}_2}{m_1 + R m_2} \tag{21.8}$$

and

$$x_{\text{new}} = \frac{\bar{x}_1 + R \bar{x}_2}{m_1 + R m_2} . \tag{21.9}$$

For a white-light emitter, $x_{\text{new}}$ and $y_{\text{new}}$ can be chosen to coincide with the chromaticity coordinates of the Illuminant C standard ($x_c = 0.3101$, $y_c = 0.3162$; CIE, 1932; Judd, 1951), i.e. $x_{\text{new}} = x_c = 0.3101$ and $y_{\text{new}} = y_c = 0.3162$. Solving Eq. (21.9) for the power ratio $R$ yields



Nichia Exhibit 1014
Page 174

$$R = \frac{\bar{y}_1 - y_c m_1}{y_c m_2 - \bar{y}_2} . \tag{21.10}$$

The power ratio as calculated from Eq. (21.10) is shown as a function of wavelength in Fig. 21.15.

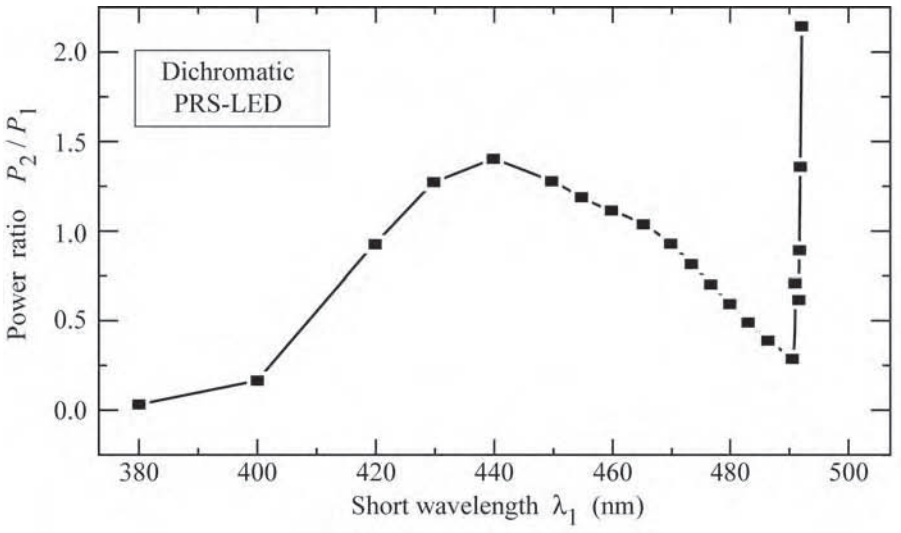


Fig. 21.15. Calculated power ratio between the two optical output powers $P_1$ and $P_2$ required to obtain white-light emission (after Guo *et al.*, 1999).

### *21.9 Calculation of the luminous efficiency of PRS-LED*

To produce the optical power $P_2$ at the wavelength of $\lambda_2$ through the recycling of photons from the primary source with wavelength $\lambda_1$, the optical power required from the primary source is given by

$$\frac{P_2}{\eta_2} \frac{\lambda_2}{hc} \frac{hc}{\lambda_1} = \frac{P_2 \lambda_2}{\eta_2 \lambda_1} \tag{21.11}$$

where $\eta_2$ is the optical-to-optical conversion efficiency of the photon-recycling light source. If $P_0$ is the electrical input power, then the optical power emitted by the primary LED source is $\eta_1 P_0$, where $\eta_1$ is the electrical-to-optical power conversion efficiency of the primary LED. Thus, the optical power emitted by the primary LED is given by

$$P_1 + \frac{P_2 \lambda_2}{\eta_2 \lambda_1} = \eta_1 P_0 . \tag{21.12}$$

Solving the equation for the electrical input power and using $P_2 = R P_1$ yields

$$P_0 = P_1 \left( \frac{1}{\eta_1} + \frac{R \lambda_2}{\eta_1 \eta_2 \lambda_1} \right) . \tag{21.13}$$

The total optical output power of the PRS-LED is given by

$$P_{\text{out}} = P_1 + P_2 = (1 + R) P_1 \tag{21.14}$$

so that the overall electrical-to-optical power efficiency of the photon-recycling dichromatic light source is given by

$$\eta = \frac{P_{\text{out}}}{P_0} = \frac{P_1 (1 + R)}{P_1 \left( \frac{1}{\eta_1} + \frac{R}{\eta_1 \eta_2} \frac{\lambda_2}{\lambda_1} \right)} = \frac{1 + R}{\frac{1}{\eta_1} + \frac{R}{\eta_1 \eta_2} \frac{\lambda_2}{\lambda_1}} . \tag{21.15}$$

The luminous flux $\Phi_{\text{lum}}$ of the device is given by

$$\Phi_{\text{lum}} = 683 \frac{\text{lm}}{\text{W}} \left( \bar{y}_1 P_1 + \bar{y}_2 P_2 \right) = 683 \frac{\text{lm}}{\text{W}} \left( \bar{y}_1 + \bar{y}_2 R \right) P_1 . \tag{21.16}$$

Then the luminous efficacy of radiation (measured in lumens per optical watt) of the photon-recycling semiconductor LED is given by

$$\frac{\Phi_{\text{lum}}}{P_{\text{out}}} = 683 \frac{\text{lm}}{\text{W}} \frac{\bar{y}_1 + \bar{y}_2 R}{1 + R} . \tag{21.17}$$

Thus, the luminous efficiency of the source (measured in lumens per electrical watt) of the PRS-LED is given by

$$\frac{\Phi_{\text{lum}}}{P_0} = 683 \frac{\text{lm}}{\text{W}} \eta \frac{\bar{y}_1 + \bar{y}_2 R}{1 + R} . \tag{21.18}$$

Using this formula, we calculate the luminous efficiency as a function of the primary wavelength. The result of the calculation is shown in Fig. 21.16 for *ideal* sources, i.e. for $\eta_1 = \eta_2 = 100\%$.

The maximum luminous efficiency occurs if the primary source emits at the wavelength 440 nm. A theoretical luminous efficiency of 336 lm/W is obtained for this wavelength. Note that in the calculation we assume that both light sources emit monochromatic light. However, the spontaneous emission from semiconductors has a 1.8 $kT$ spectral width. Taking into account a



Nichia Exhibit 1014
Page 176

finite linewidth, the expected luminous efficiency is slightly lower.

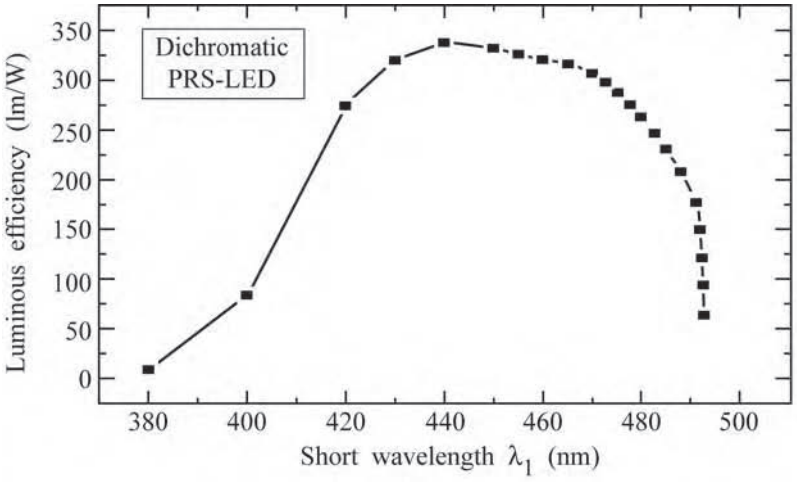


Fig. 21.16. Calculated luminous efficiency of a dichromatic PRS-LED versus its primary emission wavelength (after Guo *et al*., 1999).

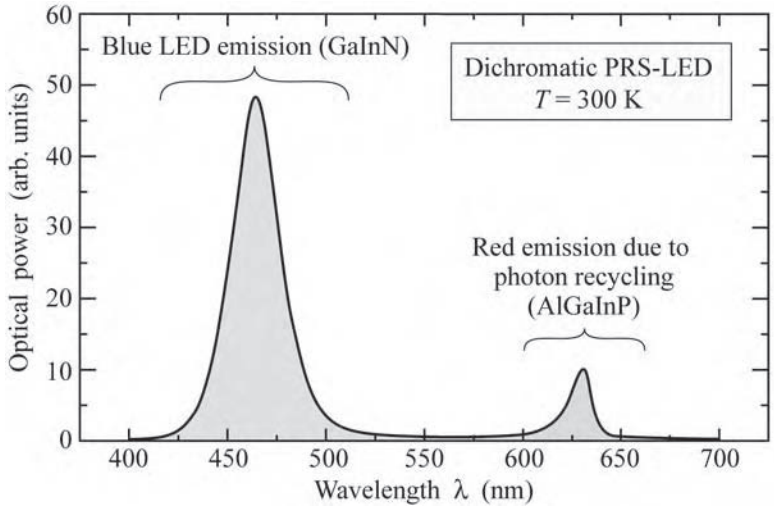


Fig. 21.17. Emission spectrum of dichromatic PRS-LED with current-injected GaInN blue LED primary source and AlGaInP photon recycling wafer (secondary source) emitting in the red (after Guo *et al*., 2000).

### *21.10 Spectrum of PRS-LED*

PRS-LEDs have been demonstrated using a GaInN/GaN LED emitting in the blue and an electrically passive AlGaInP photon-recycling semiconductor emitting in the red part of the spectrum (Guo *et al*., 1999). The emission spectrum of the device, depicted in Fig. 21.17, shows the emission line of the primary LED at 470 nm and a second emission line at 630 nm due to absorption of the 470 nm light in the AlGaInP layer and re-emission of light at 630 nm. The recycling semiconductor used in this experiment is an AlGaInP/GaAs double heterostructure. The photon-recycling semiconductor is planar and no surface texturing was performed.

To avoid absorption of light in the GaAs substrate, the GaAs substrate of the AlGaInP

epitaxial layer was removed. Firstly, the AlGaInP/GaAs recycling semiconductor was mounted on a glass slide. Subsequently, the GaAs substrate was removed by polishing and selective wet chemical etching. Then the primary LED wafer and the photon-recycling wafer were bonded together.

The approximate theoretical luminous efficiency of several types of white LED lamps is given in Table 21.2. The data show that the dichromatic light source has the highest luminous efficiency as compared to spectrally broader emitters.

| **Type of LED** | **Luminous efficiency** (lm/W) | **Chromaticity coordinates** ($x$, $y$) |
|---|---|---|
| Dichromatic PRS LED | 300–360 | (0.31, 0.32) |
| Broadened dichromatic PRS LED | 280–350 | (0.31, 0.32) |
| Trichromatic LED | 240–340 | (0.31, 0.32) |
| Phosphor-based LED | 200–280 | (0.31, 0.32) |

Table 21.2. Approximate theoretical luminous efficiencies of different types of white LEDs assuming unit quantum efficiency and the absence of resistive power losses.

Generally, dichromatic white LEDs have a higher luminous efficacy but lower color-rendering index (CRI) compared with trichromatic white LEDs. It can be shown that there is a fundamental trade-off between color rendering and the luminous efficacy of light-emitting devices (Walter, 1971). In order to improve the general CRI of dichromatic devices such as the PRS-LED, two possibilities can be considered. Firstly, the emission lines can be intentionally broadened, e.g. by compositional grading. Secondly, a second photon-recycling semiconductor can be added thus creating a trichromatic PRS-LED. However, any broadening of the two emission lines or the addition of an emission line will decrease the luminous efficacy and luminous efficiency of the device.

### *21.11 White LEDs based on dye converters*

White LEDs can also be fabricated using organic dye molecules as wavelength converter materials. The dyes can be incorporated in the epoxy encapsulant (Schlotter *et al*., 1997). Dyes can also be incorporated in optically transparent polymers.

A drawback of organic dyes is their finite lifetime. Dye molecules “bleach out”, i.e. become optically inactive, after a certain number of photon absorption events. Typically a dye molecule is stable for about $10^4$–$10^6$ optical transitions (Jones, 2000). The lack of high molecular stability



Nichia Exhibit 1014
Page 178

of dyes is a serious drawback. The lifetime of dyes is considerably shorter than the lifetime of semiconductor or phosphor wavelength converters.

Dyes have a relatively small difference between the absorption and the emission band (Stokes shift). For example, the Stokes shift for the dye *Coumarin 6* is just 50 nm, as discussed earlier in this chapter. This shift is smaller than the Stokes shift required for dichromatic white LEDs that need typical wavelength shifts of 100 nm or more, as inferred from the separation of complementary wavelengths.

## *References*


Bando K., Noguchi Y., Sakano K., and Shimizu Y. (in Japanese) *Tech. Digest, Phosphor Res. Soc*., *264th Meeting*, November 29 (1996)

CIE *Commission Internationale de l'Eclairage Proceedings, 1931* (Cambridge University Press, Cambridge, 1932)

Goetz W. "White lighting (illumination) with LEDs" *Fifth International Conference on Nitride Semiconductors*, Nara, Japan, May 25–30 (2003)

Guo X., Graff J. W., and Schubert E. F. "Photon-recycling semiconductor light-emitting diode" *IEDM Technical Digest*, **IEDM-99**, 600 (1999)

Guo X., Graff J. W., and Schubert E. F. "Photon-recycling for high brightness LEDs" *Compound Semiconductors* **6**, May/June (2000)

Holcomb M. O., Mueller-Mach R., Mueller G. O., Collins D., Fletcher R. M., Steigerwald D. A., Eberle S., Lim Y. K., Martin P. S., and Krames M. "The LED light bulb: Are we there yet? Progress and challenges for solid-state illumination" *Conference on Lasers and Electro-Optics* (*CLEO*), Baltimore, Maryland, June 1–6 (2003)

Ivey H. F. "Color and efficiency of luminescent light sources" *J. Opt. Soc. Am.* **53**, 1185 (1963)

Jones G., personal communication (2000)

Judd D. B. "Report of US secretariat committee on colorimetry and artificial daylight" in *Proceedings of the Twelfth Session of the CIE, Stockholm* Vol. **1**, p. 11 (Bureau central de la CIE, Paris, 1951)

Justel T., Nikol H., and Ronda C. R. "New developments in the field of luminescent materials for lighting and displays" *Angewandte Chemie (International Edition)* **37**, 3084 (1998)

Karlicek Jr. R. F., personal communication (1999)

Kaufmann U., Kunzer M., Köhler K., Obloh H., Pletschen W., Schlotter P., Schmidt R., Wagner J., Ellens A., Rossner W., and Kobusch M. "Ultraviolet pumped tricolor phosphor blend white emitting LEDs" *Phys. Stat. Sol. (a)* **188**, 143 (2001)

Kim J. K., personal communication (2005)

Kim J. K., Luo H., Schubert E. F., Cho J., Sone C., and Park Y. "Strongly enhanced phosphor efficiency in GaInN white light-emitting diodes using remote phosphor configuration and diffuse reflector cup" *Jpn. J. Appl. Phys. – Express Letter* **44**, L 649 (2005)

Luo H., Kim J. K., Schubert E. F., Cho J., Sone C., and Park Y. "Analysis of high-power packages for phosphor-based white-light-emitting diodes" *Appl. Phys. Lett*. **86**, 243505 (2005)

MacAdam D. L. "Maximum attainable luminous efficiency of various chromaticities" *J. Opt. Soc. Am.* **40**, 120 (1950)

MacAdam D. L. *Color Measurement: Theme and Variations* (Springer, New York, 1985)

Morita D., Yamamoto M., Akaishi K., Matoba K., Yasutomo K., Kasai Y., Sano M., Nagahama S.-I., and Mukai T. "Watt-class high-output-power 365 nm ultraviolet light-emitting diodes" *Jpn. J. Appl. Phys*. **43**, 5945 (2004)

Nakamura S., Senoh M., Iwasa N., Nagahama S., Yamada T., and Mukai T. "Superbright green InGaN single-quantum-well-structure light-emitting diodes" *Jpn. J. Appl. Phys*. (*Lett.*) **34**, L1332 (1995)

Nakamura S. and Fasol G. *The Blue Laser Diode* (Springer, Berlin, 1997)

Narendran N., Gu Y., Freyssinier-Nova J. P., and Zhu Y. "Extracting phosphor-scattered photons to

improve white LED efficiency" *Phys. Stat. Sol. (a)* **202**, R60 (2005)
Narukawa Y. "White light LEDs" *Optics & Photonics News* **15**, No. 4, p. 27 (2004)
Osram-Sylvania Corporation. Data sheet on type 4350 phosphor (2000)
Potdevin A., Chadeyron G., Boyer D., Caillier B., and Mahiou R. "Sol-gel based YAG:$Tb^{3+}$ or $Eu^{3+}$ phosphors for application in lighting sources" *J. Phys. D: Appl. Phys.* **38**, 3251 (2005)
Radkov E., Setlur A., Brown Z., and Reginelli J. "High CRI phosphor blends for near UV LED lamps" *Proc. SPIE* **5530**, 260 (2003)
Radkov E., Bompiedi R., Srivastava A. M., Setlur A. A., and Becker C. "White light with UV LEDs" *Proc. SPIE* **5187**, 171 (2004)
Reeh U., Höhn K., Stath N., Waitl G., Schlotter P., Schneider J., and Schmidt R. "Light-radiating semiconductor component with luminescence conversion element" US Patent 6,576,930 B2 (2003)
Schlotter P., Schmidt R., and Schneider J. "Luminescence conversion of blue light emitting diodes" *Appl. Phys*. *A* **64**, 417 (1997)
Schlotter P., Baur J., Hielscher C., Kunzer M., Obloh H., Schmidt R., and Schneider J. "Fabrication and characterization of GaN/InGaN/AlGaN double heterostructure LEDs and their application in luminescence conversion LEDs" *Materials Sci. Eng.* **B59**, 390 (1999)
Srivastava A. M. "Phosphors" *Encyclopedia of Physical Science and Technology* 3rd edition **11**, 855 (2004)
Srivastava A. M. and Ronda C. R. "Phosphors" *Interface (The Electrochemical Society)* **12** (2), p. 48 (2003)
Thornton W. A. "Luminosity and color-rendering capability of white light" *J. Opt. Soc. Am.* **61**, 1155 (1971)
Vos, J. J. "Colorimetric and photometric properties of a 2-degree fundamental observer" *Color Res. Appl.* **3**, 125 (1978)
Walter W. "Optimum phosphor blends for fluorescent lamps" *Appl. Opt.* **10**, 1108 (1971)
Wegh R. T., Donker H., Oskam K. D., and Meijerink A. "Visible quantum cutting in $LiGdF_4$:$Eu^{3+}$ through downconversion" *Science* **283**, 664 (1999)



Nichia Exhibit 1014
Page 180